

國立交通大學

電信工程研究所

博士論文

具低阻抗及強耦合之改良微帶線  
及被動元件之應用



Modified Microstrip Lines with Low  
Impedance and Enhanced Coupling for  
Applications in Passive Circuits

研究生：梁正憲 (Cheng-Hsien Liang)

指導教授：張志揚 (Chi-Yang Chang)

中華民國 一 百 年 七 月

具低阻抗及強耦合之改良微帶線  
及被動元件之應用

Modified Microstrip Lines with Low Impedance  
and Enhanced Coupling for Applications in  
Passive Circuits

研究生：梁正憲

Student: Cheng-Hsien Liang

指導教授：張志揚 博士

Advisor: Dr. Chi-Yang Chang



A Dissertation  
Submitted to Institute of Communication Engineering  
College of Electrical and Computer Engineering  
National Chiao Tung University  
in Partial Fulfillment of the Requirements  
for the Degree of Doctor of Philosophy  
in  
Communication Engineering  
Hsinchu, Taiwan

2011 年 7 月

# 具低阻抗及強耦合之改良微帶線及被動元件之應用

研究生：梁正憲

指導教授：張志揚 博士

國立交通大學電信工程研究所

## 摘要

本論文首先提出一種新的低阻抗微帶線結構，在傳統的微帶線內部加入接地線，使得微帶線的特性阻抗值可以由在同一平面上的訊號線及接地線所控制，以此來提升微帶線的等效電容值，使得其特性阻抗值較同樣線寬的傳統微帶線為低，此種方式對於降低厚基板特性阻抗值特別顯著，此外，我們也將訊號線加入至傳統微帶線的地，來更為降低微帶線的特性阻抗值，將此種微帶線結構應用在四分之一波長的步階阻抗諧振腔上，以此來製作對製程誤差較不敏感的小型化濾波器，同時也使得濾波器有更小的尺寸及較寬的上截止帶響應；接著，我們提出了數種可以提供強耦合量的微帶線耦合結構，分別將其應用在小型化的寬頻濾波器和單節及多節的 3-dB 方向耦合器上，雖然本論文所提出的電路結構需要有較多的導通孔，但是均可以使用標準的印刷電路板製程在一般的單層基板上完成，因此電路具有容易製作及低成本的優點。

# **Modified Microstrip Lines with Low Impedance and Enhanced Coupling for Applications in Passive Circuits**

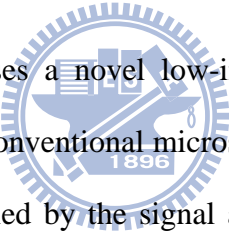
Student : Cheng-Hsien Liang

Advisor : Dr. Chi-Yang Chang

Institute of Communication Engineering

National Chiao Tung University

## **Abstract**



This dissertation first proposes a novel low-impedance microstrip line structure. By inserting ground strips inside the conventional microstrip line, the characteristic impedance of the microstrip line can be controlled by the signal and ground strips in a coplanar manner. Compared to the conventional microstrip line with the same transverse width, the effective capacitance of the microstrip line increases so that the characteristic impedance decreases. The decreasing amount is particularly large for the thick substrate. In addition, we also insert signal strips in the microstrip ground plane to further decrease the characteristic impedance. The low-impedance microstrip line is applied in the quarter-wavelength stepped-impedance resonator. The designed filter can be insensitive to fabrication tolerances and have a smaller size and a wider upper stopband. Then, we propose several coupled microstrip line structures which can provide strong coupling. These tight-coupling structures are used to design miniaturized wideband bandpass filters and single- and multi-section 3-dB directional couplers. Although the proposed circuits need more via-holes, they can be easily fabricated on a single-layer substrate by the conventional printed circuit board (PCB) process with low cost.

## 誌 謝

在近四年的博士班生涯中，能夠順利取得博士學位，首先要感謝我的指導教授張志揚博士，從大學三年級開始跟隨老師做專題，將近八年的時間裡，老師不但在專業研究領域中給我莫大的教導與幫助，而且其豁達樂觀的處世態度，更是我學習的對象，老師對於大自然及腳踏車的熱愛，讓我在辛苦做研究之餘也可以適時放鬆心情，跟隨老師遊山玩水；我也要感謝口試委員陳俊雄教授、吳瑞北教授、王暉教授、郭仁財教授、江逸群教授、湯敬文教授、鍾世忠教授以及孟慶宗教授，他們提供了寶貴的意見及指正，使論文更加豐富完整。

感謝實驗室博士班共同奮鬥的伙伴們維欣、金雄、益廷、建育、昀緯，祝福你們在追求夢想的道路上順利，也要感謝歷屆的碩士班學弟妹們鵬達、懿萱、宛蓉、祥容、梓淳、義傑、仕鈺、弘偉…等，有了大家的陪伴，使得實驗室充滿歡樂的氣氛，讓博士班的生活增添不少樂趣；我也要感謝求學過程中眾多的好友們翰丞、智仁、勝凱、文傑…等，以及登山隊的伙伴們俊哥、阿樸、英公、小胖、小花，一路上要感謝的朋友真的太多了，謝謝大家，有你們的陪伴真好。

我要感謝眾多疼愛我的親人們，有了你們的支持和鼓勵，讓我在求學路上即使遇到挫折時仍舊充滿信心不放棄，特別是台南年邁的外婆心中一直掛念著我何時才能拿到博士學位，如今她臉上終於露出了久久不見的笑容；特別感謝維欣在我口試當天一早起來辛苦為口試委員們所準備的水果，還有在新竹科學園區工作的弟弟正勳特地於百忙之中請假來幫忙我打理口試的一切，有了你們二位的協助，使得畢業論文口試可以順利圓滿結束，也謝謝修真在畢業典禮上所贈送親手完成的又大又香的花束，美麗的花朵讓實驗室飄香芬芳了好幾天，最後，我想將這篇論文，獻給辛苦養育我的父親—梁進通，母親—梁郭貴滿，讓我可以無後顧之憂完成博士學位。

梁正憲 於新竹交大

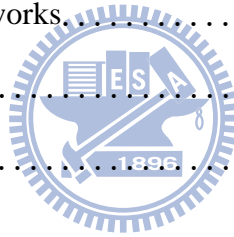
2011年7月22日

# Contents

Abstract (Chinese).....	i
Abstract.....	ii
Acknowledgment.....	iii
Contents.....	iv
List of Tables.....	vii
List of Figures.....	viii
Chapter 1 Introduction.....	1
1.1 Research motivation.....	2
1.2 Literature survey.....	3
1.3 Contribution.....	6
1.4 Organization.....	7
Chapter 2 Fundamental theory and design of coupled-resonator filters and coupled lines.....	9
2.1 Coupled resonator theory.....	9
2.1.1 Lowpass filter prototype.....	9
2.1.2 Impedance ( $K$ ) and admittance ( $J$ ) inverters.....	9
2.1.3 Impedance scaling and frequency transformation.....	12
2.1.4 Reactance and susceptance slope parameters.....	14
2.1.5 Design equations for coupled-resonator bandpass filters.....	15
2.1.6 Extraction of the external quality factor and coupling coefficient.....	16
2.1.7 Chebyshev and quasi-elliptic filters.....	17
2.2 Resonance properties of the $\lambda/4$ SIR.....	20
2.3 Microstrip line and coupled microstrip lines.....	22
2.3.1 Single microstrip line.....	22

2.3.2 Coupled microstrip lines. . . . .	24
2.3.3 Coupled line coupler. . . . .	26
Chapter 3 Novel low-impedance microstrip line for quarter-wavelength stepped-impedance resonator filters. . . . .	31
3.1 Fabrication-tolerant microstrip quarter-wavelength SIR filter. . . . .	31
3.1.1 New modified microstrip structure. . . . .	33
3.1.2 Characteristics of the proposed $\lambda/4$ SIR. . . . .	34
3.1.3 Four-pole cross-coupled filter design. . . . .	43
3.1.4 Sensitivity to etching tolerances. . . . .	49
3.2 Miniaturized microstrip quarter-wavelength SIR filter. . . . .	55
3.2.1 Analysis of the proposed structure. . . . .	55
3.2.2 Four-pole cross-coupled filter design. . . . .	57
3.3 Resonance of the low-impedance section of the SIR. . . . .	62
3.4 Discussion of the number of via-holes. . . . .	67
3.5 Summary. . . . .	69
Chapter 4 Interdigital coupling structures for wideband stepped-impedance resonator filters. . . . .	70
4.1 Interdigital coupled microstrip lines. . . . .	70
4.2 Proposed SIR configuration I. . . . .	71
4.2.1 Structure of the resonator. . . . .	71
4.2.2 Four-pole Chebyshev filter (filter I). . . . .	72
4.2.3 Four-pole generalized Chebyshev filter (filter II). . . . .	77
4.2.4 Resonance of the circumference of the low-impedance section. . . . .	79
4.3 Proposed SIR configuration II. . . . .	82
4.3.1 Structure of the resonator. . . . .	82
4.3.2 Four-pole bandpass filter design. . . . .	83

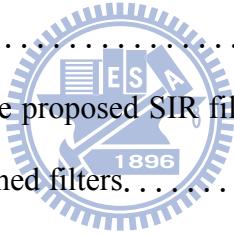
4.4 Summary.....	91
Chapter 5 Enhanced coupling structures for tight couplers and wideband filters.....	92
5.1 Proposed coupled-line structures.....	93
5.1.1 Type I.....	93
5.1.2 Type II.....	98
5.2 Wideband quarter-wavelength parallel-coupled filter.....	101
5.3 Wideband quarter-wavelength hairpin filter.....	107
5.4 Single-section 3-dB directional coupler.....	112
5.5 Three-section 3-dB directional coupler.....	118
5.6 Five-section 3-dB directional coupler.....	123
5.7 Summary.....	129
Chapter 6 Conclusion and future works.....	131
6.1 Conclusion.....	131
6.2 Future works.....	132
References.....	134





## *List of Tables*

Table 3-1 Characteristic impedance ( $\Omega$ ) for different numbers of inserted ground strips (Total line width is kept constant as 3 mm.). . . . .	34
Table 3-2 Design parameters of the proposed SIR filters. . . . .	43
Table 3-3 Dimensions of the designed filters. . . . .	45
Table 3-4 Comparison of measured passband insertion losses for the conventional and proposed SIR filters. . . . .	50
Table 3-5 Sensitivity to etching tolerances in terms of the percentage deviation of the center frequency for the conventional and proposed SIR filters. . . . .	54
Table 3-6 Characteristic impedance ( $\Omega$ ) of the conventional and proposed microstrip lines. . . . .	57
Table 3-7 Design parameters of the proposed SIR filters. . . . .	58
Table 3-8 Dimensions of the designed filters. . . . .	59
Table 3-9 Fabricated filters and measured results. . . . .	62
Table 5-1 Dimensions (in millimeters) of the three-section directional coupler. . . . .	120
Table 5-2 Design parameters of the five-section directional coupler. . . . .	123
Table 5-3 Dimensions (in millimeters) of the five-section directional coupler. . . . .	127



## *List of Figures*

Fig. 1-1. Cross-sectional view of the conventional microstrip line. . . . .	3
Fig. 1-2. Cross-sectional views of the symmetric coupled microstrip lines. (a) Conventional. (b) Modified with the ground-plane aperture. . . . .	4
Fig. 2-1. Lowpass filter prototypes and their element definitions. (a) Prototype beginning with a shunt element. (b) Prototype beginning with a series element. . . . .	10
Fig. 2-2. Lowpass filter prototypes with (a) $K$ -inverters and (b) $J$ -inverters. . . . .	11
Fig. 2-3. Bandpass filters using (a) $K$ -inverters and (b) $J$ -inverters. . . . .	13
Fig. 2-4. Generalized bandpass filters with distributed elements and (a) $K$ -inverters. (b) $J$ -in- verters. . . . .	15
Fig. 2-5. (a) Phase response of $S_{11}$ for the input and output coupling structures. (b) Resonant response of the coupled resonator pair. . . . .	17
Fig. 2-6. (a) Coupling diagram and (b) frequency response for the four-pole Chebyshev filter. . . . . .	18
Fig. 2-7. (a) Coupling diagram and (b) frequency response for the four-pole quasi-elliptic filter. . . . .	20
Fig. 2-8. (a) Conventional $\lambda/4$ microstrip SIR. (b) Normalized length and (c) normalized spurious frequency versus impedance ratio for $\theta_1 = \theta_2$ . . . . .	21
Fig. 2-9. Capacitance representation of a conventional microstrip line. . . . .	23
Fig. 2-10. Quasi-TEM modes of the conventional coupled microstrip lines. (a) Even mode. (b) Odd mode. . . . .	24
Fig. 2-11. Single-section microstrip coupled line coupler. . . . .	26
Fig. 2-12. Equivalent circuit for the even-odd mode analysis. . . . .	26
Fig. 2-13. $N$ -section symmetric multisection coupled line coupler. . . . .	30

- Fig. 3-1. (a) Conventional  $\lambda/4$  microstrip SIR. Dashed lines represent etching errors. (b) Normalized resonant frequency versus the percentage variation of the impedance ratio. .... 32
- Fig. 3-2. (a) Top view of the proposed microstrip structure. (b) Cross-sectional view of the circled portion in (a). .... 33
- Fig. 3-3. (a) Proposed  $\lambda/4$  microstrip SIR. (b) Comparison of the frequency responses of the resonators with one and two via-holes on the ends of each inserted ground strip. . . . . 35
- Fig. 3-4. Impedance ratio  $R$  of the conventional and proposed  $\lambda/4$  SIRs versus substrate thickness  $h$  and width  $W_L$  (in millimeters) for: (a)  $\epsilon_r = 3.6$ , (b)  $\epsilon_r = 6.8$ , and (c)  $\epsilon_r = 10.2$ . Conventional: solid line. Proposed: dashed line. (circle  $\bigcirc$ :  $W_L = 1.35$ ,  $N = 1$ ; triangle  $\triangle$ :  $W_L = 2.4$ ,  $N = 2$ ; cross  $\times$ :  $W_L = 3.45$ ,  $N = 3$ ; asterisk  $*$ :  $W_L = 4.5$ ,  $N = 4$ ; square  $\square$ :  $W_L = 5.55$ ,  $N = 5$ ; diamond  $\diamond$ :  $W_L = 6.6$ ,  $N = 6$ ). . . . . 37
- Fig. 3-5. Impedance ratio  $R$  versus substrate thickness  $h$  for the proposed  $\lambda/4$  SIRs with different numbers of inserted ground strips when  $W_L = 3.45$  mm. (a)  $\epsilon_r = 3.6$ . (b)  $\epsilon_r = 6.8$ . (c)  $\epsilon_r = 10.2$ . ( $N$ : number of inserted ground strips.  $N = 0$ : conventional microstrip structure.). .... 38
- Fig. 3-6. Sensitivity to etching tolerances for the conventional and proposed  $\lambda/4$  SIRs with various values of the substrate thickness  $h$  (in millimeters) when  $W_L = 3.45$  mm. (a)  $\epsilon_r = 3.6$ . (b)  $\epsilon_r = 6.8$ . (c)  $\epsilon_r = 10.2$ . Conventional: solid line. Proposed ( $N = 3$ ): dashed line. Positive: under-etching. Negative: over-etching. (circle  $\bigcirc$ :  $h = 0.5$ ; triangle  $\triangle$ :  $h = 0.625$ ; cross  $\times$ :  $h = 1$ ; square  $\square$ :  $h = 1.25$ ; diamond  $\diamond$ :  $h = 1.5$ ). .... 40
- Fig. 3-7. Sensitivity to etching tolerances for the proposed  $\lambda/4$  SIRs with different numbers of inserted ground strips. (Case I:  $W_L = 3.45$  mm,  $W_{SI} = W_I = 0.3$  mm, and  $W_G =$

$W_H = 0.225$ mm. Case II: $W_L = 3.4$ mm, $W_{SI} = W_I = 0.25$ mm, $W_G = 0.275$ mm, and $W_H = 0.175$ mm.) (a) Case I: $h = 0.5$ mm. (b) Case I: $h = 1.5$ mm. (c) Case II: $h = 0.5$ mm. (d) Case II: $h = 1.5$ mm. ( $N$ : number of inserted ground strips. $N = 0$ : conventional microstrip structure.). . . . .	43
Fig. 3-8. Coupling structures for: (a) electric coupling and (b) magnetic coupling. . . . .	45
Fig. 3-9. Coupling coefficients of the coupling structures for: (a) electric coupling and (b) magnetic coupling. . . . .	45
Fig. 3-10. Proposed layout of the four-pole cross-coupled filter. . . . .	46
Fig. 3-11. Photograph of the fabricated circuit (filter I). . . . .	46
Fig. 3-12. Simulated (dashed line) and measured (solid line) results ( $ S_{11} $ and $ S_{21} $ ) of filter I. (a) Narrowband responses. (b) Wideband responses. . . . .	47
Fig. 3-13. Photograph of the fabricated circuit (filter II). . . . .	48
Fig. 3-14. Simulated (dashed line) and measured (solid line) results ( $ S_{11} $ and $ S_{21} $ ) of filter II. (a) Narrowband responses. (b) Wideband responses. . . . .	49
Fig. 3-15. Current distribution of the proposed filter at the center frequency. . . . .	50
Fig. 3-16. Measured sensitivity to etching tolerances for the proposed SIR filter. (a) Filter I. (b) Filter II (over: over-etching; under: under-etching). . . . .	51
Fig. 3-17. Measured sensitivity to etching tolerances for the conventional SIR filter ( $W_L$ and $W_H$ are the same as those of the proposed filter). (a) Filter I. (b) Filter II (over: over-etching; under: under-etching). . . . .	52
Fig. 3-18. Measured sensitivity to etching tolerances for the conventional SIR filter ( $R$ and $W_H$ are the same as those of the proposed filter). (a) Filter I. (b) Filter II (over: over-etching; under: under-etching). . . . .	53
Fig. 3-19. Proposed microstrip structure. (a) Top view. (b) Bottom view. (c) Cross-sectional view. . . . .	56
Fig. 3-20. Proposed $\lambda/4$ microstrip SIR. . . . .	57

Fig. 3-21. Proposed layout of the four-pole cross-coupled filter. . . . .	58
Fig. 3-22. (a) Top view (left side) and bottom view (right side) of the fabricated filter I. (b) Narrowband responses. (c) Wideband responses. (simulation: dashed line; measurement: solid line.). . . . .	60
Fig. 3-23. (a) Top view (left side) and bottom view (right side) of the fabricated filter II. (b) Narrowband responses. (c) Wideband responses. (simulation: dashed line; measurement: solid line.). . . . .	61
Fig. 3-24. Resonant response of the proposed SIR in Section 3.1. . . . .	62
Fig. 3-25. Current distributions of the resonances (a) $f_{p1}$ and (b) $f_{p2}$ in Fig. 3-24. Elimination of the resonances of the circumference via (c) a bond-wire or (d) a signal strip on the bottom layer. . . . .	64
Fig. 3-26. (a) Current distribution of the resonance $f_{p3}$ in Fig. 3-24. Elimination of the resonance $f_{p3}$ via (b) two bond-wires or (c) two signal strips on the bottom layer. . . . .	64
Fig. 3-27. (a) Current distribution of the resonance $f_{p4}$ in Fig. 3-24. Elimination of the resonance $f_{p4}$ via three via-holes and (b) a bond-wire or (c) a signal strip on the bottom layer. . . . .	65
Fig. 3-28. SIR with three via-holes on each inserted ground strip and either (a) a bond-wire or (b) a signal strip on the ground plane to eliminate unwanted resonances. (c) Resonant response of the SIR in (a) or (b) . . . . .	66
Fig. 3-29. Current distributions of the resonances (a) $f_1$ , (b) $f_2$ , and (c) $f_3$ in Fig. 3-28. . . . .	67
Fig. 3-30. (a) SIRs with one to five via-holes on each inserted ground strip. (b) Comparison of the resonant responses of the SIRs in (a) . . . . .	68
Fig. 4-1. Two interdigital coupling structures for wideband filter design. . . . .	71
Fig. 4-2. Proposed $\lambda/4$ SIR configuration I. (a) Top view. (b) Bottom view ( $N = 2$ ). . . . .	72
Fig. 4-3. Configuration of the proposed filter I. (a) Top-layer layout. (b) Bottom-layer layout.	

Filter Dimensions (in millimeters): $L_Q = 11.9$ , $L_{H1} = 14.45$ , $L_{H2} = 13.525$ , $L_C = 12.5$ , $L_M = 3.25$ , $W_H = W_C = 0.25$ , $W_L = 3.45$ , $W_S = 1.05$ , and $S = d = 0.15$ . . . . .	73
Fig. 4-4. Design curves for the proposed filter I. (a) External quality factor $Q_e$ . (b) Electric coupling $k_{12}$ and $k_{34}$ . (c) Magnetic coupling $k_{23}$ . . . . .	75
Fig. 4-5. Top view (left side) and bottom view (right side) of the fabricated filter I. . . . .	76
Fig. 4-6. Simulated (dashed line) and measured (solid line) results of filter I. (a) Scattering parameters. (b) Passband group delay. . . . .	77
Fig. 4-7. Configuration of the proposed filter II. (a) Top-layer layout. (b) Bottom-layer layout. units: mm. . . . .	78
Fig. 4-8. Top view (left side) and bottom view (right side) of the fabricated filter II. . . . .	79
Fig. 4-9. Simulated (dashed line) and measured (solid line) results of filter II. (a) Scattering parameters. (b) Passband group delay. . . . .	80
Fig. 4-10. (a) Current distribution of the resonance of the circumference. (b) Elimination of the resonance in (a). . . . .	81
Fig. 4-11. Proposed $\lambda/4$ SIR configuration II. . . . .	82
Fig. 4-12. Normalized first spurious resonant frequency versus finger number $N$ , finger length $L_F$ , and width $W_L$ . . . . .	83
Fig. 4-13. Coupling structures for: (a) electric coupling and (b) magnetic coupling. . . . .	84
Fig. 4-14. Proposed layout of filter I. units: mm. . . . .	85
Fig. 4-15. Coupling coefficients of the coupling structures for: (a) electric coupling and (b) magnetic coupling. . . . .	86
Fig. 4-16. Photograph of the fabricated filter I. . . . .	86
Fig. 4-17. Simulated (dashed line) and measured (solid line) results of filter I. (a) Scattering parameters. (b) Passband group delay. . . . .	87

Fig. 4-18. Proposed layout of filter II. units: mm. ....	88
Fig. 4-19. Photograph of the fabricated filter II. ....	89
Fig. 4-20. Simulated (dashed line) and measured (solid line) results of filter II. (a) Scattering parameters. (b) Passband group delay. ....	90
Fig. 5-1. Proposed coupled microstrip lines of type I. (a) Top view. (b) Bottom view. (c) Cross-sectional view. ....	93
Fig. 5-2. Quasi-TEM modes of the proposed coupled microstrip lines (type I). (a) Even mode. (b) Odd mode. ....	95
Fig. 5-3. Coupling factor $C$ versus microstrip line width $W$ for two aperture sizes $W_R = 1.65$ mm (circle $\bigcirc$ ) and 2.85 mm (triangle $\triangle$ ). Conventional (Fig. 1-2(a)): dashed-dotted line. Modified with the ground-plane aperture (Fig. 1-2(b)): dashed line. Proposed: solid line. ....	96
Fig. 5-4. Comparison of the coupling factor $C$ for three different coupled lines with two aperture sizes $W_R = 1.65$ mm (circle $\bigcirc$ ) and 2.85 mm (triangle $\triangle$ ). Structure in [62]: dashed-dotted line. Proposed without via-holes: dashed line. Proposed with via-holes: solid line. ....	98
Fig. 5-5. Proposed coupled microstrip lines of type II. (a) Top view. (b) Bottom view. (c) Cross-sectional view. ....	99
Fig. 5-6. Quasi-TEM modes of the proposed coupled microstrip lines (type II). (a) Even mode. (b) Odd mode. ....	100
Fig. 5-7. Comparison of the (a) even- and odd-mode impedances ( $Z_e, Z_o$ ) and (b) coupling factor $C$ versus microstrip line width $W$ for types I (dashed line) and II (solid line) with two aperture sizes $W_R = 1.65$ mm (circle $\bigcirc$ ) and 2.85 mm (triangle $\triangle$ ) ...	101
Fig. 5-8. Even- and odd-mode impedances ( $Z_e, Z_o$ ) and effective dielectric constants ( $\epsilon_{ree}, \epsilon_{reo}$ ) versus normalized values $W/h, W_R/h, W_S/h, S/h, S_G/h,$ and $S_R/h$ . (a) $W_R/h = 3.5,$	

$S/h = S_G/h = 0.5$ , and  $(W_S + S_R)/h = 1.5$ . (b)  $W_R/h = 4.1$ ,  $S/h = S_G/h = 0.5$ , and  $(W_S + S_R)/h = 1.8$ . (c)  $W_R/h = 4.1$ ,  $S/h = S_G/h = 1.1$ , and  $(W_S + S_R)/h = 1.5$   
 ..... 103

Fig. 5-9. Configuration of the four-pole  $\lambda/4$  parallel-coupled filter. (a) Top-layer layout. (b) Bottom-layer layout. Filter dimensions:  $L_1 = 22.8$  mm,  $L_2 = 4.8$  mm,  $L_3 = 2.35$  mm,  $L_Q = 1.55$  mm,  $L_M = 6.55$  mm,  $L_{S1} = 21.9$  mm,  $S_1 = S_G = 0.55$  mm,  $S_T = 0.15$  mm,  $S_R = 0.25$  mm,  $W = 1.1$  mm,  $W_S = 0.5$  mm, and  $W_T = 0.3$  mm  
 ..... 104

Fig. 5-10. Top view and bottom view of the fabricated  $\lambda/4$  parallel-coupled filter. .... 105

Fig. 5-11. Simulated (dashed line) and measured (solid line) results of the  $\lambda/4$  parallel-coupled filter. (a) Scattering parameters. (b) Passband group delay. .... 106

Fig. 5-12. Measured sensitivity to etching tolerances for the  $\lambda/4$  parallel-coupled filter (over: over-etching; under: under-etching) ..... 106

Fig. 5-13. Proposed  $\lambda/4$  hairpin resonator. (a) Top view. (b) Bottom view. .... 108

Fig. 5-14. Coupling structures and design curves for the proposed  $\lambda/4$  hairpin filter. (a) Electric coupling and (b) magnetic coupling. .... 109

Fig. 5-15. Configuration of the proposed four-pole  $\lambda/4$  hairpin filter. (a) Top-layer layout. (b) Bottom-layer layout. Filter dimensions:  $L_1 = 15.5$  mm,  $L_2 = 2.5$  mm,  $L_3 = 14.35$  mm,  $L_Q = 11.1$  mm,  $L_M = 1.65$  mm,  $L_{S1} = 14.6$  mm,  $L_{S2} = 13.45$  mm,  $W = 0.75$  mm,  $W_S = 0.3$  mm, and  $S_1 = S_2 = S_R = S_G = 0.15$  mm. .... 110

Fig. 5-16. Top view (left side) and bottom view (right side) of the fabricated  $\lambda/4$  hairpin filter.  
 ..... 111

Fig. 5-17. Simulated (dashed line) and measured (solid line) results of the  $\lambda/4$  hairpin filter. (a) Scattering parameters. (b) Passband group delay. .... 112

Fig. 5-18. Even- and odd-mode impedances ( $Z_e, Z_o$ ) and effective dielectric constants ( $\epsilon_{ree}$ ,



$\epsilon_{reo}$ ) versus normalized values  $W/h$ ,  $W_R/h$ ,  $W_S/h$ ,  $S/h$ ,  $S_G/h$ , and  $S_R/h$ . (a)  $W_R/h = 4.1$ ,  $S/h = S_G/h = 0.3$ , and  $(W_S + S_R)/h = 1.9$ . (b)  $W_R/h = 4.7$ ,  $S/h = S_G/h = 0.3$ , and  $(W_S + S_R)/h = 2.2$ . (c)  $W_R/h = 4.4$ ,  $S/h = S_G/h = 0.6$ , and  $(W_S + S_R)/h = 1.9$ ..... 114

Fig. 5-19. Configuration of the proposed 3-dB coupler. (a) Top-layer layout. (b) Bottom-layer layout. Coupler dimensions:  $L_1 = 35.95$  mm,  $L_2 = 33.75$  mm,  $L_{S1} = 32.85$  mm,  $L_{S2} = 31.5$  mm,  $S_1 = S_2 = S_T = S_G = 0.15$  mm,  $S_R = 0.5$  mm,  $W = 0.75$  mm,  $W_S = 0.6$  mm,  $W_T = 0.3$  mm, and  $W_R = 0.15$  mm..... 115

Fig. 5-20. Top view and bottom view of the fabricated coupler..... 115

Fig. 5-21. Simulated (dashed line) and measured (solid line) results of the coupler. (a) Insertion losses  $|S_{21}|$  and  $|S_{31}|$ . (b) Return loss  $|S_{11}|$  and isolation  $|S_{41}|$ . (c) Phase difference between the coupled and through ports..... 117

Fig. 5-22. Measured sensitivity to etching tolerances for the proposed 3-dB coupler (over: over-etching; under: under-etching)..... 118

Fig. 5-23. Schematic of the tight-coupling section (section 2) ..... 119

Fig. 5-24. Design chart for the tight-coupling section with  $S = 0.15$  mm..... 119

Fig. 5-25. Simulated response of the proposed three-section directional coupler..... 120

Fig. 5-26. Top view and bottom view of the fabricated three-section directional coupler..... 121

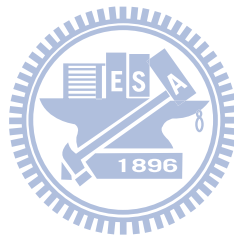
Fig. 5-27. Measured response of the three-section directional coupler..... 121

Fig. 5-28. Simulated and measured amplitude and phase imbalances between the coupled and through ports. (a) Amplitude imbalance. (b) Phase imbalance..... 122

Fig. 5-29. Cross-sectional view of the enhanced coupling structure in sections 2 and 4..... 123

Fig. 5-30. Even- and odd-mode impedances ( $Z_e$ ,  $Z_o$ ) and effective dielectric constants ( $\epsilon_{re}$ ,  $\epsilon_{ro}$ ) versus normalized values  $S/h$  and  $W/h$  for  $S_R/h = 0.3$  and  $W_S/h = 0.6$ . (a)

Even-mode. (b) Odd-mode. ....	125
Fig. 5-31. Cross-sectional view of the enhanced coupling structure in section 3. ....	125
Fig. 5-32. Even- and odd-mode impedances ( $Z_e, Z_o$ ) and effective dielectric constants ( $\epsilon_{re}, \epsilon_{ro}$ ) versus normalized values $W/h$ and $W_R/h$ for $S/h = 0.3$ . (a) Even-mode. (b) Odd-mode. ....	126
Fig. 5-33. Top view and bottom view of the fabricated five-section directional coupler. ....	127
Fig. 5-34. Simulated result of the five-section directional coupler. ....	128
Fig. 5-35. Measured result of the five-section directional coupler. ....	128
Fig. 5-36. (a) Amplitude difference between the coupled and through ports. (b) Phase difference between the coupled and through ports. ....	129



## *Chapter 1 INTRODUCTION*

A microstrip line is one of the most popular transmission lines and plays an important role in commercialized portable devices and microwave systems. The advantages of a microstrip line are: 1) planar structure; 2) easy fabrication by photolithographic processes for low cost; and 3) easy integration with passive and active microwave devices. Due to the rapid growth in modern wireless communication systems, passive components such as filters, directional couplers, and etc., are largely constructed by a microstrip line for easy integration into the printed circuit board (PCB). However, fabrication tolerances and limitations in the conventional PCB process seriously limit the application of a microstrip line.

Filters are essential components in microwave systems. The trend of bandpass filters (BPFs) is toward compact size, low cost, high selectivity, and wide stopband. Another important issue regarding the narrowband filter design is the low sensitivity to fabrication tolerances, especially for some resonator structures. Recently, wideband communication systems attract much attention for the high data-rate capacity. To design passive components for wideband applications, tightly coupled lines are usually required to obtain strong coupling. Generally speaking, due to fabrication limitations, it is difficult to implement a microstrip filter with the fractional bandwidth larger than 20% and a microstrip directional coupler with a 3-dB coupling on a commonly used single-layer substrate (for example, a RO4003 substrate with a dielectric constant of 3.58 and a thickness of 0.508 mm). In this chapter, we discuss the difficulties to realize fabrication-tolerant filters, wideband filters, and tightly coupled lines using the conventional microstrip line and coupled microstrip lines. Previous studies for compact filters, wideband filters, and tight couplers are described and summarized. Finally, we give an outline of this dissertation.

## 1.1 Research Motivation

High performance BPFs have become more and more important in recent years due to the rapid growth in modern wireless communication systems. The microstrip filter plays an important role in modern filter applications due to its planar structure and suitability for circuit integration. Recently, the stepped-impedance resonator (SIR) filter has been a hot topic because of its ability to reduce the circuit size and to improve the upper stopband performance. Theoretical analysis reveals that the fundamental frequency and the first spurious frequency of the SIR are mainly controlled by the impedance ratio of the high- and low-impedance line sections. As a result, small fabrication errors may cause a large variation of the impedance ratio, which will degrade the filter performance seriously. Although numerous studies have been performed on the advantages of SIRs, how to decrease the effect of fabrication tolerances is still critically lacking.

Next generation wireless systems and high data-rate communication systems require wideband components. However, it is difficult to achieve moderate to tight coupling in the conventional coupled microstrip lines due to the minimum allowable line width and gap spacing. This causes a challenge to design wideband BPFs and tight couplers. In addition, for wideband BPFs, the first spurious frequency should be far apart from the center frequency, or the stopband rejection may be poor. Therefore, strong coupling strength and wide spurious-free performance are the two challenges to design small wideband BPFs. On the other hand, a directional coupler with a 3-dB coupling is usually required in practical applications. The high even-mode impedance and the low odd-mode impedance lead to the very narrow line width and gap spacing, especially for the multisection 3-dB directional coupler.

This dissertation is to demonstrate several novel microstrip lines and coupled microstrip lines to overcome the drawbacks described above. Fabrication-tolerant filters, small wideband filters, and 3-dB directional couplers are experimented on the basis of the proposed structures.

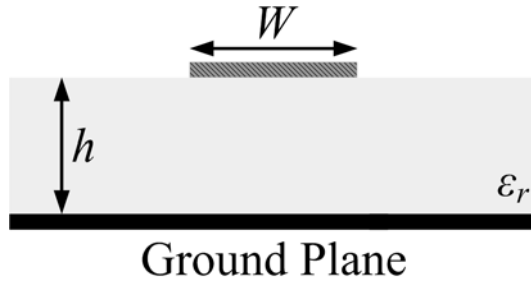


Fig. 1-1. Cross-sectional view of the conventional microstrip line.

In addition, to facilitate the implementation process and to minimize the fabrication cost, all the circuits should be able to realize on a single-layer substrate by the conventional PCB process.

## 1.2 Literature Survey

A microstrip line, as shown in Fig. 1-1, supports a quasi-TEM mode of propagation and is widely applied to design microwave circuits, such as filters, couplers, and etc. The microstrip parallel-coupled filter proposed by Cohn [1] in 1958 has been extensively used in the microwave area because of its planar structure, insensitivity to fabrication tolerances, and well-known synthesis method. However, there are two drawbacks limiting the application of this type of filter. One is that the whole length of the filter is too long as the order of the filter becomes high. The other is that due to the unequal even- and odd-mode phase velocities, it suffers from the existence of the spurious response at  $2f_0$  (i.e., twice the center frequency), which may cause a poor attenuation level in the stopband [2].

SIR filters have been proposed to solve the drawbacks mentioned above [3]-[17]. They can be categorized into three major types, namely: 1) quarter-wavelength; 2) half-wavelength; and 3) one-wavelength SIR filters. The resonant frequency of the SIR is primarily controlled by the impedance ratio of the line sections. For the same substrate, the characteristic impedance of the conventional microstrip line is only controlled by the width of the conductor.

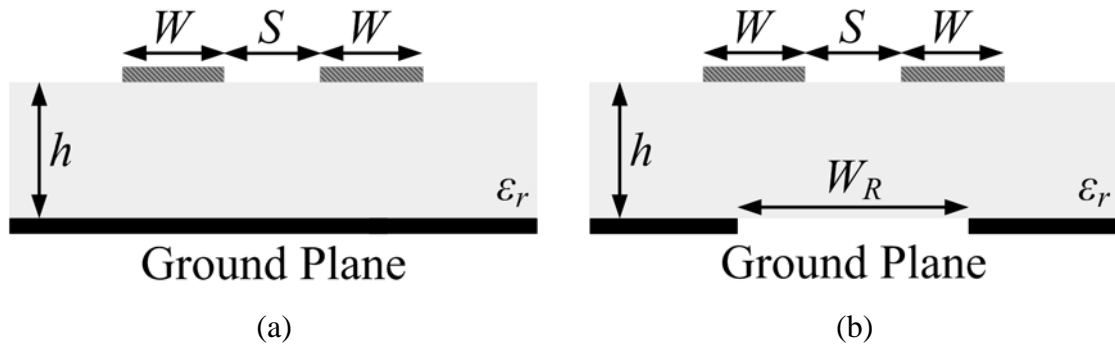


Fig. 1-2. Cross-sectional views of the symmetric coupled microstrip lines. (a) Conventional. (b) Modified with the ground-plane aperture.

Due to the restriction of the fabrication process, manufacturing tolerances may influence the performance of the filter and cause a shift of the center frequency. These effects are much more obvious on the SIR than on the uniform-impedance resonator (UIR). This is because for a constant amount of etching error on the conventional microstrip line, the percentage width variation (i.e., etching error divided by the normal width in percent) in the high-impedance section is much larger than that in the low-impedance section. Thus, the variation of the characteristic impedance of the high-impedance line is different from that of the low-impedance line, and this may cause the impedance ratio of the SIR to change largely. Thereby, the conventional microstrip SIR is very sensitive to fabrication tolerances. However, until now, there is still no works related to the sensitivity of microstrip SIR filters.

Coupled microstrip lines are extensively used to design directional couplers and edge-coupled filters. Tightly coupled directional couplers (especially a 3-dB coupler) and wideband filters are essential components in modern wireless communication systems. For the tight coupler and wideband filter design, strongly coupled microstrip lines [see Fig. 1-2(a)] are required. Nonetheless, the minimum line width and gap spacing in the conventional PCB process are only approximately 0.15 mm. On the other hand, most of the popularly used PCBs have low dielectric constants. It is inherently difficult to implement tightly coupled lines with low-dielectric-constant substrates.

Various approaches have been proposed to design a single-section 3-dB coupler. The most famous one is the Lange coupler [18]-[20], which is used extensively in the monolithic microwave integrated circuit (MMIC). However, the line width and gap spacing for either a four- or six-line 3-dB Lange coupler will be far below the fabrication limitation of the PCB process if a common substrate (for example, a RO4003 substrate with a dielectric constant of 3.58 and a thickness of 0.508 mm) is used. The vertically installed planar (VIP) structure [21], [22] could fit the PCB process, but it needs some special tools to solder the vertical substrate. The multilayer structure [23]-[27] requires multilayer substrates. A floating conductor along with a small dielectric layer [28]-[30] can be placed above the signal strips or between the signal strips and the microstrip ground plane. All the structures in [23]-[30] lead to higher fabrication costs compared to a single-layer substrate structure. A 3-dB coupler can also be fabricated on a single-layer substrate with broadside-coupled structures employing coplanar waveguides (CPWs) [31], [32]. Nevertheless, these structures may have the input and output ports on different sides of the substrate and might be difficult to apply to wideband filter design. Since there must be ground plane metals on two sides of the top layer, filter topologies such as interdigital, combline, or hairpin filters are not suitable.

Since broadband communication systems (e.g., ultra-wideband (UWB) system) are highly developed, multisection 3-dB directional couplers are necessary to increase the bandwidth. It is much more difficult to implement a multisection 3-dB directional coupler on the PCB since a very high even-mode impedance and a very low odd-mode impedance are required for the extremely tight-coupling inner sections. Although the Lange coupler [33] and the tandem coupler [34] have been used to design the tight-coupling section of a three-section 3-dB directional coupler, they require wire crossovers and may be unable to achieve very tight coupling on the low-dielectric-constant substrate. Thus, they are not appropriate to realize the tight-coupling section of a multisection directional coupler. The broadside-coupled and slot-coupled approaches can be applied to construct very tight-coupling structures [35]-[40],

but they require multilayer substrates. The VIP structure has been used in the tight-coupling sections to design a five-section directional coupler with a wide bandwidth of 160% [41]. As mentioned above, it is complicated from the manufacturing point of view.

To design a microstrip, wideband, coupled-resonator BPF on the PCB, there are many published works. The ground-plane aperture technique and the defected ground structure (DGS), as shown in Fig. 1-2(b), are commonly used to enhance the coupling [42]-[44]. In Fig. 1-2(b), the aperture width  $W_R$  varies according to the required coupling strength. Dual-plane and broadside-coupled structures [45]-[48] enable the stronger coupling, and filters with these structures inherently exhibit wideband characteristics. Other techniques, such as multilayer structures [30], [49], three-line microstrips [50], multimode resonators [51], [52], the cascade of lowpass and highpass filters [53], and the new coupling scheme in [54] are used to design wideband BPFs. However, the above-mentioned filters may be large, require multilayer technology, or have a narrow upper stopband. To summarize, it is more appropriate to design new coupling structures suitable for tight couplers, wideband filters, and other circuits that require strong coupling.

### 1.3 Contribution

In this dissertation, we propose a new microstrip line with the signal and ground strips on the same plane. Accordingly, the characteristic impedance of the proposed microstrip line can be controlled by the signal and ground strips in a coplanar manner, in addition to the total line width and substrate thickness. The proposed microstrip line is easily adopted in the low-impedance section of the SIR not only to reduce the resonator size but also to decrease the sensitivity of dimensional errors of the SIR. As a result, the SIR filter has a further smaller size and is insensitive to fabrication tolerances.

To implement a small wideband BPF with a high spurious passband, the low-impedance



section of the SIR is modified to have parallel thin strips. Since the magnetic coupling is much stronger than the electric coupling and can be increased easily by a short-circuited stub, it is much less constrained. The purpose of the thin strips in the low-impedance section of the SIR is to obtain a strong interdigital coupling between adjacent SIRs. Consequently, the filter can have a compact size, a wide passband, and a wide upper stopband.

Two novel microstrip coupling structures are also proposed to solve the coupling strength problem of the conventional coupled microstrip lines. The proposed coupled-line structures both have a rectangular ground-plane aperture and two inserted signal strips in the aperture to increase the coupling strength significantly. The proposed two structures have good compatibility with the conventional coupled microstrip lines so that they are applied to implement the single- and multi-section directional couplers. In addition, since these two coupling structures are easily adopted in any part of the resonator where the strong coupling is required, they are used to design wideband BPFs. All the proposed circuits can be fabricated on a single-layer substrate by the conventional PCB process.

## 1.4 Organization

This dissertation is organized as follows. Chapter 1 describes the conventional microstrip line and coupled microstrip lines, together with their difficulties to design some microwave components. Chapter 2 introduces the basic filter prototypes and coupled-resonator circuits for BPFs. The theory of the microstrip parallel coupled line coupler is also expressed.

In Chapter 3, a novel microstrip structure is proposed to design miniaturized filters. The proposed microstrip line has another degree of freedom to control the characteristic impedance. It is easily incorporated in the conventional microstrip SIR not only to reduce the resonator size but also to decrease its sensitivity to fabrication tolerances. The concepts and characteristics of the modified resonator structure are discussed in detail. The filters con-

structed by the conventional microstrip SIR are also designed and fabricated to compare with the proposed filters.

In Chapter 4, we propose two interdigital coupling structures to design several wideband SIR BPFs. Generally speaking, it is very difficult to design small wideband BPFs since the coupling strength would be too weak for small-size resonators, especially for a SIR. However, the SIR has a high spurious frequency so that it is very appropriate for wideband filter design. Here, compact wideband BPFs are developed by modifying the low-impedance section of the SIR. With a proper coupling scheme, the coupling strength between adjacent resonators can be very large so as to design small wideband SIR BPFs.

In Chapter 5, two novel enhanced coupling structures are presented to achieve moderate to tight coupling. The proposed two coupling structures have many physical parameters for design flexibility to meet practical applications. These two coupling structures only require a single-layer substrate. No fine lines and narrow gaps are required so as to fit the conventional PCB process. In addition, they are both compatible with the conventional microstrip line and coupled microstrip lines. Therefore, we design several 3-dB directional couplers and wideband filters by combining the conventional and proposed microstrip structures.

In Chapter 6, we conclude the dissertation and provide suggestions for future works.

## ***Chapter 2 FUNDAMENTAL THEORY AND DESIGN OF COUPLED-RESONATOR FILTERS AND COUPLED LINES***

This chapter focuses on the theory of coupled resonator circuits and symmetric microstrip parallel coupled lines. These are the two basic topics for the design of microstrip filters and couplers in this dissertation. In addition, the coupling schemes of the Chebyshev and quasi-elliptic filters are illustrated. The characteristics of the  $\lambda/4$  stepped-impedance resonator (SIR) are also discussed since it is used in the proposed filter design.

### **2.1 Coupled Resonator Theory**

In 1951, Dishal [55], [56] proposed an approach to design any lumped-element or distributed bandpass filter (BPF) by three parameters: 1) the resonator frequency,  $f_0$ ; 2) the coupling between adjacent resonators,  $k$ ; and 3) the external quality factor,  $Q_e$ . Afterwards, this approach is summarized by Hong and Lancaster [57].

#### **2.1.1 Lowpass Filter Prototype**

For the filter design, it is usually from the ladder circuits for lowpass filter prototypes, as shown in Fig. 2-1, with a source resistance or conductance equal to one (i.e.,  $g_0 = 1$ ) and a cutoff frequency  $\Omega_c = 1$ . Both the circuits in Fig. 2-1 give the same response. The element values  $g_i$ ,  $i = 1$  to  $n$ , represent a series inductor or a shunt capacitor.  $g_{n+1}$  is a load resistance or conductance. The element values of the lowpass filter prototypes can be tabulated as long as the filter specifications are given.

#### **2.1.2 Impedance ( $K$ ) and Admittance ( $J$ ) Inverters**

The circuits in Fig. 2-1 have series and shunt elements. It is often desirable to use only

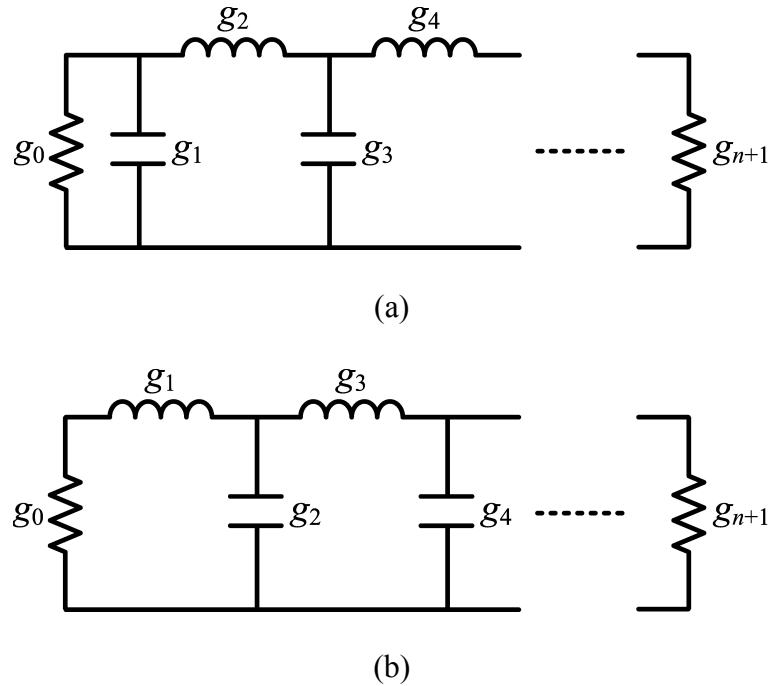


Fig. 2-1. Lowpass filter prototypes and their element definitions. (a) Prototype beginning with a shunt element. (b) Prototype beginning with a series element.

series or shunt elements to implement filters. The  $K$ - or  $J$ -inverter is a two-port network. Ideally, the inverter parameter is frequency invariable. The  $ABCD$  matrix of an ideal  $K$ -inverter is

$$\begin{bmatrix} A & B \\ C & D \end{bmatrix} = \begin{bmatrix} 0 & \mp jK \\ \pm \frac{1}{jK} & 0 \end{bmatrix} \quad (2.1)$$

where  $K$  is a real value and is defined as the characteristic impedance of the inverter. Thereby, for a  $K$ -inverter terminated with an impedance  $Z_2$ , the impedance  $Z_1$  seen from the other port of a  $K$ -inverter is

$$Z_1 = \frac{K^2}{Z_2} \quad (2.2)$$

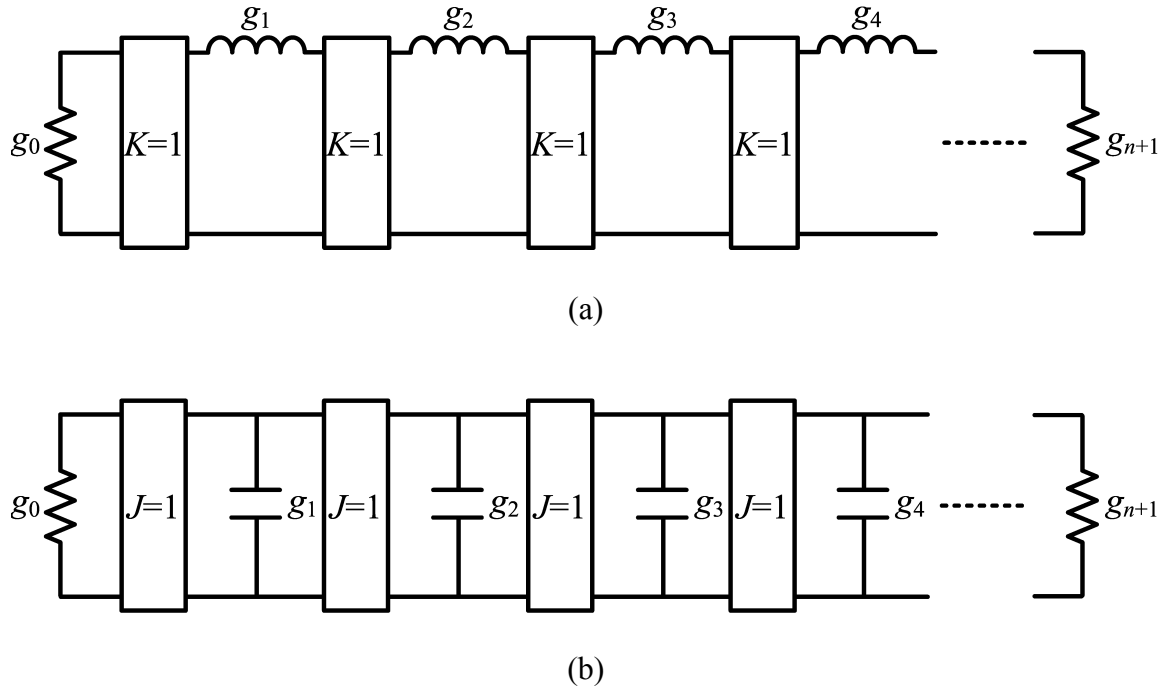


Fig. 2-2. Lowpass filter prototypes with (a)  $K$ -inverters and (b)  $J$ -inverters.

It is seen that if  $Z_2$  is inductive,  $Z_1$  becomes capacitive, and vice versa. The inverter has a phase shift of  $\pm 90^\circ$ .

The  $ABCD$  matrix of an ideal  $J$ -inverter is

$$\begin{bmatrix} A & B \\ C & D \end{bmatrix} = \begin{bmatrix} 0 & \pm \frac{1}{jJ} \\ \mp jJ & 0 \end{bmatrix} \quad (2.3)$$

where  $J$  is a real value and is defined as the characteristic admittance of the inverter. Again, if a  $J$ -inverter is terminated with an admittance  $Y_2$ , the input admittance  $Y_1$  seen looking in the other port is

$$Y_1 = \frac{J^2}{Y_2}. \quad (2.4)$$

Apparently, a  $J$ -inverter has the same property as a  $K$ -inverter.

A series inductor with a  $K$ -inverter on each side looks like a shunt capacitor. On the other hand, a shunt capacitor with a  $J$ -inverter on each side represents a series inductor. As a result, the lowpass filter prototypes in Fig. 2-1 are modified to have only series or shunt elements by including the  $K$ - or  $J$ -inverters, as shown in Fig. 2-2.

### 2.1.3 Impedance Scaling and Frequency Transformation

Since the source resistance is unity in the lowpass filter prototype (i.e.,  $g_0 = 1$ ), a source resistance  $Z_0$  can be obtained by multiplying the impedances of the prototype circuit by  $Z_0$ . If  $\omega_1$  and  $\omega_2$  denote the passband edges of a BPF, the center frequency  $\omega_0$  and the fractional bandwidth  $\Delta$  are expressed as:



$$\omega_0 = \sqrt{\omega_1 \omega_2} \quad (2.5)$$

$$\Delta = \frac{\omega_2 - \omega_1}{\omega_0} \quad (2.6)$$

Therefore, the frequency transformation from a lowpass prototype response to a bandpass response is

$$\Omega = \frac{\Omega_c}{\Delta} \left( \frac{\omega}{\omega_0} - \frac{\omega_0}{\omega} \right). \quad (2.7)$$

This transformation is applied to the reactive elements of the lowpass filter prototype. As a result, the lowpass filter elements are transformed to series  $LC$  resonant circuits in the series arms, and to parallel  $LC$  resonant circuits in the shunt arms. To summarize, the new element values after the impedance and frequency scaling for the series  $LC$  circuit are

$$L_s = \frac{g\Omega_c Z_0}{\Delta\omega_0} \quad (2.8)$$

$$C_s = \frac{\Delta}{\omega_0 g\Omega_c Z_0} \quad (2.9)$$

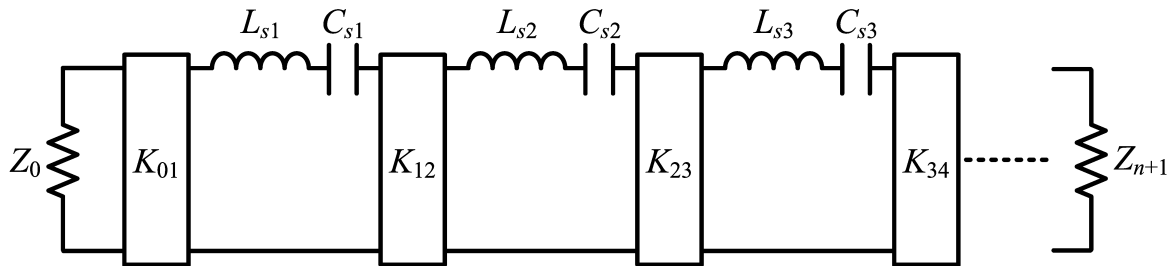
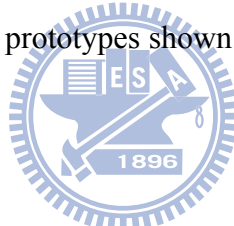
where  $g$  represents the series inductor in the lowpass filter prototype. Similarly, the new element values for the shunt  $LC$  circuit are

$$L_p = \frac{\Delta Z_0}{\omega_0 g\Omega_c} \quad (2.10)$$

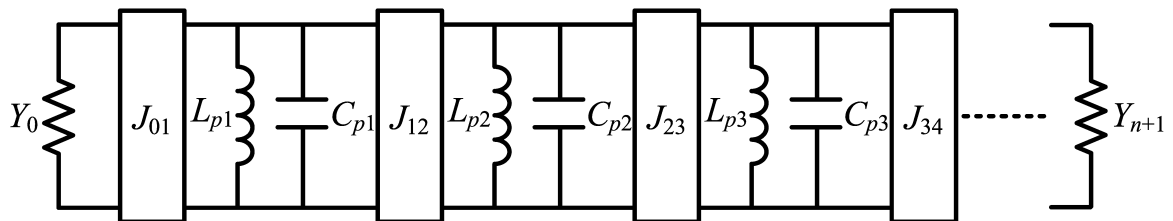
$$C_p = \frac{g\Omega_c}{\Delta\omega_0 Z_0} \quad (2.11)$$

where  $g$  represents the shunt capacitor in the lowpass filter prototype.

As a result, the lowpass filter prototypes shown in Fig. 2-2 are converted to the bandpass filters, as shown in Fig. 2-3.



(a)



(b)

Fig. 2-3. Bandpass filters using (a)  $K$ -inverters and (b)  $J$ -inverters.

## 2.1.4 Reactance and Susceptance Slope Parameters

At microwave frequencies, distributed-element forms are easier to construct than lumped-element forms. For the distributed resonator, the reactance or susceptance and the slope parameter are made equal to those of the corresponding lumped resonator at the center frequency  $\omega_0$ . For a resonator with a series-type resonance (i.e., zero reactance at  $\omega_0$ ), the reactance slope parameter  $x$  is defined as follows:

$$x = \frac{\omega_0}{2} \left. \frac{dX(\omega)}{d\omega} \right|_{\omega=\omega_0} \quad (2.12)$$

where  $X$  is the reactance of the resonator. For a lumped series  $LC$  resonator,  $x$  is equal to  $\omega_0 L$  or  $1/(\omega_0 C)$ . On the other hand, for a resonator exhibiting a shunt-type resonance (i.e., zero susceptance at  $\omega_0$ ), the susceptance slope parameter  $b$  is

$$b = \frac{\omega_0}{2} \left. \frac{dB(\omega)}{d\omega} \right|_{\omega=\omega_0} \quad (2.13)$$

where  $B$  is the susceptance of the resonator. For a lumped parallel  $LC$  resonator,  $b$  is equal to  $\omega_0 C$  or  $1/(\omega_0 L)$ . Accordingly, the properties of the lumped resonators in Fig. 2-3 can be defined in terms of the reactance or susceptance slope parameter. Fig. 2-4 shows the bandpass filters with the general terms  $X$  and  $B$  to represent the distributed resonators. For the  $N$ th-order filter (i.e.,  $n = N$ ), the values of the  $K$ -inverters in Fig. 2-4(a) are

$$K_{01} = \sqrt{\frac{\Delta x_1 Z_0}{\Omega_c g_0 g_1}}, \quad K_{i,i+1} = \frac{\Delta}{\Omega_c} \sqrt{\frac{x_i x_{i+1}}{g_i g_{i+1}}}_{i=1,2,\dots,N-1}, \quad K_{N,N+1} = \sqrt{\frac{\Delta x_N Z_{N+1}}{\Omega_c g_N g_{N+1}}}. \quad (2.14)$$



The values of the  $J$ -inverters in Fig. 2-4(b) are

$$J_{01} = \sqrt{\frac{\Delta b_1 Y_0}{\Omega_c g_0 g_1}}, \quad J_{i,i+1} = \frac{\Delta}{\Omega_c} \sqrt{\frac{b_i b_{i+1}}{g_i g_{i+1}}}, \quad J_{N,N+1} = \sqrt{\frac{\Delta b_N Y_{N+1}}{\Omega_c g_N g_{N+1}}}. \quad (2.15)$$

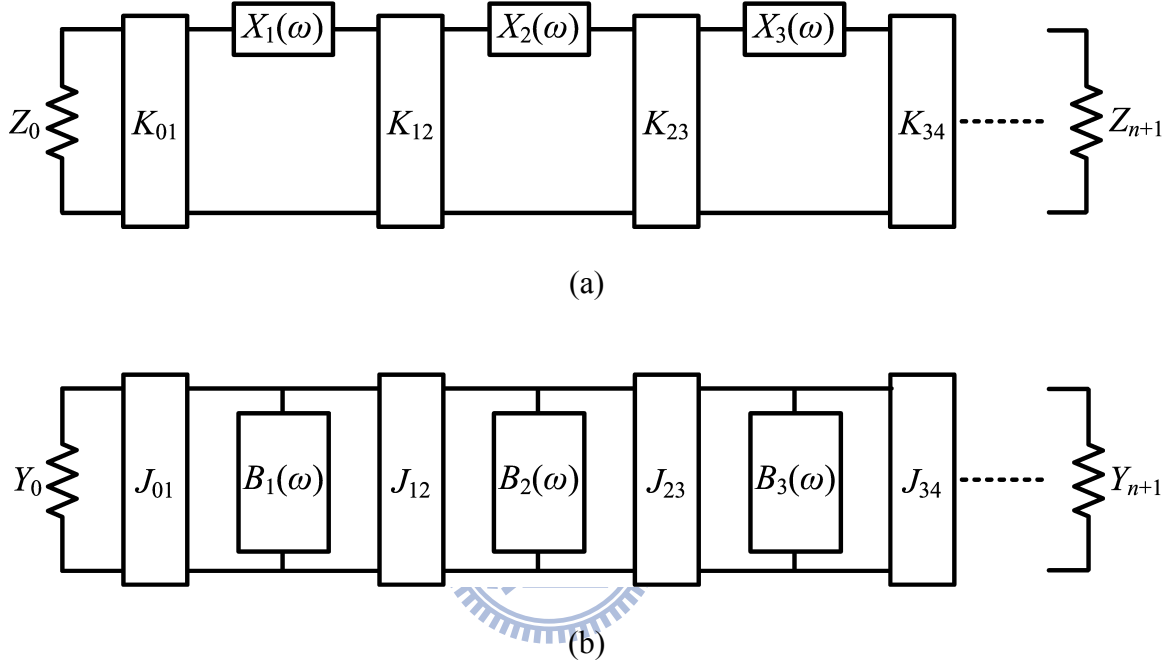


Fig. 2-4. Generalized bandpass filters with distributed elements and (a)  $K$ -inverters. (b)  $J$ -inverters.

### 2.1.5 Design Equations for Coupled-Resonator Bandpass Filters

Finally, the filter can be expressed in terms of the external quality factor  $Q_e$  and the coupling coefficient  $k$ . For the filter with the  $K$ -inverters, as shown in Fig. 2-4(a), the external quality factors of the input ( $Q_{ei}$ ) and output ( $Q_{eo}$ ) ports are

$$Q_{ei} = \frac{x_1}{K_{01}^2 / Z_0} = \frac{g_0 g_1 \Omega_c}{\Delta} \quad (2.16)$$

$$Q_{eo} = \frac{x_n}{K_{n,n+1}^2 / Z_{n+1}} = \frac{g_n g_{n+1} \Omega_c}{\Delta}. \quad (2.17)$$

The coupling coefficient  $k$  between adjacent resonators is obtained as

$$k_{i,i+1} \Big|_{i=1,2,\dots,n-1} = \frac{K_{i,i+1}}{\sqrt{x_i x_{i+1}}} = \frac{\Delta}{\Omega_c \sqrt{g_i g_{i+1}}} . \quad (2.18)$$

Likewise, the design equations for the filter with the  $J$ -inverters, as shown in Fig. 2-4(b), are the same as (2.16) to (2.18). Consequently, the filter is specified by the external quality factors and the coupling coefficients. The values of these parameters are extracted through the electromagnetic (EM) simulation as long as the filter specifications are given.

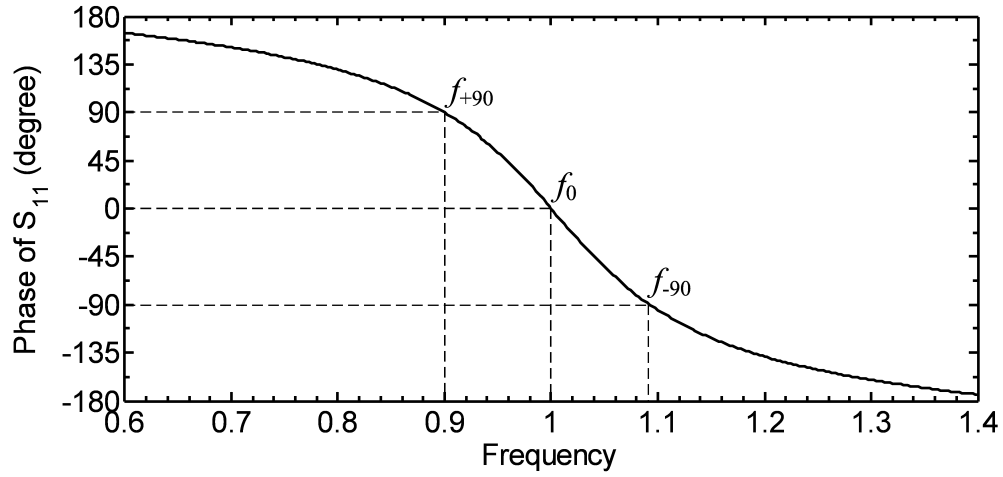
### 2.1.6 Extraction of the External Quality Factor and Coupling Coefficient

As the input or output resonator has a single loading, the reflection coefficient ( $S_{11}$ ) at the excitation port has the phase response presented in Fig. 2-5(a).  $f_{+90}$  and  $f_{-90}$  represent the frequencies which have the phase shifts of  $+90^\circ$  and  $-90^\circ$ , respectively, versus the absolute phase at the center frequency  $f_0$ . The external quality factor  $Q_e$  can be obtained as

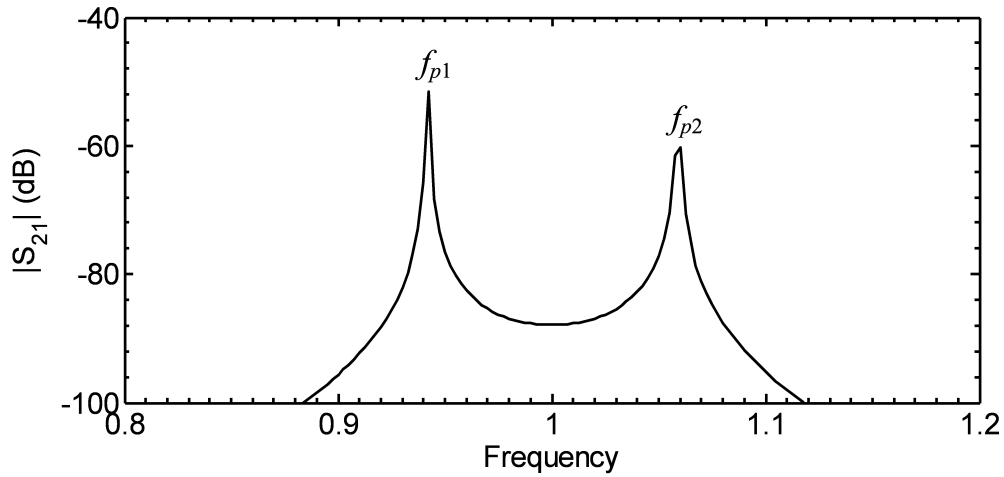
$$Q_e = \frac{f_0}{f_{-90} - f_{+90}} . \quad (2.19)$$

To extract the coupling coefficient  $k$ , very weak coupling is applied to the coupled resonator pair. The typical resonant response of the coupled resonator structure is shown in Fig. 2-5(b), where there are two resonant peaks corresponding to  $f_{p1}$  and  $f_{p2}$ . Consequently, the coupling coefficient  $k$  is

$$k = \frac{f_{p2}^2 - f_{p1}^2}{f_{p2}^2 + f_{p1}^2} . \quad (2.20)$$



(a)



(b)

Fig. 2-5. (a) Phase response of  $S_{11}$  for the input and output coupling structures. (b) Resonant response of the coupled resonator pair.

### 2.1.7 Chebyshev and Quasi-Elliptic Filters

The Chebyshev filter has the equal-ripple passband and maximally flat stopband. The transfer function corresponding to this type of filter is

$$|S_{21}(j\Omega)|^2 = \frac{1}{1 + \varepsilon^2 T_n^2(\Omega)} \quad (2.21)$$

where  $\Omega$  is a frequency variable for the lowpass filter prototype,  $n$  is the order of the filter, and  $\varepsilon$  is a ripple constant related to a passband ripple  $L_A$  (dB) by

$$\varepsilon = \sqrt{10^{\frac{L_A}{10}} - 1}. \quad (2.22)$$

$T_n(\Omega)$  represents a Chebyshev function of the first kind of order  $n$  and is defined as

$$T_n(\Omega) = \begin{cases} \cos(n \cos^{-1} \Omega) & |\Omega| \leq 1 \\ \cosh(n \cosh^{-1} \Omega) & |\Omega| \geq 1 \end{cases}. \quad (2.23)$$

For a four-pole Chebyshev filter, Fig. 2-6 shows the coupling scheme and frequency response.

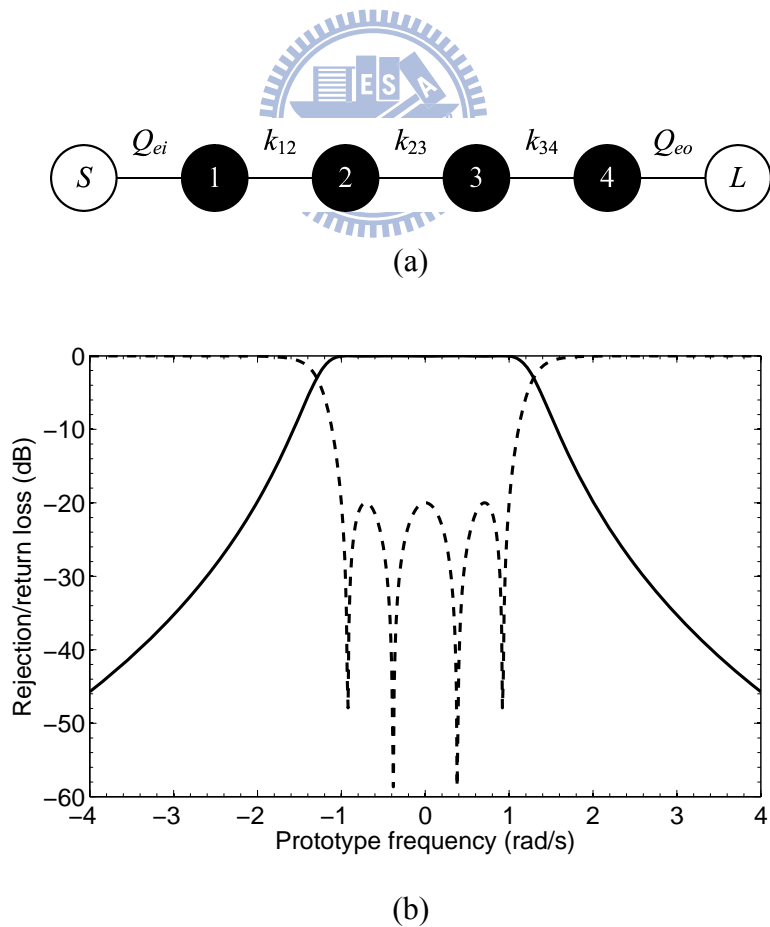


Fig. 2-6. (a) Coupling diagram and (b) frequency response for the four-pole Chebyshev filter.

The quasi-elliptic filter, also called the generalized Chebyshev filter, has a pair of transmission zeros at the finite frequencies to improve the selectivity. The transfer function of this type of filter is

$$|S_{21}(j\Omega)|^2 = \frac{1}{1 + \varepsilon^2 F_n^2(\Omega)} \quad (2.24)$$

$$\varepsilon = \frac{1}{\sqrt{10^{\frac{L_R}{10}} - 1}} \quad (2.25)$$

$$F_n(\Omega) = \cosh\left\{(n-2)\cosh^{-1}(\Omega) + \cosh^{-1}\left(\frac{\Omega_a\Omega-1}{\Omega_a-\Omega}\right) + \cosh^{-1}\left(\frac{\Omega_a\Omega+1}{\Omega_a+\Omega}\right)\right\} \quad (2.26)$$

where  $\Omega$  is a frequency variable for the lowpass filter prototype, and  $\Omega = \pm\Omega_a$  are the frequencies of a pair of transmission zeros.  $n$  is the order of the filter, and  $\varepsilon$  is a ripple constant corresponding to a return loss  $L_R$ . It should be noted that as  $\Omega_a$  approaches infinite, the function  $F_n(\Omega)$  becomes the Chebyshev function. After the lowpass-to-bandpass transformation, the transmission zeros of the BPF can be obtained as follows:

$$\omega_{a1} = \omega_0 \frac{-\Omega_a\Delta + \sqrt{(\Omega_a\Delta)^2 + 4}}{2} \quad (2.27)$$

$$\omega_{a2} = \omega_0 \frac{\Omega_a\Delta + \sqrt{(\Omega_a\Delta)^2 + 4}}{2} \quad (2.28)$$

Fig. 2-7 shows the coupling scheme and frequency response for a four-pole quasi-elliptic filter. To generate a pair of transmission zeros on both sides of the passband, the sign of the cross coupling  $k_{14}$  should be opposite to that of  $k_{23}$ . In practical realizations, this means that if  $k_{14}$  represents a magnetic coupling,  $k_{23}$  must be an electric coupling, and vice versa.

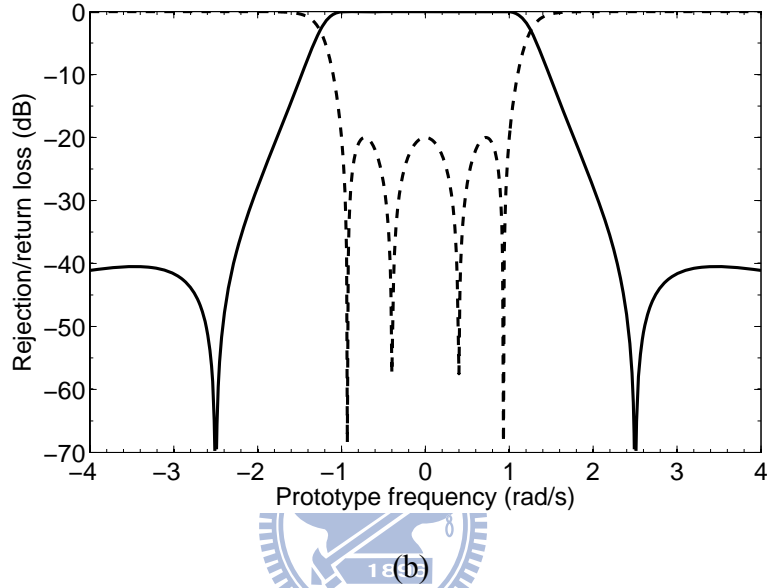
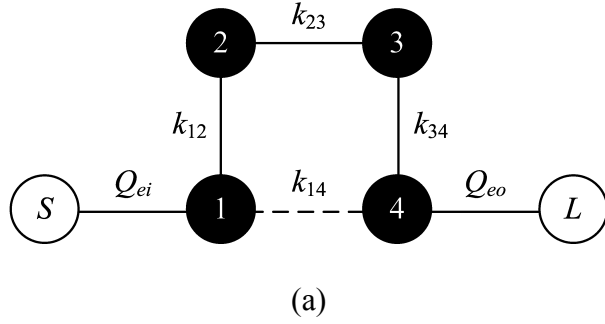
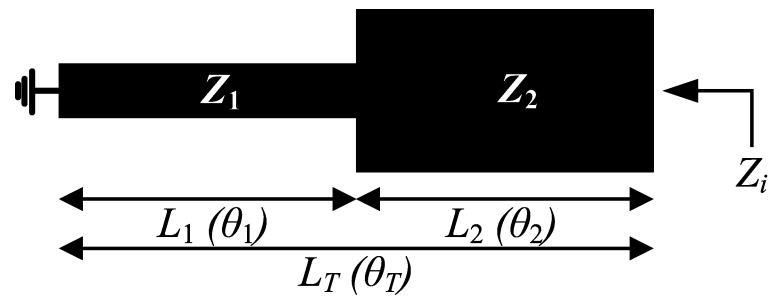


Fig. 2-7. (a) Coupling diagram and (b) frequency response for the four-pole quasi-elliptic filter.

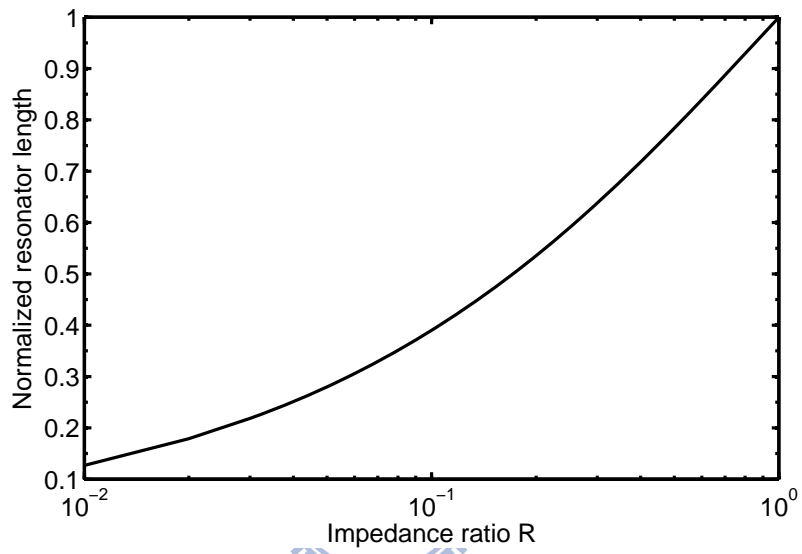
## 2.2 Resonance Properties of the $\lambda/4$ SIR

Fig. 2-8(a) shows the structure of a conventional  $\lambda/4$  microstrip SIR. It comprises a section of high-impedance ( $Z_1$ ) and a section of low-impedance ( $Z_2$ ) transmission line with corresponding physical (electrical) lengths  $L_1$  ( $\theta_1$ ) and  $L_2$  ( $\theta_2$ ), respectively. By ignoring the effect of the step discontinuity, the input impedance  $Z_i$  at the open end is given by

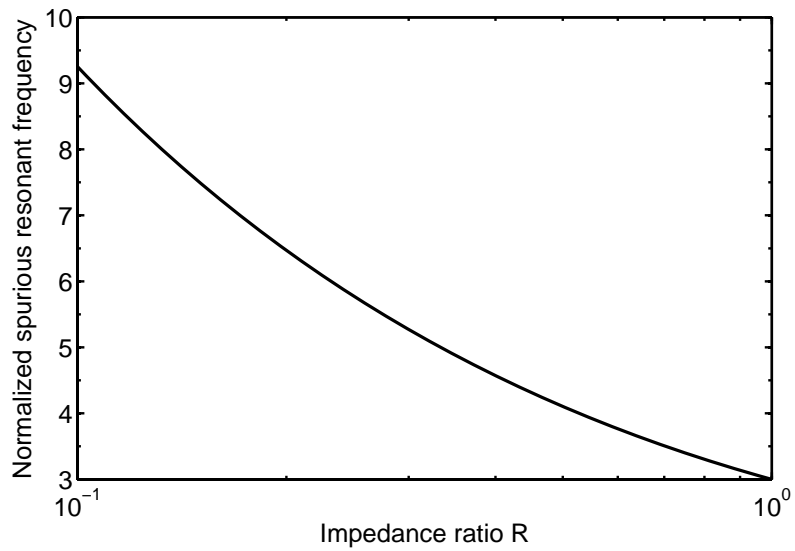
$$Z_i = jZ_2 \frac{Z_1 \tan \theta_1 + Z_2 \tan \theta_2}{Z_2 - Z_1 \tan \theta_1 \tan \theta_2}. \quad (2.29)$$



(a)



(b)



(c)

Fig. 2-8. (a) Conventional  $\lambda/4$  microstrip SIR. (b) Normalized length and (c) normalized spurious frequency versus impedance ratio for  $\theta_1 = \theta_2$ .

The resonance condition from  $Z_i = \infty$  can be obtained as follows:

$$\tan \theta_1 \tan \theta_2 = R \quad (2.30)$$

where the impedance ratio  $R$  of the SIR is defined as

$$R = \frac{Z_2}{Z_1}. \quad (2.31)$$

The SIR has a minimum length when the high- and low-impedance sections are equal in length. The resonator length reaches a minimum value of  $\theta_T = 2 \tan^{-1} \sqrt{R}$ . The normalized resonator length versus impedance ratio is plotted in Fig. 2-8(b) for  $0 < R \leq 1$  and  $\theta_1 = \theta_2$ , where  $R = 1$  corresponds to the uniform-impedance  $\lambda/4$  resonator. Moreover, the relationship between the fundamental frequency ( $f_0$ ) and the first spurious frequency ( $f_{s1}$ ) is given by

$$\frac{f_{s1}}{f_0} = \frac{\pi}{\tan^{-1} \sqrt{R}} - 1 \quad (2.32)$$

and is shown in Fig. 2-8(c). Therefore, to minimize the filter size and to enlarge the span between the fundamental and first spurious frequencies, we have  $L_1 = L_2$  and make  $R$  as small as possible.

## 2.3 Microstrip Line and Coupled Microstrip Lines

### 2.3.1 Single Microstrip Line

Since the fields in a microstrip line are not contained within a homogeneous dielectric region, it cannot support a pure transverse electromagnetic (TEM) wave. Therefore, the



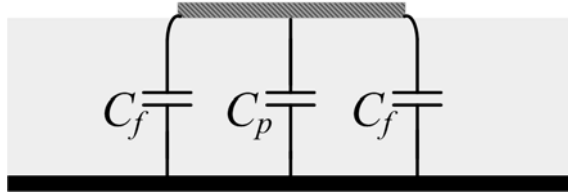


Fig. 2-9. Capacitance representation of a conventional microstrip line.

dominated mode of a microstrip line is a quasi-TEM mode. In the quasi-TEM analysis, the capacitance representation of a microstrip line is shown in Fig. 2-9. Here,  $C_p$  denotes the parallel-plate capacitance per unit length between the signal strip and the ground plane, and  $C_f$  is the fringe capacitance per unit length from the edge of a microstrip line. The total per-unit-length capacitance  $C_t$  of a microstrip line is

$$C_t = C_p + 2C_f. \quad (2.33)$$

The transmission characteristics of a microstrip line are described by the effective dielectric constant  $\epsilon_e$  and the characteristic impedance  $Z_c$ . These two parameters are determined from the values of two capacitances as follows:

$$\epsilon_e = \frac{C_t}{C_a} \quad (2.34)$$

$$Z_c = \frac{1}{c\sqrt{C_t C_a}} \quad (2.35)$$

where  $C_t$  is the total capacitance per unit length with the dielectric substrate present, and  $C_a$  is the total capacitance per unit length with the dielectric substrate replaced by air.  $c$  is the free-space light velocity ( $c \approx 3 \times 10^8$  m/s).

### 2.3.2 Coupled Microstrip Lines

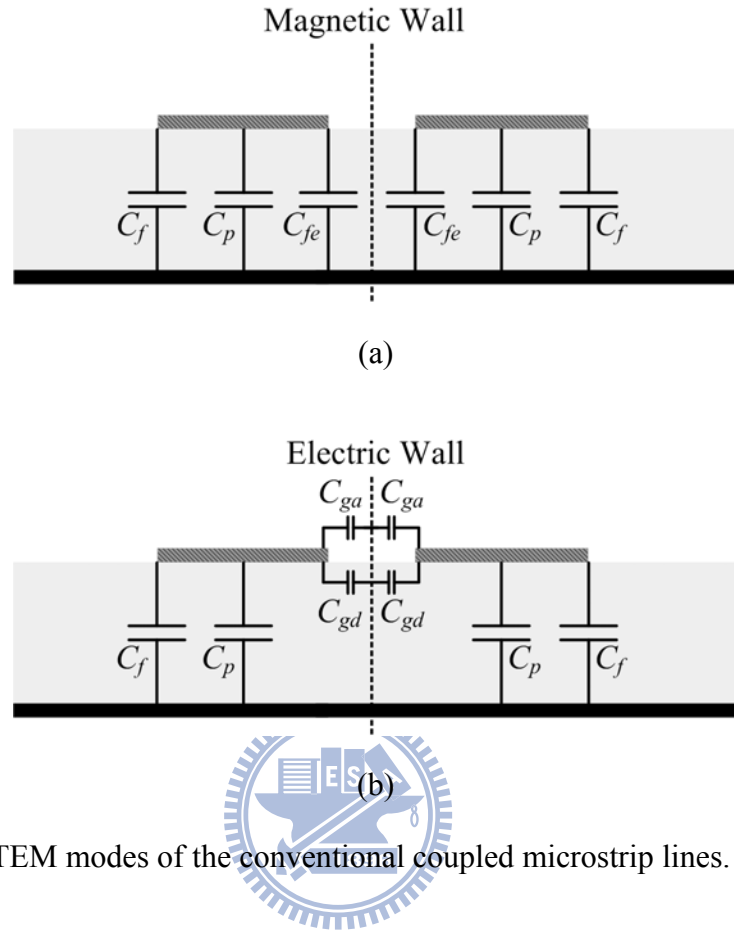


Fig. 2-10. Quasi-TEM modes of the conventional coupled microstrip lines. (a) Even mode. (b) Odd mode.

Symmetric coupled microstrip lines, as shown in Fig. 1-2(a), can be analyzed by the even-odd mode analysis. For the even-mode excitation, the normal component of the electric field at the symmetry plane is zero, which leads to a magnetic wall. For the odd-mode excitation, the symmetry plane behaves like an electric wall. Fig. 2-10 shows the capacitance representation for the even- and odd-mode excitations. The even- and odd-mode capacitances ( $C_e$ ,  $C_o$ ) for either of the coupled lines are given by

$$C_e = C_p + C_f + C_{fe} \quad (2.36)$$

$$C_o = C_p + C_f + C_{gd} + C_{ga} \quad (2.37)$$

where  $C_p$  is a parallel-plate capacitance per unit length between the signal and ground planes.  $C_f$  is the fringe capacitance per unit length from the edge of an uncoupled microstrip line, and  $C_{fe}$  is the fringe capacitance per unit length due to the presence of another line.  $C_{ga}$  and  $C_{gd}$  are the fringe capacitances per unit length across the coupling gap in the air and dielectric regions, respectively.

The even- and odd-mode effective dielectric constants  $\epsilon_{re}$  and  $\epsilon_{ro}$  are determined as

$$\epsilon_{re} = \frac{C_e}{C_{ae}} \quad (2.38)$$

$$\epsilon_{ro} = \frac{C_o}{C_{ao}} \quad (2.39)$$

where  $C_{ae}$  and  $C_{ao}$  are the even- and odd-mode capacitances of either of the coupled lines with air as a dielectric substrate. For the coupled microstrip lines, the even-mode electric field distributions are much more concentrated in a dielectric substrate compared to the odd-mode electric field distributions. Consequently, the value of (2.38) is larger than that of (2.39), which means that the even-mode phase velocity is smaller than the odd-mode phase velocity. This will influence the directivity and isolation of the microstrip directional coupler. The even- and odd-mode impedances  $Z_{0e}$  and  $Z_{0o}$  are given as follows:

$$Z_{0e} = \frac{1}{c\sqrt{C_{ae}C_e}} \quad (2.40)$$

$$Z_{0o} = \frac{1}{c\sqrt{C_{ao}C_o}} \quad (2.41)$$

where  $c$  is the free-space light velocity ( $c \approx 3 \times 10^8$  m/s).

### 2.3.3 Coupled Line Coupler

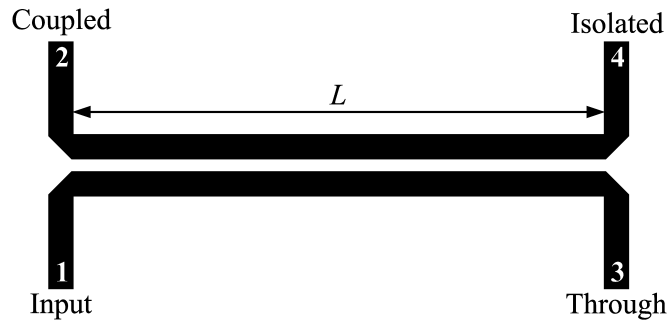


Fig. 2-11. Single-section microstrip coupled line coupler.

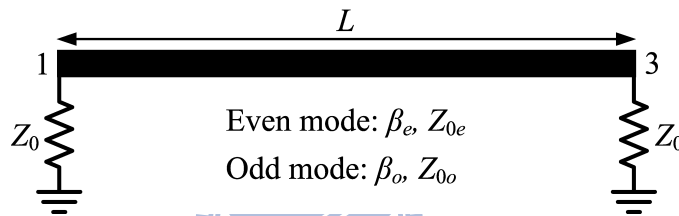


Fig. 2-12. Equivalent circuit for the even-odd mode analysis.

A single-section microstrip coupled line coupler with a coupling length  $L$  is depicted in Fig. 2-11. With the definitions of the even- and odd-mode impedances described above, the design equations for the coupler can be obtained by applying the even-odd mode analysis. The equivalent circuit for the even- and odd-mode excitations is shown in Fig. 2-12. For simplicity, assume that the coupler has a terminated impedance  $Z_0$ , and the even and odd modes of the coupled lines have the same velocity of propagation (i.e.,  $\beta_e = \beta_o = \beta$ ). Therefore, the  $ABCD$  matrices for the even and odd modes are given by

$$\begin{bmatrix} A_e & B_e \\ C_e & D_e \end{bmatrix} = \begin{bmatrix} \cos \theta & jZ_{0e} \sin \theta \\ \frac{j \sin \theta}{Z_{0e}} & \cos \theta \end{bmatrix} \quad (2.42)$$

$$\begin{bmatrix} A_o & B_o \\ C_o & D_o \end{bmatrix} = \begin{bmatrix} \cos \theta & jZ_{0o} \sin \theta \\ \frac{j \sin \theta}{Z_{0o}} & \cos \theta \end{bmatrix} \quad (2.43)$$

where  $\theta = \beta_e L = \beta_o L = \beta L$ . As a result, the even- and odd-mode reflection coefficients can be obtained as follows:

$$S_{11e} = S_{33e} = \frac{j\left(\frac{Z_{0e}}{Z_0} - \frac{Z_0}{Z_{0e}}\right) \sin \theta}{2 \cos \theta + j\left(\frac{Z_{0e}}{Z_0} + \frac{Z_0}{Z_{0e}}\right) \sin \theta} \quad (2.44)$$

$$S_{11o} = S_{33o} = \frac{j\left(\frac{Z_{0o}}{Z_0} - \frac{Z_0}{Z_{0o}}\right) \sin \theta}{2 \cos \theta + j\left(\frac{Z_{0o}}{Z_0} + \frac{Z_0}{Z_{0o}}\right) \sin \theta}. \quad (2.45)$$

The even- and odd-mode transmission coefficients are calculated as

$$S_{31e} = S_{13e} = \frac{2}{2 \cos \theta + j\left(\frac{Z_{0e}}{Z_0} + \frac{Z_0}{Z_{0e}}\right) \sin \theta} \quad (2.46)$$

$$S_{31o} = S_{13o} = \frac{2}{2 \cos \theta + j\left(\frac{Z_{0o}}{Z_0} + \frac{Z_0}{Z_{0o}}\right) \sin \theta}. \quad (2.47)$$

Since

$$S_{11} = \frac{S_{11e} + S_{11o}}{2} \quad (2.48)$$

$$S_{33} = \frac{S_{33e} + S_{33o}}{2}, \quad (2.49)$$

to make  $S_{11} = S_{33} = 0$  for any length  $L$ , we have the following equation:

$$Z_{0e}Z_{0o} = Z_0^2. \quad (2.50)$$

Thus, the scattering parameters for the single-section coupler can be obtained as follows:

$$S_{11} = S_{22} = S_{33} = S_{44} = 0 \quad (2.51)$$

$$S_{14} = S_{41} = S_{23} = S_{32} = \frac{S_{31e} - S_{31o}}{2} = 0 \quad (2.52)$$

$$S_{12} = S_{21} = S_{34} = S_{43} = \frac{S_{11e} - S_{11o}}{2} = \frac{j\left(\frac{Z_{0e}}{Z_0} - \frac{Z_{0o}}{Z_0}\right) \sin \theta}{2 \cos \theta + j\left(\frac{Z_{0e}}{Z_0} + \frac{Z_{0o}}{Z_0}\right) \sin \theta} \quad (2.53)$$

$$S_{13} = S_{31} = S_{24} = S_{42} = \frac{S_{31e} + S_{31o}}{2} = \frac{2}{2 \cos \theta + j\left(\frac{Z_{0e}}{Z_0} + \frac{Z_{0o}}{Z_0}\right) \sin \theta}. \quad (2.54)$$

Now we define the coupling factor  $C$  as

$$C = \frac{Z_{0e} - Z_{0o}}{Z_{0e} + Z_{0o}} \quad (2.55)$$

so that (2.53) and (2.54) become

$$S_{21} = \frac{jC \sin \theta}{\sqrt{1-C^2} \cos \theta + j \sin \theta} \quad (2.56)$$

$$S_{31} = \frac{\sqrt{1-C^2}}{\sqrt{1-C^2} \cos \theta + j \sin \theta}. \quad (2.57)$$

For the coupler with  $L = \lambda/4$  (i.e.,  $\theta = \pi/2$ ) and port 1 excitation, the coupling amount to port 2 is at its maximum. Under this condition, the scattering matrix is

$$[S] = \begin{bmatrix} 0 & C & -j\sqrt{1-C^2} & 0 \\ C & 0 & 0 & -j\sqrt{1-C^2} \\ -j\sqrt{1-C^2} & 0 & 0 & C \\ 0 & -j\sqrt{1-C^2} & C & 0 \end{bmatrix}. \quad (2.58)$$

As a result, the maximum value of coupling is  $C$  for the coupled line coupler. The design equations for the even- and odd-mode impedances and the coupling factor are given by

$$Z_{0e} = Z_0 \sqrt{\frac{1+C}{1-C}} \quad (2.59)$$

$$Z_{0o} = Z_0 \sqrt{\frac{1-C}{1+C}}. \quad (2.60)$$

Thus, the coupling strength of the microstrip coupled line coupler can be determined by the even- and odd-mode impedances. Furthermore, the stronger the coupling is, the larger the difference between the even- and odd-mode impedances is. This implies the narrow line width and gap spacing.

The coupling, directivity, and isolation are the three quantities to characterize a directional coupler and are defined as follows:

$$\text{Coupling (dB)} = 10 \log \frac{P_1}{P_2} = 20 \log \frac{1}{|S_{21}|} \quad (2.61)$$

$$\text{Directivity (dB)} = 10 \log \frac{P_2}{P_4} = 20 \log \frac{|S_{21}|}{|S_{41}|} \quad (2.62)$$

$$\text{Isolation (dB)} = 10 \log \frac{P_1}{P_4} = 20 \log \frac{1}{|S_{41}|} \quad (2.63)$$

where  $P_1$  is the power incident at port 1, and  $P_2$  and  $P_4$  are the power outputs at ports 2 and 4, respectively.

The bandwidth of a single-section coupled line coupler is usually limited. Therefore, a

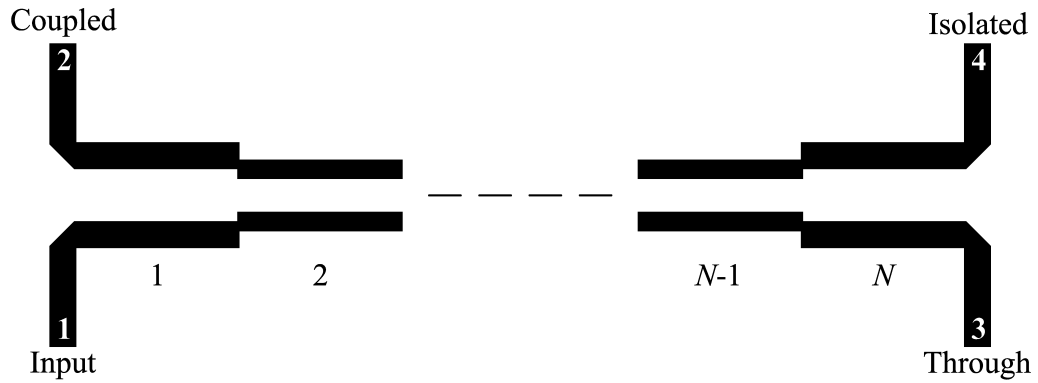


Fig. 2-13.  $N$ -section symmetric multisection coupled line coupler.

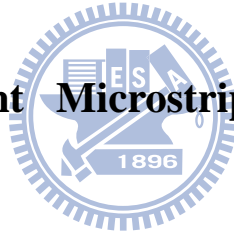
multisection coupled line coupler is required to increase the bandwidth. A multisection coupled line coupler can be either symmetric or asymmetric depending on whether it has end-to-end symmetry. In this dissertation, we design a symmetric multisection coupled line coupler which has an odd number of coupling sections, as depicted in Fig. 2-13. For a multisection coupled line coupler, each coupling section is a quarter-wavelength long at the center frequency and is specified by the even- and odd-mode impedances [58]. The even- and odd-mode impedances for each coupling section have been tabulated in [59].



# ***Chapter 3 NOVEL LOW-IMPEDANCE MICROSTRIP LINE FOR QUARTER-WAVELENGTH STEPPED-IMPEDANCE RESONATOR FILTERS***

In this chapter, a new low-impedance microstrip line is proposed and applied in the conventional microstrip quarter-wavelength stepped-impedance resonator (SIR). The proposed microstrip line has the signal and ground strips on the same plane to provide another degree of freedom to control the characteristic impedance. The experimental filters have compact sizes, high selectivity, and wide stopband range. More importantly, it can be used to decrease the sensitivity of the SIR to fabrication tolerances.

## **3.1 Fabrication-Tolerant Microstrip Quarter-Wavelength SIR Filter**



The etching error causes the serious resonant frequency drift of a microstrip SIR. Fig. 3-1(a) depicts the fabrication tolerance in the conventional  $\lambda/4$  microstrip SIR (i.e.,  $\Delta W_U$  for under-etching and  $\Delta W_O$  for over-etching). The normalized resonant frequency versus the percentage variation of the impedance ratio  $R$  is shown in Fig. 3-1(b), where different curves correspond to different amounts of variation in  $R$  due to etching errors. It is observed that small changes in the impedance ratio would contribute to obvious variations in the resonant frequency. As an example, consider two conventional  $\lambda/4$  microstrip SIRs, as shown in Fig. 3-1(a), with different physical dimensions on the substrate with a dielectric constant of 3.6 and a thickness of 0.5 mm. The first case is  $W_H = 0.225$  mm and  $W_L = 3.45$  mm, which corresponds to  $R = 0.204$ . The second case is  $W_H = 1.25$  mm and  $W_L = 1.45$  mm, which corresponds to  $R = 0.906$ . For  $\Delta W_O = 0.025$  mm (i.e., over-etching 0.05 mm), the im-

pedance ratio  $R$  is changed to 0.189 for the first case and to 0.904 for the second case. The percentage variations of the impedance ratio  $R$  for the first and second cases due to the over-etching are -7.35% and -0.22%, respectively. As a result, the first case would have -3.334% of the frequency drift, and the second case would only have -0.073% of the frequency drift. The frequency drift due to etching errors becomes larger as the impedance ratio becomes smaller. Therefore, the conventional microstrip SIR structure is very sensitive to fabrication tolerances, such as over-etching, under-etching, and errors in substrate thickness. Sometimes the filter requires a substantial amount of tuning and even additional iteration to meet the desired performance specification.

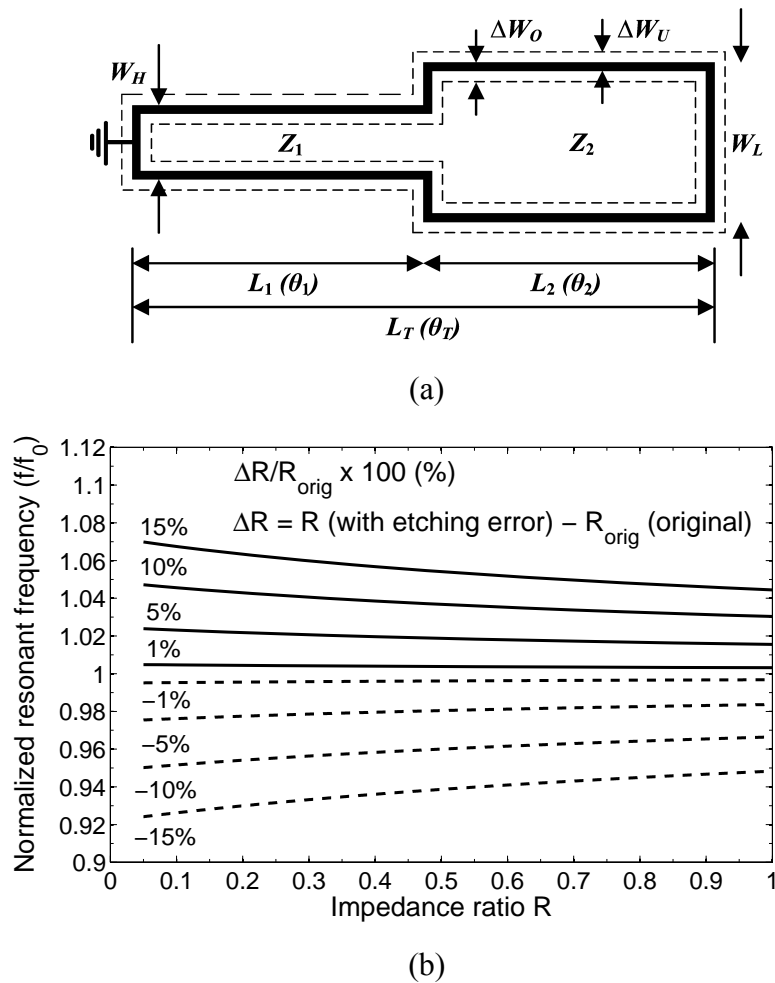


Fig. 3-1. (a) Conventional  $\lambda/4$  microstrip SIR. Dashed lines represent etching errors. (b) Normalized resonant frequency versus the percentage variation of the impedance ratio.

### 3.1.1 New Modified Microstrip Structure

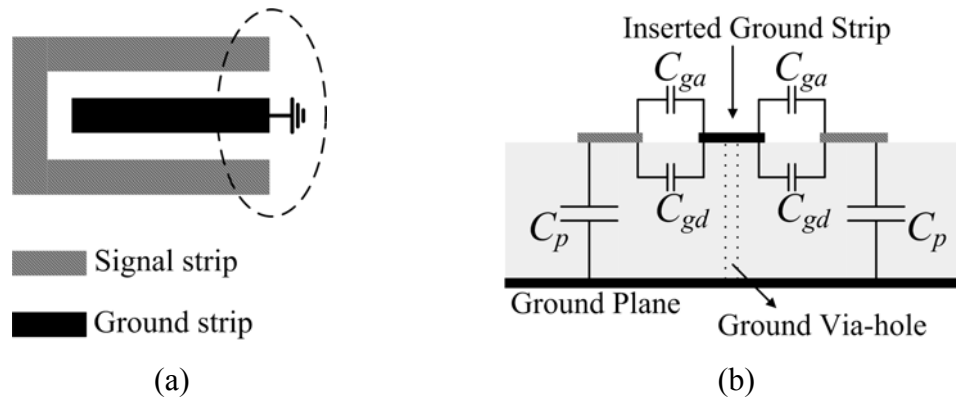


Fig. 3-2. (a) Top view of the proposed microstrip structure. (b) Cross-sectional view of the circled portion in (a).

Fig. 3-2 shows the top and cross-sectional views of the proposed microstrip structure. This structure is based on the conventional microstrip line where a ground strip is inserted in the signal plane and a ground via-hole is used. In Fig. 3-2(b),  $C_p$  denotes the parallel-plate capacitance per unit length between the signal strip and the microstrip ground plane;  $C_{ga}$  and  $C_{gd}$  represent the fringe capacitances per unit length across the gap between the signal strip and the inserted ground strip in the air and dielectric regions, respectively. While the capacitance  $C_p$  diminishes due to the inserted ground strip, however, the capacitances  $C_{ga}$  and  $C_{gd}$  can compensate for the decrease of  $C_p$ . Furthermore, if the strip spacing is small enough compared with the substrate thickness,  $C_{ga}$  and  $C_{gd}$  become large, which effectively decreases the characteristic impedance. This concept could be used to minimize the resonator size if the lower characteristic impedance is needed, especially for the thick substrate. In addition, this method increases the coplanar capacitance and makes the characteristic impedance less sensitive to the variation of the substrate thickness.

To demonstrate the properties mentioned above, take the substrates with a dielectric constant of 3.6 and two thicknesses ( $h$ ) of 0.5 and 1.5 mm as an example. If the total

transverse width of a microstrip line is fixed at 3 mm, Table 3-1 compares the characteristic impedance of the microstrip line for different numbers  $N$  of inserted ground strips, where  $N = 0$  corresponds to the conventional microstrip line. We first perform the full-wave electromagnetic (EM) simulation for the proposed microstrip structure by using Sonnet software, and then load the two-port  $S$ -parameter file in AWR Microwave Office to obtain the characteristic impedance. Or we can obtain the characteristic impedance by using the microstrip  $N$ -coupled line model ( $N = 2$  to 16) in AWR Microwave Office. Here, the widths of the inner signal and ground strips are all 0.3 mm, and the spacing between adjacent strips is 0.15 mm. Two via-holes are added on both ends of each inserted ground strip, which will be explained later. Apparently, for a microstrip line with a fixed transverse width, the characteristic impedance decreases as the number of inserted ground strips increases. The decreasing amount is particularly large for the thick substrate. Furthermore, the characteristic impedance difference between the microstrip lines on the thin and thick substrates is smallest as  $N = 3$ .

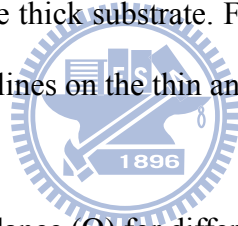


Table 3-1 Characteristic impedance ( $\Omega$ ) for different numbers of inserted ground strips

(Total line width is kept constant as 3 mm.)

$N$	0	1	2	3
$h = 0.5$ mm	24.5	22.9	21.8	21.2
$h = 1.5$ mm	50.9	37.4	30.8	27

### 3.1.2 Characteristics of the Proposed $\lambda/4$ SIR

On the basis of the structure in Fig. 3-2(a), Fig. 3-3(a) shows the proposed  $\lambda/4$  microstrip SIR structure. It is seen in the figure that the high-impedance ( $Z_1$ ) and low-impedance ( $Z_2$ ) sections are cascaded together and the high-impedance section is short-ended. In comparison with the conventional  $\lambda/4$  microstrip SIR structure shown in Fig. 3-1(a), the proposed one has ground strips in its low-impedance section. The high-impedance section has a physical

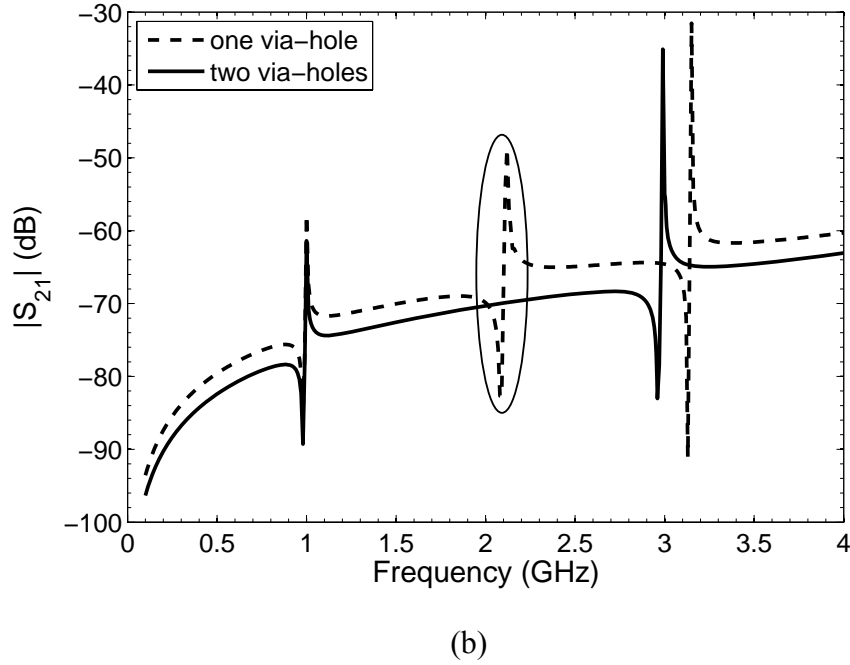
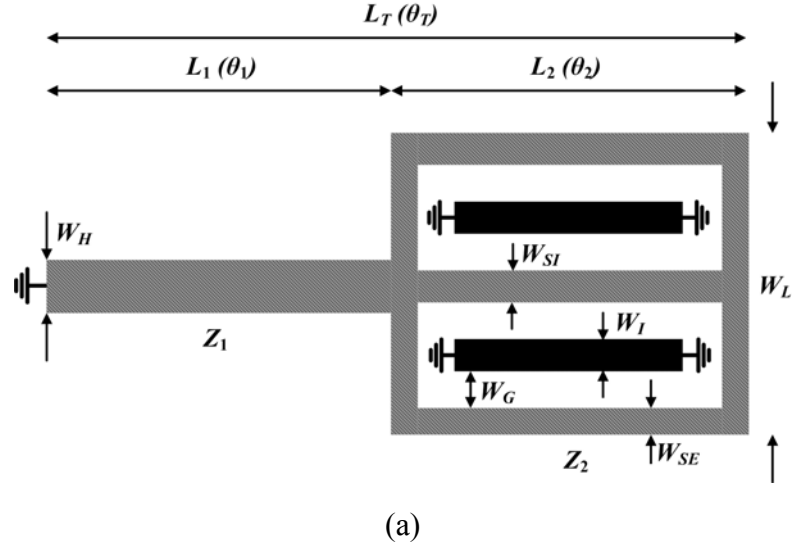


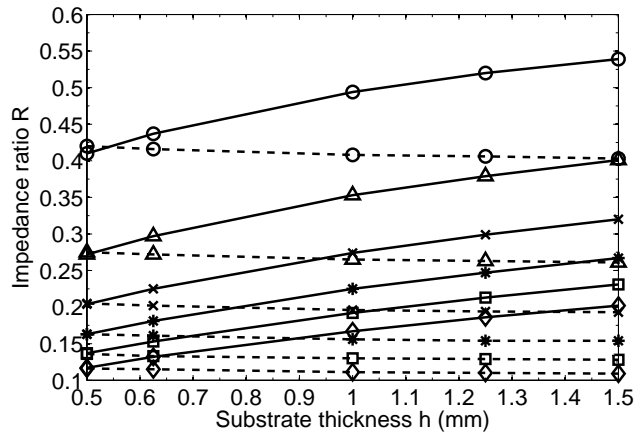
Fig. 3-3. (a) Proposed  $\lambda/4$  microstrip SIR. (b) Comparison of the frequency responses of the resonators with one and two via-holes on the ends of each inserted ground strip.

(electrical) length of  $L_1(\theta_1)$  and a width of  $W_H$ . The low-impedance section has a physical (electrical) length of  $L_2(\theta_2)$  and a total width of  $W_L$ . The total physical (electrical) length of the resonator is  $L_T(\theta_T)$ . In the low-impedance section, the width of inserted ground strips is  $W_I$ , the width of inner signal strips is  $W_{SI}$ , the width of outmost signal strips is  $W_{SE}$ , and the spacing between strips is  $W_G$ . Thus,  $W_L = 2N \times W_G + N \times W_I + (N - 1) \times W_{SI} + 2 \times W_{SE}$ , where  $N$

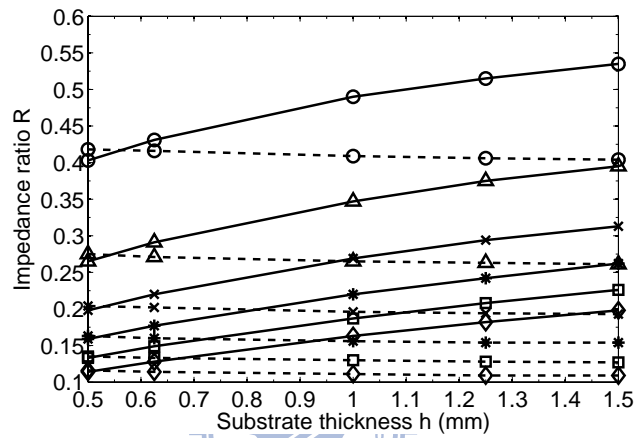
is the number of inserted ground strips. Note that an additional ground via-hole is added on the other end of each inserted ground strip in Fig. 3-3(a) so as to push the resonant frequency of the ground strip to higher frequency. To understand this better, consider the simple case of the resonator with  $N=1$ ,  $L_1=L_2$ ,  $W_{SE}=W_I=0.3$  mm,  $W_L=W_H=1.35$  mm, and  $W_G=0.225$  mm on the substrate with a dielectric constant of 3.6 and a thickness of 0.5 mm. Fig. 3-3(b) compares the frequency responses of two resonators where the inserted ground strips have one and two via-holes on their ends, respectively. It is apparent that the resonator with two via-holes on the ends of each inserted ground strip has better spurious response. The SIRs with different numbers of via-holes in the low-impedance section are described in Section 3.4.

Now, we compare the characteristics of the proposed  $\lambda/4$  SIR with the conventional one. In the following discussion, a lossless metal is assumed during the simulation. Since the capability of the available fabrication process is taken into account, each via-hole is 0.3 mm in diameter and the following physical dimensions are fixed as  $L_1=L_2$ ,  $W_H=W_G=0.225$  mm, and  $W_{SI}=W_I=0.3$  mm.

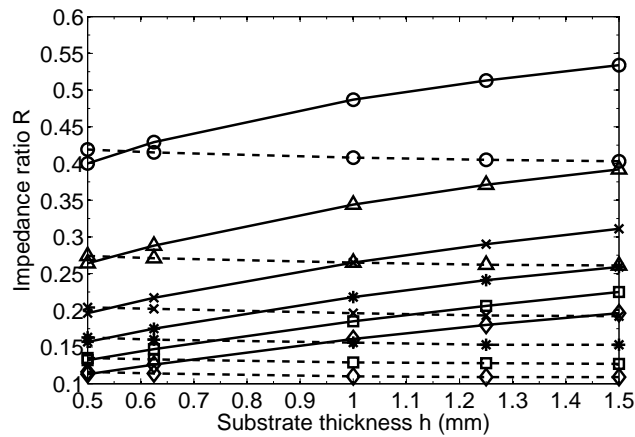
For the same  $W_L$  and  $W_H$ , the impedance ratio  $R$  versus substrate thickness  $h$  for the conventional and proposed  $\lambda/4$  SIRs is shown in Fig. 3-4 for comparison, where solid lines belong to the conventional SIRs and dashed lines belong to the proposed ones. In Fig. 3-4, the number of inserted ground strips of the proposed SIRs is maximized so that  $W_{SE}=W_{SI}=0.3$  mm. Thus, different  $W_L$  in each figure corresponds to different numbers of inserted ground strips (i.e., from  $N=1$  to 6). Fig. 3-4(a)-(c) are similar, except substrate dielectric constants  $\epsilon_r$  are different. As shown in Fig. 3-4, it can be obviously found that the impedance ratio  $R$  of the proposed SIR is lower than that of the conventional one in most of the substrate thickness values (i.e.,  $h \geq 0.57$  mm in all cases). One extra benefit is that the proposed SIR has a nearly constant impedance ratio  $R$  versus substrate thickness  $h$ . The phenomenon implies that the impedance ratio of the proposed SIR is insensitive to the variation of the substrate thickness.



(a)



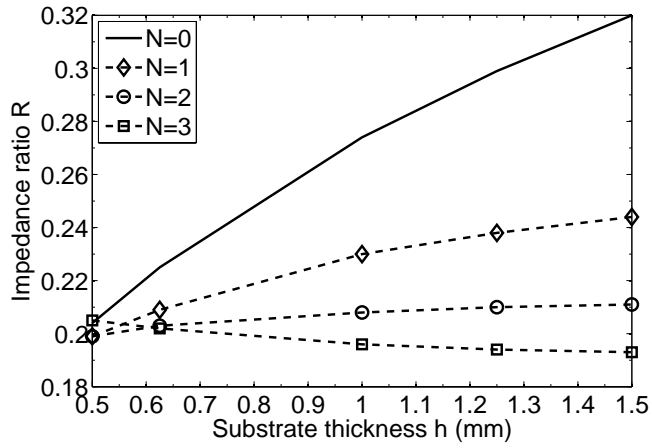
(b)



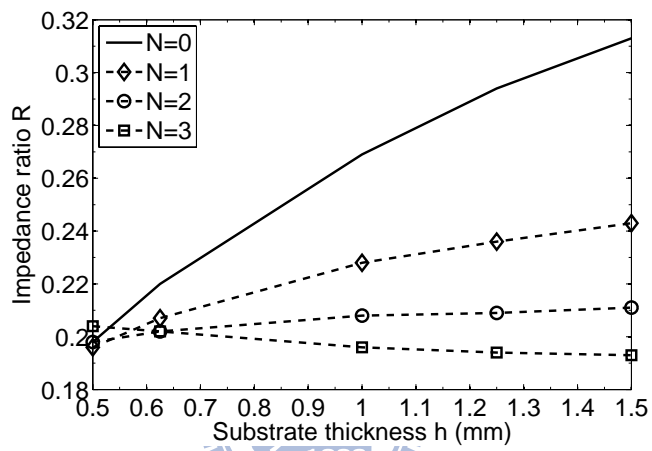
(c)

Fig. 3-4. Impedance ratio  $R$  of the conventional and proposed  $\lambda/4$  SIRs versus substrate thickness  $h$  and width  $W_L$  (in millimeters) for: (a)  $\epsilon_r = 3.6$ , (b)  $\epsilon_r = 6.8$ , and (c)  $\epsilon_r = 10.2$ .

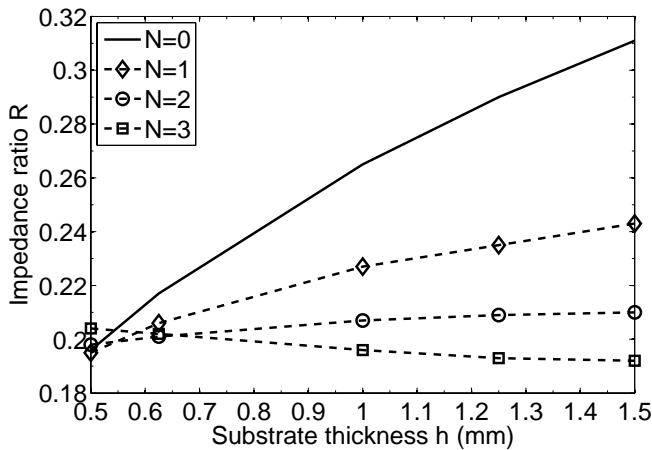
Conventional: solid line. Proposed: dashed line. (circle  $\circ$ :  $W_L = 1.35$ ,  $N = 1$ ; triangle  $\triangle$ :  $W_L = 2.4$ ,  $N = 2$ ; cross  $\times$ :  $W_L = 3.45$ ,  $N = 3$ ; asterisk  $*$ :  $W_L = 4.5$ ,  $N = 4$ ; square  $\square$ :  $W_L = 5.55$ ,  $N = 5$ ; diamond  $\diamond$ :  $W_L = 6.6$ ,  $N = 6$ .)



(a)



(b)



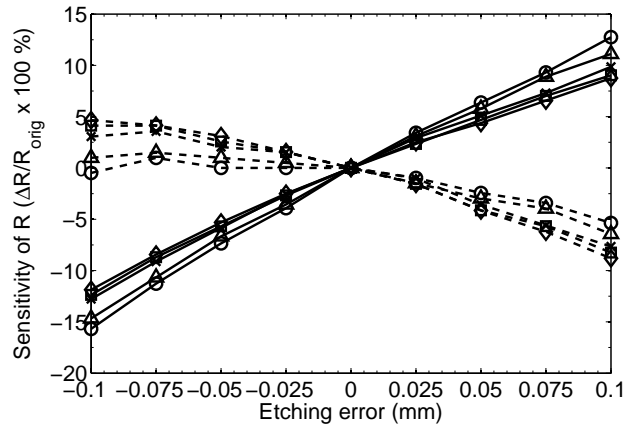
(c)

Fig. 3-5. Impedance ratio  $R$  versus substrate thickness  $h$  for the proposed  $\lambda/4$  SIRs with different numbers of inserted ground strips when  $W_L = 3.45$  mm. (a)  $\epsilon_r = 3.6$ . (b)  $\epsilon_r = 6.8$ . (c)  $\epsilon_r = 10.2$ . ( $N$ : number of inserted ground strips.  $N = 0$ : conventional microstrip structure.)

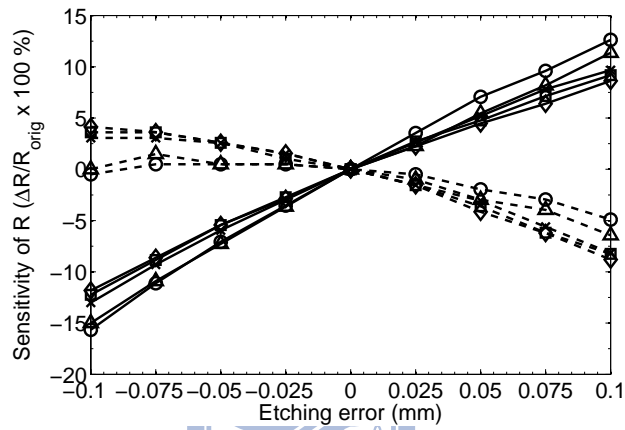


Another interesting issue is about the number of inserted ground strips. As the number of inserted ground strips is not maximized, what will be the performance? Taking  $W_L = 3.45$  mm as an example, Fig. 3-5 depicts the impedance ratio  $R$  versus substrate thickness  $h$  with the number of inserted ground strips as a parameter. The number  $N$  of inserted ground strips is varied from 0 to 3, where  $N = 0$  corresponds to the conventional microstrip structure. It is observed that the proposed SIR structure ( $N = 1, 2, 3$ ) is less sensitive to the substrate thickness variation compared with the conventional one and  $N = 2$  or  $N = 3$  has the best performance. For the conventional  $\lambda/4$  microstrip SIR, the percentage variation of the characteristic impedance of the high-impedance line is much less than that of the low-impedance line under the variation of the substrate thickness. Therefore, the impedance ratio  $R$  varies largely for the conventional microstrip SIR structure. The principle behind the proposed  $\lambda/4$  microstrip SIR is that in the low-impedance microstrip section, the coplanar signal and ground strips also control the characteristic impedance. As a result, the proposed low-impedance microstrip structure is much less sensitive to the variation of the substrate thickness. Taking Fig. 3-5(a) as an example, when the substrate thickness  $h$  is changed from 0.5 to 1.5 mm,  $Z_1$  is changed from 108.4 to 149.7  $\Omega$ , and  $Z_2$  is changed from 22.1 to 47.9  $\Omega$  for the conventional microstrip structure and from 22.2 to 28.9  $\Omega$  for the proposed one with  $N = 3$ . Consequently, the impedance ratio  $R$  is changed from 0.204 to 0.32 for the  $N = 0$  case and from 0.205 to 0.193 for the  $N = 3$  case.

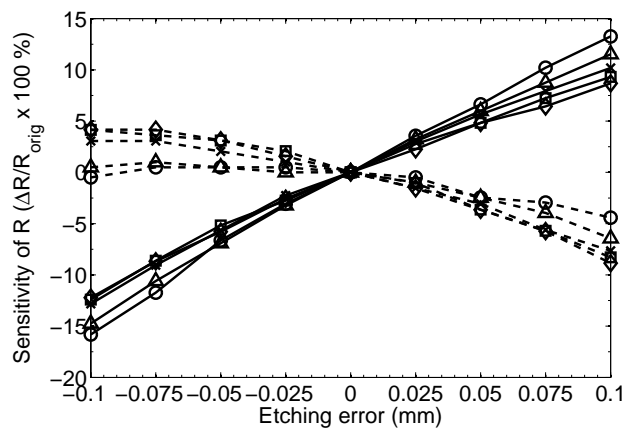
During the printed circuit board (PCB) manufacturing process, the most serious error is the etching error. The over-etching or under-etching occurs frequently from lot to lot. The proposed SIR structure further shows much better tolerance to etching errors than the conventional one. For the case of  $W_L = 3.45$  mm in Figs. 3-4 and 3-5, Fig. 3-6 shows the percentage variation of the impedance ratio  $R$  of the conventional and proposed ( $N = 3$ )  $\lambda/4$  SIRs versus etching error (from over-etching 0.1 mm to under-etching 0.1 mm). In each figure, different curves correspond to different substrate thicknesses. Fig. 3-6(a)-(c) are similar,



(a)



(b)

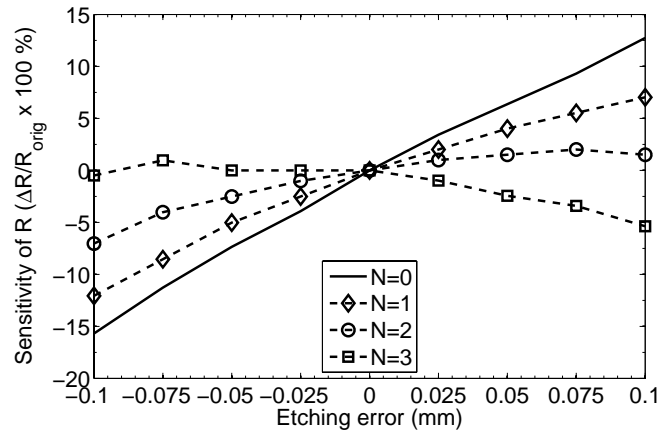


(c)

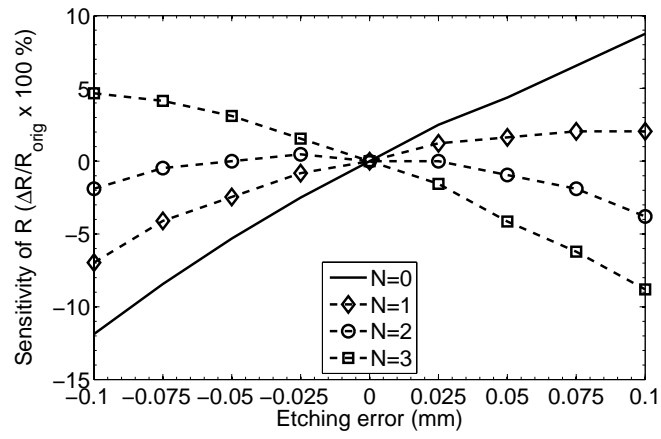
Fig. 3-6. Sensitivity to etching tolerances for the conventional and proposed  $\lambda/4$  SIRs with various values of the substrate thickness  $h$  (in millimeters) when  $W_L = 3.45$  mm. (a)  $\epsilon_r = 3.6$ . (b)  $\epsilon_r = 6.8$ . (c)  $\epsilon_r = 10.2$ . Conventional: solid line. Proposed ( $N = 3$ ): dashed line. Positive: under-etching. Negative: over-etching. (circle  $\circ$ :  $h = 0.5$ ; triangle  $\triangle$ :  $h = 0.625$ ; cross  $\times$ :  $h = 1$ ; square  $\square$ :  $h = 1.25$ ; diamond  $\diamond$ :  $h = 1.5$ .)

except substrate dielectric constants  $\epsilon_r$  are different. From Fig. 3-6, it can be clearly observed that the percentage change of the impedance ratio  $R$  of the proposed SIR structure is much less than that of the conventional one. The mechanism behind this is that the proposed low-impedance microstrip structure is more sensitive to etching tolerances than the conventional one to keep the impedance ratio unchanged. In other words, for the conventional  $\lambda/4$  microstrip SIR, the characteristic impedance variation of the high-impedance line is much larger than that of the low-impedance line under the same amount of etching error, and this causes the impedance ratio to change largely. For example, under the condition of over-etching 0.05 mm and the substrate thickness  $h = 0.5$  mm in Fig. 3-6(a),  $Z_1$  is changed 9.13% (from 108.4 to 118.3  $\Omega$ ), and  $Z_2$  is changed 0.9% (from 22.1 to 22.3  $\Omega$ ) for the conventional microstrip structure. Consequently,  $R$  is changed from 0.204 to 0.189 ( $\Delta R / R = -7.35\%$ ). However, for the proposed low-impedance microstrip structure,  $Z_2$  is changed 9.46% (from 22.2 to 24.3  $\Omega$ ) so that  $R$  is almost unchanged ( $R = 0.205$  and  $\Delta R / R = 0.299\%$ ). Here,  $W_L = 3.45$  mm is just an example and other  $W_L$ 's in Fig. 3-4 also show similar results.

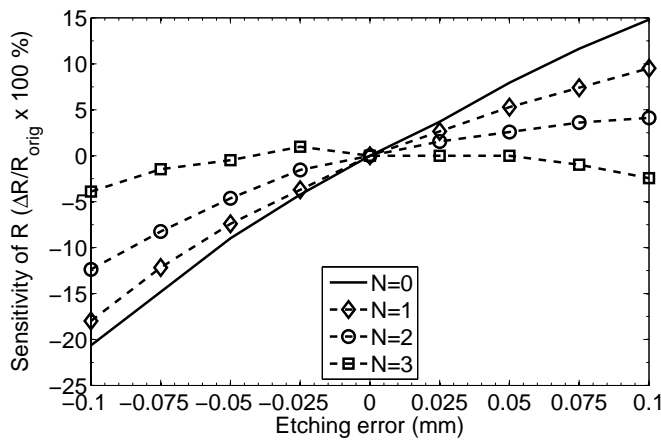
Again, it is interesting to change the number of inserted ground strips. Fig. 3-7 shows the percentage variation of the impedance ratio  $R$  of the proposed  $\lambda/4$  SIR versus etching error for different numbers of inserted ground strips. There are two sets of physical dimensions to be used for the simulation. The first one is  $W_L = 3.45$  mm,  $W_{SI} = W_I = 0.3$  mm, and  $W_G = W_H = 0.225$  mm. The second one is  $W_L = 3.4$  mm,  $W_{SI} = W_I = 0.25$  mm,  $W_G = 0.275$  mm, and  $W_H = 0.175$  mm. During the simulation, substrates with thicknesses of 0.5 and 1.5 mm and a dielectric constant of 3.6 are used. As shown in Fig. 3-7, for the given dimensions, the best choice for the number of inserted ground strips can be determined. Taking Fig. 3-7(a) as an example,  $N = 3$  (the maximum allowable number) is the best choice for the first set of dimensions on the given substrate. It is demonstrated that the impedance ratio  $R$  of the proposed  $\lambda/4$  microstrip SIR is less sensitive to etching tolerances compared with that of the conventional one, even if  $N = 1$ .



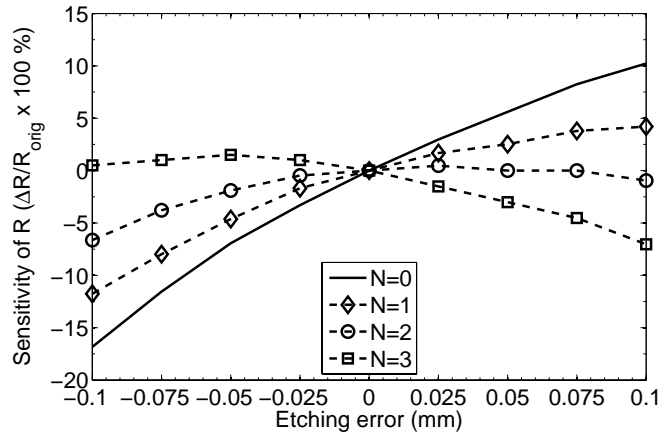
(a)



(b)



(c)



(d)

Fig. 3-7. Sensitivity to etching tolerances for the proposed  $\lambda/4$  SIRs with different numbers of inserted ground strips. (Case I:  $W_L = 3.45$  mm,  $W_{SI} = W_I = 0.3$  mm, and  $W_G = W_H = 0.225$  mm. Case II:  $W_L = 3.4$  mm,  $W_{SI} = W_I = 0.25$  mm,  $W_G = 0.275$  mm, and  $W_H = 0.175$  mm.) (a) Case I:  $h = 0.5$  mm. (b) Case I:  $h = 1.5$  mm. (c) Case II:  $h = 0.5$  mm. (d) Case II:  $h = 1.5$  mm. ( $N$ : number of inserted ground strips.  $N = 0$ : conventional microstrip structure.)

Table 3-2 Design parameters of the proposed SIR filters

	Filter I	Filter II
Substrate $\epsilon_r = 3.58$	$h = 0.508$ mm	$h = 1.524$ mm
Center frequency $f_0$ (GHz)	1	1
Bandwidth $\Delta$	7%	10%
Impedance ratio $R$	0.205	0.199
$Q_{ext}$	13.697	9.58792
$k_{12} = k_{34}$	0.0627716	0.0896737
$k_{23}$	0.0484737	0.0692482

### 3.1.3 Four-Pole Cross-Coupled Filter Design

To demonstrate the proposed structure, two four-pole cross-coupled bandpass filters were fabricated. Since the cross coupling, which produces transmission zeros, is very weak, the

initial design procedure is based on the four-pole Chebyshev response filter with a 0.05-dB equal-ripple passband characteristic. Both filters have the same topology, and their specifications and coupling coefficients are listed in Table 3-2. Filter I was fabricated on a Rogers RO4003 substrate with a dielectric constant of 3.58, a loss tangent of 0.0021, and a thickness of 0.508 mm. Filter II was fabricated on the same substrate as filter I, except the thickness is 1.524 mm.

In the design process, we first fix the widths of  $W_H$ ,  $W_L$ ,  $W_{SI}$ ,  $W_I$ , and  $W_G$ , and then plot the variation of the impedance ratio versus etching error for different numbers of inserted ground strips. The proper number of inserted ground strips could be chosen for the prescribed dimensions and the available fabrication process.

Fig. 3-8 shows the two basic coupling structures for our filter design. Note that each SIR is folded for size reduction. There are two kinds of couplings involved in the filter. At resonance, each of the  $\lambda/4$  SIRs has the maximum electric fringe fields near the open end and the maximum magnetic fringe fields at the short end. Hence, Fig. 3-8(a) is for the electric coupling and Fig. 3-8(b) is for the magnetic coupling. For filter I, the resonator dimensions are  $W_L = 3.45$  mm,  $W_{SE} = W_{SI} = W_I = 0.3$  mm, and  $W_G = W_H = 0.225$  mm. For filter II, they are  $W_L = 3.4$  mm,  $W_{SE} = W_{SI} = W_I = 0.25$  mm,  $W_G = 0.275$  mm, and  $W_H = 0.175$  mm. In both filters, the number of inserted ground strips is three. All diameters of via-holes have the same size of 0.3 mm. Based on the structures presented in Fig. 3-8, the relation between the coupling coefficient and the spacing between adjacent SIRs is shown in Fig. 3-9.

Fig. 3-10 depicts the layout of the filters where the physical parameters corresponding to those of Table 3-3 are indicated. Here, we number these four resonators as 1-4 from left to right. The coupling  $k_{23}$  is magnetic, whereas  $k_{12}$  and  $k_{34}$  are electric. The source coupling and load coupling are both achieved by a tapped feed line because it is space saving and easy to design [60]. The tap position  $L_Q$  is chosen to match the  $Q_{\text{ext}}$  value for the 50- $\Omega$  source/load impedance. A thin microstrip line provides the small cross coupling [57], [61] between

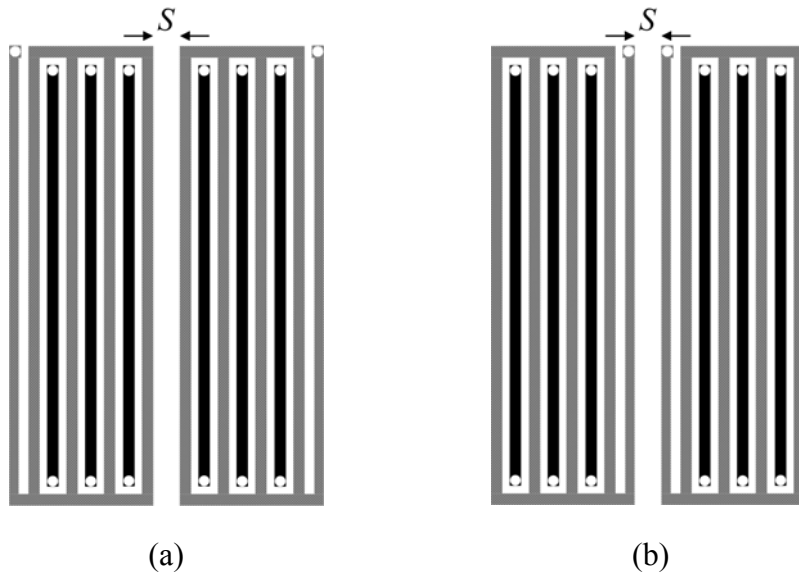


Fig. 3-8. Coupling structures for: (a) electric coupling and (b) magnetic coupling.

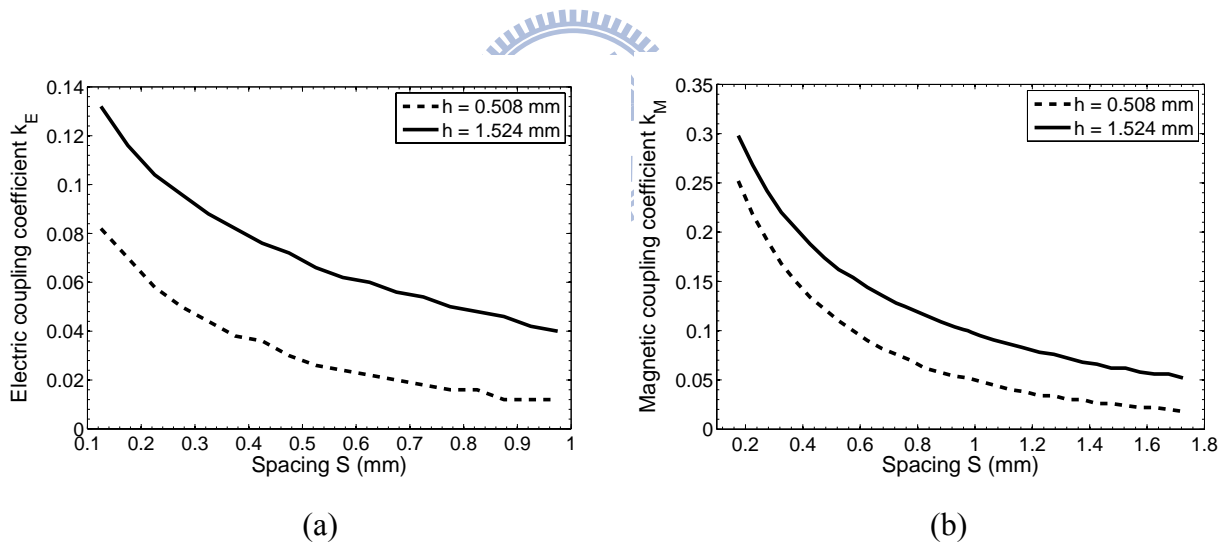


Fig. 3-9. Coupling coefficients of the coupling structures for: (a) electric coupling and (b) magnetic coupling.

Table 3-3 Dimensions of the designed filters

(mm)	$L_{H1}$	$L_{H2}$	$W_H$	$W_{SE}$	$W_{SI}$	$W_I$	$W_G$	$W_L$	$L_Q$	$L_Z$	$W_Z$	$S_Z$	$S_1$	$S_2$
Filter I	12.925	12.75	0.225	0.3	0.3	0.3	0.225	3.45	4.125	15.225	0.225	0.175	0.175	0.925
Filter II	13.075	12.725	0.175	0.25	0.25	0.25	0.275	3.4	4.1	15.75	0.175	0.225	0.325	1.3

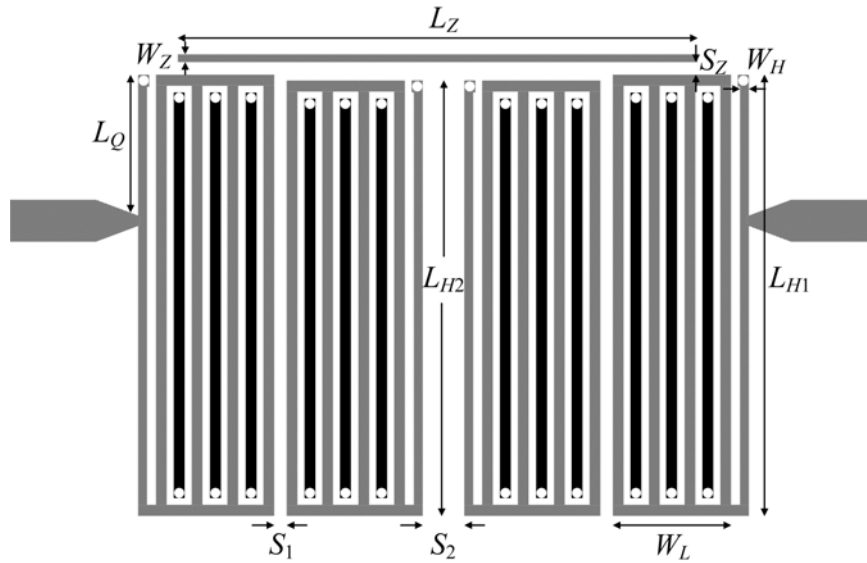


Fig. 3-10. Proposed layout of the four-pole cross-coupled filter.

resonators 1 and 4 to produce a pair of transmission zeros on both sides of the passband. The passband response almost remains unchanged when the cross coupling is applied. The strength of the cross coupling is determined by the length  $L_Z$ , the width  $W_Z$  of the coupling microstrip, and the gap  $S_Z$  between the coupling microstrip and resonators 1 and 4. Herein, two transmission zeros are placed at 0.8 and 1.2 GHz. The commercial full-wave EM simulation software Sonnet is used to perform the simulation.

Fig. 3-11 shows the fabricated filter I with a size of 17.2 mm  $\times$  13.3 mm. Fig. 3-12

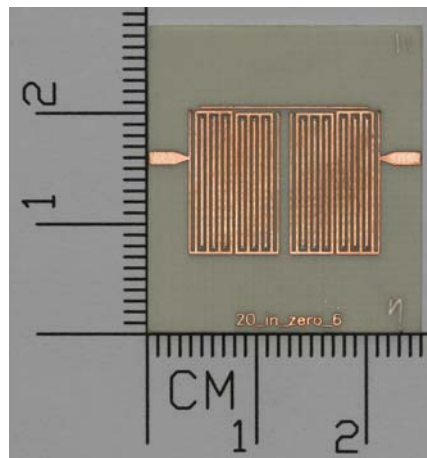
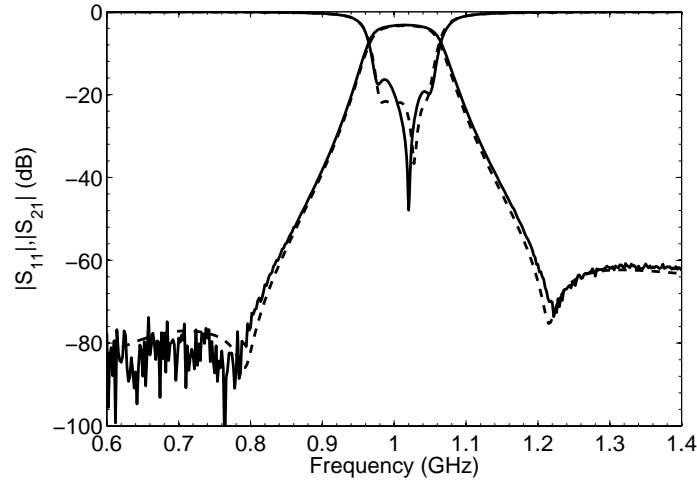
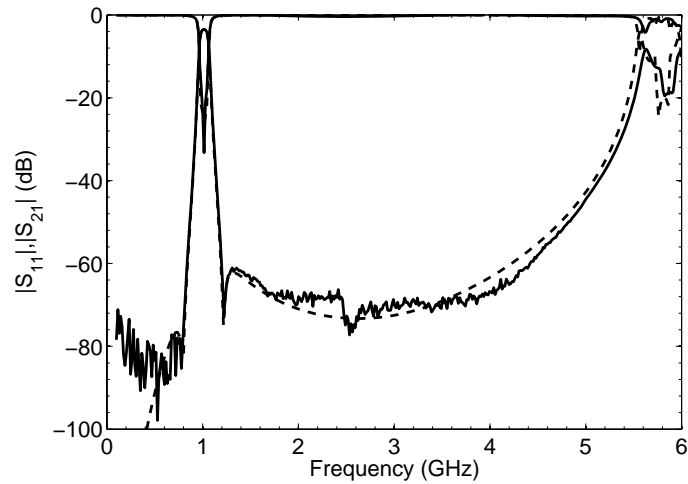


Fig. 3-11. Photograph of the fabricated circuit (filter I).





(a)



(b)

Fig. 3-12. Simulated (dashed line) and measured (solid line) results ( $|S_{11}|$  and  $|S_{21}|$ ) of filter I. (a) Narrowband responses. (b) Wideband responses.

illustrates its simulated and measured responses. The measured results show that the filter has a center frequency of 1.015 GHz and two transmission zeros at 0.784 and 1.222 GHz. The measured passband insertion loss is approximately 3.1 dB, and the passband return loss is better than 16 dB. The first spurious response is at 5.631 GHz, and the rejection level is better than 30 dB from 1.116 to 5.364 GHz. The comparison between the simulated and measured results gives good agreement.

For filter II, Fig. 3-13 shows a photograph of the fabricated circuit, which has a size of

17.7 mm × 13.5 mm. The simulated and measured responses of filter II are presented in Fig. 3-14. The measured results show that the filter has a center frequency of 1.023 GHz and two transmission zeros at 0.796 and 1.214 GHz. The measured passband insertion loss is approximately 2.2 dB, and the passband return loss is better than 15 dB. The first spurious frequency is at 5.085 GHz, which is a little down-shifted due to the resonance of the cross-coupling microstrip. The rejection level is better than 30 dB from 1.147 to 4.967 GHz.

It can be seen that both filters have symmetric insertion loss responses and sharp skirt

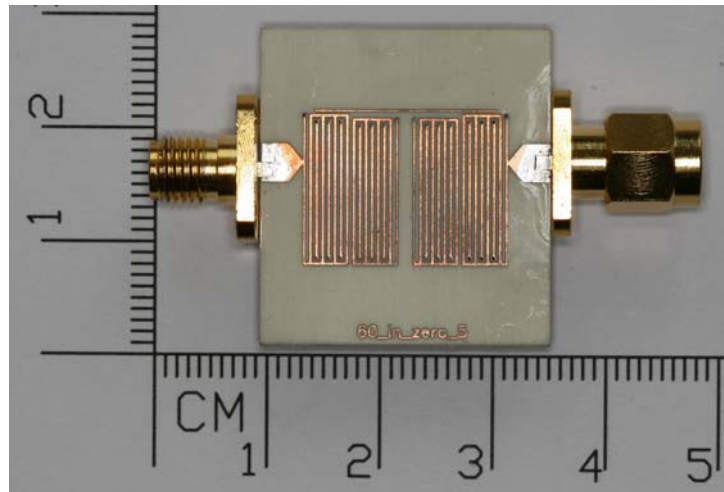
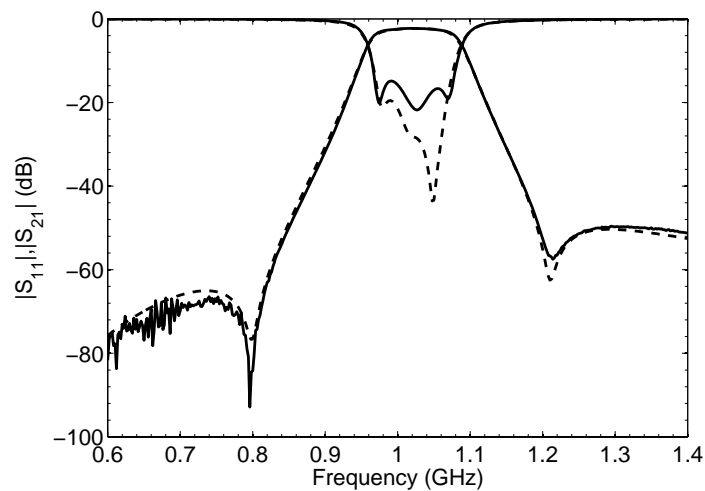


Fig. 3-13. Photograph of the fabricated circuit (filter II).



(a)

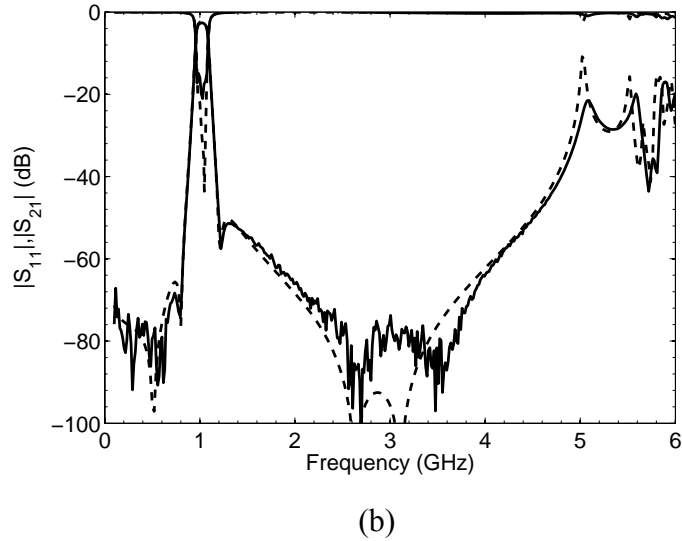


Fig. 3-14. Simulated (dashed line) and measured (solid line) results ( $|S_{11}|$  and  $|S_{21}|$ ) of filter II. (a) Narrowband responses. (b) Wideband responses.

characteristics. The insertion loss is mainly due to the conductor loss. Although a lot of via-holes are used in the proposed low-impedance microstrip structure, they have little effect on the passband insertion loss. This is because in the passband of the filter, the current is mainly distributed in the high-impedance section, as shown in Fig. 3-15 for filter I. There is little current through the via-holes on the inserted ground strips in the low-impedance section. Therefore, the loss is attributed to the high current density in the high-impedance section. Table 3-4 compares the measured passband insertion losses for the conventional and proposed SIR filters with the same specifications. The conventional SIR filters were designed to have: 1) the same  $W_L$  and  $W_H$ , and 2) the same  $R$  and  $W_H$  as the proposed SIR filters. Since the filters in the same group have the same  $W_H$ , it is apparent that the filters in the same group have nearly the same passband insertion losses.

### 3.1.4 Sensitivity to Etching Tolerances

To show the sensitivity to etching tolerances for the proposed SIR filters, we modify the masks during the fabrication process because PCB factories cannot change their processing

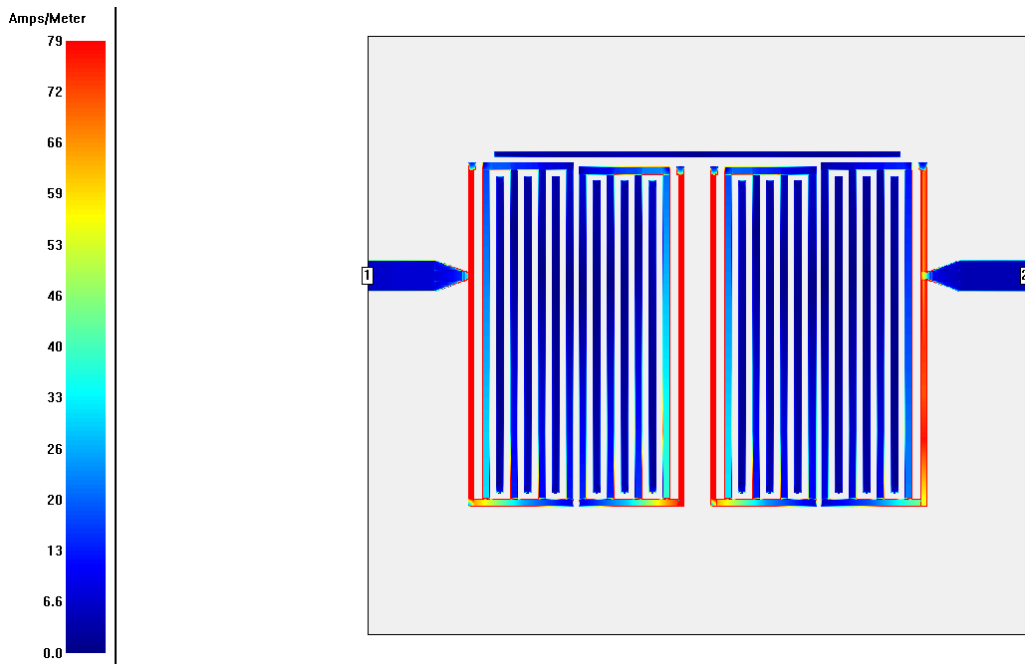
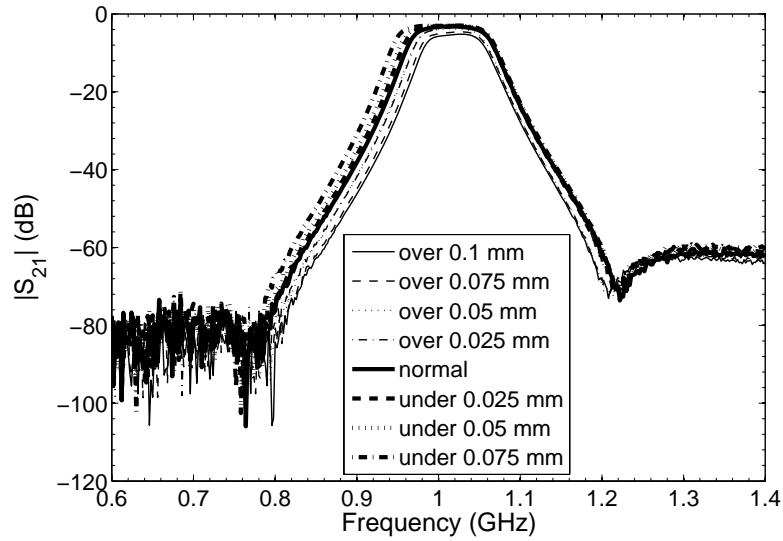


Fig. 3-15. Current distribution of the proposed filter at the center frequency.

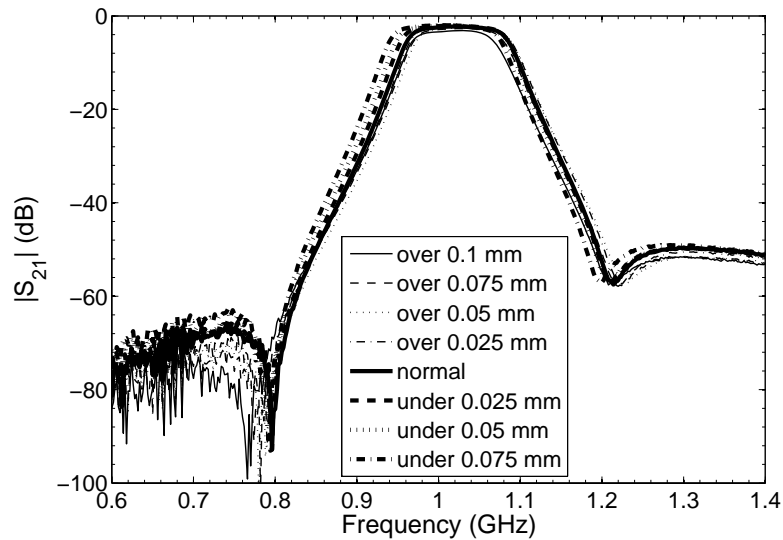
Table 3-4 Comparison of measured passband insertion losses for the conventional and proposed SIR filters

Passband insertion loss (dB)	Filter I	Filter II
Proposed	3.1	2.2
Conventional : the same $W_L$ and $W_H$	3.1	2.1
Conventional : the same $R$ and $W_H$	3	2.1

parameters to match our study. Fig. 3-16 presents the measured responses of both proposed filters versus etching error, i.e., from over-etching 0.1 mm (4 mil) to under-etching 0.075 mm (3 mil), to demonstrate their sensitivity. Only the insertion loss curves are shown for clarity. As observed in Fig. 3-16(a), the center frequency and two transmission zeros of filter I are almost unshifted in spite of inaccurate fabrication. The passband return losses, although not shown, are all better than 10 dB. The passband insertion loss and bandwidth are slightly changed. The passband insertion loss is higher for the over-etched case owing to the lower unloaded quality factor and narrower bandwidth. The bandwidth is wider for the under-etched



(a)

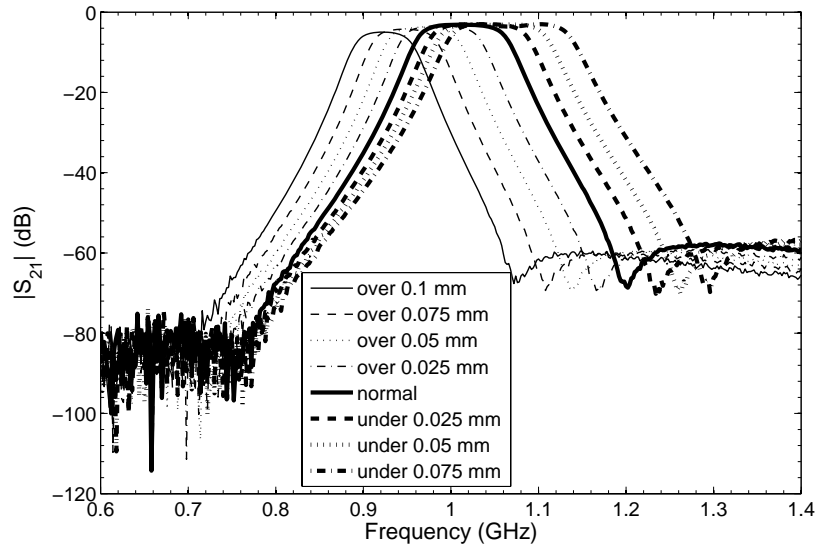


(b)

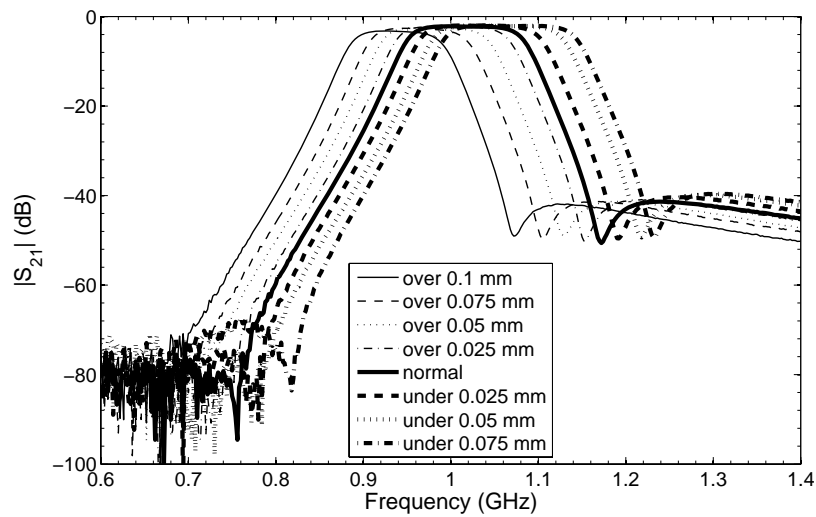
Fig. 3-16. Measured sensitivity to etching tolerances for the proposed SIR filter. (a) Filter I. (b) Filter II (over: over-etching; under: under-etching).

case because the narrower gap results in the stronger coupling between the resonators. The same results are applied to filter II, as shown in Fig. 3-16(b), except the passband return losses are better than 12 dB in all cases.

The conventional  $\lambda/4$  microstrip SIR filters were also designed and fabricated on the same substrates to compare with the proposed ones. The conventional SIR filters have the



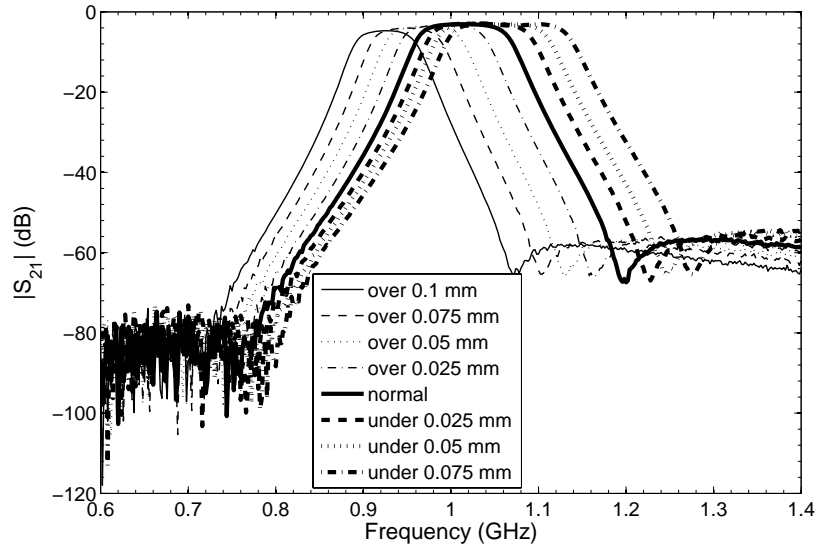
(a)



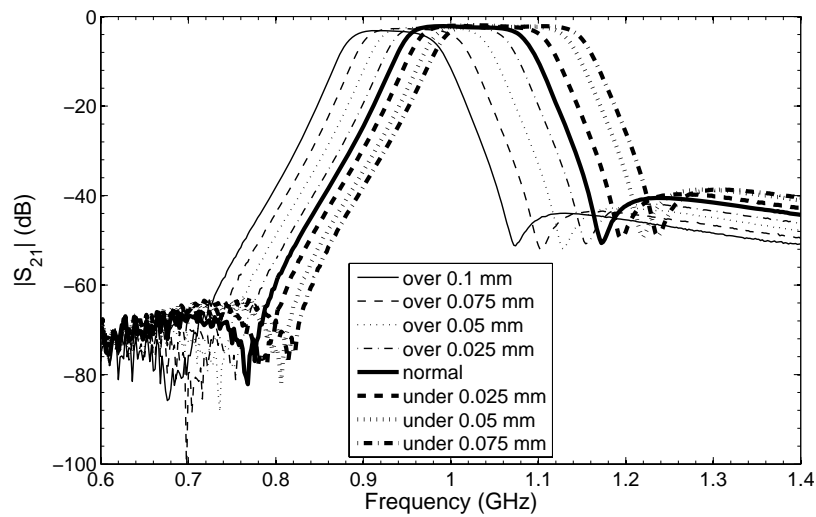
(b)

Fig. 3-17. Measured sensitivity to etching tolerances for the conventional SIR filter ( $W_L$  and  $W_H$  are the same as those of the proposed filter). (a) Filter I. (b) Filter II (over: over-etching; under: under-etching).

same center frequencies and bandwidths, as given in Table 3-2, and similar layout configurations, as shown in Fig. 3-10, except that there is no inserted ground strip in the low-impedance section. We set two groups of parameters for comparison. The first group of the conventional SIR filters keeps the same dimensions  $W_L$  and  $W_H$  as those of the proposed SIR



(a)



(b)

Fig. 3-18. Measured sensitivity to etching tolerances for the conventional SIR filter ( $R$  and  $W_H$  are the same as those of the proposed filter). (a) Filter I. (b) Filter II (over: over-etching; under: under-etching).

filters. The second group of the conventional SIR filters is designed with the same impedance ratio  $R$  and width  $W_H$  as those of the proposed SIR filters. Their measured responses versus etching error are shown in Figs. 3-17 and 3-18, respectively. Again, only the insertion loss curves are shown for both groups of filters. As expected from the figures for both groups of

the conventional SIR filters, the center frequency and two transmission zeros are significantly shifted. The passband return losses of the conventional SIR filters, although not shown, are worse than those of the proposed ones when the etching error occurs. An extra benefit of the proposed SIR filters is that an obvious size reduction is achieved. For example, there is a size reduction of 39% for the proposed filter II compared with the conventional SIR filter when they have the same impedance ratio  $R$  and width  $W_H$ . Table 3-5 summarizes the percentage of the center frequency drift due to etching errors for the proposed SIR filters and two groups of the conventional SIR filters. Apparently, the proposed  $\lambda/4$  microstrip SIR filters show much less sensitivity to fabrication tolerances and have better performance.

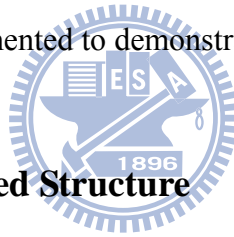
Table 3-5 Sensitivity to etching tolerances in terms of the percentage deviation of the center frequency for the conventional and proposed SIR filters

	$\Delta f / f_0 \times 100$ (%) $\Delta f$ : the amount of center frequency drift	normal	under etching 0.025 mm	under etching 0.05 mm	under etching 0.075 mm
Filter I	Proposed	0	-0.311	-0.48	-0.796
	Conventional: the same $W_L$ and $W_H$	0	1.921	3.385	5.346
	Conventional: the same $R$ and $W_H$	0	1.898	3.359	5.112
Filter II	Proposed	0	-0.365	-0.752	-1.252
	Conventional: the same $W_L$ and $W_H$	0	1.638	3.598	4.985
	Conventional: the same $R$ and $W_H$	0	1.919	3.918	5.372
	$\Delta f / f_0 \times 100$ (%) $\Delta f$ : the amount of center frequency drift	over etching 0.025 mm	over etching 0.05 mm	over etching 0.075 mm	over etching 0.1 mm
Filter I	Proposed	0.351	-0.107	0.454	0.52
	Conventional: the same $W_L$ and $W_H$	-2.36	-4.267	-6.356	-8.738
	Conventional: the same $R$ and $W_H$	-2.23	-4.077	-6.216	-8.637
Filter II	Proposed	0.27	0.663	0.096	-0.453
	Conventional: the same $W_L$ and $W_H$	-1.52	-3.441	-5.368	-7.758
	Conventional: the same $R$ and $W_H$	-1.657	-3.749	-5.941	-8.314



## 3.2 Miniaturized Microstrip Quarter-Wavelength SIR Filter

The impedance ratio of the SIR is a key point influencing the resonator length and the resonant frequency. Hence, if the characteristic impedance difference between the high- and low-impedance transmission lines is required to be large, the widths of the high- and low-impedance microstrip lines would be very thin and wide, respectively. However, in practical applications, the achievable line width is limited by the PCB process for a thin microstrip line and by the appearance of high-order modes for a wide microstrip line. The area of a conventional  $\lambda/4$  microstrip SIR is usually limited by these factors, especially at low frequency bands. In this section, on the basis of the structure in Fig. 3-2, a microstrip line with a characteristic impedance even lower than the low-impedance line shown in section 3.1 is further proposed and applied in the low-impedance section of a SIR. Two miniaturized  $\lambda/4$  microstrip SIR filters were implemented to demonstrate the proposed structure.



### 3.2.1 Analysis of the Proposed Structure

Fig. 3-19(a)-(b) show the top and bottom views of the proposed low-impedance microstrip line, which is an extension of the structure in Fig. 3-2. In this structure, signal strips are inserted in the microstrip ground plane (bottom layer) and ground strips are inserted in the microstrip signal metal (top layer). The inserted strips are parallel to each other to form interdigital capacitors on both the top and bottom layers of the PCB. Again, each inserted strip uses two via-holes on both ends for better spurious response. Fig. 3-19(c) depicts the cross-sectional view of the proposed structure. In Fig. 3-19(c),  $C_p$  denotes the parallel-plate capacitance per unit length located vertically between the signal and ground strips, whereas  $C_{ga}$  and  $C_{gd}$  represent the fringe capacitances per unit length across the gap between the coplanar signal and ground strips in the air and dielectric regions, respectively. While the capacitance  $C_p$  diminishes due to the inserted strip, however, the capacitances  $C_{ga}$  and  $C_{gd}$  can

compensate for the decrease of  $C_p$ . Furthermore, if the strip spacing is small enough compared with the substrate thickness,  $C_{ga}$  and  $C_{gd}$  become dominant terms. This effectively decreases the characteristic impedance of the microstrip line.

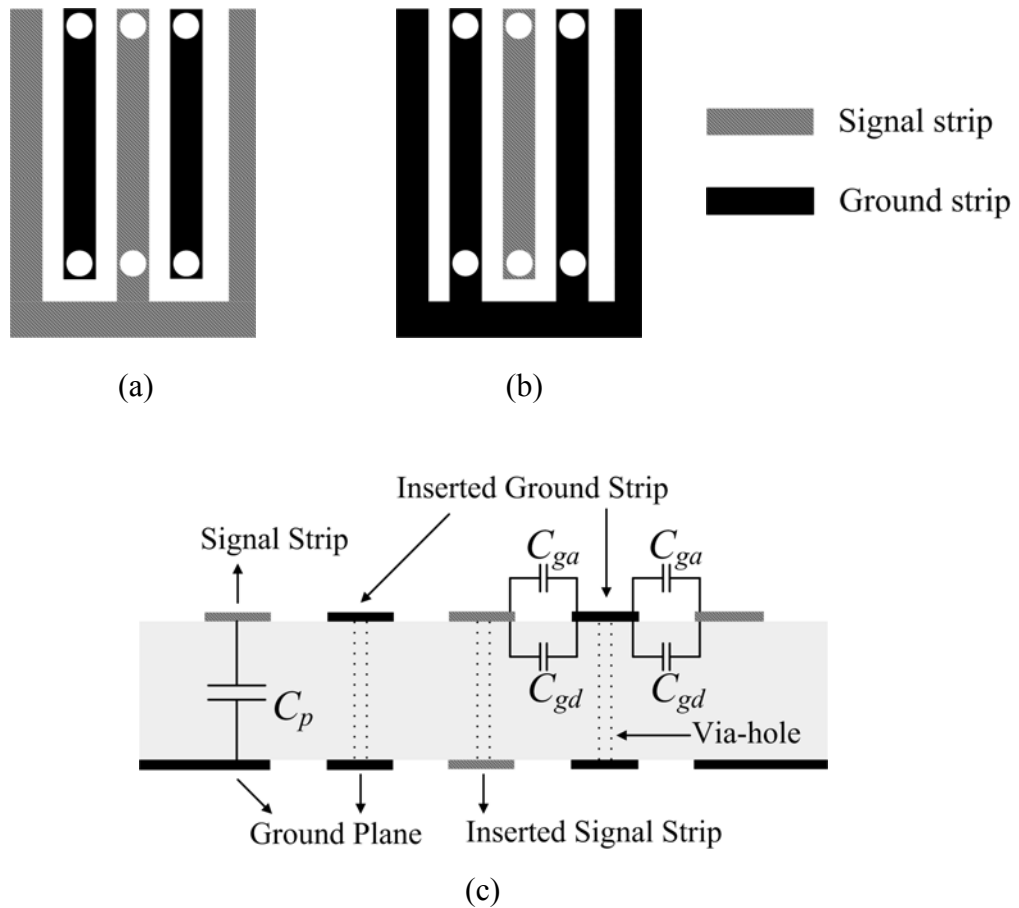


Fig. 3-19. Proposed microstrip structure. (a) Top view. (b) Bottom view. (c) Cross-sectional view.

Take the substrates with a dielectric constant of 3.58 and two thicknesses of 0.508 and 1.524 mm as an example. If the total transverse width of a microstrip line is fixed at 3 mm, Table 3-6 compares the characteristic impedance of the conventional and proposed microstrip lines. Here, the numbers of inserted ground strips on the top layer and inserted signal strips on the bottom layer are three and two, respectively. The widths of the signal and ground strips are all 0.3 mm, and the spacing between adjacent strips is 0.15 mm. The structure in Fig. 3-2 with

the same dimensions is also included for comparison. For the fixed transverse width, the microstrip line with the signal and ground strips on both layers has the smallest characteristic impedance. The decreasing amount is particularly large in the thick substrate case.

Table 3-6 Characteristic impedance ( $\Omega$ ) of the conventional and proposed microstrip lines

Thickness (mm)	0.508	1.524
Conventional	25.2	53.3
Structure in Fig. 3-2	21.4	26.7
Structure in Fig. 3-19	16.6	18.8

### 3.2.2 Four-Pole Cross-Coupled Filter Design

Fig. 3-20 shows the proposed  $\lambda/4$  SIR, which comprises a high-impedance ( $Z_1$ ) and a low-impedance ( $Z_2$ ) section. The high-impedance section has a physical length of  $L_1$  and the low-impedance section has  $L_2$ , and their respective widths are  $W_H$  and  $W_L$ . Here, we have  $L_1 = L_2$  to obtain a minimum resonator length. In comparison with the conventional SIR structure, the modified one uses the proposed microstrip structure in the low-impedance section to decrease the characteristic impedance. The width of ground strips is  $W_G$ , the width of inner signal strips is  $W_{SI}$ , the width of outmost signal strips is  $W_{SE}$ , and the spacing between

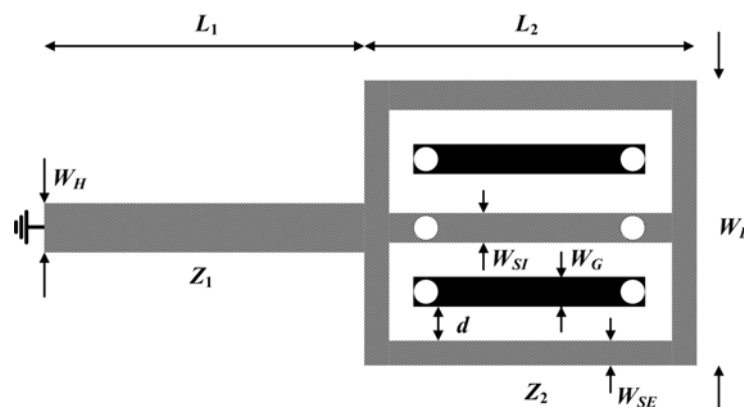


Fig. 3-20. Proposed  $\lambda/4$  microstrip SIR.

Table 3-7 Design parameters of the proposed SIR filters

	Filter I	Filter II
Center frequency (MHz)	1000	900
Bandwidth (%)	6	9
$Z_2 / Z_1$ ( $\Omega$ )	16.6 / 97.7	18.8 / 139
Substrate thickness (mm)	0.508	1.524

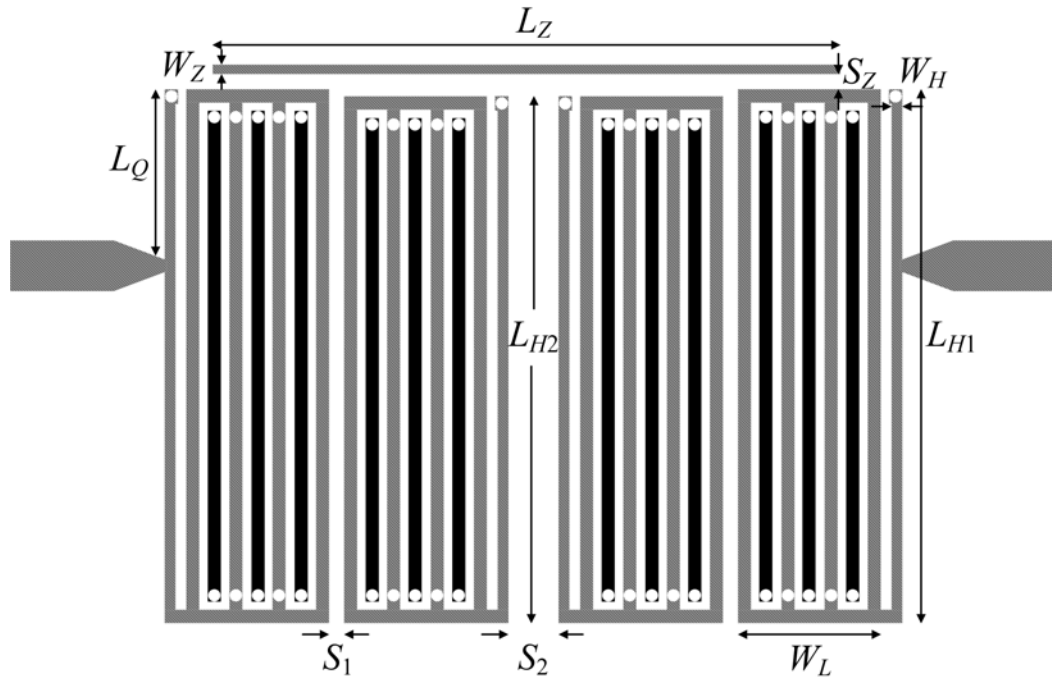
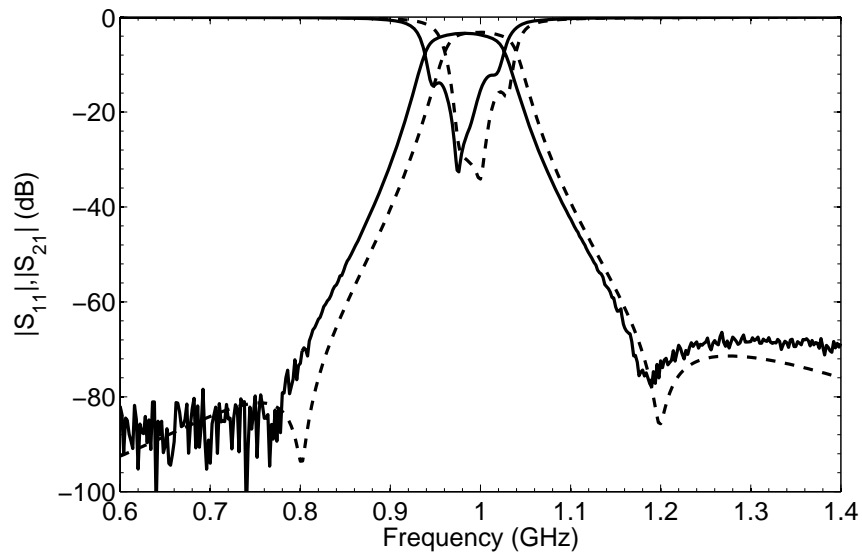
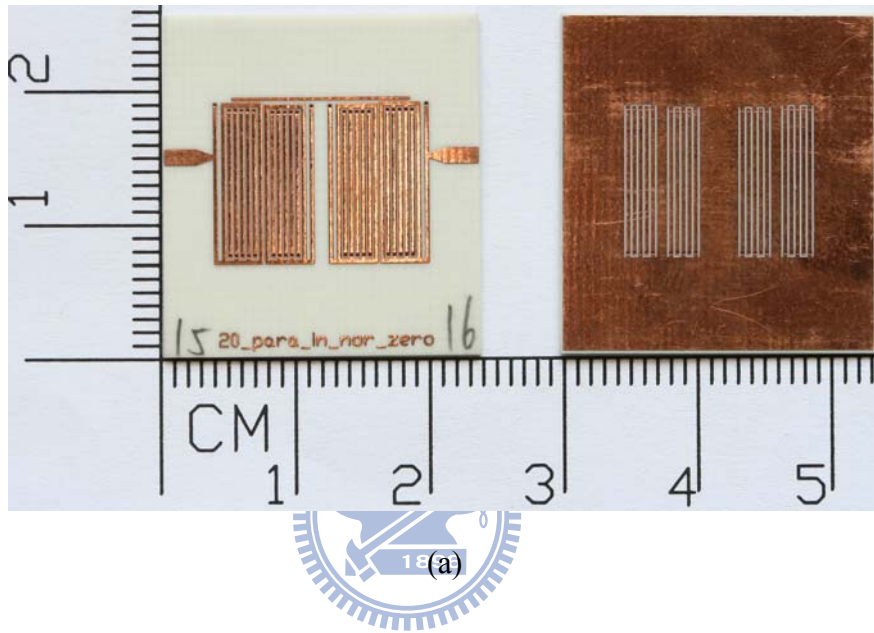


Fig. 3-21. Proposed layout of the four-pole cross-coupled filter.

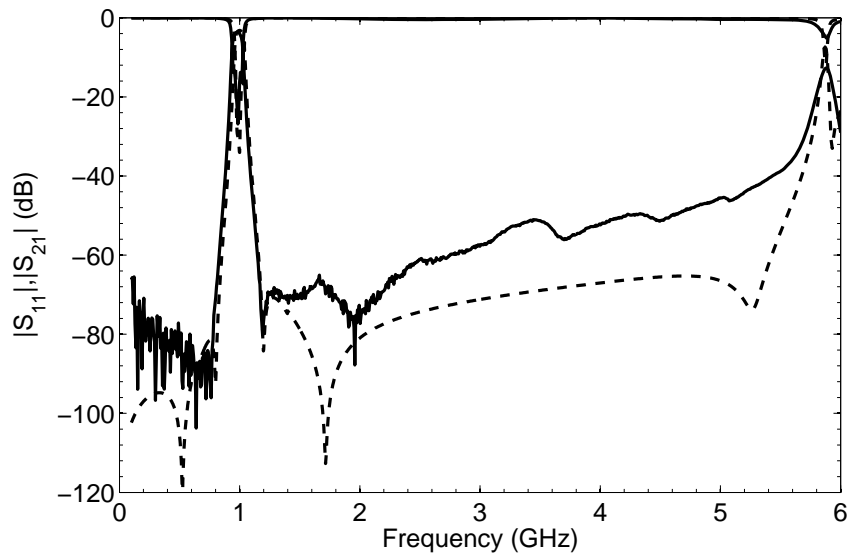
adjacent strips is  $d$ . Two four-pole cross-coupled bandpass filters with the same configuration were designed and fabricated on a Rogers RO4003 substrate ( $\epsilon_r = 3.58$ ) with different substrate thicknesses. The specifications and design parameters of two filters are listed in Table 3-7. The filter layout is depicted in Fig. 3-21, where the physical parameters corresponding to those of Table 3-8 are indicated. The via-hole is 0.3 mm in diameter. Each SIR is folded to make the electric or magnetic coupling possible and the size compact. A thin microstrip line provides the small cross coupling between resonators 1 and 4 to produce a pair of transmission zeros on both sides of the passband.

Table 3-8 Dimensions of the designed filters

(mm)	$L_{H1}$	$L_{H2}$	$W_H$	$W_{SE}$	$W_{SI}$	$W_G$	$d$	$W_L$	$L_Q$	$L_Z$	$W_Z$	$S_Z$	$S_1$	$S_2$
Filter I	11.85	11.7	0.3	0.3	0.3	0.3	0.15	3	3.825	13.05	0.225	0.15	0.15	1.05
Filter II	10.9	10.6	0.3	0.3	0.3	0.3	0.15	3	3.65	14.6	0.225	0.15	0.15	1.6

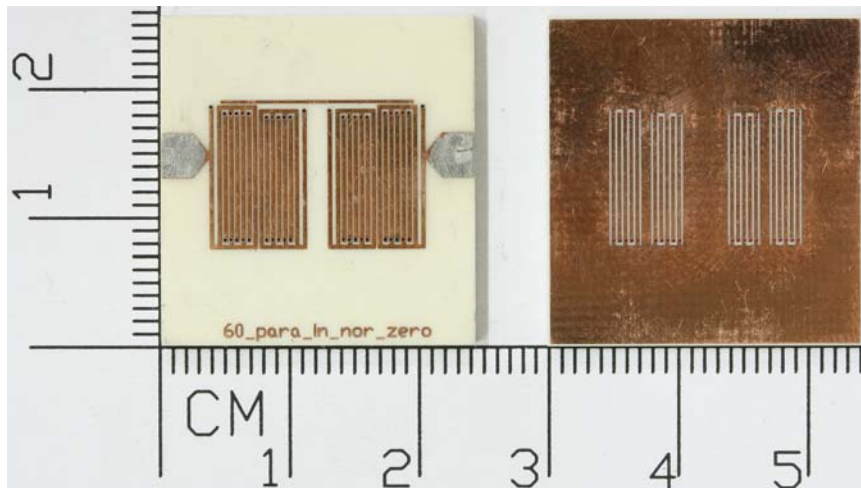


(b)

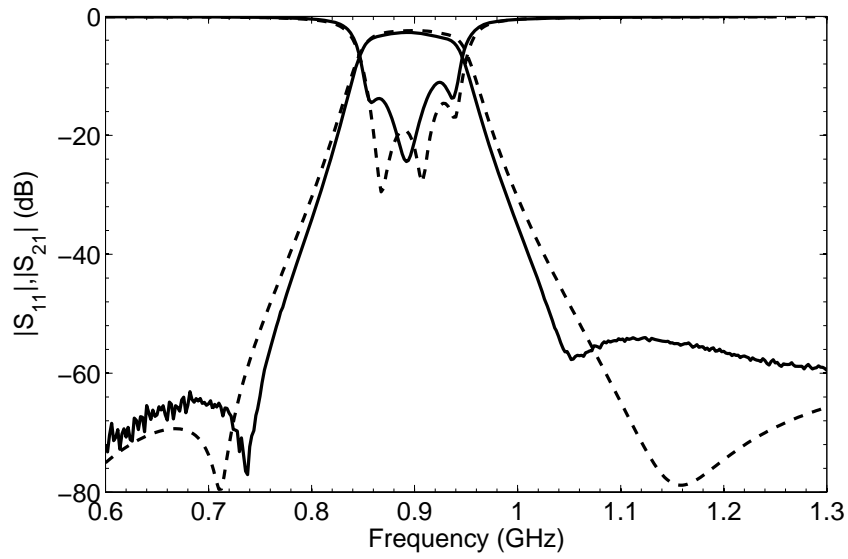


(c)

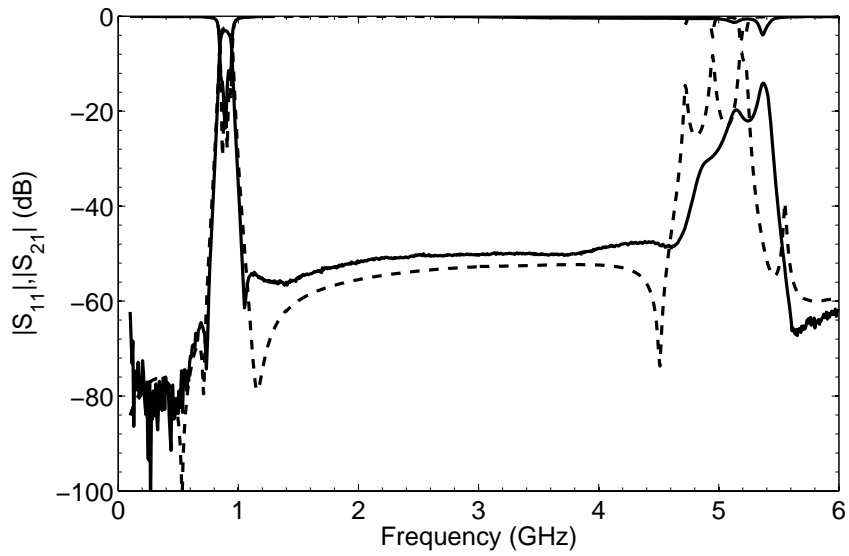
Fig. 3-22. (a) Top view (left side) and bottom view (right side) of the fabricated filter I. (b) Narrowband responses. (c) Wideband responses. (simulation: dashed line; measurement: solid line.)



(a)



(b)



(c)

Fig. 3-23. (a) Top view (left side) and bottom view (right side) of the fabricated filter II. (b) Narrowband responses. (c) Wideband responses. (simulation: dashed line; measurement: solid line.)

Figs. 3-22(a) and 3-23(a) show the top and bottom pictures of two filters. Their simulated and measured narrow- and wide-band responses are illustrated in Figs. 3-22(b)-(c) and 3-23(b)-(c), respectively. The measured results of both filters are summarized in Table 3-9. Table 3-9 also shows the percentage of size reduction for the proposed  $\lambda/4$  SIR filters compared with the conventional ones when they have the same impedance ratio  $R$  and high characteristic impedance  $Z_1$ . It can be seen that the proposed filters have a significant size reduction, especially for the thick substrate case (filter II).

Table 3-9 Fabricated filters and measured results

	Circuit size $\lambda_g$ : guided wave-length of 50- $\Omega$ line	Size reduction (%)	Center frequency (MHz)	Transmission zeros (MHz)	Insertion loss (dB)	Return loss better than (dB)	Rejection level better than 30 dB (GHz)
Filter I	$0.088\lambda_g \times 0.068\lambda_g$	26.1	982	778, 1190	3.3	12	1.067 - 5.7
Filter II	$0.082\lambda_g \times 0.057\lambda_g$	69.5	897	738, 1052	2.6	11	0.9878 - 4.926

### 3.3 Resonance of the Low-Impedance Section of the SIR

The proposed low-impedance microstrip line has another resonance to be considered. Taking the dimensions of the SIRs in filter I of Table 3-3 as an example, their resonant

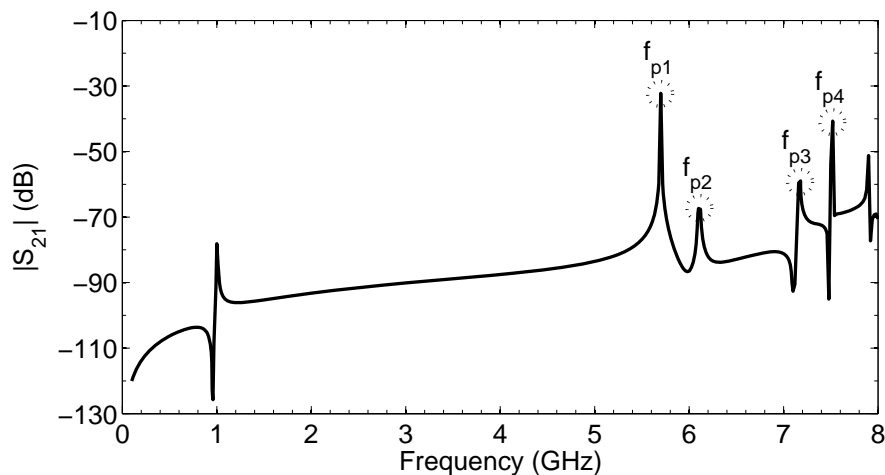
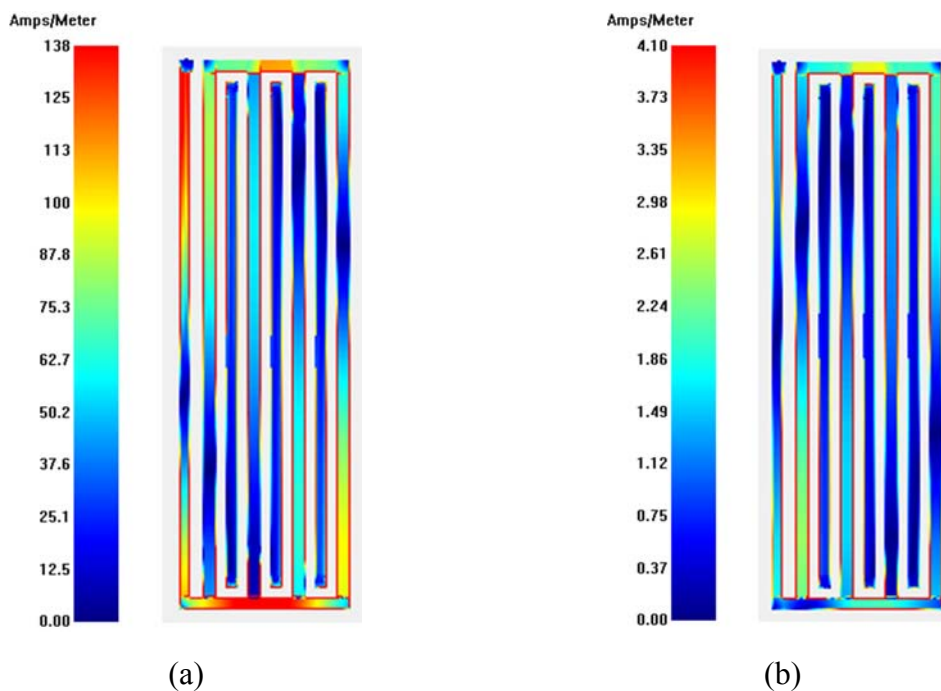


Fig. 3-24. Resonant response of the proposed SIR in Section 3.1.



response is presented in Fig. 3-24. The frequencies  $f_{p1}$  and  $f_{p2}$  correspond to the second resonance of the SIR, along with the resonances of the circumference (i.e., two outmost signal strips of the low-impedance microstrip line) which is one-wavelength long, and their current distributions are illustrated in Fig. 3-25(a) and (b). To eliminate the resonances of the circumference of the low-impedance section, we can add either a bond-wire or a thin signal strip on the ground plane to connect the middle of the two outmost signal strips for equal potential, as shown in Fig. 3-25(c) and (d). Furthermore, the resonances of the circumference are the most important items among the resonances labeled in Fig. 3-24 since they have a lower frequency and may occur before the first spurious frequency of the  $\lambda/4$  SIR (i.e., in the stopband of the filter).

In the proposed microstrip line, the ring resonance corresponding to one outmost signal strip and one inner signal strip is labeled  $f_{p3}$  in Fig. 3-24, and its current distribution is shown in Fig. 3-26(a). To eliminate this resonance, either two bond-wires or two signal strips on the ground plane are used to connect the middle of each pair of one outmost and one inner signal strip, as depicted in Fig. 3-26(b) and (c).



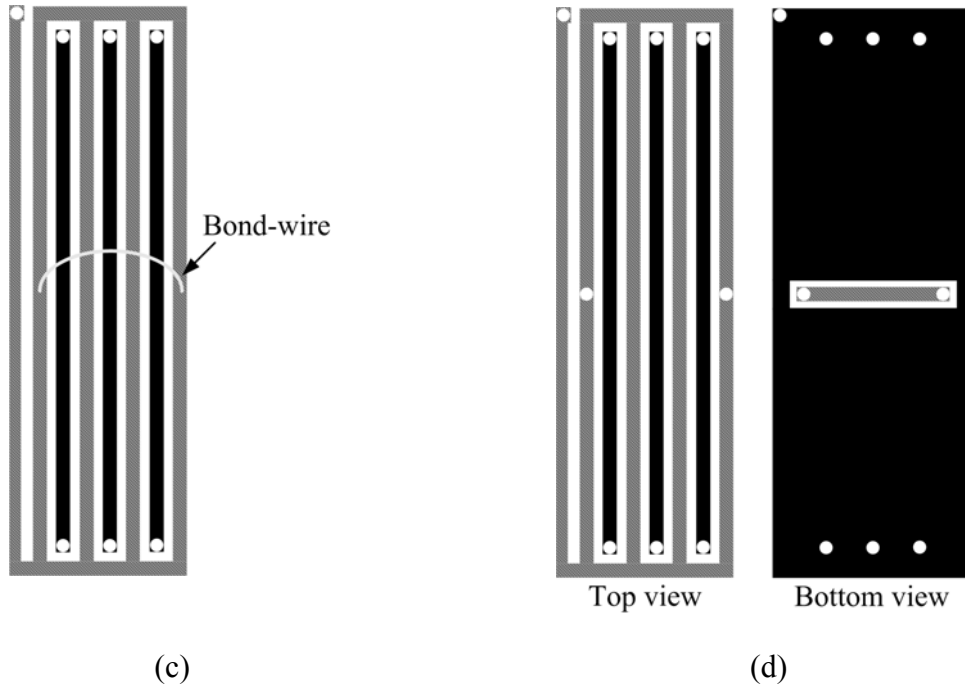


Fig. 3-25. Current distributions of the resonances (a)  $f_{p1}$  and (b)  $f_{p2}$  in Fig. 3-24. Elimination of the resonances of the circumference via (c) a bond-wire or (d) a signal strip on the bottom layer.

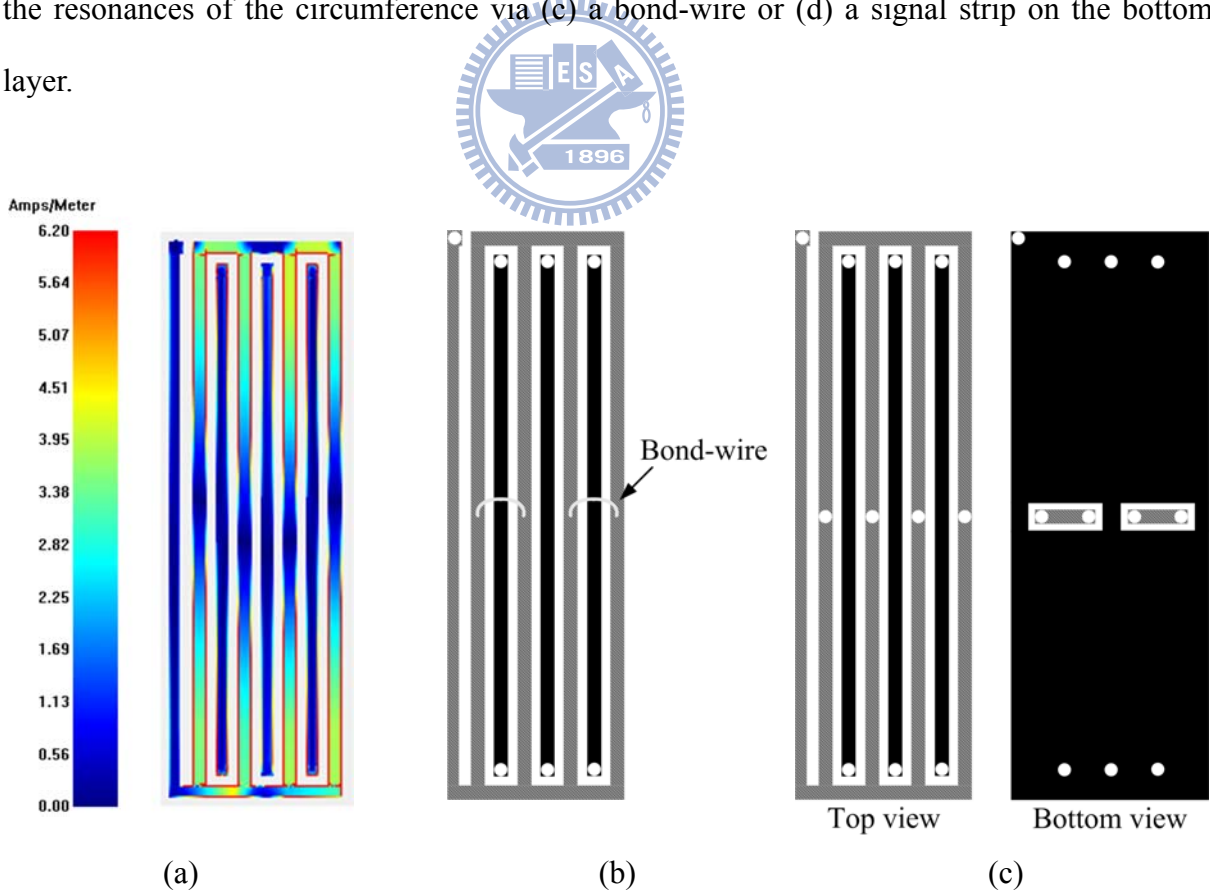


Fig. 3-26. (a) Current distribution of the resonance  $f_{p3}$  in Fig. 3-24. Elimination of the resonance  $f_{p3}$  via (b) two bond-wires or (c) two signal strips on the bottom layer.

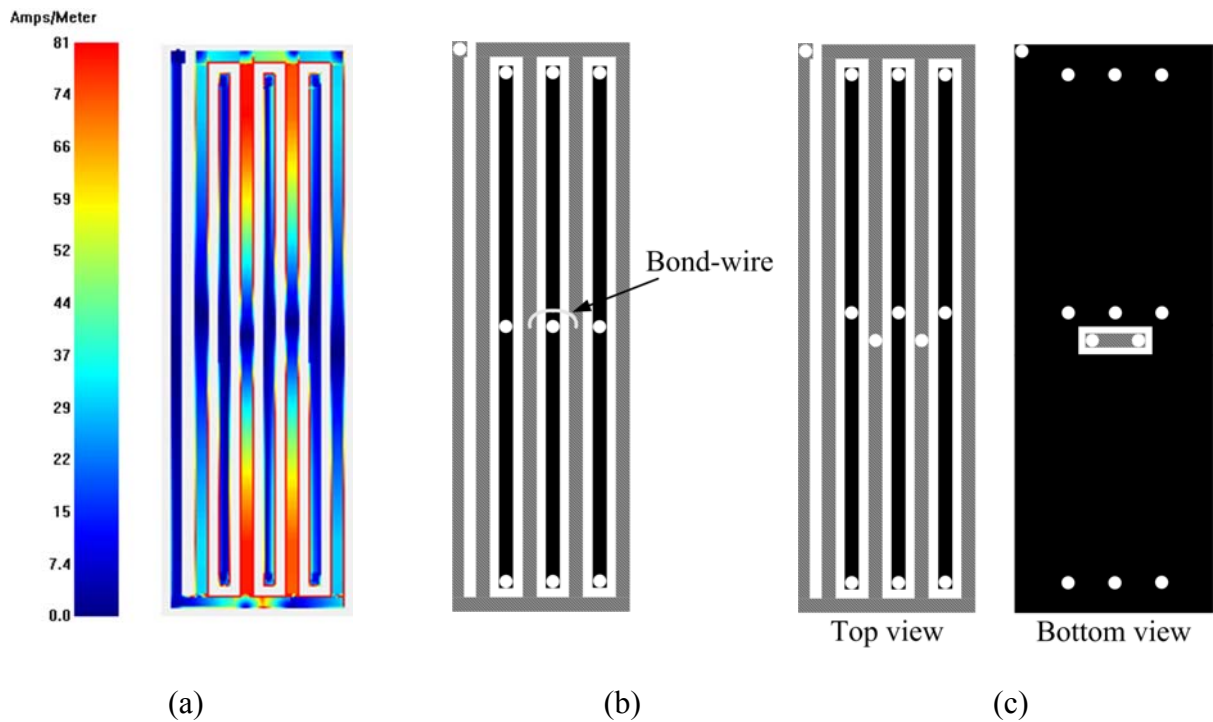


Fig. 3-27. (a) Current distribution of the resonance  $f_{p4}$  in Fig. 3-24. Elimination of the resonance  $f_{p4}$  via three via-holes and (b) a bond-wire or (c) a signal strip on the bottom layer.

The frequency  $f_{p4}$  in Fig. 3-24 is due to the ring resonance of the two inner signal strips and the resonance of each inserted ground strip. The current distributions of these resonances are shown in Fig. 3-27(a). To eliminate these resonances, we add one via-hole on the middle of each inserted ground strip and either a bond-wire or a signal strip on the ground plane to connect the middle of the two inner signal strips, as depicted in Fig. 3-27(b) and (c).

According to the steps discussed above, the final SIR structure with either a bond-wire or a signal strip on the ground plane is shown in Fig. 3-28(a) and (b). Its resonant response is presented in Fig. 3-28(c). The current distributions of the three resonant peaks  $f_1$ ,  $f_2$ , and  $f_3$  are shown in Fig. 3-29. Apparently, they are consistent with the first three resonances of the conventional  $\lambda/4$  SIR, indicating that the unwanted resonances of the proposed microstrip line are all eliminated. Comparing Fig. 3-24 with Fig. 3-28(c), the resonant frequencies of the circumference (i.e.,  $f_{p1}$  and  $f_{p2}$  in Fig. 3-24) are almost equal to the second resonant frequency

of the SIR in Fig. 3-28 (i.e.,  $f_2$  in Fig. 3-28(c)). Therefore, the SIR structure in Fig. 3-28(a) or (b) is not used in Section 3.1. The same approach can be applied to the SIR in Section 3.2 for better spurious response.

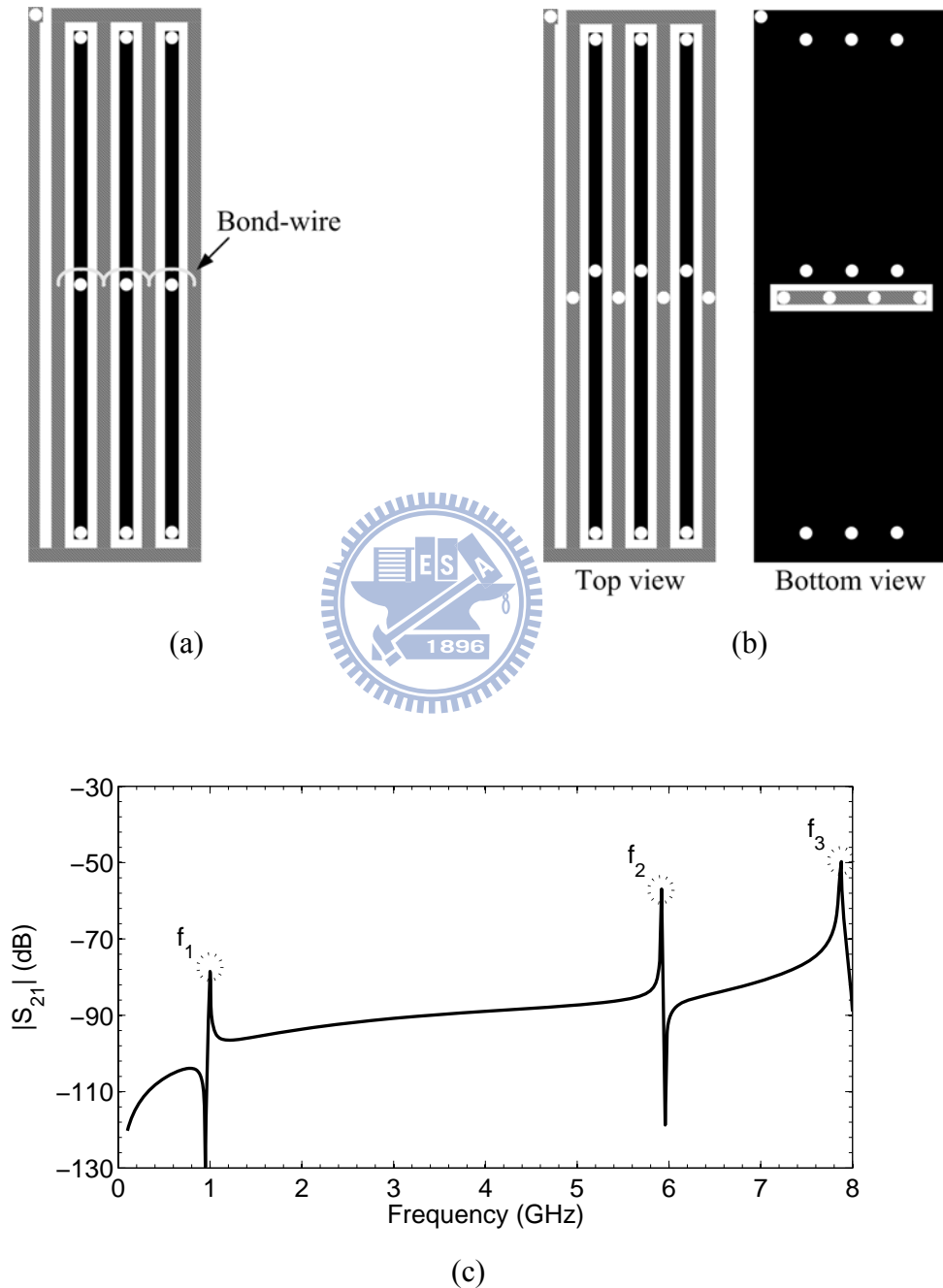


Fig. 3-28. SIR with three via-holes on each inserted ground strip and either (a) a bond-wire or (b) a signal strip on the ground plane to eliminate unwanted resonances. (c) Resonant response of the SIR in (a) or (b).

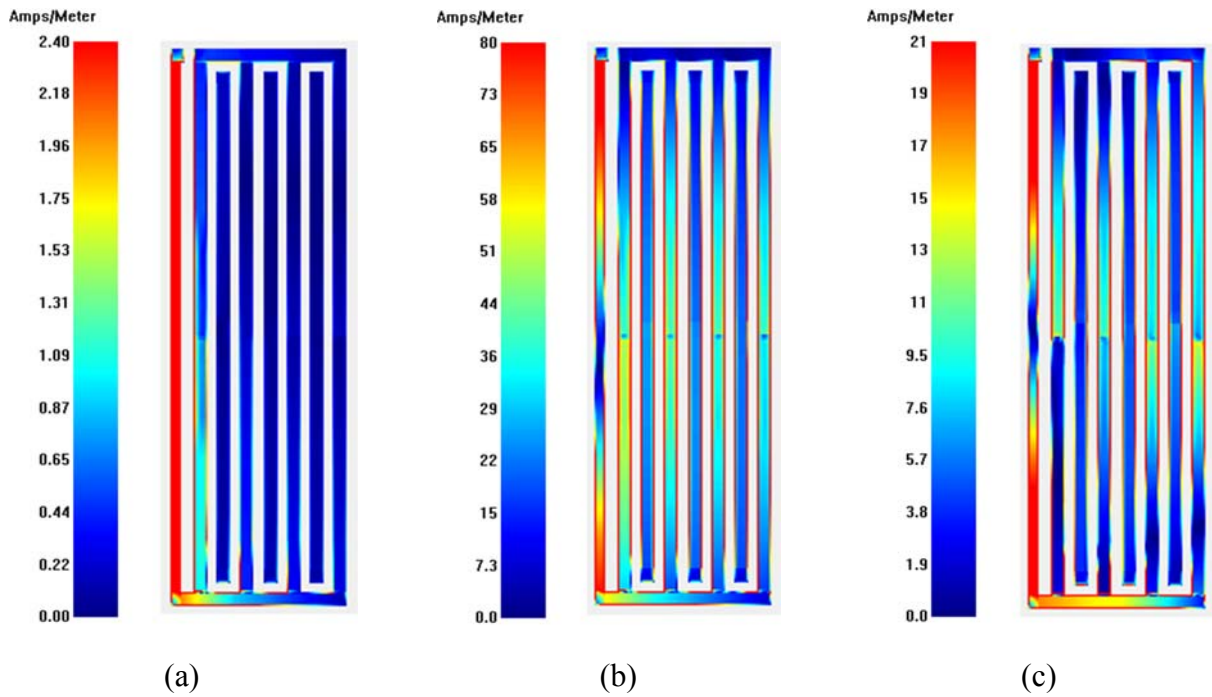
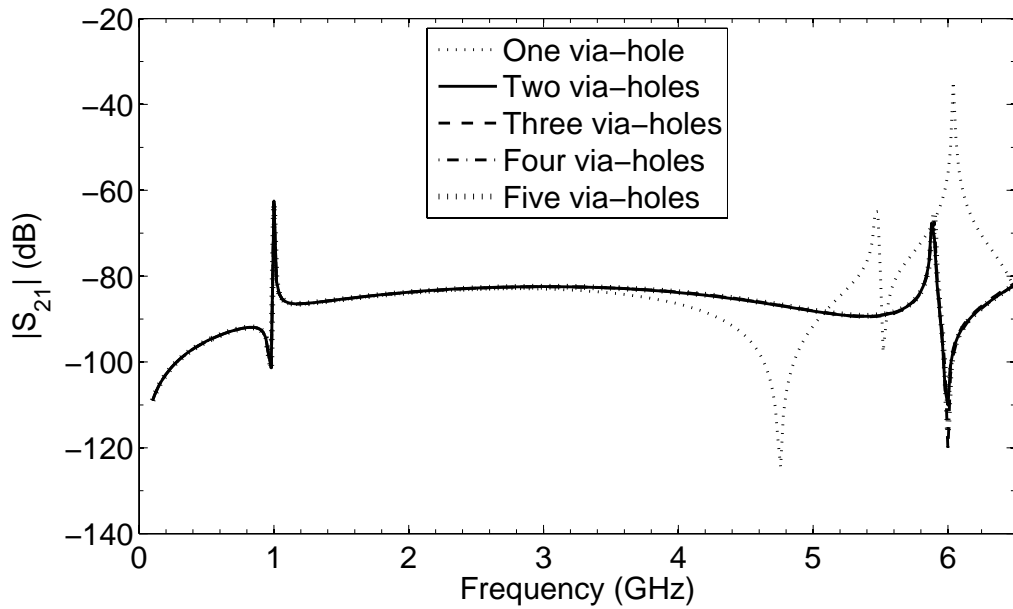
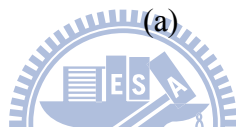
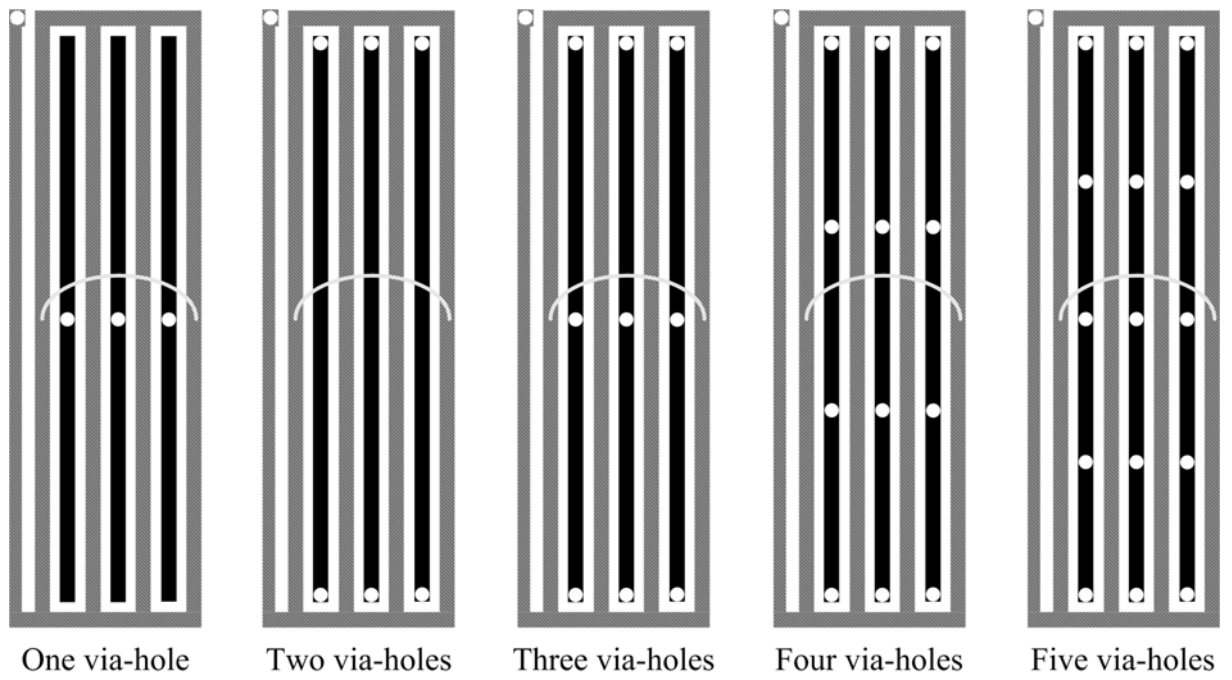


Fig. 3-29. Current distributions of the resonances (a)  $f_1$ , (b)  $f_2$ , and (c)  $f_3$  in Fig. 3-28.

### 3.4 Discussion of the Number of Via-Holes

Since there are many via-holes in the proposed low-impedance microstrip line, it is worthwhile to know how many via-holes are required in the inserted strips. To eliminate the effect of the resonance of the circumference mentioned above, the SIRs with the same dimensions as in Fig. 3-25(c) are adopted. Here, we compare the SIRs with different numbers of via-holes on the inserted ground strips (i.e., from one to five), as depicted in Fig. 3-30(a). The resonant responses of these SIRs are shown in Fig. 3-30(b). Apparently, the SIR with one via-hole on the middle of each ground strip has a lower second resonant frequency, while the lines corresponding to the SIRs with two to five via-holes on each ground strip are all overlapped, indicating that these four SIRs have the same second resonant frequency. The same result also holds for the SIR in section 3.2. Therefore, throughout this chapter, we use the SIR only with two via-holes on each end of the inserted strip.

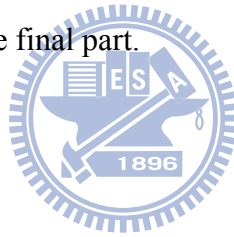


(b)

Fig. 3-30. (a) SIRs with one to five via-holes on each inserted ground strip. (b) Comparison of the resonant responses of the SIRs in (a).

### 3.5 Summary

A new microstrip structure appropriate for  $\lambda/4$  microstrip SIRs has been presented in this chapter. By inserting ground strips inside the low-impedance microstrip line, a new low-impedance transmission line, which makes the proposed SIR less sensitive to substrate thickness variations and etching tolerances, has been achieved. Moreover, the proposed microstrip SIR has shown an extra benefit of size reduction. To further reduce the resonator size, the signal strips are inserted in the microstrip ground plane to achieve an even lower characteristic impedance. A pair of transmission zeros are introduced to obtain higher selectivity by a cross-coupling microstrip line. Four four-pole cross-coupled filters with the proposed SIR structures have been designed and fabricated to demonstrate the feasibility. The elimination of extra resonances and the number of via-holes of the proposed microstrip line have been discussed in detail in the final part.



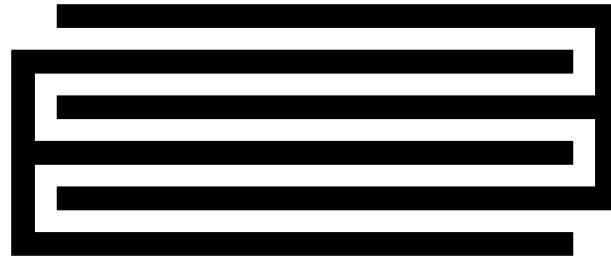
# ***Chapter 4 INTERDIGITAL COUPLING STRUCTURES FOR WIDEBAND STEPPED-IMPEDANCE RESONATOR FILTERS***

It is usually difficult to design microstrip edge-coupled wideband bandpass filters (BPFs) due to very strong coupling and small gaps between resonators. In addition, as mentioned in chapters 2 and 3, stepped-impedance resonators (SIRs) have advantages to reduce the circuit size and to improve the upper stopband performance compared to uniform-impedance resonators (UIRs). For the SIR structure, the lower the impedance ratio  $R$  is, the shorter the resonator length and the farther the first spurious resonant frequency will be. Hence, the  $\lambda/4$  microstrip SIR with a low impedance ratio  $R$  has a much weaker coupling between adjacent resonators than the  $\lambda/2$  and  $\lambda/4$  UIRs. This is especially obvious for the electric coupling in the low-impedance section of a SIR on a thin substrate. As a result, it is particularly difficult to obtain enough coupling for wideband SIR BPFs. In this chapter, we propose two types of coupled microstrip lines which can provide interdigital coupling between adjacent resonators. They are adopted in the low-impedance section of the  $\lambda/4$  SIR to significantly enhance the coupling between adjacent resonators. All filters were fabricated on a Rogers RO4003 substrate with a dielectric constant of 3.58, a loss tangent of 0.0021, and a thickness of 0.508 mm. All diameters of via-holes have the same size of 0.3 mm. The commercial full-wave electromagnetic (EM) simulation software Sonnet was used to perform the simulation. The measurements of all circuits were carried out using an Agilent 8720ES network analyzer.

## **4.1 Interdigital Coupled Microstrip Lines**

Fig. 4-1 shows two types of proposed coupled microstrip lines. These two structures have interdigital coupling elements to provide strong coupling between microstrip lines easily. As a result, they are very suitable for planar edge-coupled wideband BPFs. We replace the





(a)



(b)

Fig. 4-1. Two interdigital coupling structures for wideband filter design.

low-impedance section of the conventional  $\lambda/4$  SIR with these two interdigital structures.



## 4.2 Proposed SIR Configuration I

### 4.2.1 Structure of the Resonator

Fig. 4-2 shows the top and bottom layouts of the first proposed  $\lambda/4$  interdigital SIR. Specifically, the proposed  $\lambda/4$  SIR consists of several parallel-connected thin strips to form the low-impedance section ( $Z_L$ ) and a short-circuited thin strip to form the high-impedance section ( $Z_H$ ). Note that in Fig. 4-2(a), via-holes are applied on the open end of each strip in the low-impedance section where these via-holes are connected through a thin strip on the bottom layer, as shown in Fig. 4-2(b). This structure enables the resonator to maintain the low impedance ratio  $R$  and to have better spurious response. Due to the slots in the low-impedance section of the proposed SIR, the impedance ratio  $R$  is slightly larger than that of the conventional microstrip SIR without slots.

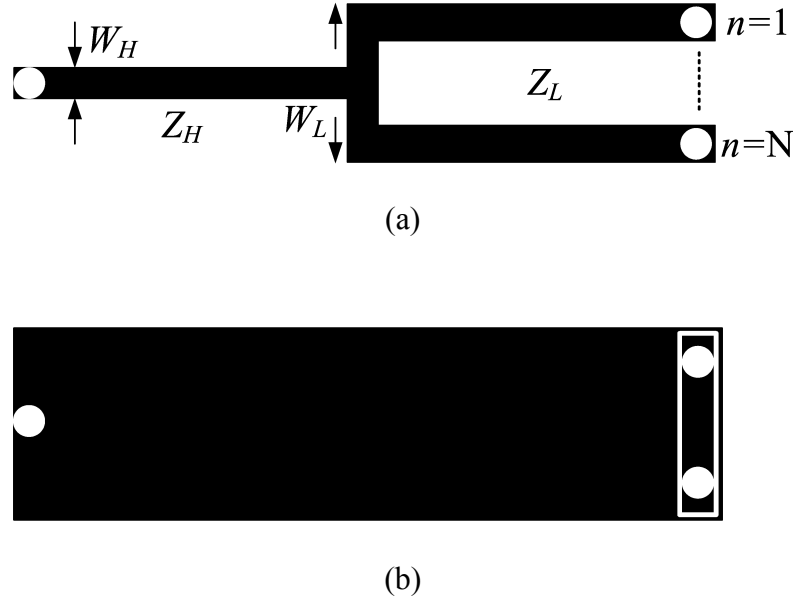
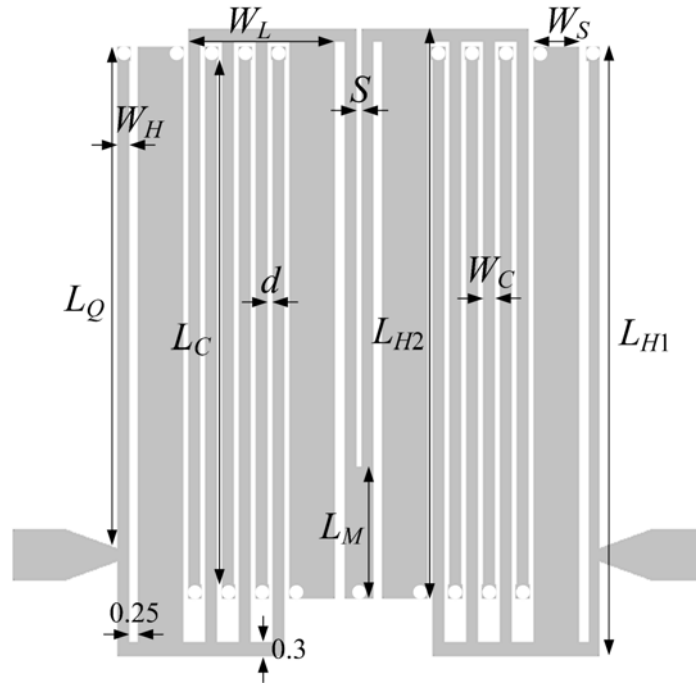


Fig. 4-2. Proposed  $\lambda/4$  SIR configuration I. (a) Top view. (b) Bottom view ( $N = 2$ ).

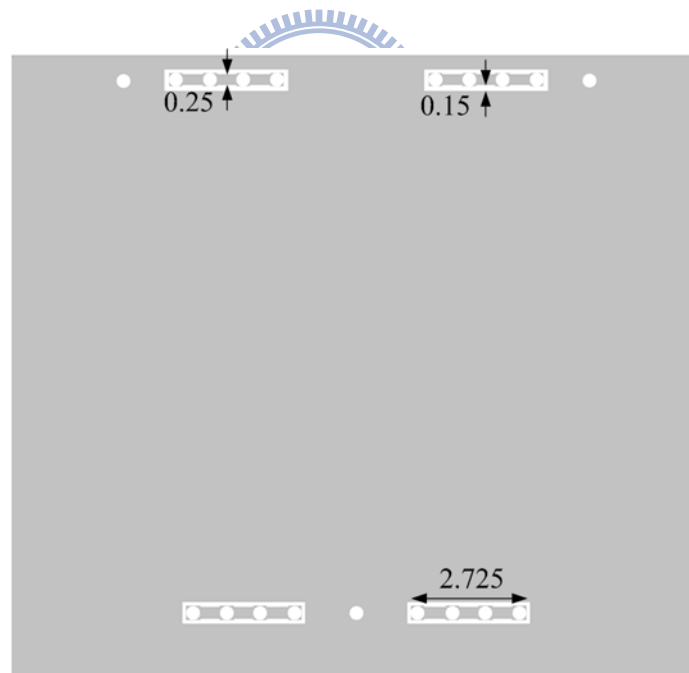
#### 4.2.2 Four-Pole Chebyshev Filter (Filter I)

The proposed four-pole filter I is a Chebyshev filter with a passband ripple of 0.05 dB, a center frequency ( $f_0$ ) of 1 GHz, and a fractional bandwidth of 48%. The first spurious frequency is set more than  $5f_0$ . According to the specifications, the filter is implemented using the design procedures based on the coupling coefficient  $k$  and the external quality factor  $Q_e$  [57]. Here,  $Q_e = 1.9975$ ,  $k_{12} = k_{34} = 0.4304$ , and  $k_{23} = 0.3324$ .

Fig. 4-3 depicts the top and bottom layouts of filter I. Here, we number these four resonators as 1 to 4 from left to right. Each SIR is folded in order to apply the electric or magnetic coupling and to reduce the filter size. As shown in Fig. 4-3(a), the parallel-connected thin strips in the low-impedance section of the SIR are interdigitally coupled to the adjacent SIR (i.e., Fig. 4-1(a)). This forms a strong capacitive coupling between resonators 1 and 2 as well as 3 and 4. The coupling strength is determined by the gap width  $d$ , the strip width  $W_C$ , the number  $N$  of parallel-connected strips, and the interleave length  $L_C$ . By adjusting these parameters, various degrees of coupling between adjacent SIRs can be obtained. The strong coupling between resonators 2 and 3 is realized by the common



(a)



(b)

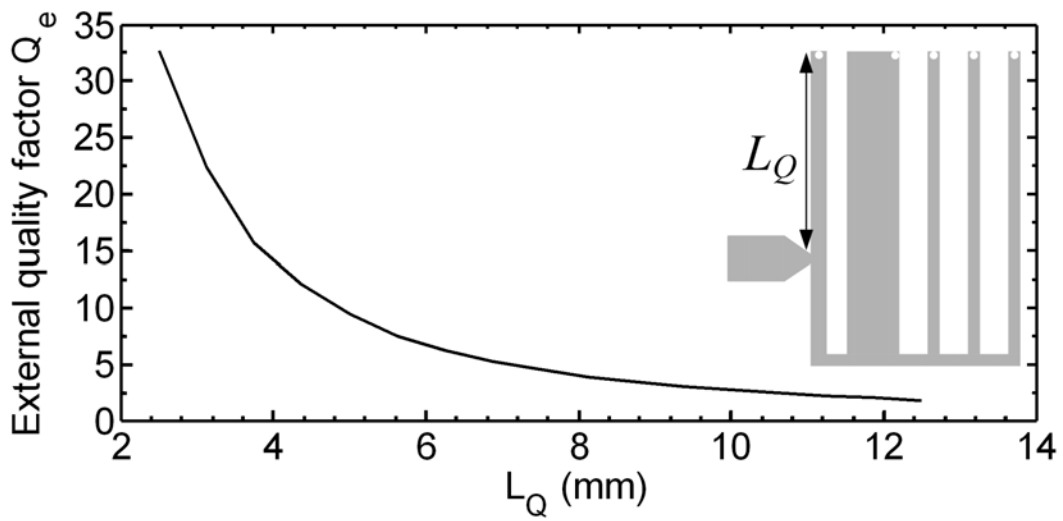
Fig. 4-3. Configuration of the proposed filter I. (a) Top-layer layout. (b) Bottom-layer layout.

Filter Dimensions (in millimeters):  $L_Q = 11.9$ ,  $L_{H1} = 14.45$ ,  $L_{H2} = 13.525$ ,  $L_C = 12.5$ ,

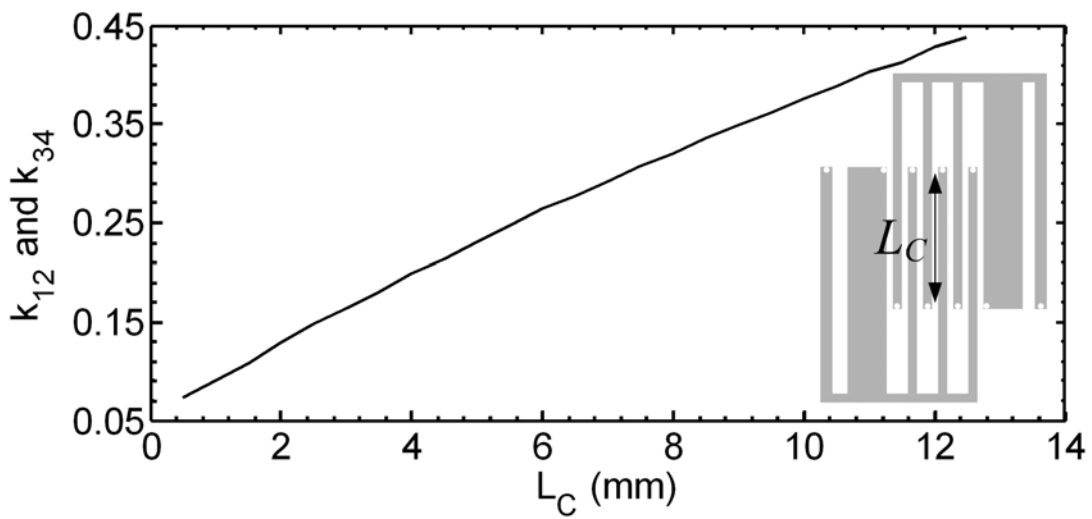
$L_M = 3.25$ ,  $W_H = W_C = 0.25$ ,  $W_L = 3.45$ ,  $W_S = 1.05$ , and  $S = d = 0.15$ .

transmission line connected to ground. The strength of the coupling is adjusted by the length  $L_M$  of the common short-circuited stub. In this filter configuration, the coupling  $k_{23}$  is magnetic, while  $k_{12}$  and  $k_{34}$  are mainly electric. The tap position  $L_Q$  of the input and output feed lines is chosen to match the  $Q_e$  value for the 50- $\Omega$  source/load impedance.

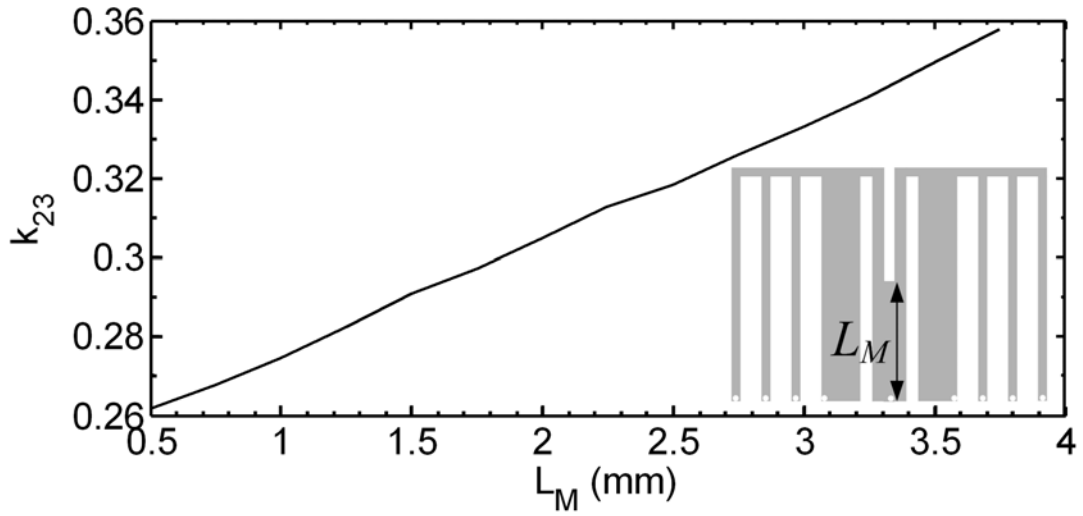
In the design process, we first fix the widths of  $W_H$ ,  $W_C$ ,  $S$ , and  $d$ , and then determine the number  $N$  roughly for a given filter specification.  $W_S$  (i.e.,  $n=1$ ) can be adjusted for the



(a)



(b)



(c)

Fig. 4-4. Design curves for the proposed filter I. (a) External quality factor  $Q_e$ . (b) Electric coupling  $k_{12}$  and  $k_{34}$ . (c) Magnetic coupling  $k_{23}$ .

prescribed normalized spurious resonant frequency. Here, the resonator dimensions are  $W_H = W_C = 0.25$  mm,  $S = d = 0.15$  mm,  $W_S = 1.05$  mm,  $W_L = 3.45$  mm, and  $N = 4$ . On the basis of the structures in Fig. 4-3, the design curves for the external quality factor and the coupling coefficients with  $L_Q$ ,  $L_C$ , and  $L_M$  as parameters are shown in Fig. 4-4, respectively.

Fig. 4-5 shows the photograph of the fabricated filter I with a size of  $11.45$  mm  $\times$   $14.9$  mm, which is  $0.0655\lambda_g \times 0.0853\lambda_g$ , where  $\lambda_g$  is the guided wavelength of the  $50\text{-}\Omega$  line on the substrate at the center frequency. Fig. 4-6 illustrates its simulated and measured responses. The measured results show that the filter has a center frequency of  $1.0105$  GHz. The measured 3-dB fractional bandwidth is 64.83% from  $0.7149$  to  $1.37$  GHz. Within the pass-band, the minimum insertion loss is  $0.63$  dB, and the return loss is better than  $18.9$  dB. The first spurious response is at  $5.152$  GHz ( $= 5.1f_0$ ), and the rejection level is better than  $20$  dB from  $1.76$  to  $4.357$  GHz.

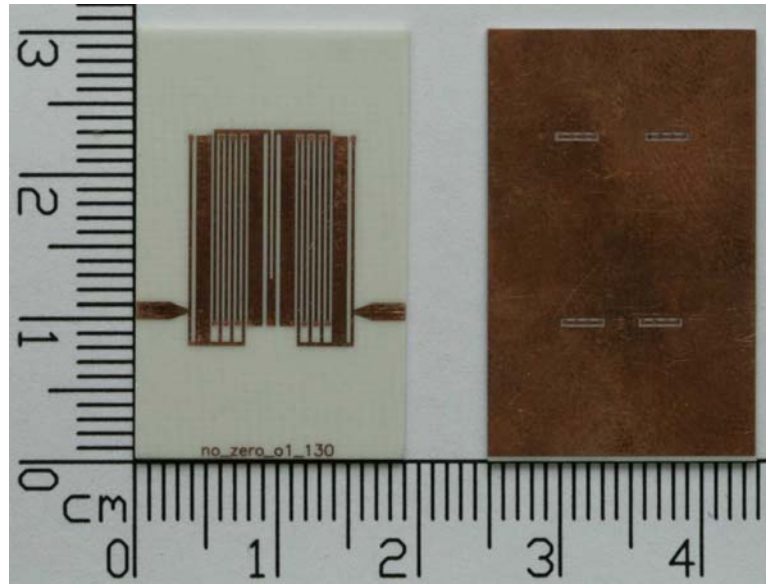
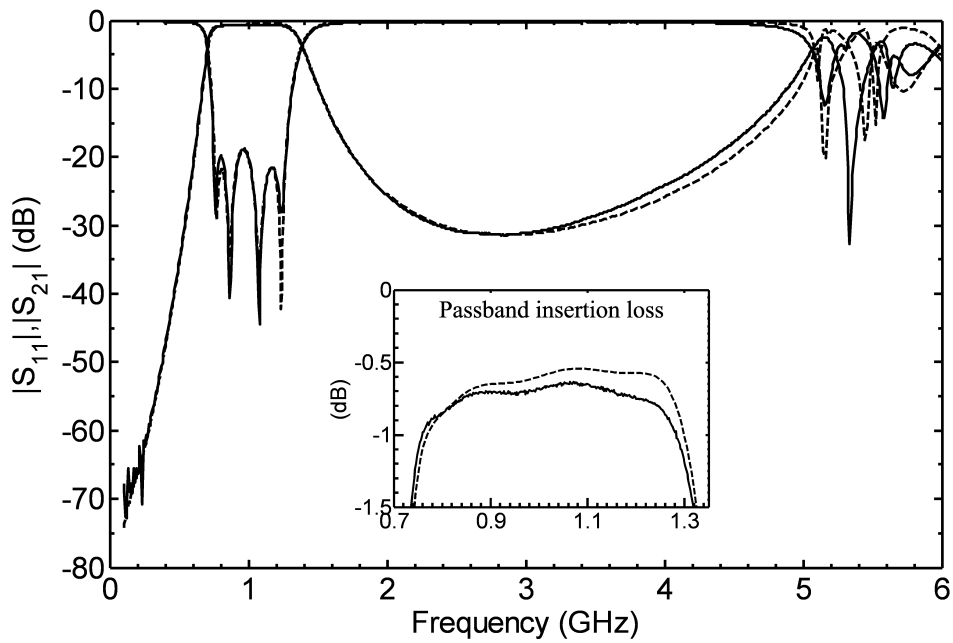
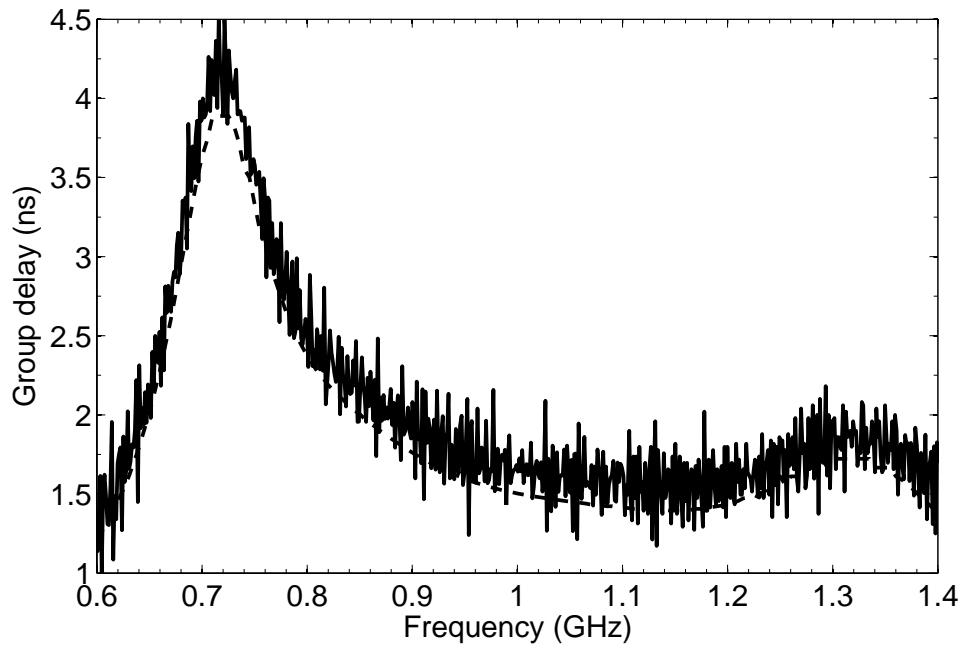


Fig. 4-5. Top view (left side) and bottom view (right side) of the fabricated filter I.

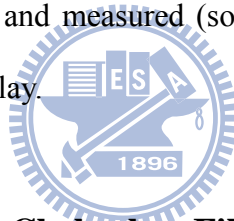


(a)



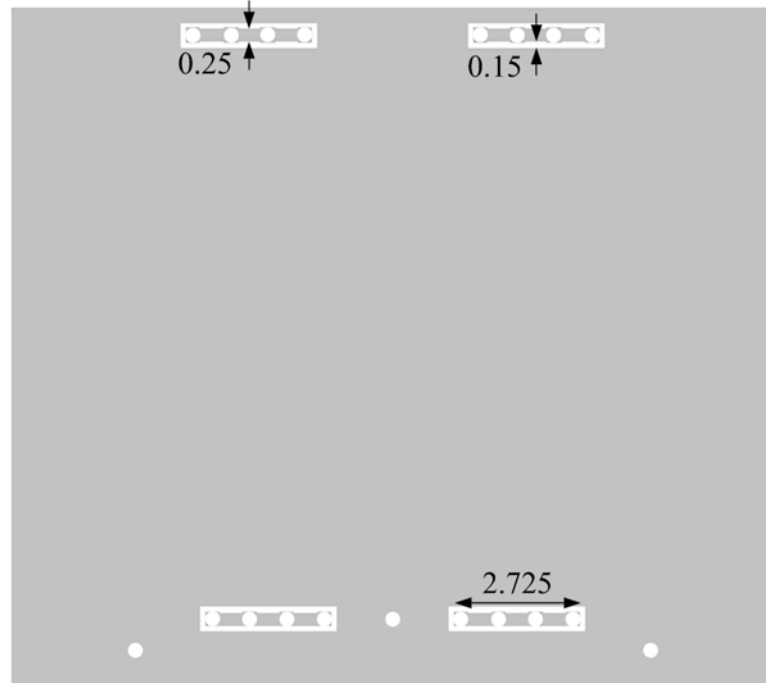
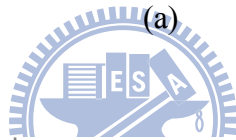
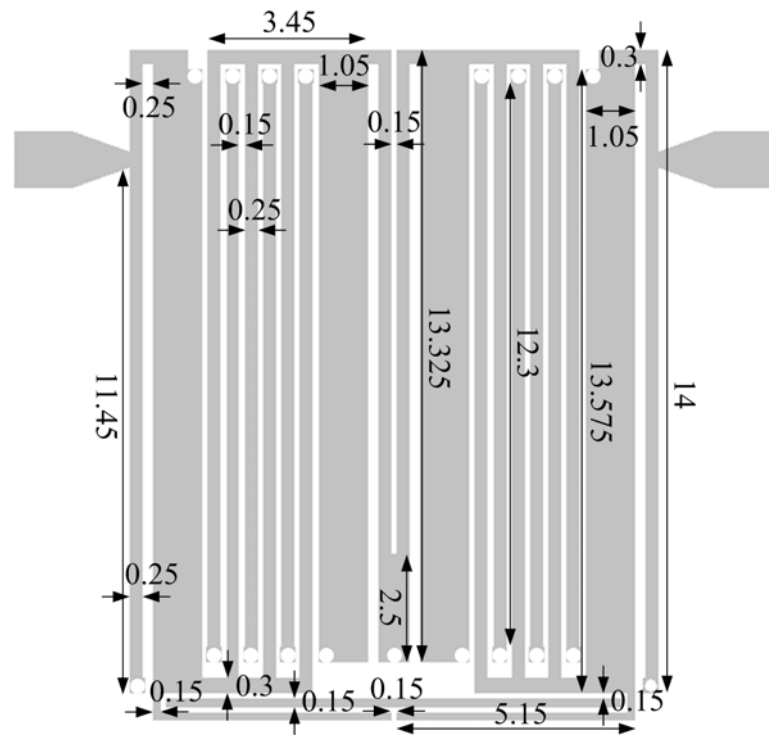
(b)

Fig. 4-6. Simulated (dashed line) and measured (solid line) results of filter I. (a) Scattering parameters. (b) Passband group delay.



### 4.2.3 Four-Pole Generalized Chebyshev Filter (Filter II)

Since planar wideband Chebyshev BPFs usually have the poor upper stopband rejection, a generalized Chebyshev wideband BPF is proposed using the four-pole cross-coupled configuration. Fig. 4-7 depicts the top and bottom layouts of filter II along with its physical dimensions. In this configuration, a thin microstrip line is applied at the bottom of the filter to provide the small cross coupling between resonators 1 and 4. This cross coupling produces a pair of transmission zeros on either side of the stopband. Because the cross coupling is weak, the initial design procedure is based on the four-pole Chebyshev response filter with a 0.05 dB equal-ripple passband characteristic and follows the design process discussed above. After that, put a thin cross-coupling microstrip line and then slightly fine tune the whole filter. The proposed filter II is designed at a center frequency ( $f_0$ ) of 1 GHz with a fractional bandwidth of 46%.



(b)

Fig. 4-7. Configuration of the proposed filter II. (a) Top-layer layout. (b) Bottom-layer layout.

units: mm.



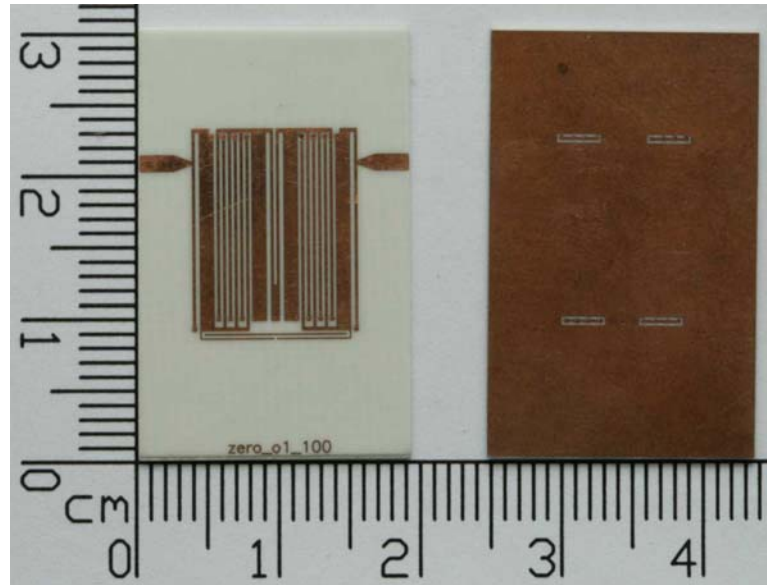
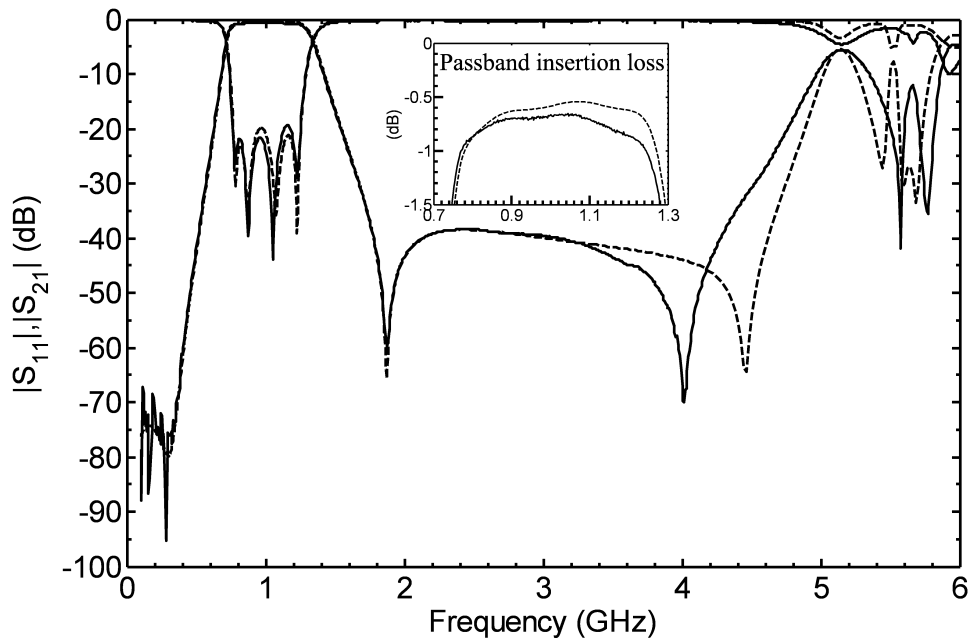


Fig. 4-8. Top view (left side) and bottom view (right side) of the fabricated filter II.

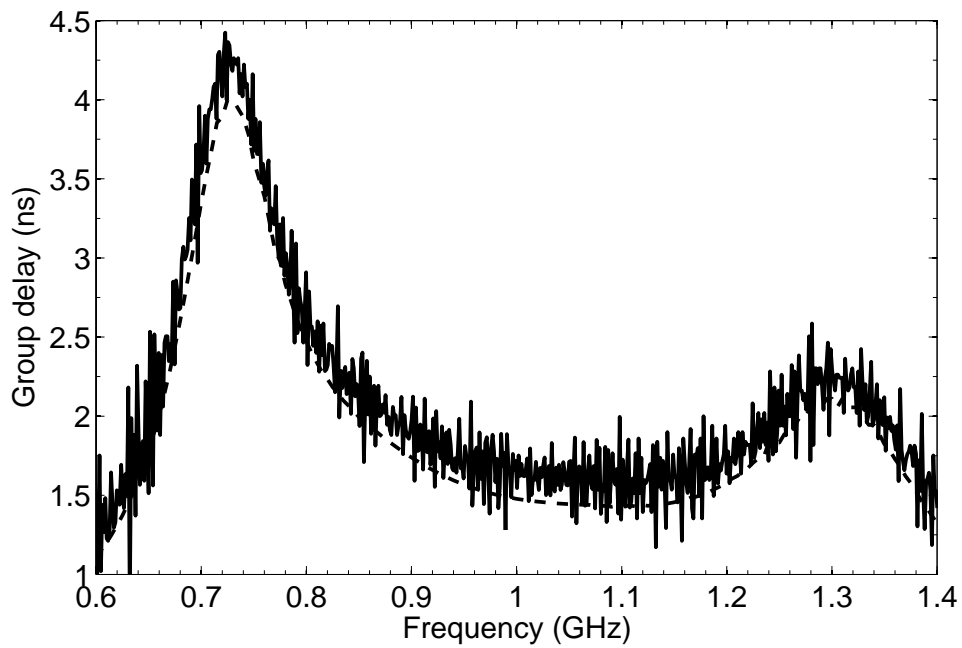
Fig. 4-8 shows the photograph of the fabricated filter II with a size of  $11.45 \text{ mm} \times 14.6 \text{ mm}$ , i.e.,  $0.0654\lambda_g \times 0.0833\lambda_g$ . The simulated and measured responses of filter II are presented in Fig. 4-9. The measured results show that the filter has a center frequency of 1.0076 GHz and two transmission zeros at 0.3185 and 1.877 GHz. The measured 3-dB fractional bandwidth is 59.19% from 0.7256 to 1.322 GHz. The filter has a minimum insertion loss of 0.64 dB and a return loss better than 19.5 dB within the passband. The first spurious frequency is at 5.159 GHz ( $= 5.12f_0$ ). The rejection level is better than 20 dB from 1.542 to 4.761 GHz. Apparently, the stopband depth is largely improved compared to that of filter I.

#### 4.2.4 Resonance of the Circumference of the Low-Impedance Section

As the circumference of the low-impedance section of the SIR is one-wavelength long, there will be a resonance. Taking the dimensions of the SIRs in filters I and II as an example, the current distribution of this resonance is illustrated in Fig. 4-10(a). In section 3.3, we indicates that this resonance is the most concerned factor since it may occur in the stopband of



(a)



(b)

Fig. 4-9. Simulated (dashed line) and measured (solid line) results of filter II. (a) Scattering parameters. (b) Passband group delay.

the filter. To eliminate this resonance, we connect the middle of the outmost signal strips via a thin strip on the bottom layer, as depicted in Fig. 4-10(b). In both filters I and II, the resonance of the circumference is beyond the second resonance of the SIR which is approximately  $5.2f_0$ , so that the structure in Fig. 4-10(b) is not used in this section.

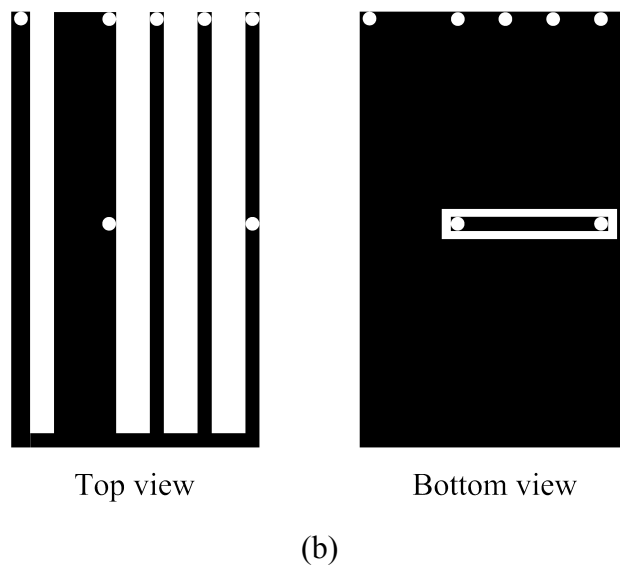
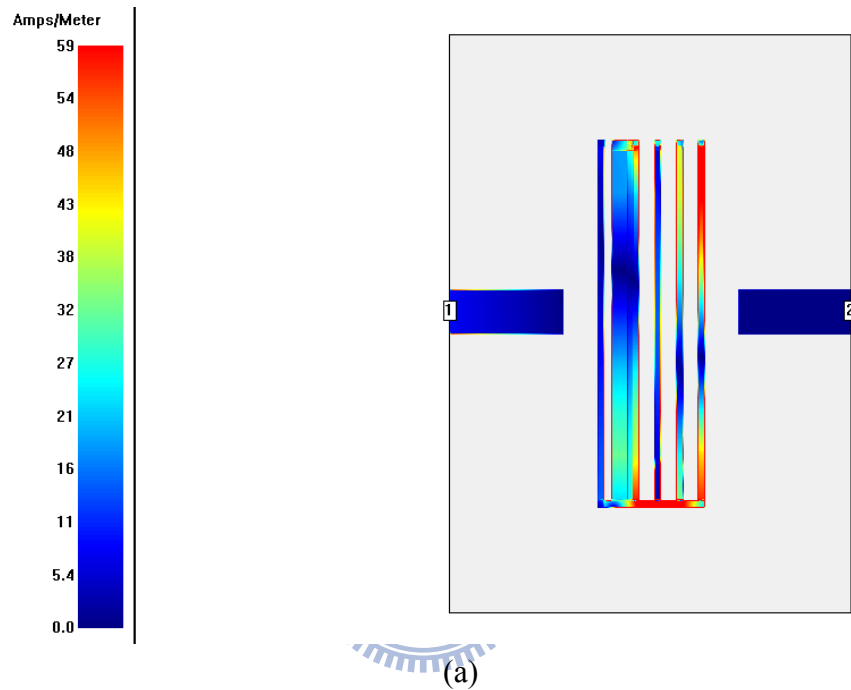


Fig. 4-10. (a) Current distribution of the resonance of the circumference. (b) Elimination of the resonance in (a).

## 4.3 Proposed SIR Configuration II

### 4.3.1 Structure of the Resonator

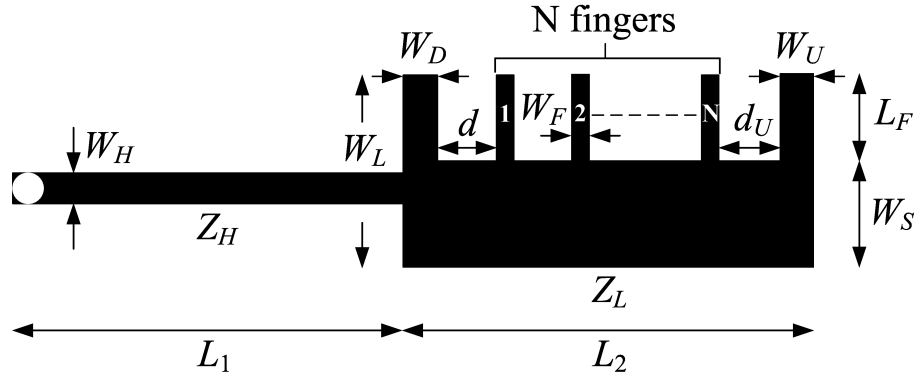


Fig. 4-11. Proposed  $\lambda/4$  SIR configuration II.

Fig. 4-11 depicts the layout of the second proposed  $\lambda/4$  SIR. It consists of a section of a short-circuited high-impedance line ( $Z_H$ ) and a section of a low-impedance line ( $Z_L$ ) with corresponding physical lengths  $L_1$  and  $L_2$ , respectively. Since the electric coupling in the low-impedance section of the conventional  $\lambda/4$  microstrip SIR is the main challenging issue for large coupling strength, the addition of thin strips on one side of the low-impedance section forms the interdigital coupling elements (i.e., Fig. 4-1(b)). Therefore, the coupling strength between two low-impedance sections can be easily adjusted by changing the number  $N$ , the width  $W_F$ , and the length  $L_F$  of fingers. Furthermore, the impedance ratio  $R$  of the SIR can be kept low so that the resonator would maintain the small size.

To observe the spurious property of the proposed resonator, we fix the widths  $W_H = 0.225$  mm,  $W_D = W_U = 0.325$  mm, the gap spacing  $d_U = 0.575$  mm, and the lengths  $L_1 = L_2 = 12.425$  mm. Then we perform the full-wave EM simulation for the proposed structure. Fig. 4-12 shows the normalized first spurious resonant frequency versus finger number  $N$  and finger length  $L_F$  on the substrate with a dielectric constant of 3.58 and a

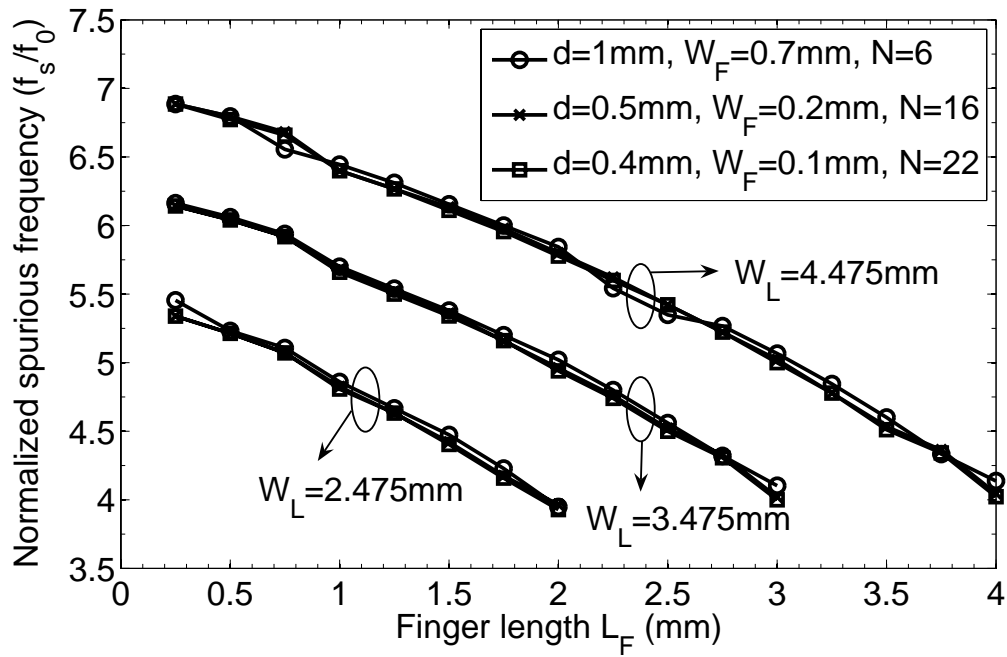


Fig. 4-12. Normalized first spurious resonant frequency versus finger number  $N$ , finger length  $L_F$ , and width  $W_L$ .

thickness of 0.508 mm. As shown in the figure, the resonator is set with three different widths  $W_L$  and three different finger dimensions for the cases  $N = 6, 16,$  and  $22$ . It is clearly observed that the normalized first spurious resonant frequency is much closely related to the width  $W_L$  and the finger length  $L_F$ , as compared to the finger number  $N$ .

### 4.3.2 Four-Pole Bandpass Filter Design

To demonstrate the proposed structure, two four-pole wideband BPFs were designed and fabricated. The filter is implemented using the design procedures based on the external quality factor  $Q_e$  and the coupling coefficient  $k$  [57].

#### A. Filter I

The proposed four-pole filter I is a Chebyshev filter with a passband ripple of 0.1 dB, a center frequency ( $f_0$ ) of 1.04 GHz, and a fractional bandwidth of 38%. According to the

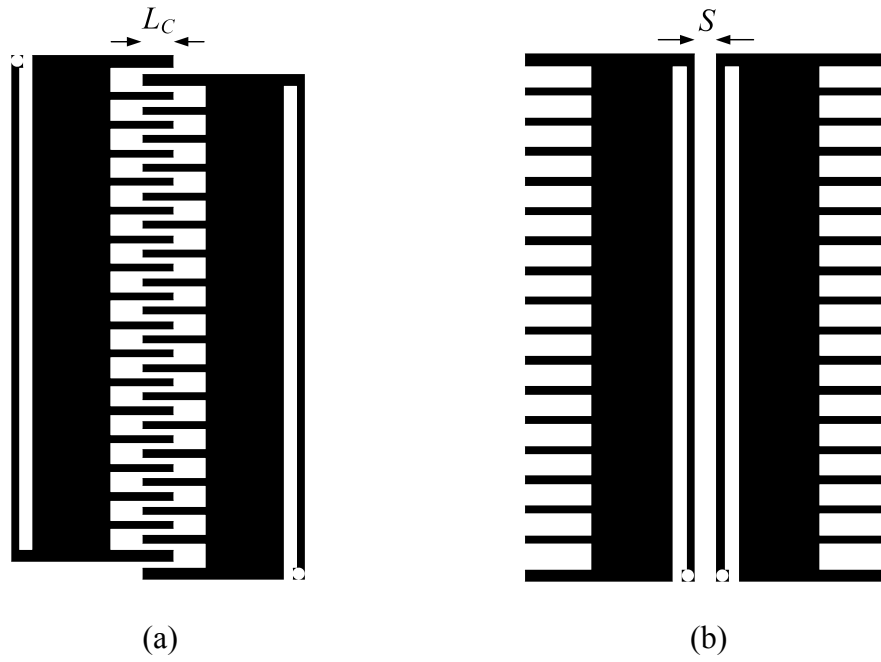


Fig. 4-13. Coupling structures for: (a) electric coupling and (b) magnetic coupling.

specifications,  $Q_e = 2.9179$ ,  $k_{12} = k_{34} = 0.3158$ , and  $k_{23} = 0.2499$ . In the design process, we first fix the width  $W_H$ , and then determine the width  $W_F$ , the length  $L_F$ , the spacing  $d$  between fingers, and the finger number  $N$  roughly for a given filter specification.  $W_S$  can be adjusted for the prescribed upper stopband width. Fig. 4-13 shows the two basic coupling structures for filter I. As shown in the figure, each SIR is folded to make the electric or magnetic coupling possible and the size compact. There are two kinds of couplings involved in the filter. Fig. 4-13(a) is for the electric coupling, whereas Fig. 4-13(b) is for the magnetic coupling. Fig. 4-14 exhibits the physical layout and dimensions of the proposed filter I, where we number these four resonators as 1-4 from left to right. The coupling  $k_{23}$  is magnetic, whereas  $k_{12}$  and  $k_{34}$  are mainly electric. The tap position  $L_Q$  is chosen to match the  $Q_e$  value for the 50- $\Omega$  source/load impedance. Here, the resonator dimensions are set as follows:  $W_H = 0.225$  mm,  $W_S = 1.925$  mm,  $W_L = 3.475$  mm,  $d_U = 0.575$  mm,  $L_F = 1.55$  mm, and  $N = 16$ . A half number of fingers have the width  $W_F = 0.2$  mm and the corresponding gap spacing  $d = 0.5$  mm. The other half number of fingers have dimensions of  $W_F = 0.225$  mm and  $d = 0.475$

mm. Fig. 4-15 shows the design curves for the coupling coefficients with the interleave length  $L_C$  and the spacing  $S$  as parameters, respectively.

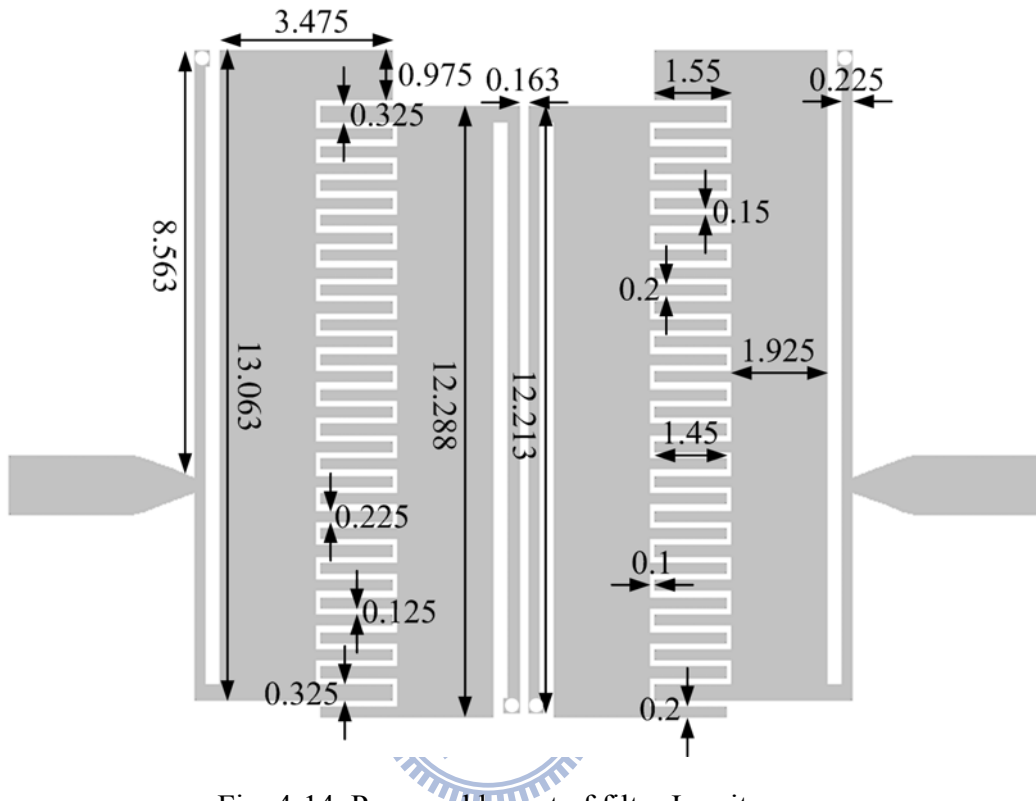
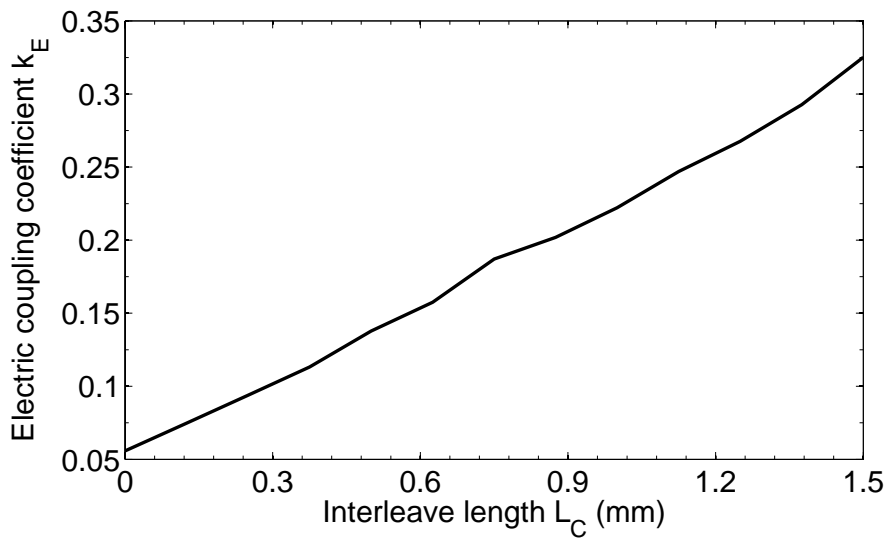
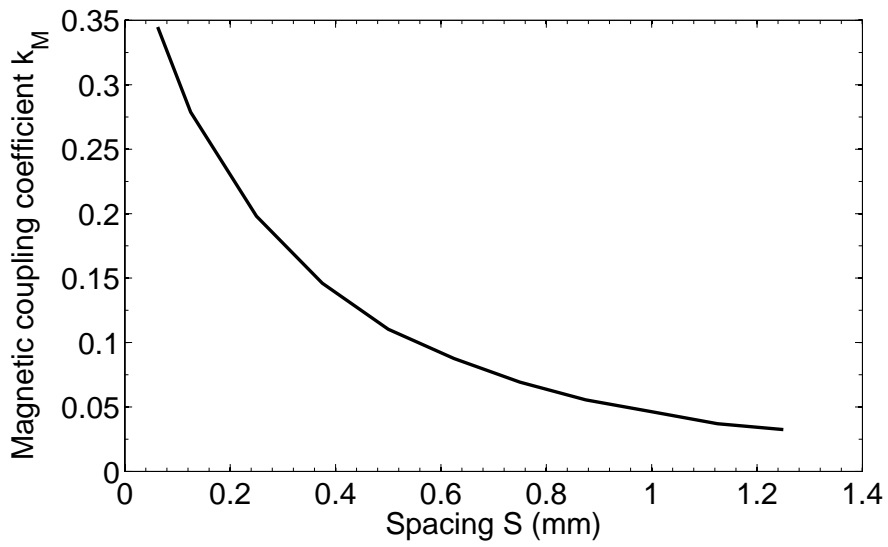


Fig. 4-14. Proposed layout of filter I. units: mm.



(a)



(b)

Fig. 4-15. Coupling coefficients of the coupling structures for: (a) electric coupling and (b) magnetic coupling.

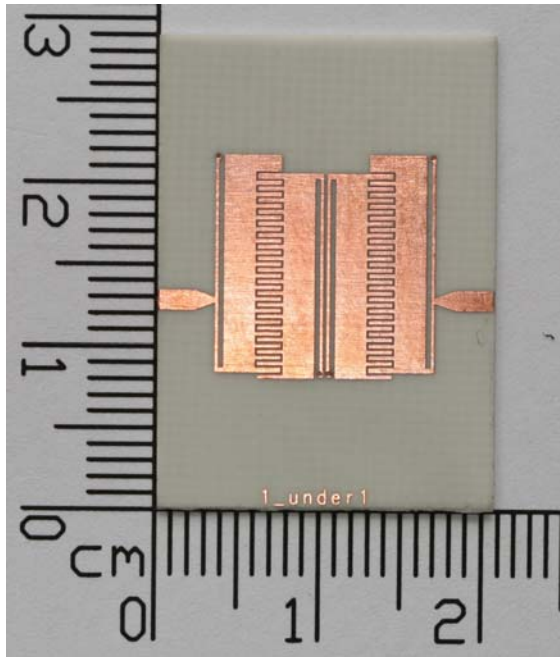
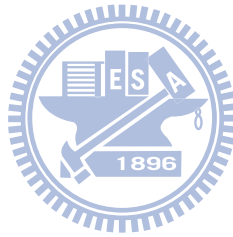
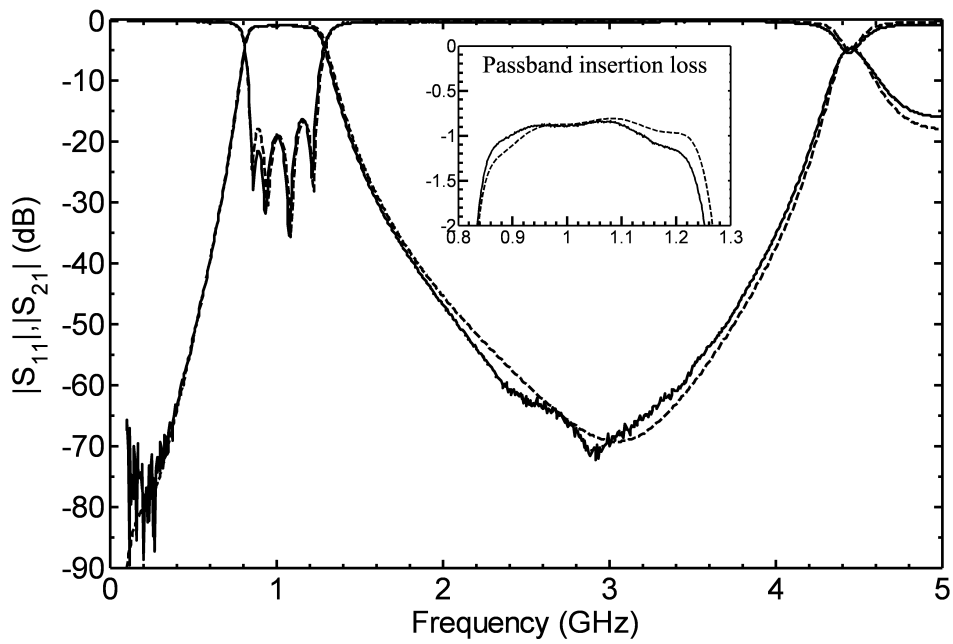
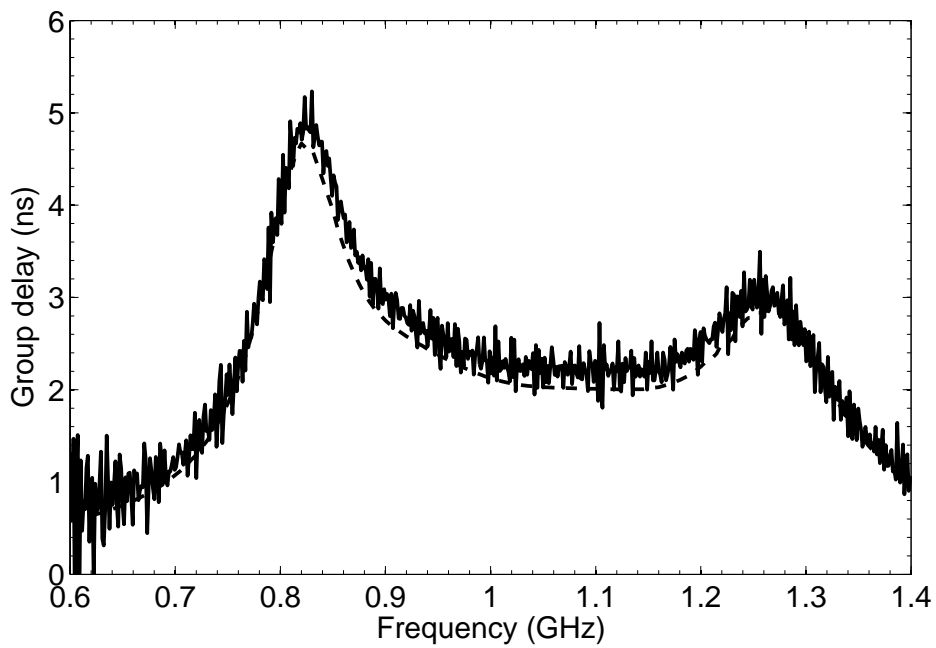


Fig. 4-16. Photograph of the fabricated filter I.





(a)



(b)

Fig. 4-17. Simulated (dashed line) and measured (solid line) results of filter I. (a) Scattering parameters. (b) Passband group delay.

Fig. 4-16 shows the photograph of the fabricated filter I. The size of the filter is 13.26 mm  $\times$  13.39 mm, which is  $0.077\lambda_g \times 0.078\lambda_g$ , where  $\lambda_g$  is the guided wavelength of the 50- $\Omega$  line on the substrate at the center frequency. Fig. 4-17 illustrates the simulated and measured responses. The measured results show that the filter has a center frequency of 1.042 GHz. The measured 3-dB fractional bandwidth is 43.05% from 0.8234 to 1.272 GHz. Within the passband, the minimum insertion loss is 0.83 dB, and the return loss is better than 16.2 dB. The maximum passband group delay variation is 2 ns. The first spurious response is at 4.455 GHz ( $= 4.28f_0$ ), and the rejection level is better than 20 dB from 1.455 to 4.223 GHz.

### B. Filter II

On the basis of the design process discussed above, we design another filter with a wider bandwidth to show the feasibility of the proposed structure. Filter II, which resembles the configuration of filter I, is a Chebyshev filter with a passband ripple of 0.1 dB, a center

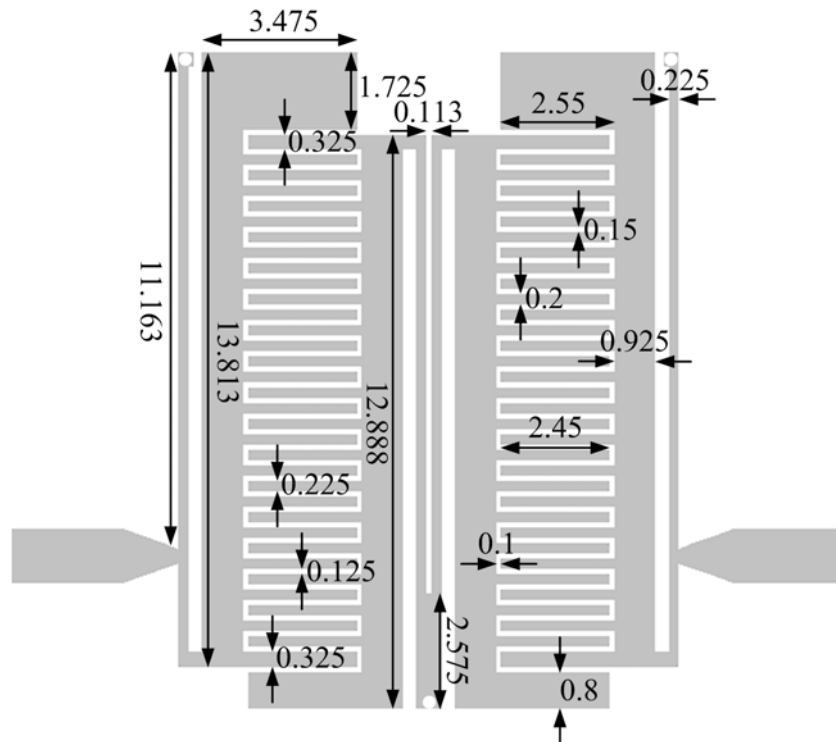


Fig. 4-18. Proposed layout of filter II. units: mm.

frequency ( $f_0$ ) of 1.04 GHz, and a fractional bandwidth of 55%. Fig. 4-18 shows its physical layout and dimensions. Again, the finger number is set as  $N = 16$ . The resonator dimensions  $W_H$ ,  $W_L$ ,  $W_F$ ,  $d$ , and  $d_U$  are the same as those of filter I. Due to the wider bandwidth, we choose  $L_F = 2.55$  mm for the electric coupling. The strong magnetic coupling between resonators 2 and 3 is achieved by the common transmission line connected to ground, as shown in Fig. 4-18.

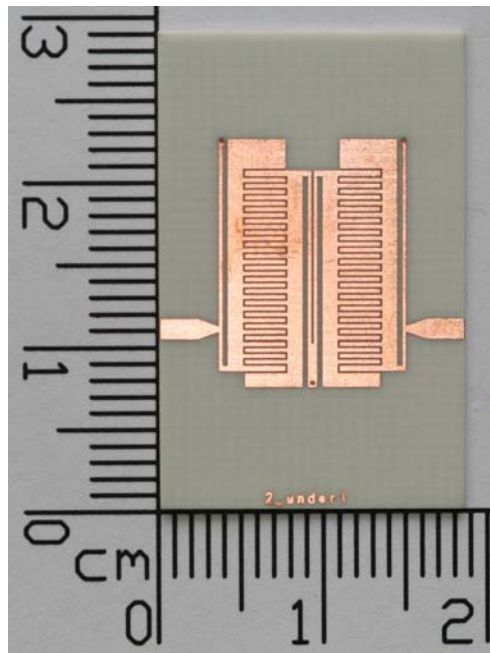


Fig. 4-19. Photograph of the fabricated filter II.

Fig. 4-19 shows the photograph of the fabricated filter II with a size of 11.21 mm  $\times$  14.74 mm, i.e.,  $0.065\lambda_g \times 0.086\lambda_g$ . The simulated and measured responses of filter II are presented in Fig. 4-20. The measured results show that the filter has a center frequency of 1.043 GHz. The measured 3-dB fractional bandwidth is 64.57% from 0.7215 to 1.395 GHz. The filter has a minimum insertion loss of 0.57 dB and a return loss better than 16.4 dB within the passband. The maximum passband group delay variation is 1.5 ns. The first spurious frequency is at 3.33 GHz ( $= 3.19f_0$ ). The rejection level is better than 20 dB from 1.654 to

2.885 GHz. Note that the first spurious resonant frequency is smaller than that of filter I. This is consistent with the spurious property according to Fig. 4-12.

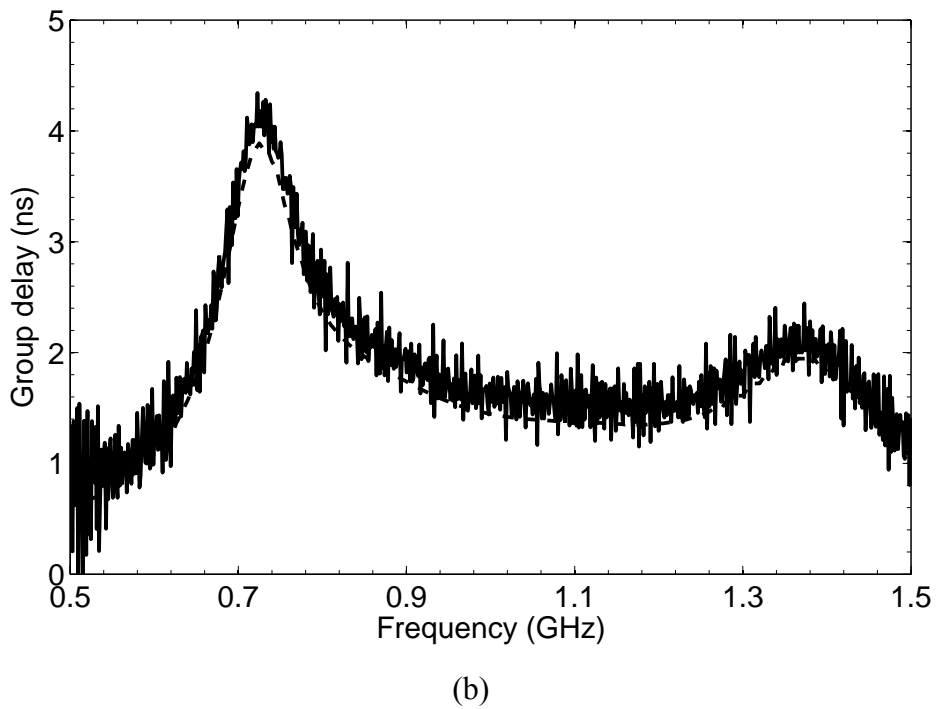
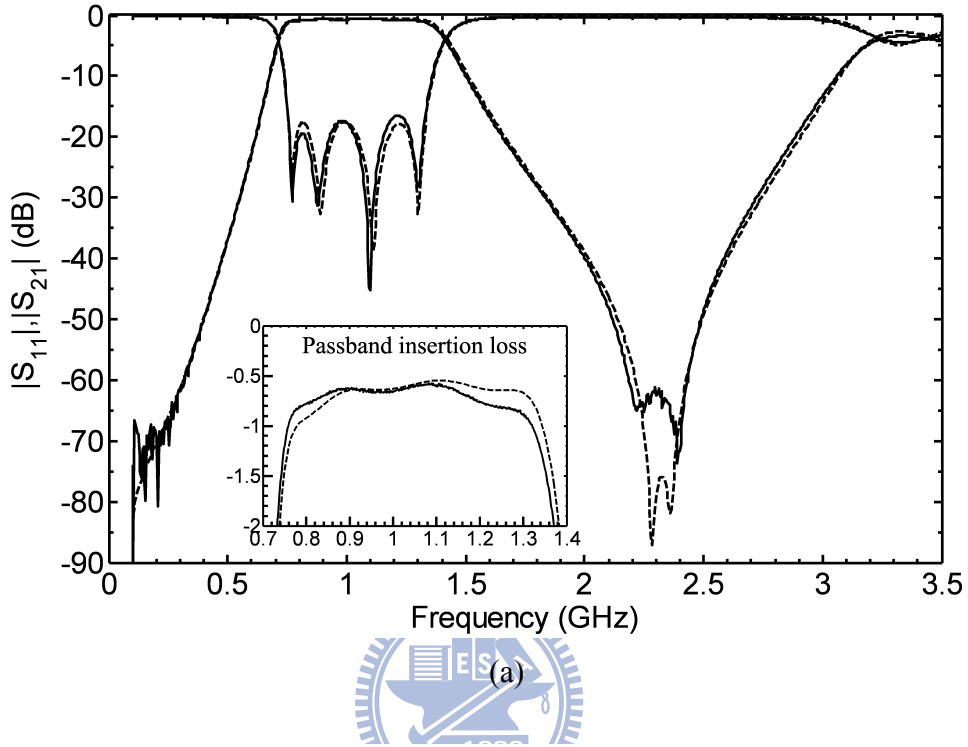
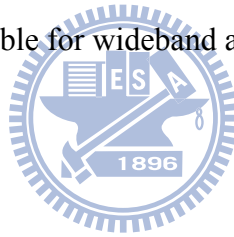


Fig. 4-20. Simulated (dashed line) and measured (solid line) results of filter II. (a) Scattering parameters. (b) Passband group delay.

## 4.4 Summary

The two proposed  $\lambda/4$  interdigital SIRs have successfully solved the coupling strength problem of the conventional  $\lambda/4$  microstrip SIR. By utilizing interdigital fingers in the low-impedance section of the SIR, strong coupling between adjacent resonators is achieved. The filter fractional bandwidth can be easily varied by changing the number of interdigital strips and the interleave length. In the meantime, the impedance ratio  $R$  of the SIR is still kept low so as to reduce the filter size and to extend the upper stopband. The filter with a generalized Chebyshev response is easily achieved by applying a thin cross-coupling microstrip line. Furthermore, the coupling mechanisms between resonators in the filter are all on the same plane so that misalignment between different layers during the fabrication process can be avoided. Each of the four filters has a very compact size, a wide passband, and a wide upper stopband. Therefore, they are suitable for wideband applications.



## ***Chapter 5 ENHANCED COUPLING STRUCTURES FOR TIGHT COUPLERS AND WIDEBAND FILTERS***

Tightly coupled lines are difficult to realize on the conventional printed circuit board (PCB). In chapter 4, two interdigital coupling structures were used for coupling enhancement to design miniaturized wideband bandpass filters (BPFs). However, these two structures are unable to realize a tight coupler. In this chapter, we propose two types of novel enhanced coupled-line structures appropriate for tightly coupled directional couplers and wideband filters. The proposed coupled-line structures both have a rectangular ground-plane aperture and two inserted signal strips in the aperture to increase the coupling strength significantly. Compared to the conventional coupled lines with or without the ground-plane aperture shown in Fig. 1-2, the proposed ones have a much stronger coupling strength. Both proposed coupled-line structures have the advantages of process compatibility with the conventional PCB process, top-layer signal traces, and same-side input/output ports. In addition, they only need a single-layer substrate. Moreover, for the wideband filter design, they are conveniently adopted in any part of the resonator where the strong coupling is required. To demonstrate the feasibility of the proposed structures, two compact wideband BPFs and three 3-dB quadrature directional couplers with one, three, and five coupling sections, respectively, were designed and implemented. All circuits were fabricated on a Rogers RO4003 substrate with a dielectric constant of 3.58, a loss tangent of 0.0021, and a thickness of 0.508 mm. Each via-hole has a diameter of 0.3 mm. The commercial full-wave electromagnetic (EM) software Sonnet is employed in the simulation. The measurements of all circuits with subminiature A (SMA) connectors were carried out using an Agilent 8720ES network analyzer.

## 5.1 Proposed Coupled-Line Structures

### 5.1.1 Type I

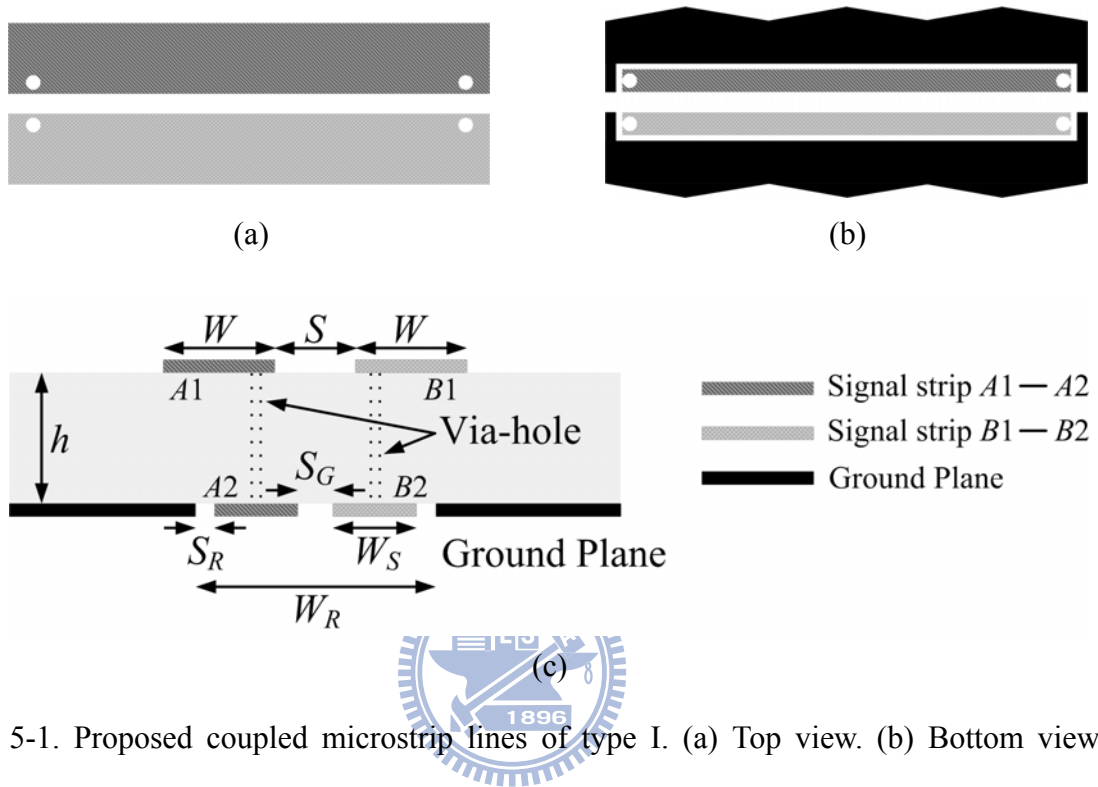


Fig. 5-1. Proposed coupled microstrip lines of type I. (a) Top view. (b) Bottom view. (c) Cross-sectional view.

Fig. 5-1 shows the top, bottom, and cross-sectional views of the proposed coupled microstrip lines of type I. The proposed structure, where there are two inserted signal strips in the ground plane, is basically an extension of the modified coupled lines shown in Fig. 1-2(b). Note that two via-holes are added on each end of the inserted signal strip on the bottom layer, penetrate through the substrate, and appear on both ends of each signal strip on the top layer. Therefore, the strip conductor  $A1$  is connected to  $A2$  and  $B1$  is connected to  $B2$ . To separate the inserted signal strip from the microstrip ground plane on the bottom layer, there is a narrow gap between them. In the proposed structure, the width of two microstrip lines on the top layer is  $W$  and the spacing between them is  $S$ . The width of two inserted signal strips with

a spacing  $S_G$  on the bottom layer is  $W_S$ . The spacing between the inserted signal strips and the microstrip ground plane is  $S_R$ . Accordingly, the width of the ground-plane aperture is  $W_R = 2 \times (W_S + S_R) + S_G$ . In the quasi-static analysis, the coupling strength of the symmetric coupled lines is determined by the even- and odd-mode capacitances  $C_e$  and  $C_o$  or by the even- and odd-mode impedances  $Z_e$  and  $Z_o$ . The voltage coupling factor  $C$  for the coupled lines is given by [20]

$$C = \frac{Z_e - Z_o}{Z_e + Z_o}. \quad (5.1)$$

Consequently, the larger the difference between the even- and odd-mode impedances is, the stronger the coupling between the lines will be.

Fig. 5-2 shows the even- and odd-mode excitations of the proposed coupled-line structure. For the even-mode excitation shown in Fig. 5-2(a), the normal component of the electric field at the symmetry plane is zero, which results in a magnetic wall. On the other hand, under the odd-mode excitation, the symmetry plane behaves like an electric wall, as indicated in Fig. 5-2(b). In Fig. 5-2,  $C_p$  denotes the parallel-plate capacitance per unit length located vertically between the signal and ground planes.  $C_f$  is the fringe capacitance per unit length from the edge of an uncoupled microstrip line.  $C_{sa}$  and  $C_{sd}$  represent the fringe capacitances per unit length across the gap between the inserted signal strip and the ground plane in the air and dielectric regions, respectively. For the odd-mode excitation in Fig. 5-2(b),  $C_{ta}$  and  $C_{td}$  are the fringe capacitances per unit length across the coupling gap in the air and dielectric regions, respectively, on the top layer, whereas  $C_{ga}$  and  $C_{gd}$  are those on the bottom layer. Therefore, the even- and odd-mode capacitances ( $C_e, C_o$ ) of either of the coupled lines are given by



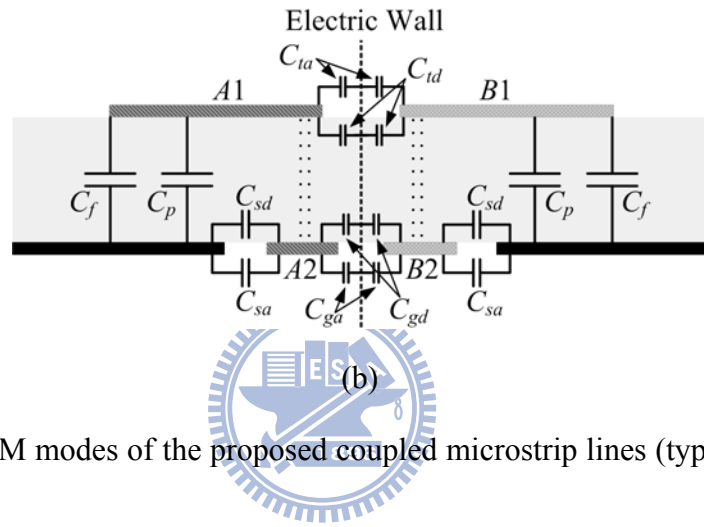
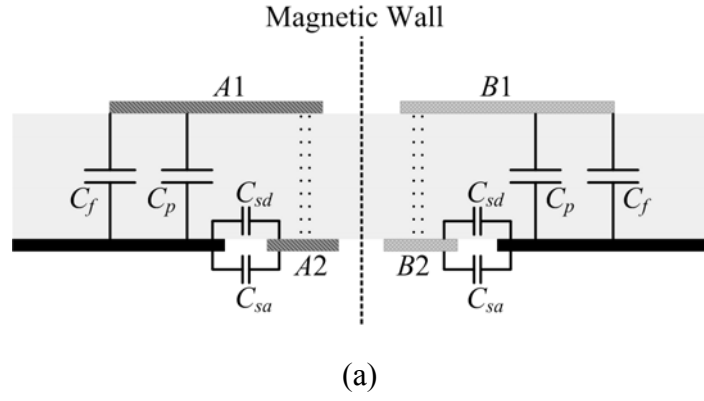


Fig. 5-2. Quasi-TEM modes of the proposed coupled microstrip lines (type I). (a) Even mode. (b) Odd mode.

$$C_e = C_f + C_p + C_{sa} + C_{sd} \quad (5.2)$$

$$C_o = C_f + C_p + C_{sa} + C_{sd} + C_{ta} + C_{td} + C_{ga} + C_{gd}. \quad (5.3)$$

To compare the characteristics of the conventional and proposed coupled lines shown in Figs. 1-2 and 5-1, first of all, it is necessary to obtain the even- and odd-mode impedances of coupled lines. We first perform the full-wave EM simulation for coupled lines by using Sonnet software, and then load the four-port  $S$ -parameter file in AWR Microwave Office to obtain the even- and odd-mode impedances. During the simulation, a lossless metal is assumed, and a substrate with a dielectric constant  $\epsilon_r = 3.58$  and a thickness  $h = 0.508$  mm

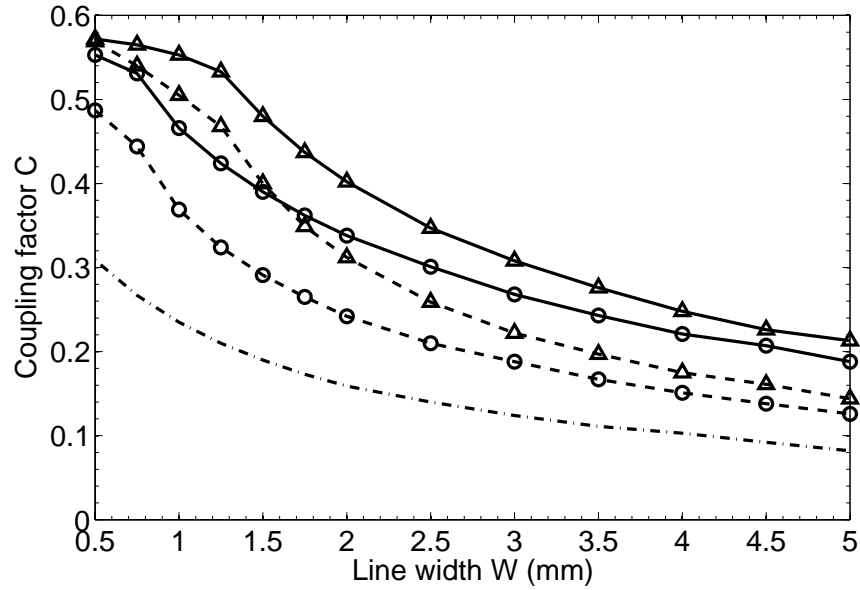


Fig. 5-3. Coupling factor  $C$  versus microstrip line width  $W$  for two aperture sizes  $W_R = 1.65$  mm (circle  $\circ$ ) and 2.85 mm (triangle  $\triangle$ ). Conventional (Fig. 1-2(a)): dashed-dotted line. Modified with the ground-plane aperture (Fig. 1-2(b)): dashed line. Proposed: solid line.

is used. Since the capability of the available fabrication process is taken into account, each via-hole is 0.3 mm in diameter, and the minimum line width and gap spacing are limited to be 0.15 mm. Since there are too many physical parameters in the proposed structure, the dimensions  $S$ ,  $S_G$ , and  $S_R$  are fixed at 0.15 mm.

Fig. 5-3 plots the coupling factor  $C$  versus microstrip line width  $W$  for two different aperture sizes  $W_R = 1.65$  mm and 2.85 mm, corresponding to  $W_S = 0.6$  mm and 1.2 mm. The lengths of the coupled lines and the ground-plane aperture are 33.75 and 33.15 mm, respectively. The figure shows that as  $W$  varies from 0.5 to 5 mm, the proposed structure always has the largest coupling factor compared to the conventional parallel coupled lines with or without the ground-plane aperture under the same physical dimensions. Furthermore, the wider the width  $W_R$  of the ground-plane aperture is, the larger the coupling factor  $C$  will be. The increasing percentage of the coupling factor is especially larger for wide lines. This property is very advantageous since, for the filter application, it is very difficult to obtain

strong coupling for wide lines.

To explain the mechanism behind the proposed structure in Fig. 5-3, first, consider the conventional coupled lines with and without the ground-plane aperture, as shown in Fig. 1-2. For the coupled lines without the ground-plane aperture, the even-mode impedance  $Z_e$  is larger than the odd-mode impedance  $Z_o$  since the even-mode capacitance  $C_e$  is smaller than the odd-mode capacitance  $C_o$ . For the coupled lines with the ground-plane aperture in Fig. 1-2(b), the decreasing percentage of  $C_e$  is greater than that of  $C_o$  owing to the ground-plane aperture. For this reason, the increasing percentage of  $Z_e$  is greater than that of  $Z_o$ , which results in a stronger coupling compared to the conventional structure in Fig. 1-2(a). On the basis of the structure in Fig. 1-2(b), now consider the proposed structure shown in Fig. 5-1 and the even- and odd-mode excitations given in Fig. 5-2. It is seen that the inserted signal strip in the ground-plane aperture increases  $C_e$  and  $C_o$  simultaneously due to capacitances  $C_{sa}$  and  $C_{sd}$  in both even- and odd-mode excitations. As the width  $W_s$  of the inserted signal strip increases, both capacitances  $C_e$  and  $C_o$  increase due to the increases of  $C_{sa}$  and  $C_{sd}$ . Additionally, the inserted signal strip introduces  $C_{ga}$  and  $C_{gd}$  in the odd-mode excitation. Thus, the increasing percentage of  $C_o$  is much greater than that of  $C_e$ . In other words, the proposed structure decreases  $Z_e$  and  $Z_o$  at the same time, and the decreasing percentage of  $Z_e$  is much smaller than that of  $Z_o$ . This method effectively enhances the coupling strength compared to the structure in Fig. 1-2(b).

It is interesting to compare the proposed coupled lines with and without via-holes and the coupled-line structure with a floating ground-plane conductor in [62]. Here, the dimensions in Fig. 5-3 are used as an example so that  $W_R = 1.65$  mm and 2.85 mm correspond to the width of the floating ground-plane conductor 1.35 and 2.55 mm in [62], respectively. Since the coupling enhancement is concerned in this study, Fig. 5-4 shows the coupling factor  $C$  for these three structures. As shown in the figure, the structure in Fig. 5-1 always has the largest coupling factor, and via-holes are necessary for strong coupling. The via-holes in the proposed

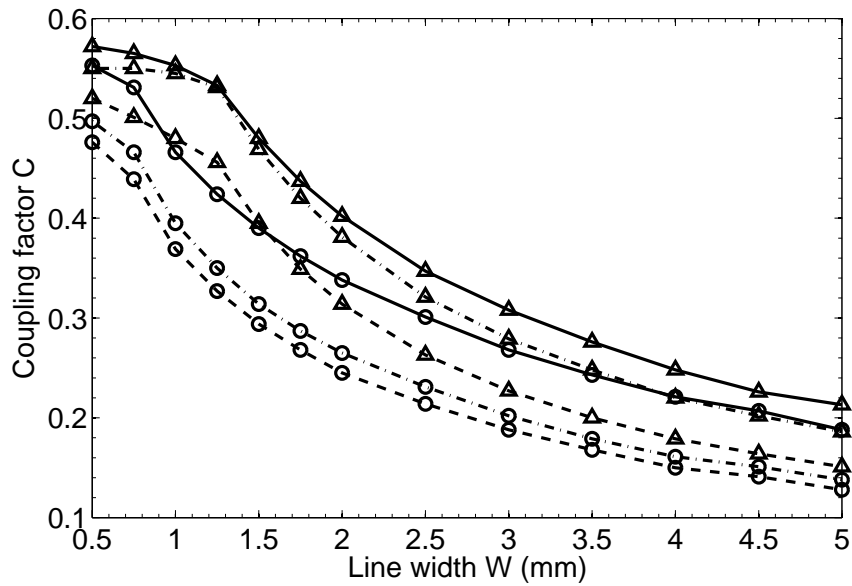


Fig. 5-4. Comparison of the coupling factor  $C$  for three different coupled lines with two aperture sizes  $W_R = 1.65$  mm (circle  $\circ$ ) and 2.85 mm (triangle  $\triangle$ ). Structure in [62]: dashed-dotted line. Proposed without via-holes; dashed line. Proposed with via-holes: solid line.



structure have an extremely small size and are primarily used for maintaining equal potentials on the top and bottom signal strips. In other words, they are not used to connect the signal strip to the ground plane. Accordingly, the current on the coupled lines is mainly along the longitudinal direction so that the inductive effect of via-holes is not severe and can be neglected. In the following circuit design, we ignore the effect of via-holes and consider them just as an interconnection between the top and bottom signal strips.

### 5.1.2 Type II

Fig. 5-5 depicts the top, bottom, and cross-sectional views of the proposed coupled microstrip lines of type II. In comparison with type I, type II has the same cross-sectional profile, except that the signal strips on the top layer are cross-connected to the inserted signal strips in the ground plane. Therefore, in Fig. 5-5(b) and 5-5(c), the strip conductor  $A1$  is

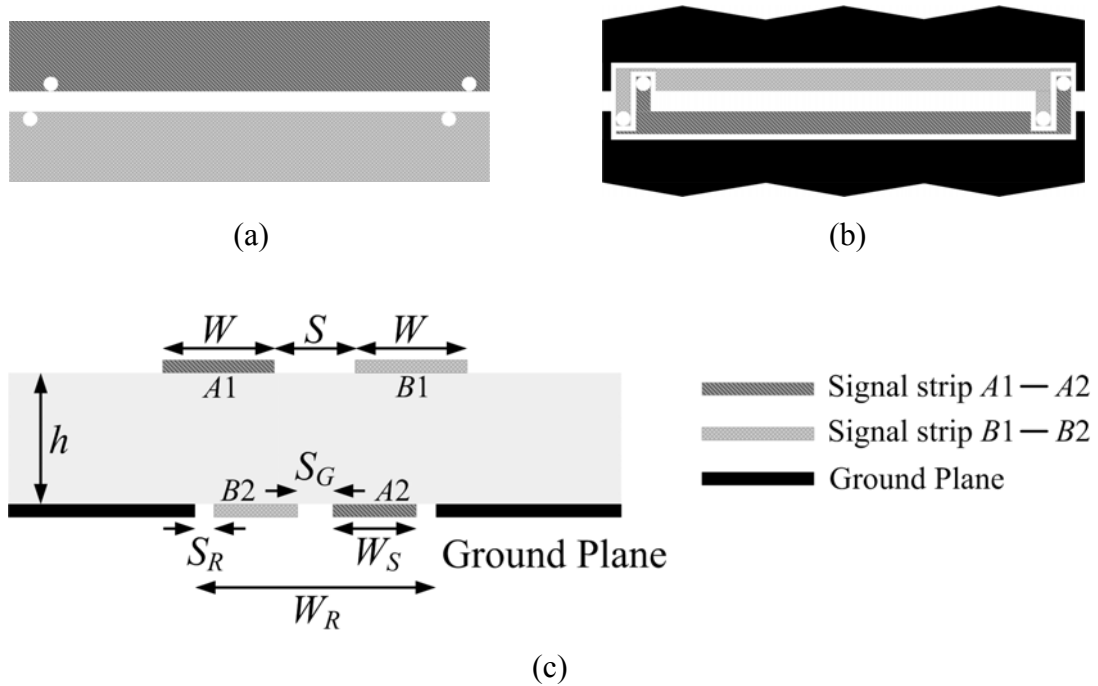
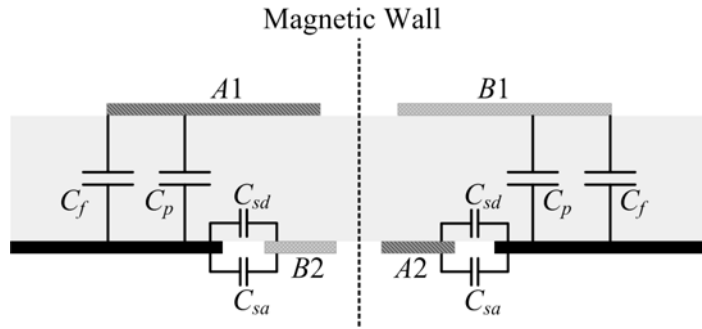
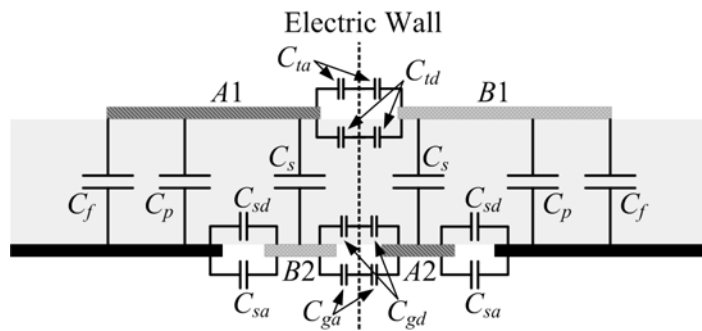


Fig. 5-5. Proposed coupled microstrip lines of type II. (a) Top view. (b) Bottom view. (c) Cross-sectional view.

connected to  $A2$  and  $B1$  is connected to  $B2$ . Although two pairs of via-holes are not placed symmetrically on both sides with respect to the central vertical plane, the even- and odd-mode excitations are still applied since the via-holes are very small compared to the whole circuit. The even- and odd-mode excitations of type II are shown in Fig. 5-6. Under the same physical dimensions, the even-mode excitation in Fig. 5-6(a) is the same as that in Fig. 5-2(a) so that this structure has little influence on the even-mode impedance  $Z_e$  of type I. However, comparing the odd-mode excitations in Figs. 5-2(b) and 5-6(b), this structure further decreases the odd-mode impedance  $Z_o$  of type I due to additional capacitance  $C_s$ . Thereby, types I and II have nearly the same even-mode impedance, whereas type II has a much smaller odd-mode impedance compared to type I. As a result, the coupling factor of type II is larger than that of type I. Take the dimensions given in Fig. 5-3 as an example. Fig. 5-7 compares the even- and odd-mode impedances ( $Z_e, Z_o$ ) and the coupling factor  $C$  versus microstrip line width  $W$  for types I and II to verify that type II has a much stronger coupling strength than type I.

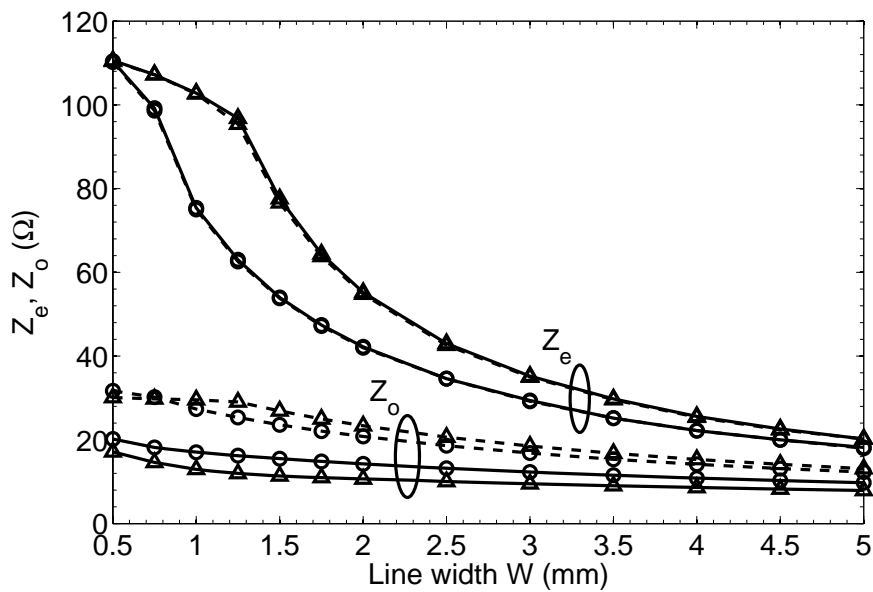


(a)

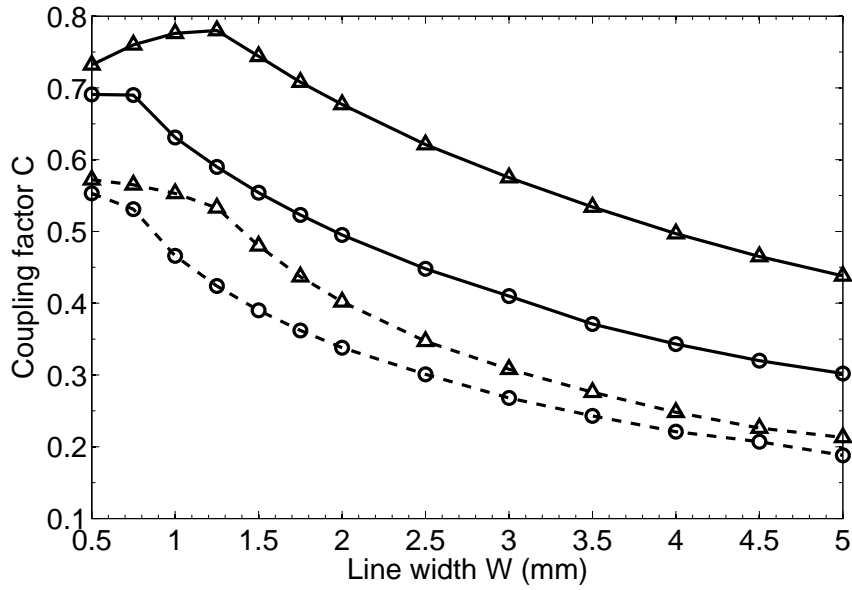


(b)

Fig. 5-6. Quasi-TEM modes of the proposed coupled microstrip lines (type II). (a) Even mode.  
(b) Odd mode.

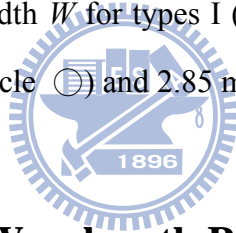


(a)



(b)

Fig. 5-7. Comparison of the (a) even- and odd-mode impedances ( $Z_e$ ,  $Z_o$ ) and (b) coupling factor  $C$  versus microstrip line width  $W$  for types I (dashed line) and II (solid line) with two aperture sizes  $W_R = 1.65$  mm (circle  $\odot$ ) and 2.85 mm (triangle  $\triangle$ ).

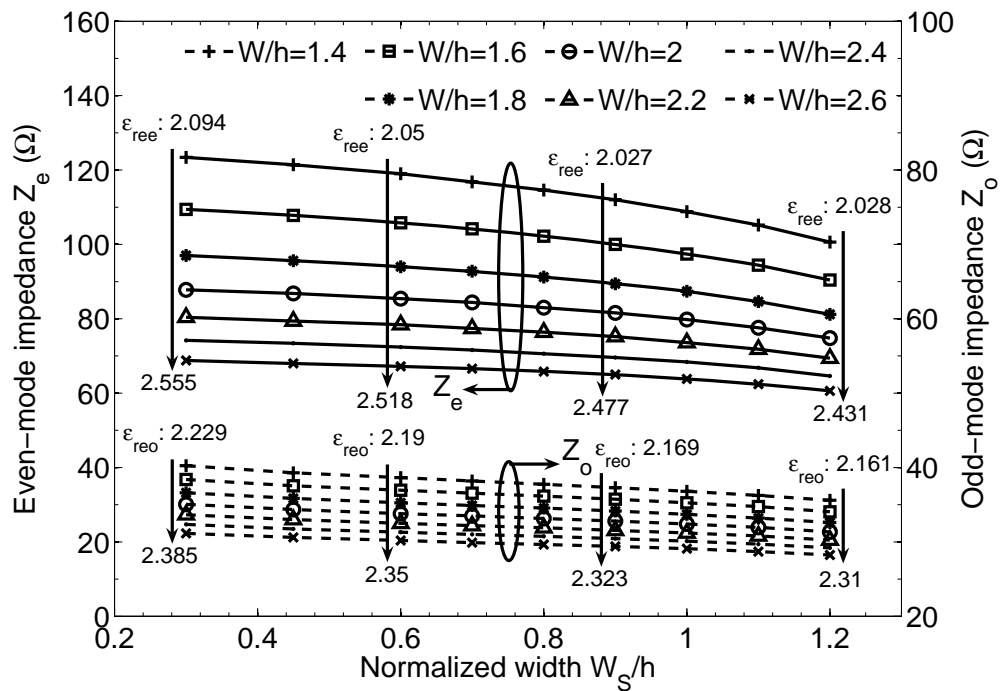


## 5.2 Wideband Quarter-Wavelength Parallel-Coupled Filter

Since a  $\lambda/4$  resonator has a smaller size and fewer spurious modes than a  $\lambda/2$  resonator, it is suitable for microstrip filters. The  $\lambda/4$  parallel-coupled filter presented in [63] was adopted to design a four-pole Chebyshev filter with a passband ripple of 0.05 dB, a center frequency ( $f_0$ ) of 1.5 GHz, and a fractional bandwidth of 40%. According to the analysis and design process in [63], the initial even- and odd-mode impedances of the coupling sections are  $Z_e = 72.0728 \Omega$  and  $Z_o = 38.7455 \Omega$ . Since the formulas in [63] are suitable for narrow-band filters, the developed filter should be fine tuned after the first design phase. Finally, the even- and odd-mode impedances of the coupling sections are  $Z_e = 72.4 \Omega$  and  $Z_o = 38.8 \Omega$ . However, in this example, the spacing of the conventional parallel coupled lines is only 0.075 mm (i.e., smaller than 0.15 mm), which is beyond the fabrication capability. Hence, the

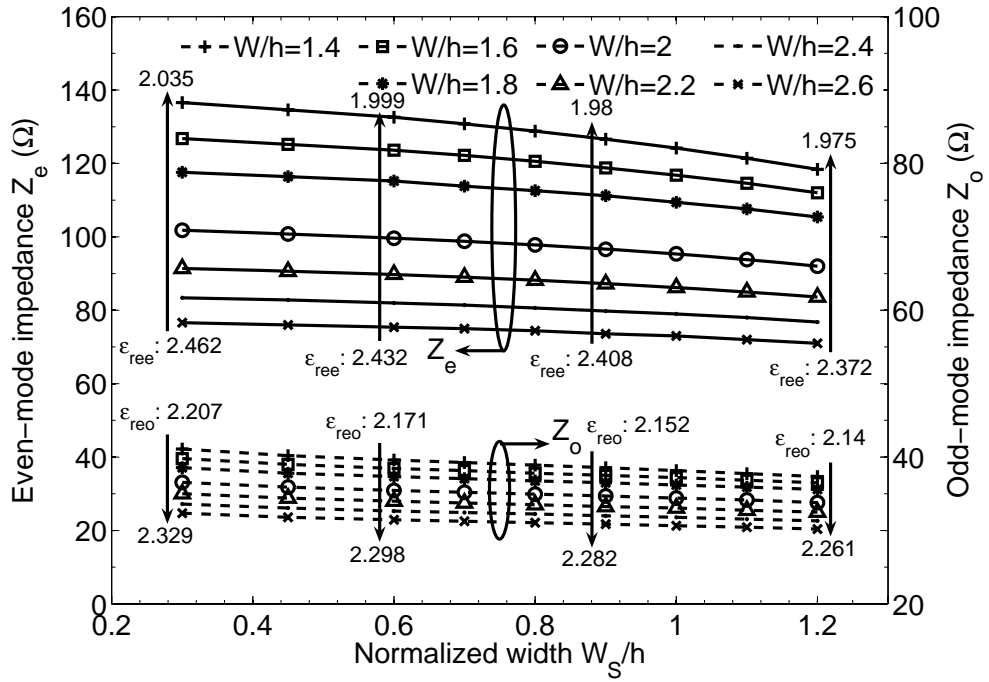
proposed structure of type I [see Fig. 5-1] is used to obtain enough coupling.

Fig. 5-8 plots the even- and odd-mode impedances versus normalized widths  $W/h$  (from 1.4 to 2.6) and  $W_S/h$  (from 0.3 to 1.2), together with the variations of the even- and odd-mode effective dielectric constants  $\epsilon_{ree}$  and  $\epsilon_{reo}$ . For easy comparison between parameters, we set  $S/h = S_G/h = 0.5$  in Fig. 5-8(a) and 5-8(b) and  $S/h = S_G/h = 1.1$  in Fig. 5-8(c). Therefore, the normalized ground-plane aperture width  $W_R/h = 3.5$  and  $4.1$  in Fig. 5-8(a) and 5-8(b) correspond to  $(W_S + S_R)/h = 1.5$  and  $1.8$ , respectively, and  $W_R/h = 4.1$  in Fig. 5-8(c) corresponds to  $(W_S + S_R)/h = 1.5$ . As shown in the figure, both  $Z_e$  and  $Z_o$  decrease as  $W/h$  and  $W_S/h$  increase. From Fig. 5-8(a) and 5-8(b), as  $W_R/h$  varies from 3.5 to 4.1,  $Z_e$  increases obviously while  $Z_o$  increases slightly. Comparing Fig. 5-8(a) and 5-8(c), as  $S/h$  and  $S_G/h$  increase from 0.5 to 1.1,  $Z_o$  increases, whereas  $Z_e$  remains almost the same. On the basis of the above discussion, we first choose  $W/h$ ,  $W_S/h$ , and  $S_R/h$  for  $Z_e$ , and then determine  $S/h$  and  $S_G/h$  according to  $Z_o$ . The even- and odd-mode effective dielectric constants are estimated using the linear interpolation method.

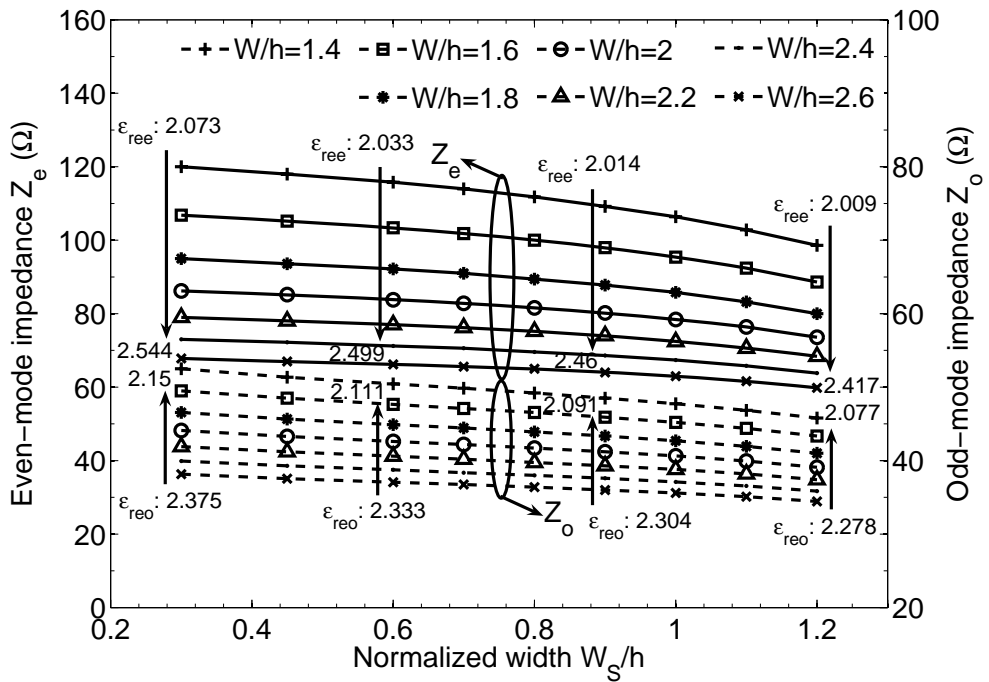


(a)





(b)



(c)

Fig. 5-8. Even- and odd-mode impedances ( $Z_e$ ,  $Z_o$ ) and effective dielectric constants ( $\epsilon_{ree}$ ,  $\epsilon_{reo}$ ) versus normalized values  $W/h$ ,  $W_R/h$ ,  $W_S/h$ ,  $S/h$ ,  $S_G/h$ , and  $S_R/h$ . (a)  $W_R/h = 3.5$ ,  $S/h = S_G/h = 0.5$ , and  $(W_S + S_R)/h = 1.5$ . (b)  $W_R/h = 4.1$ ,  $S/h = S_G/h = 0.5$ , and  $(W_S + S_R)/h = 1.8$ . (c)  $W_R/h = 4.1$ ,  $S/h = S_G/h = 1.1$ , and  $(W_S + S_R)/h = 1.5$ .

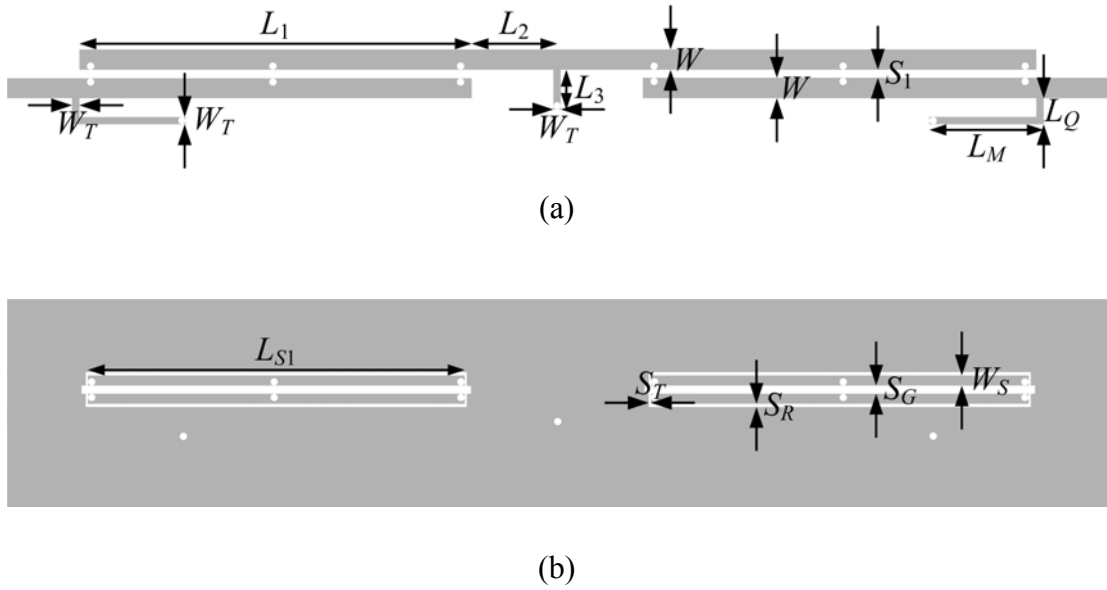


Fig. 5-9. Configuration of the four-pole  $\lambda/4$  parallel-coupled filter. (a) Top-layer layout. (b) Bottom-layer layout. Filter dimensions:  $L_1 = 22.8$  mm,  $L_2 = 4.8$  mm,  $L_3 = 2.35$  mm,  $L_Q = 1.55$  mm,  $L_M = 6.55$  mm,  $L_{S1} = 21.9$  mm,  $S_1 = S_G = 0.55$  mm,  $S_T = 0.15$  mm,  $S_R = 0.25$  mm,  $W = 1.1$  mm,  $W_S = 0.5$  mm, and  $W_T = 0.3$  mm.

Once the even- and odd-mode impedances are determined, the dimensions of the coupling sections can be obtained using the design charts in Fig. 5-8. The physical layout and dimensions of the  $\lambda/4$  parallel-coupled filter are shown in Fig. 5-9. Note that two additional via-holes are added on the middle of each coupling section to eliminate the resonance. The two additional via-holes have little effect on the even- and odd-mode impedances and the coupling factor since they are very small compared to the whole circuit.

Fig. 5-10 shows a photograph of the fabricated filter. The size of the filter is  $55.8 \text{ mm} \times 4.3 \text{ mm}$ , which is  $0.4801\lambda_g \times 0.037\lambda_g$ , where  $\lambda_g$  is the guided wavelength of the 50- $\Omega$  line on the substrate at the center frequency. The simulated and measured responses of the filter are presented in Fig. 5-11. The measured results show that the filter has a center frequency of 1.519 GHz. The measured 3-dB fractional bandwidth is 49.11% from 1.18 to 1.926 GHz. The

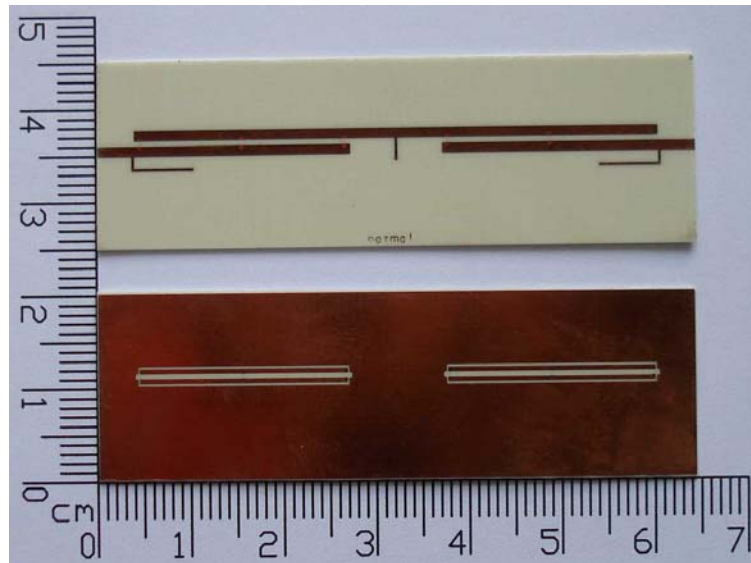
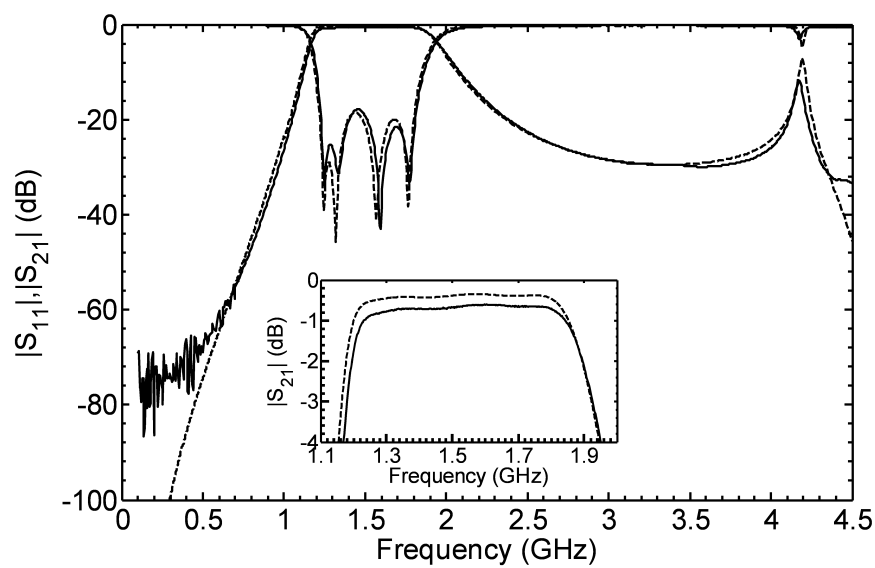
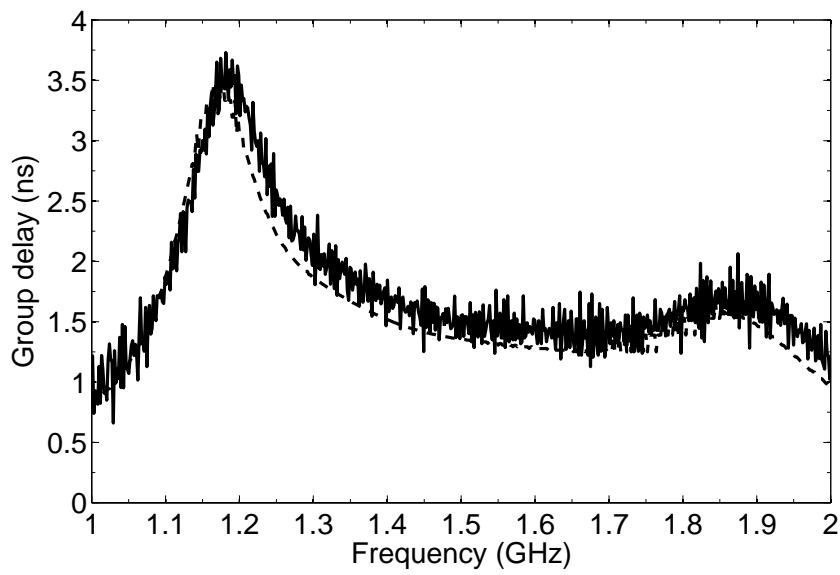


Fig. 5-10. Top view and bottom view of the fabricated  $\lambda/4$  parallel-coupled filter.

filter has a minimum insertion loss of 0.5934 dB and a return loss better than 18.1 dB within the passband. The maximum passband group delay variation is 1.5 ns. The first spurious frequency is at 4.176 GHz ( $= 2.75f_0$ ), and the rejection level is better than 20 dB from 2.381 to 4.109 GHz.



(a)



(b)

Fig. 5-11. Simulated (dashed line) and measured (solid line) results of the  $\lambda/4$  parallel-coupled filter. (a) Scattering parameters. (b) Passband group delay.

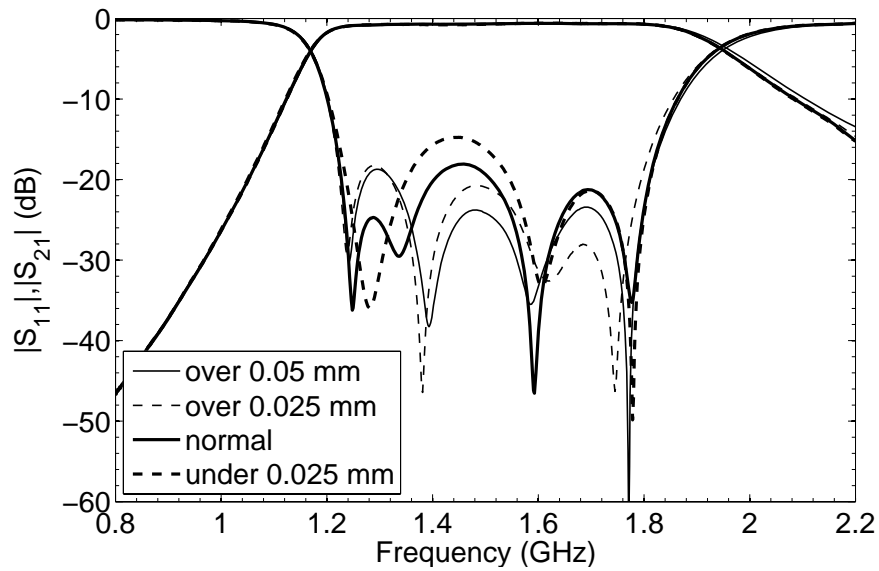


Fig. 5-12. Measured sensitivity to etching tolerances for the  $\lambda/4$  parallel-coupled filter (over: over-etching; under: under-etching).

To show the sensitivity to fabrication tolerances for the proposed coupled-line structure, we modify the mask during the fabrication process because PCB factories cannot change their processing parameters to match our study. Fig. 5-12 presents the measured responses of the  $\lambda/4$  parallel-coupled filter versus etching error, i.e., from over-etching 0.05 mm (2 mil) to under-etching 0.025 mm (1 mil). In spite of inaccurate fabrication, the center frequency and the bandwidth are almost unchanged. The passband return losses for all cases are better than 14.8 dB. Hence, the filter is insensitive to fabrication tolerances.

### 5.3 Wideband Quarter-Wavelength Hairpin Filter

The proposed coupling structures are easily incorporated in any part of the resonator where the strong coupling is needed. Fig. 5-13 depicts the top and bottom layouts of the folded microstrip  $\lambda/4$  resonator with the proposed type I structure. Here, the resonator is folded in a hairpin shape in order to apply the electric and magnetic couplings easily. In comparison with the conventional  $\lambda/4$  hairpin structure, the proposed one has an inserted signal strip in the ground plane along the edge of the open-end section of the resonator. The resonator has a top linewidth of  $W$ , and the width of the inserted signal strip in the ground plane is  $W_S$ . The spacing between the inserted signal strip and the microstrip ground plane is  $S_R$ . The length of the inserted signal strip is  $L_S$ , and the total physical length of the resonator is  $2 \times L_1 + L_2$ . Since, in this example, the length of the coupling section and the width of the resonator are arbitrarily chosen, the design procedure is conveniently based on the coupling coefficient  $k$  and the external quality factor  $Q_{ext}$  [57]. In the design process, we first fix  $W$  and  $S_R$ , and then adjust  $W_S$  iteratively to assure that the required coupling coefficient can be achieved for the minimum allowable spacing between resonators.

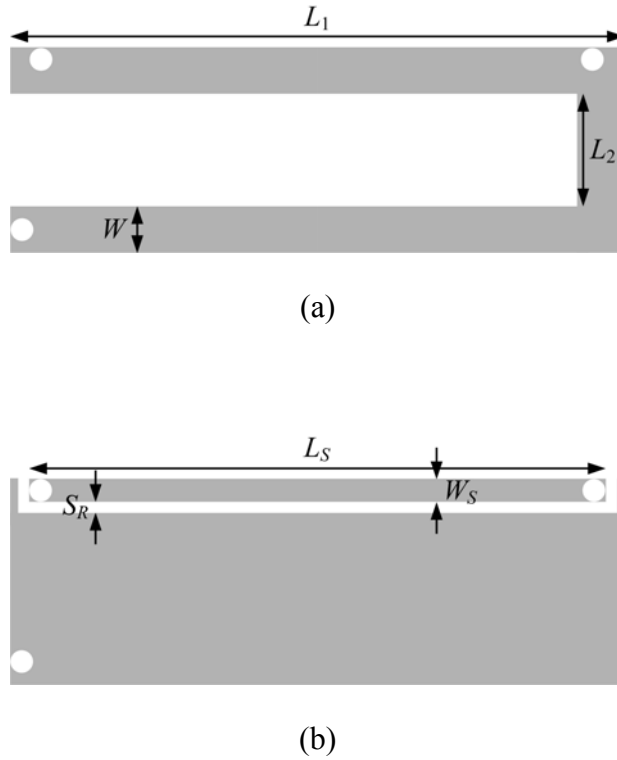
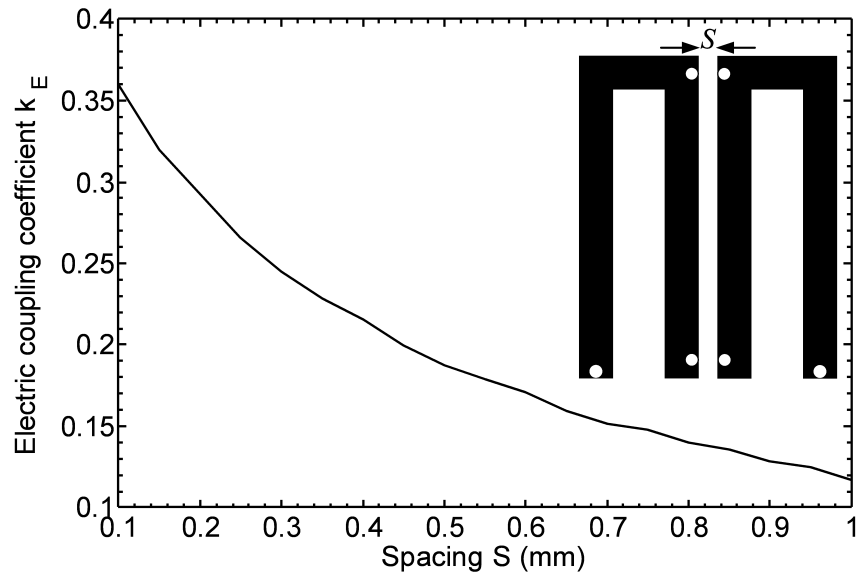


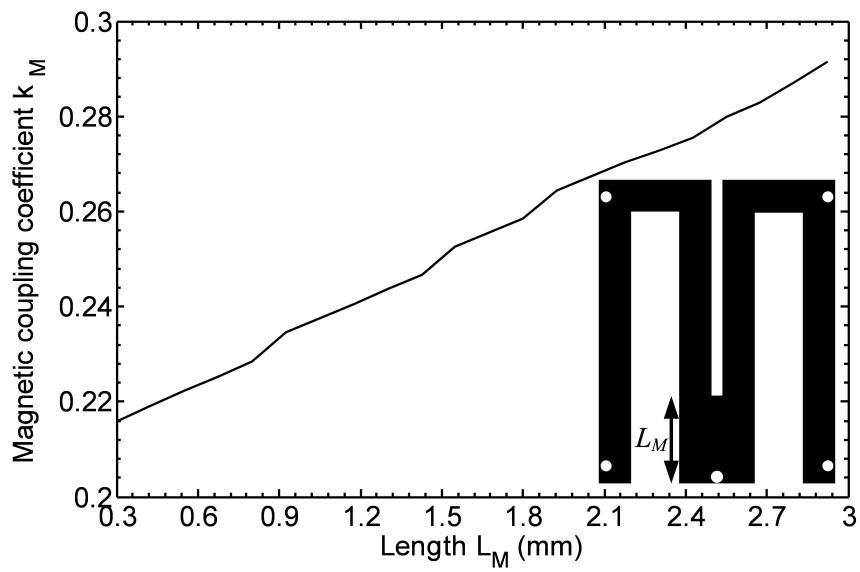
Fig. 5-13. Proposed  $\lambda/4$  hairpin resonator. (a) Top view. (b) Bottom view.

The designed four-pole  $\lambda/4$  hairpin filter is a Chebyshev filter with a passband ripple of 0.05 dB, a center frequency ( $f_0$ ) of 1.4 GHz, and a fractional bandwidth of 37%. According to the specifications,  $Q_{ext} = 2.5913$ ,  $k_{12} = k_{34} = 0.3318$ , and  $k_{23} = 0.2562$ . The resonator dimensions are determined as follows:  $L_2 = 2.5$  mm,  $W = 0.75$  mm,  $W_S = 0.3$  mm, and  $S_R = 0.15$  mm.

For the resonator dimensions listed above, Fig. 5-14 plots the two basic coupling structures and the design curves for the proposed  $\lambda/4$  hairpin filter. There are two kinds of couplings involved in the filter. Fig. 5-14(a) is for the electric coupling and Fig. 5-14(b) is for the magnetic coupling. The proposed type I structure forms a strong capacitive coupling between resonators where the coupling strength is determined by the widths  $W$  and  $W_S$  and the spacings  $S$  and  $S_R$ . The strong magnetic coupling is realized by a common transmission line connected to ground. The coupling strength is adjusted by the length  $L_M$  of the common short-circuited stub.

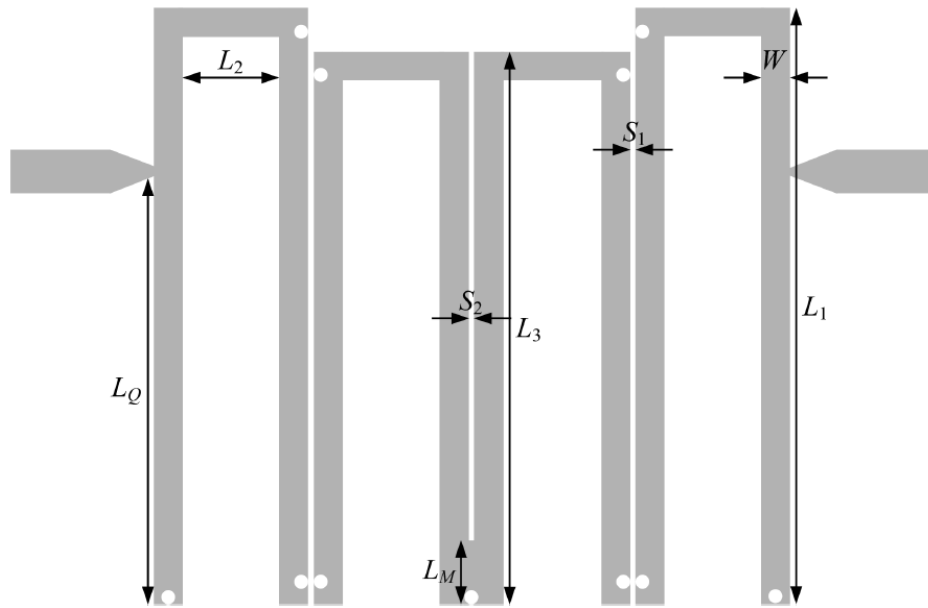


(a)

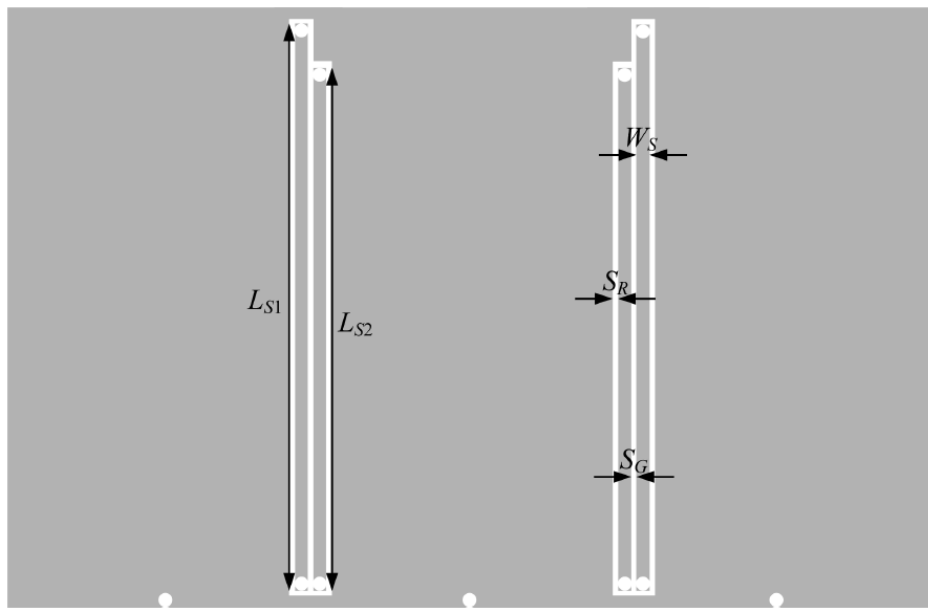


(b)

Fig. 5-14. Coupling structures and design curves for the proposed  $\lambda/4$  hairpin filter. (a) Electric coupling and (b) magnetic coupling.



(a)



(b)

Fig. 5-15. Configuration of the proposed four-pole  $\lambda/4$  hairpin filter. (a) Top-layer layout. (b) Bottom-layer layout. Filter dimensions:  $L_1 = 15.5$  mm,  $L_2 = 2.5$  mm,  $L_3 = 14.35$  mm,  $L_Q = 11.1$  mm,  $L_M = 1.65$  mm,  $L_{S1} = 14.6$  mm,  $L_{S2} = 13.45$  mm,  $W = 0.75$  mm,  $W_S = 0.3$  mm, and  $S_1 = S_2 = S_R = S_G = 0.15$  mm.



Fig. 5-15 depicts the physical layout and dimensions of the  $\lambda/4$  hairpin filter. Here, we number these four resonators as 1-4 from left to right. The coupling  $k_{23}$  is magnetic, whereas  $k_{12}$  and  $k_{34}$  are electric. A tapped-line input/output structure is used for the external coupling since it is space saving and easy to design. The tap position  $L_Q$  is chosen to match the  $Q_{ext}$  value for the 50- $\Omega$  source/load impedance.

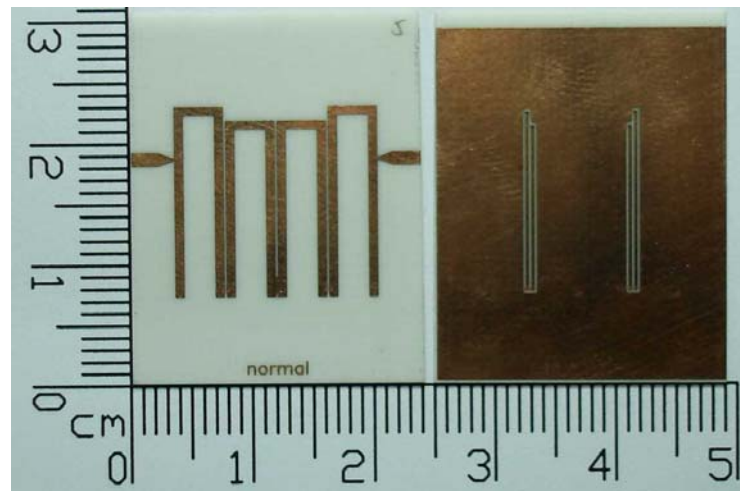
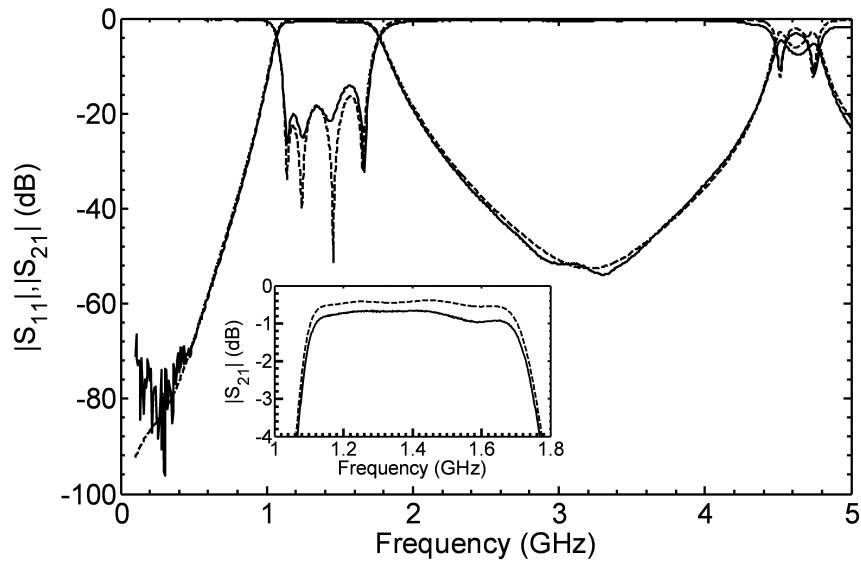
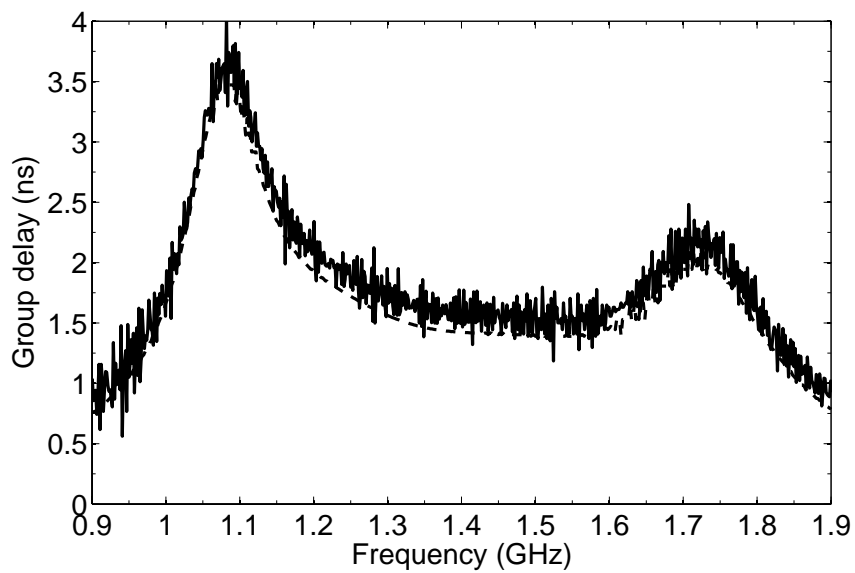


Fig. 5-16. Top view (left side) and bottom view (right side) of the fabricated  $\lambda/4$  hairpin filter.

Fig. 5-16 shows a photograph of the fabricated  $\lambda/4$  hairpin filter with a size of 16.45 mm  $\times$  15.5 mm, i.e.,  $0.1313\lambda_g \times 0.1237\lambda_g$ . Fig. 5-17 illustrates the simulated and measured responses. The measured results show that the filter has a center frequency of 1.409 GHz. The measured 3-dB fractional bandwidth is 47.84% from 1.077 to 1.751 GHz. Within the passband, the minimum insertion loss is 0.6526 dB, and the return loss is better than 14.2 dB. The maximum passband group delay variation is 1.5 ns. The first spurious response is at 4.522 GHz ( $= 3.21f_0$ ), and the rejection level is better than 20 dB from 2.016 to 4.334 GHz.



(a)



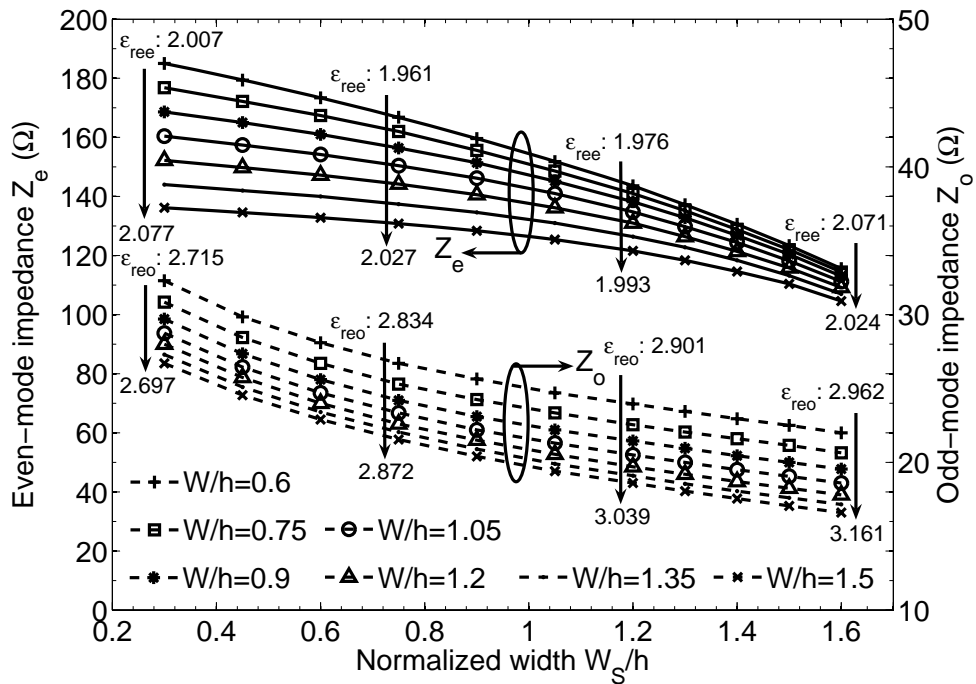
(b)

Fig. 5-17. Simulated (dashed line) and measured (solid line) results of the  $\lambda/4$  hairpin filter. (a) Scattering parameters. (b) Passband group delay.

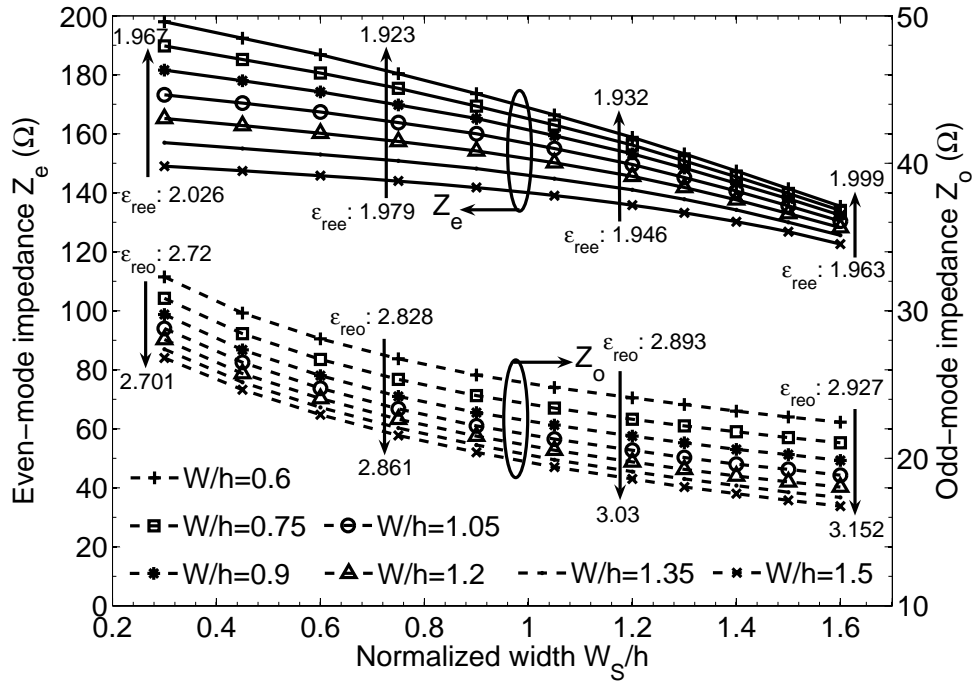
## 5.4 Single-Section 3-dB Directional Coupler

To realize a tight coupler, the proposed structure of type II [see Fig. 5-5] is chosen. Fig. 5-18 plots the even- and odd-mode impedances versus normalized widths  $W/h$  (from 0.6 to

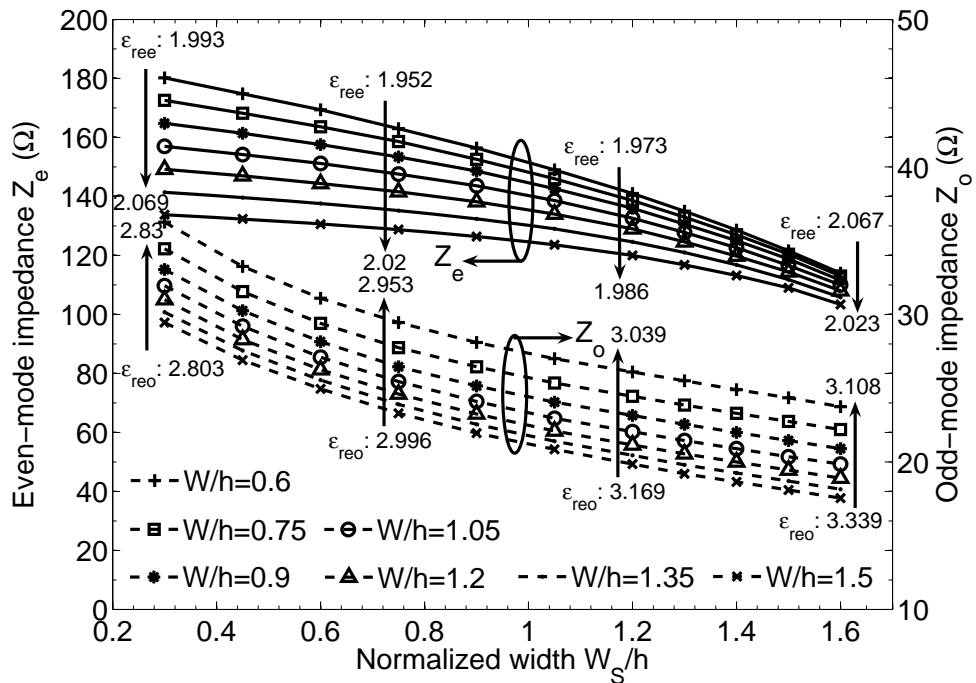
1.5) and  $W_S/h$  (from 0.3 to 1.6). Since there are many physical parameters in the proposed structure, we set  $S/h = S_G/h = 0.3$  in Fig. 5-18(a) and 5-18(b) and  $S/h = S_G/h = 0.6$  in Fig. 5-18(c) for easy comparison between parameters. Accordingly, the normalized ground-plane aperture width  $W_R/h = 4.1$  and  $4.7$  in Fig. 5-18(a) and 5-18(b) correspond to  $(W_S + S_R)/h = 1.9$  and  $2.2$ , respectively, and  $W_R/h = 4.4$  in Fig. 5-18(c) corresponds to  $(W_S + S_R)/h = 1.9$ . The figures show that both  $Z_e$  and  $Z_o$  decrease as  $W/h$  and  $W_S/h$  increase. Comparing Fig. 5-18(a) and 5-18(b), as  $W_R/h$  varies from  $4.1$  to  $4.7$ ,  $Z_e$  increases, whereas  $Z_o$  remains almost unchanged. From Fig. 5-18(a) and 5-18(c), as  $S/h$  and  $S_G/h$  increase from  $0.3$  to  $0.6$ ,  $Z_o$  increases, whereas  $Z_e$  remains almost the same. Thus, in the design process, we first determine  $W/h$ ,  $W_S/h$ , and  $S_R/h$  according to  $Z_e$ , and then choose  $S/h$  and  $S_G/h$  for  $Z_o$ . In addition, Fig. 5-18 gives the variations of the even- and odd-mode effective dielectric constants. The linear interpolation method is applied to estimate the even- and odd-mode effective dielectric constants owing to their small variations.



(a)

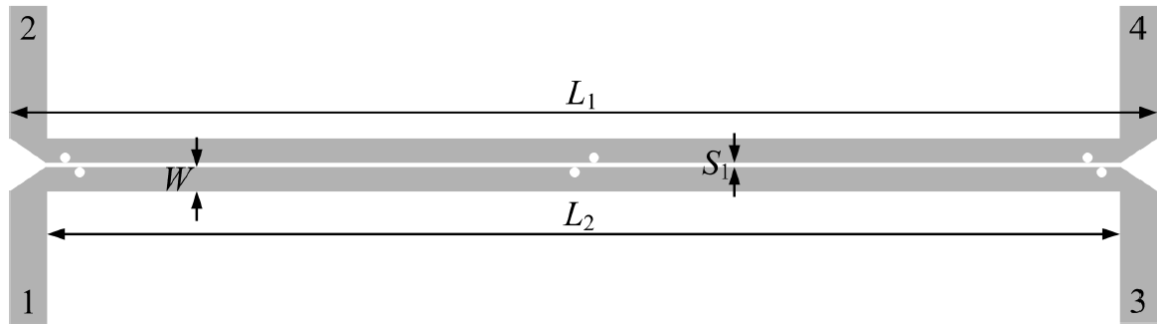


(b)

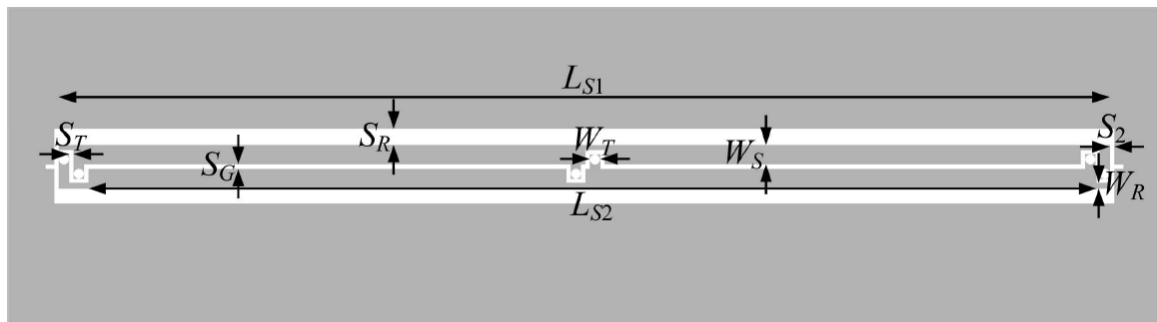


(c)

Fig. 5-18. Even- and odd-mode impedances ( $Z_e$ ,  $Z_o$ ) and effective dielectric constants ( $\epsilon_{ree}$ ,  $\epsilon_{reo}$ ) versus normalized values  $W/h$ ,  $W_R/h$ ,  $W_S/h$ ,  $S/h$ ,  $S_G/h$ , and  $S_R/h$ . (a)  $W_R/h = 4.1$ ,  $S/h = S_G/h = 0.3$ , and  $(W_S + S_R)/h = 1.9$ . (b)  $W_R/h = 4.7$ ,  $S/h = S_G/h = 0.3$ , and  $(W_S + S_R)/h = 2.2$ . (c)  $W_R/h = 4.4$ ,  $S/h = S_G/h = 0.6$ , and  $(W_S + S_R)/h = 1.9$ .



(a)



(b)

Fig. 5-19. Configuration of the proposed 3-dB coupler. (a) Top-layer layout. (b) Bottom-layer layout. Coupler dimensions:  $L_1 = 35.95$  mm,  $L_2 = 33.75$  mm,  $L_{S1} = 32.85$  mm,  $L_{S2} = 31.5$  mm,  $S_1 = S_2 = S_T = S_G = 0.15$  mm,  $S_R = 0.5$  mm,  $W = 0.75$  mm,  $W_S = 0.6$  mm,  $W_T = 0.3$  mm, and  $W_R = 0.15$  mm.

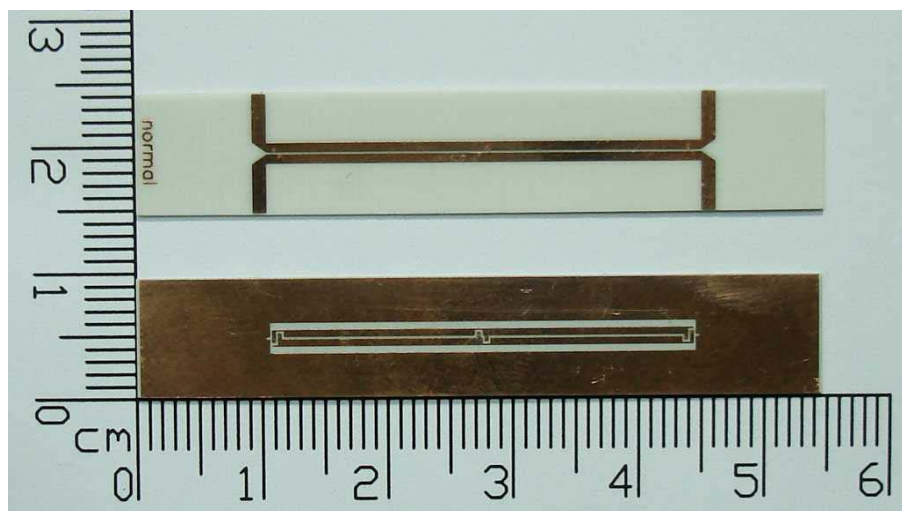
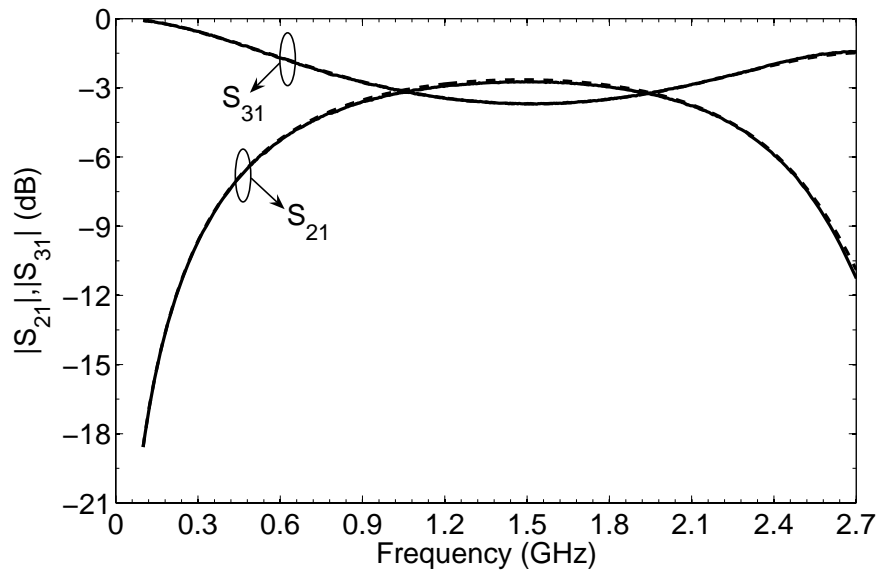


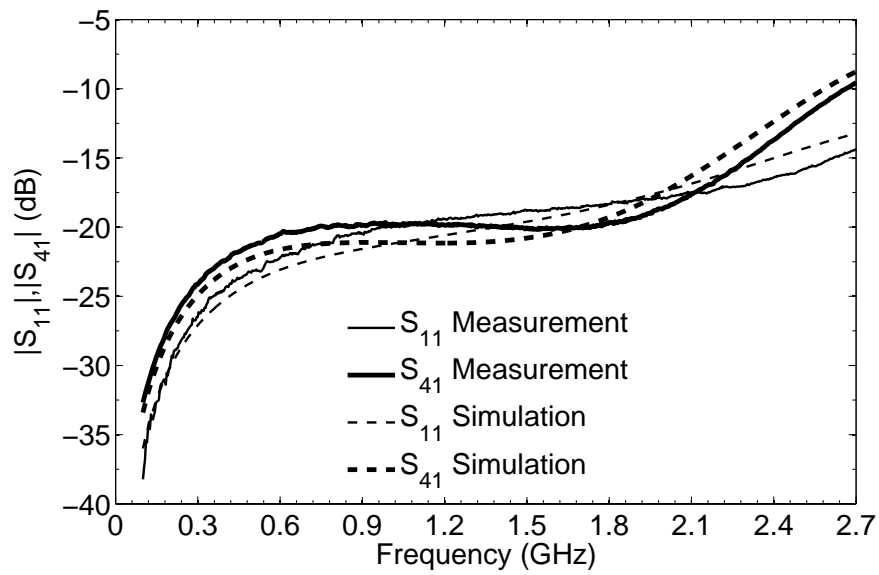
Fig. 5-20. Top view and bottom view of the fabricated coupler.

In this study, the coupler with a  $3 \pm 0.5$ -dB coupling factor was designed at the center frequency of 1.5 GHz. The corresponding even- and odd-mode impedances are  $Z_e = 132.3 \Omega$  and  $Z_o = 18.9 \Omega$ . On the basis of the analytical results and the design curves presented in Fig. 5-18(a)-(c), Fig. 5-19 depicts the top and bottom layouts of the directional coupler along with its physical dimensions. Again, two additional via-holes are added on the middle of the coupler to eliminate the resonance.

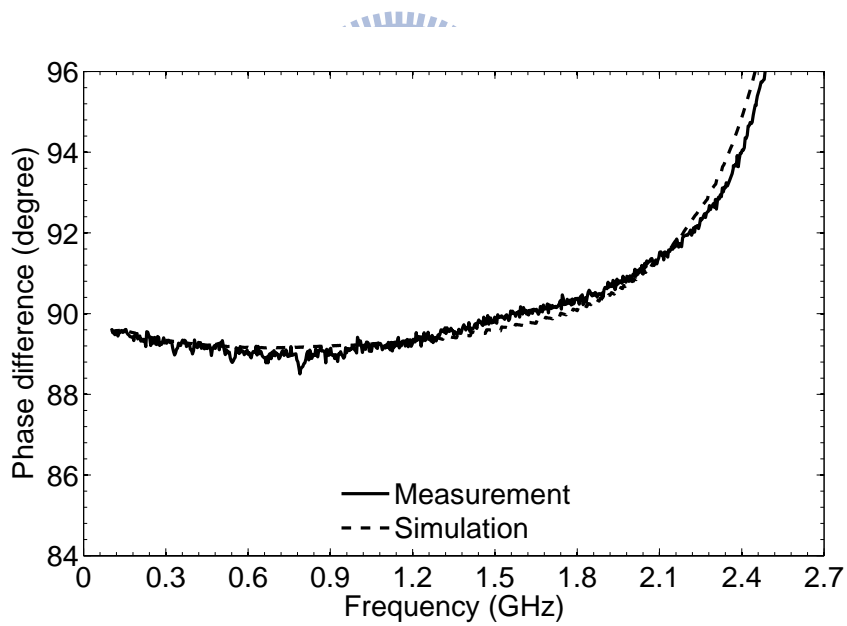
Fig. 5-20 displays the photograph of the fabricated coupler. The overall size of the coupler is  $9.85 \text{ mm} \times 35.95 \text{ mm}$ . Fig. 5-21 shows the simulated and measured responses. The measured results show that the coupling strength is 2.671 dB at the center frequency. The amplitude difference between port 2 (coupled port) and port 3 (through port) is less than 1 dB over the frequency range of 0.875-2.112 GHz, corresponding to a fractional bandwidth of 82.47%. The phase difference between the coupled and through ports is  $89.9^\circ$  at the center frequency and remains  $90 \pm 1.5^\circ$  from 0.1 to 2.132 GHz. The return loss and isolation are both better than 17.5 dB in the operating band.



(a)



(b)



(c)

Fig. 5-21. Simulated (dashed line) and measured (solid line) results of the coupler. (a) Insertion losses  $|S_{21}|$  and  $|S_{31}|$ . (b) Return loss  $|S_{11}|$  and isolation  $|S_{41}|$ . (c) Phase difference between the coupled and through ports.

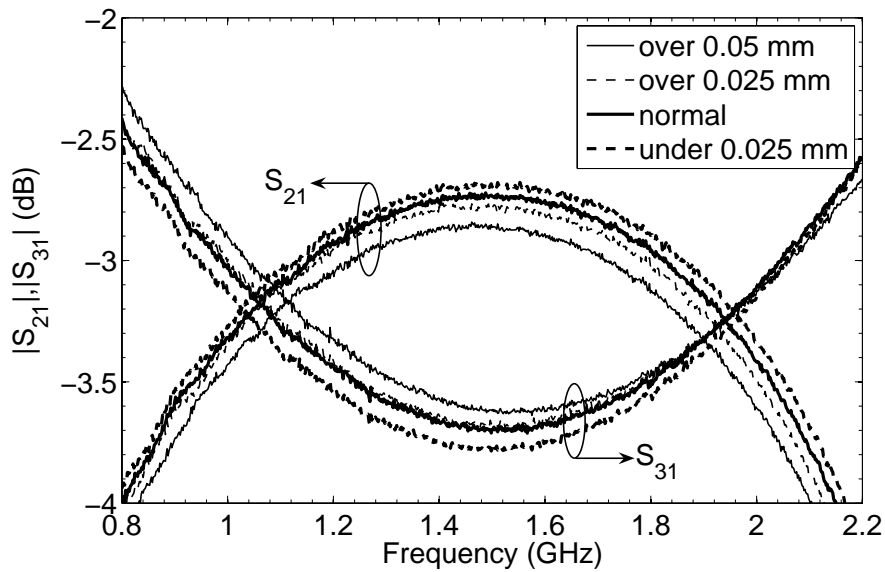


Fig. 5-22. Measured sensitivity to etching tolerances for the proposed 3-dB coupler (over: over-etching; under: under-etching).

Fig. 5-22 presents the measured responses of the proposed 3-dB coupler versus etching error, i.e., from over-etching 0.05 mm (2 mil) to under-etching 0.025 mm (1 mil), to demonstrate its sensitivity. Only the insertion losses for the through port and the coupled port are shown for clarity. It is seen that the coupler is insensitive to manufacturing inaccuracies.

As discussed above, there are many physical parameters for design flexibility in the proposed two coupling structures. In the next sections, the design criteria regarding these parameters are illustrated to achieve a very high even-mode impedance and a very low odd-mode impedance for a multisection 3-dB directional coupler. In addition, the proposed two coupling structures facilitate the connection between coupling sections so that they are very appropriate for multisection directional coupler design.

## 5.5 Three-Section 3-dB Directional Coupler

A three-section directional coupler with a passband ripple of 0.4 dB was designed to



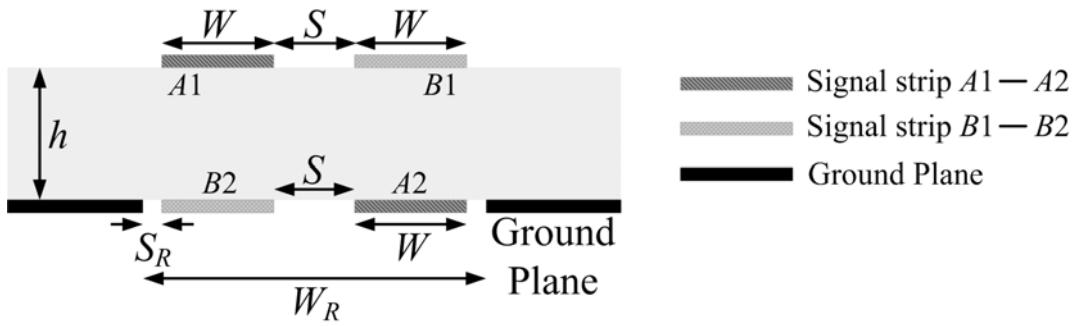


Fig. 5-23. Schematic of the tight-coupling section (section 2).

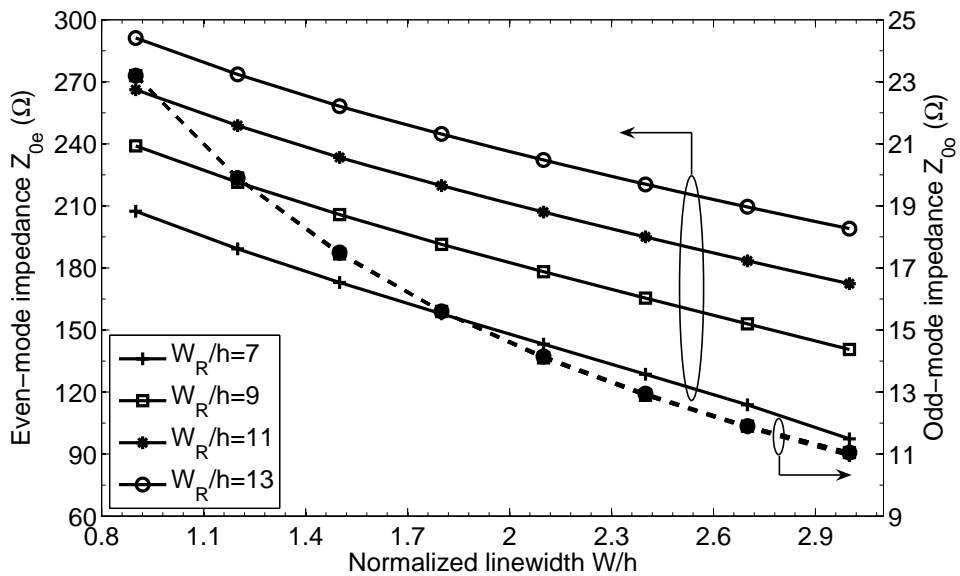


Fig. 5-24. Design chart for the tight-coupling section with  $S = 0.15$  mm.

cover the ultra-wideband (UWB) (i.e., 3.1-10.6 GHz). In the design process, first, the dimensions of each coupling section are designed based on the even- and odd-mode impedances ( $Z_{0e}$ ,  $Z_{0o}$ ). According to the multisection TEM coupler theory [59], the two outer sections have  $Z_{0e} = 63.52 \Omega$  and  $Z_{0o} = 39.36 \Omega$ . These two sections can be implemented by the conventional coupled microstrip lines. Their dimensions are easily synthesized using the commercial circuit simulator. The central section has  $Z_{0e} = 183.28 \Omega$  and  $Z_{0o} = 13.64 \Omega$  and is realized by the enhanced coupling structure of type II. To facilitate the design

Table 5-1 Dimensions (in millimeters) of the three-section directional coupler

Section	$W$	$W_R$	$S$	$S_R$	$L$
1 and 3	0.95	-	0.15	-	5.7
2	1.15	4.85	0.15	1.2	7.7

$L$ : Length of the coupling section.

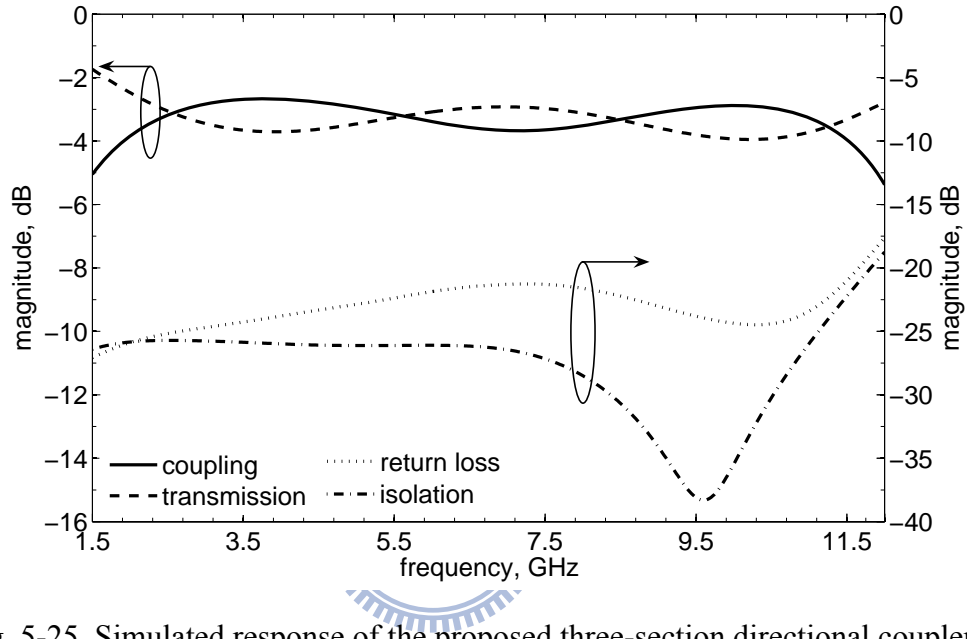


Fig. 5-25. Simulated response of the proposed three-section directional coupler.

process and to obtain a very low odd-mode impedance, here, the widths of the top and bottom signal strips are all set equal to  $W$ . The spacings between the signal strips on the top and bottom layers are both  $S$ . Consequently, the cross-sectional view of the center section is depicted in Fig. 5-23. On the basis of the minimum allowable spacing  $S = 0.15$  mm, Fig. 5-24 shows the design chart for the tight-coupling section. Apparently, the four dashed lines corresponding to  $Z_{0o}$  for different ground-plane aperture sizes are all overlapped. Therefore, we first determine  $W$  for  $Z_{0o}$ , and then choose  $W_R$  or  $S_R$  according to  $Z_{0e}$ .

After each section has been designed individually, the three sections are connected together. Since the discontinuities between the coupling sections would degrade the coupler behavior, the overall performance of the coupler is fine-tuned by using the full-wave EM

simulation software. The final dimensions of the coupler are given in Table 5-1. The simulated results are presented in Fig. 5-25.

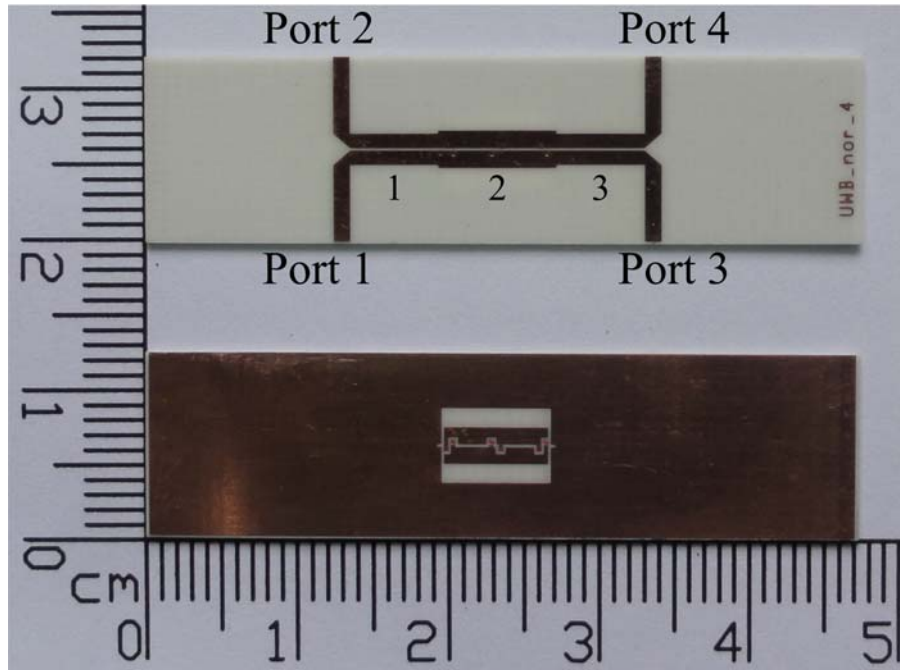


Fig. 5-26. Top view and bottom view of the fabricated three-section directional coupler.

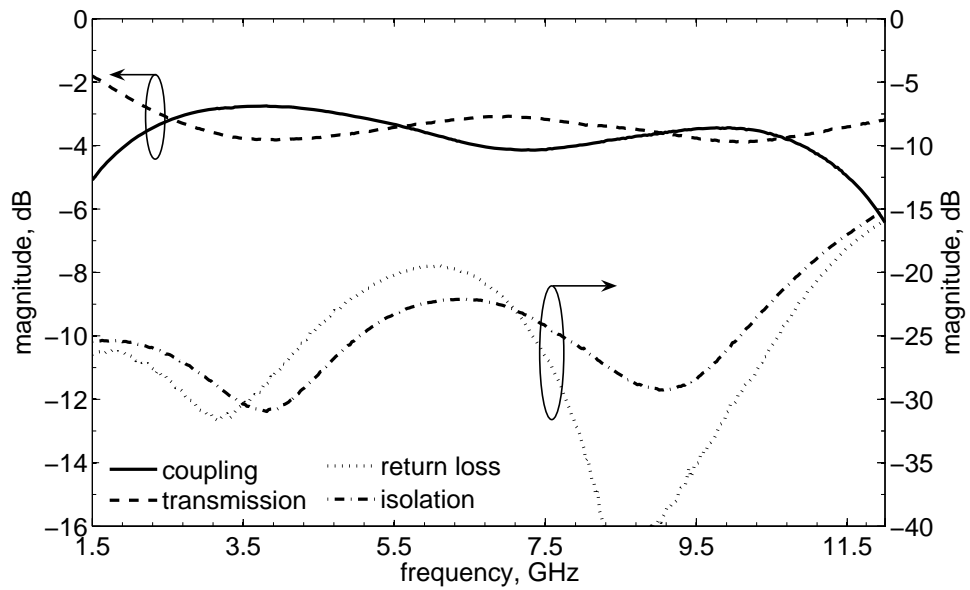
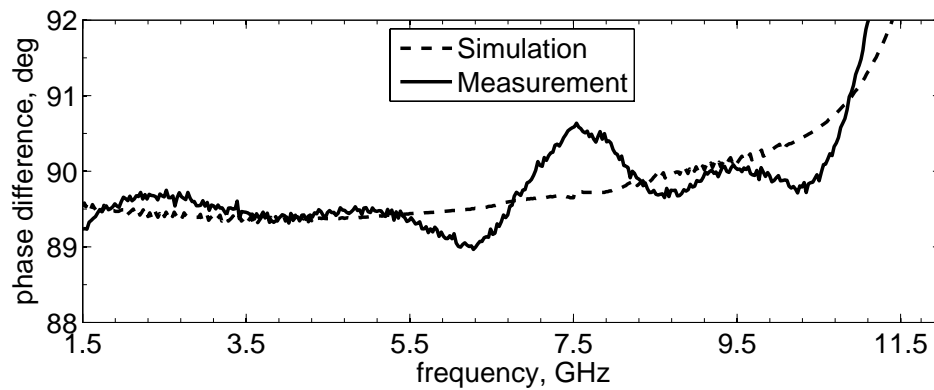
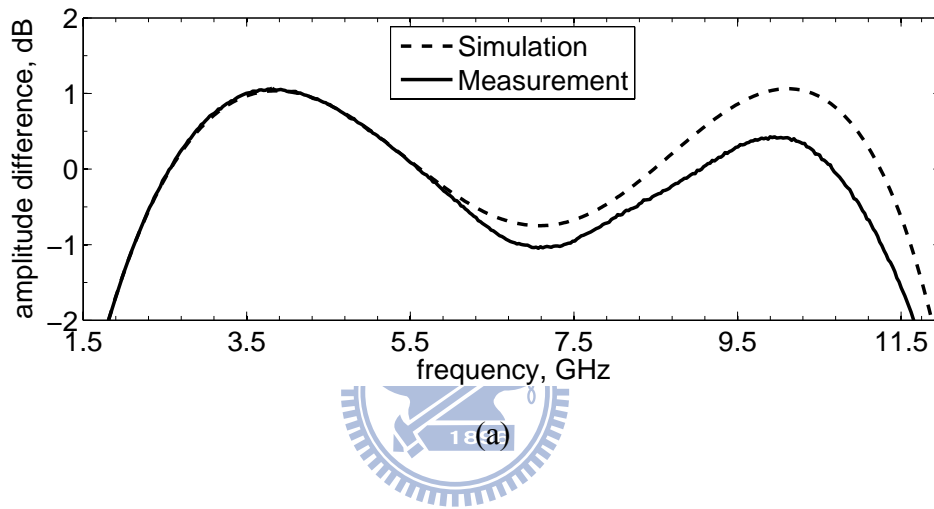


Fig. 5-27. Measured response of the three-section directional coupler.

Fig. 5-26 shows the photograph of the fabricated directional coupler, which has a size of  $12.35 \text{ mm} \times 21.3 \text{ mm}$ . The measured results in Fig. 5-27 show that the return loss  $S_{11}$  and the isolation  $S_{41}$  are both better than 19.5 dB up to 11 GHz. Fig. 5-28 indicates that the amplitude imbalance between the coupled and through ports is less than 1.1 dB from 2.09 to 11.3 GHz, and the phase imbalance is less than  $1^\circ$  up to 10.9 GHz. As a result, the proposed directional coupler performs well over the UWB band.



(b)

Fig. 5-28. Simulated and measured amplitude and phase imbalances between the coupled and through ports. (a) Amplitude imbalance. (b) Phase imbalance.

## 5.6 Five-Section 3-dB Directional Coupler

For the five-section directional coupler, the two outer sections use the conventional parallel-coupled microstrip lines, and the three inner sections consist of the proposed two enhanced coupling structures. Here, we design a five-section 3-dB directional coupler with a passband ripple of 0.3 dB and a center frequency of 3 GHz. Following the multisection TEM coupler theory, the even- and odd-mode impedances for each coupling section can be found in [59] and are listed in Table 5-2. The conventional coupled microstrip lines are used for sections 1 and 5. Their dimensions can be synthesized using the commercial circuit simulator.

Table 5-2 Design parameters of the five-section directional coupler

Section	$Z_e (\Omega)$	$Z_o (\Omega)$	$C$ (dB)
1 and 5	56.83	43.99	-17.9
2 and 4	74.78	33.43	-8.36
3	220	11.36	-0.9

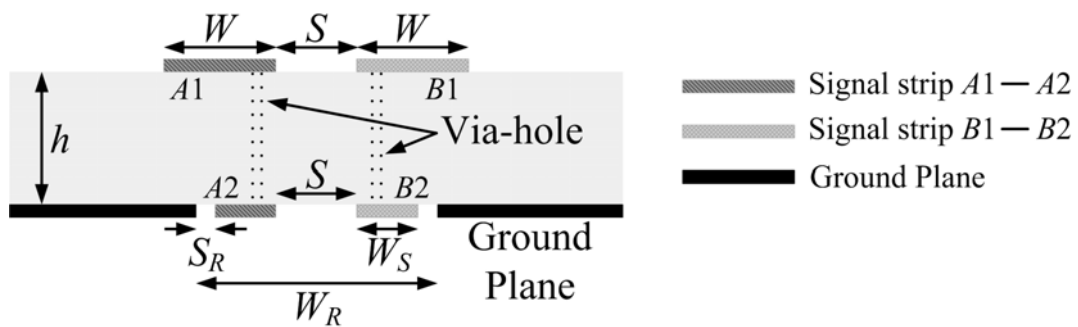
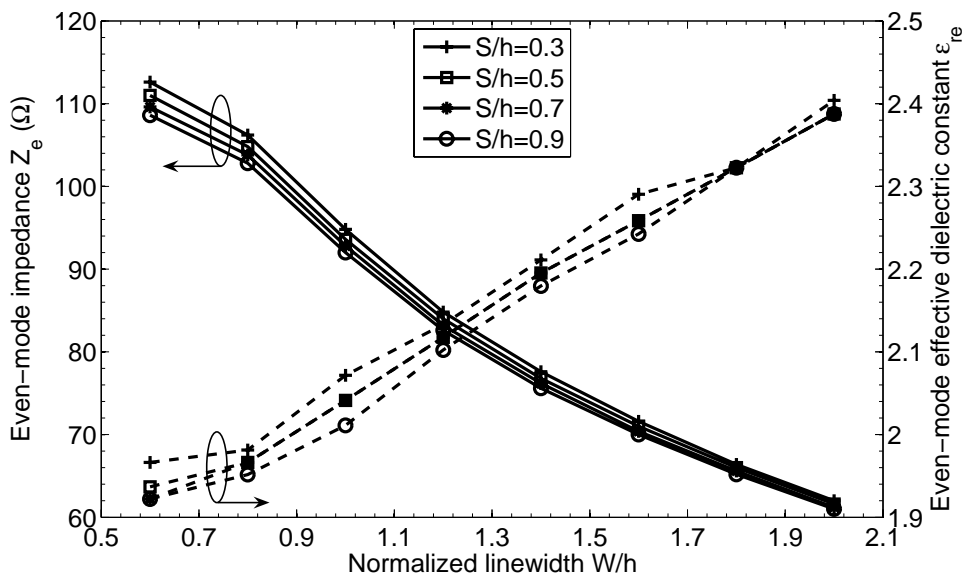


Fig. 5-29. Cross-sectional view of the enhanced coupling structure in sections 2 and 4.

For sections 2 and 4, the coupling structure of type I is selected. This structure can implement a coupler with a moderate coupling factor. Here, the cross-sectional view of this structure is shown in Fig. 5-29. The width of two microstrip lines on the top layer is  $W$  and the

spacing between them is  $S$ . The width of two inserted signal strips on the bottom layer is  $W_S$  and the spacing between them is also  $S$ . The spacing between the inserted signal strip and the microstrip ground plane is  $S_R$ . Thereby, the width of the ground-plane aperture is  $W_R = 2 \times (W_S + S_R) + S$ . Among these physical parameters, we fix  $S_R = 0.15$  mm (i.e.,  $S_R/h = 0.3$ ) according to the minimum allowable spacing and  $W_S = 0.3$  mm (i.e.,  $W_S/h = 0.6$ ) based on the minimum available diameter of via-holes to obtain design curves. Fig. 5-30 shows the even- and odd-mode impedances ( $Z_e$ ,  $Z_o$ ) and effective dielectric constants ( $\epsilon_{re}$ ,  $\epsilon_{ro}$ ) versus normalized strip linewidth  $W/h$  and spacing  $S/h$ . Apparently,  $W$  affects  $Z_e$  and  $Z_o$ , whereas  $S$  primarily controls  $Z_o$ . Consequently, we first determine  $W$  according to  $Z_e$ , and then choose  $S$  based on  $Z_o$ .

To implement the extremely tight-coupling section 3, the structure of type II is chosen. The cross-sectional view of the structure is shown in Fig. 5-31. Since  $Z_o$  is very small in this section and is mainly dominated by the overlap region between the top and bottom signal strips, these four signal strips have the same width  $W$ . The spacings between the adjacent signal strips on the top and bottom layers are both equal to  $S = 0.15$  mm (i.e.,  $S/h = 0.3$ )



(a)

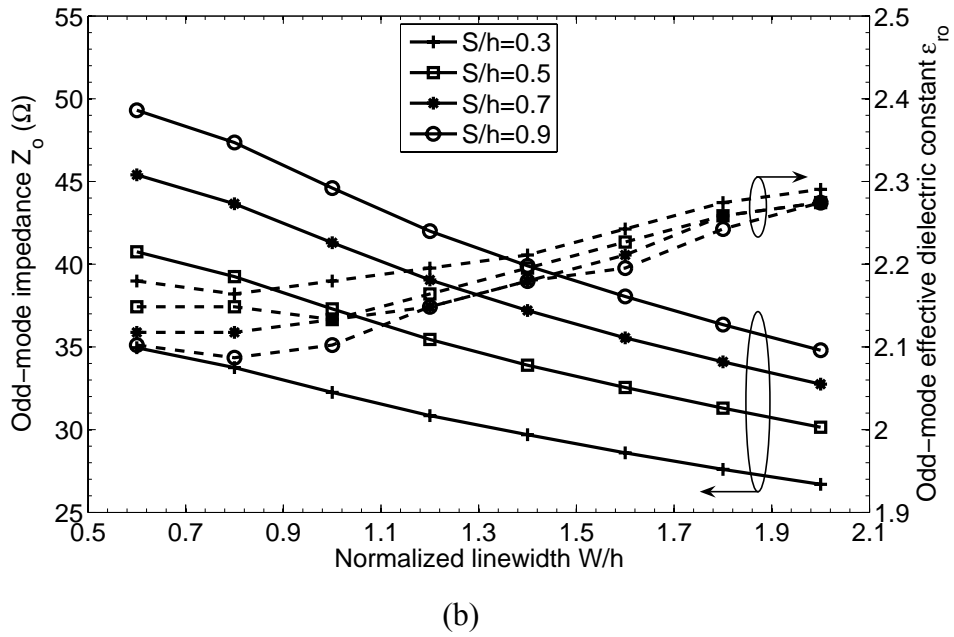


Fig. 5-30. Even- and odd-mode impedances ( $Z_e$ ,  $Z_o$ ) and effective dielectric constants ( $\epsilon_{re}$ ,  $\epsilon_{ro}$ ) versus normalized values  $S/h$  and  $W/h$  for  $S_R/h = 0.3$  and  $W_S/h = 0.6$ . (a) Even-mode. (b) Odd-mode.



based on the minimum allowable spacing. In addition,  $Z_e$  is very large in this section so that  $W_R$  is initially set large enough so as to determine  $W$  for a specific  $Z_o$ . Once  $W$  is obtained,  $W_R$  or  $S_R$  is adjusted for  $Z_e$ . Fig. 5-32 plots the even- and odd-mode impedances and effective dielectric constants versus  $W/h$  and  $W_R/h$  for  $S/h = 0.3$ . The figure indicates that both  $Z_e$  and  $Z_o$  decrease as  $W$  increases. Moreover, as  $W$  is fixed,  $W_R$  primarily influences  $Z_e$  and has little effect on  $Z_o$ . Hence,  $W$  is first chosen based on  $Z_o$ , and then  $W_R$  is determined according to  $Z_e$ .

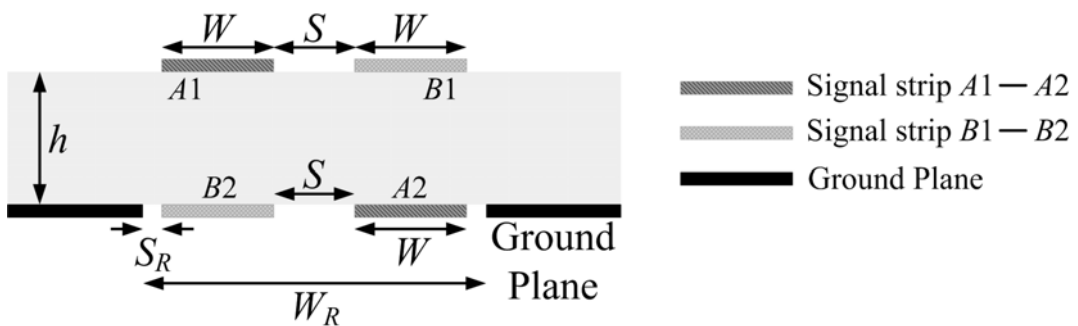
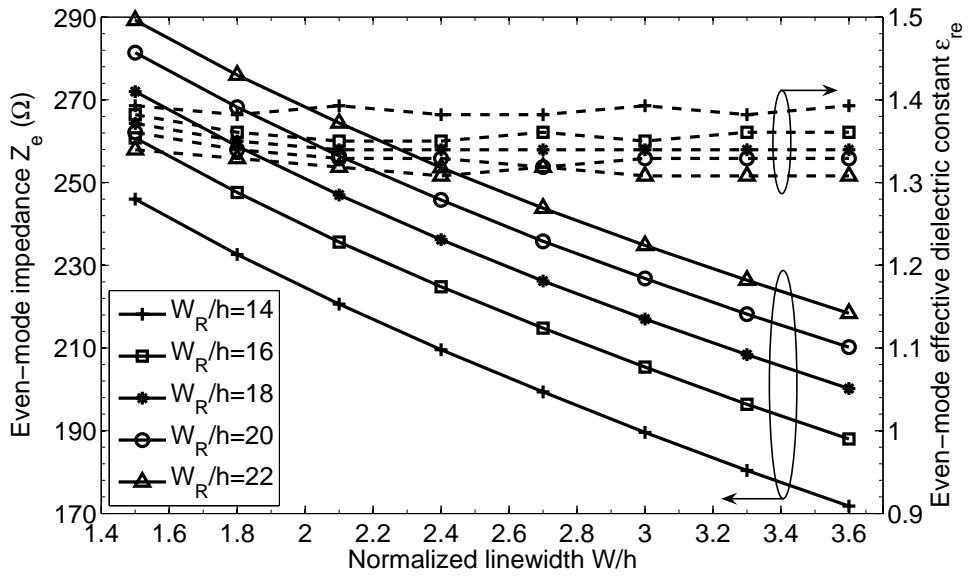
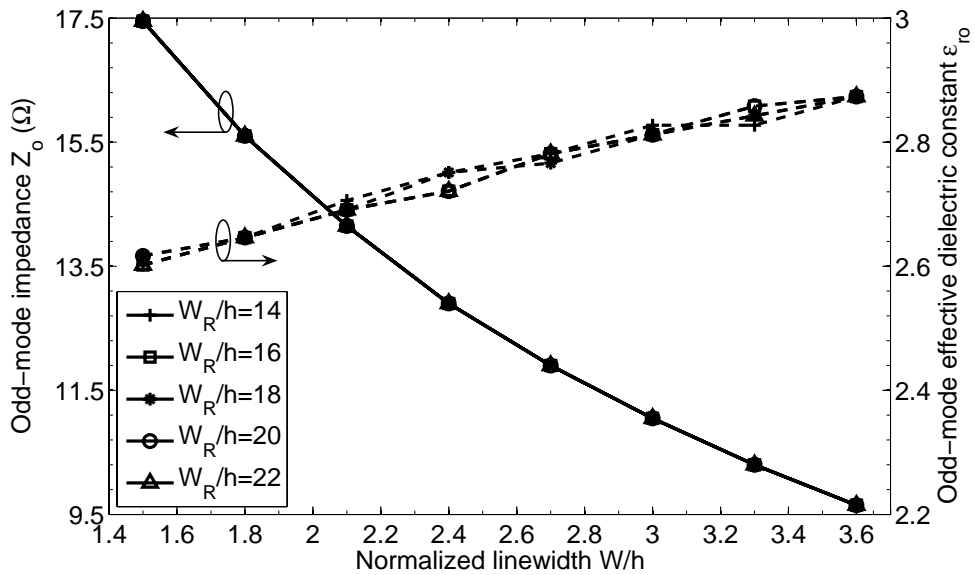


Fig. 5-31. Cross-sectional view of the enhanced coupling structure in section 3.



(a)



(b)

Fig. 5-32. Even- and odd-mode impedances ( $Z_e$ ,  $Z_o$ ) and effective dielectric constants ( $\epsilon_{re}$ ,  $\epsilon_{ro}$ ) versus normalized values  $W/h$  and  $W_R/h$  for  $S/h = 0.3$ . (a) Even-mode. (b) Odd-mode.

According to the even- and odd-mode impedances in Table 5-2, each coupling section was individually designed from Figs. 5-30 and 5-32, and then the five sections were joined together. Finally, the whole directional coupler was simulated by using full-wave EM simulation software, and the preliminary physical dimensions were slightly adjusted to



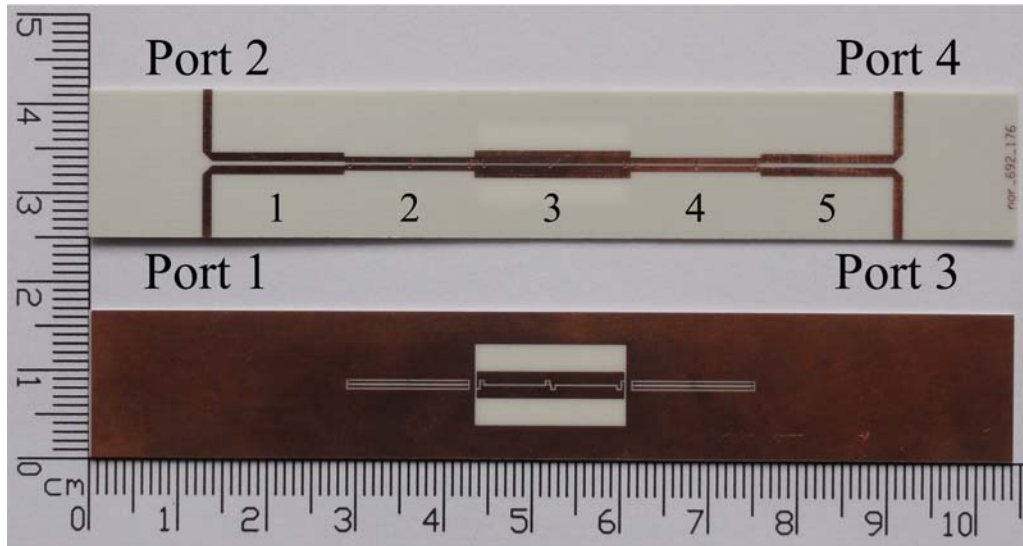


Fig. 5-33. Top view and bottom view of the fabricated five-section directional coupler.

Table 5-3 Dimensions (in millimeters) of the five-section directional coupler

Section	$W$	$W_S$	$W_R$	$S$	$S_R$	$L$
1 and 5	1.05	-	-	0.4	-	14.65
2 and 4	0.7	0.3	-	0.2	0.15	14.3
3	1.45	-	8.95	0.15	3.3	17.3

$L$ : Length of the coupling section.

compensate for the parasitics encountering in the discontinuities between sections. Fig. 5-33 displays the photograph of the fabricated five-section directional coupler, where the physical dimensions of each coupling section are given in Table 5-3. The three ground-plane apertures of sections 2, 3, and 4 are separated with each other by a ground metal with a length of 0.6 mm, i.e., 0.3 mm long for each section. The overall size of the circuit is 16.45 mm  $\times$  77.4 mm. Figs. 5-34 and 5-35 show the simulated and measured responses. The measured return loss and isolation are both better 15 dB for the frequency range of 0.1 to 5.22 GHz. The amplitude difference between port 2 (coupled port) and port 3 (through port) is shown in Fig. 5-36(a) and is less than 0.85 dB over the frequency range of 0.63-5.24 GHz, corresponding to a

fractional bandwidth of 157%. The phase difference between the coupled and through ports is presented in Fig. 5-36(b) and remains  $90\pm 5^\circ$  from 0.1 to 5.22 GHz.

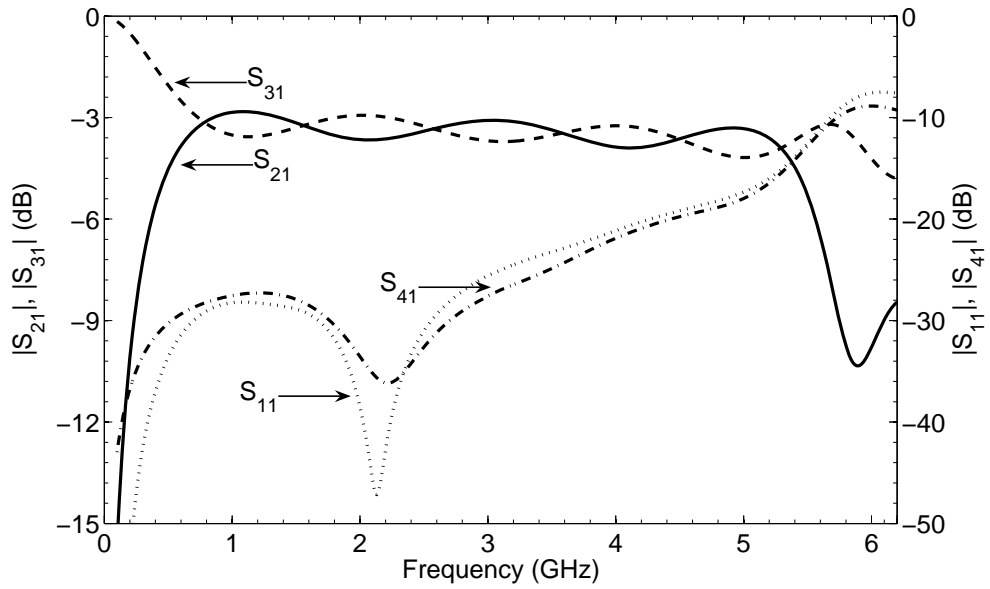


Fig. 5-34. Simulated result of the five-section directional coupler.

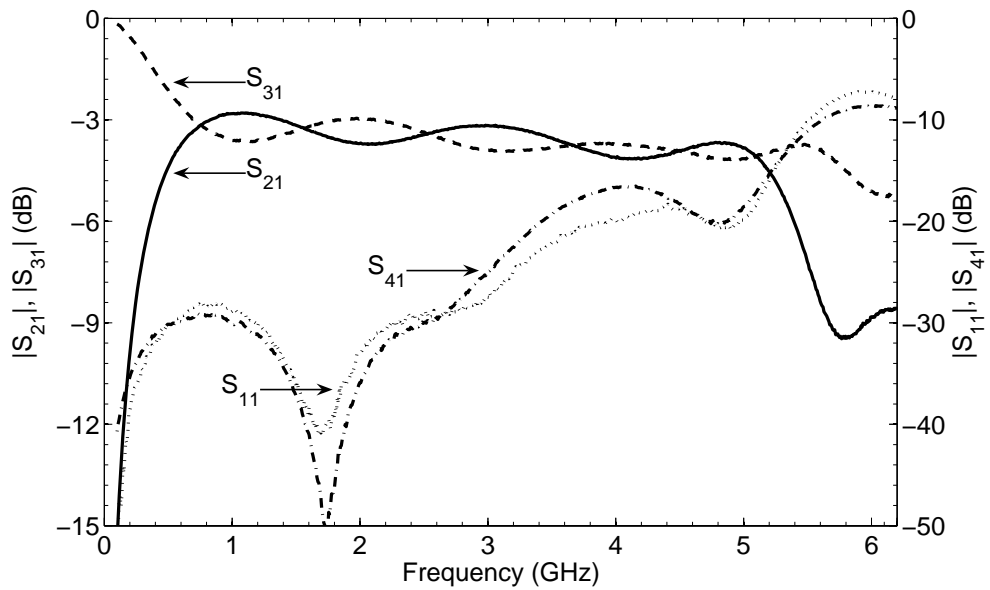
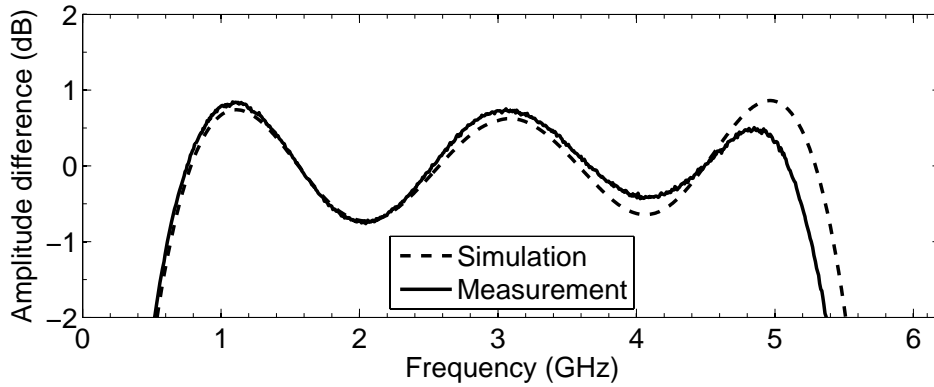
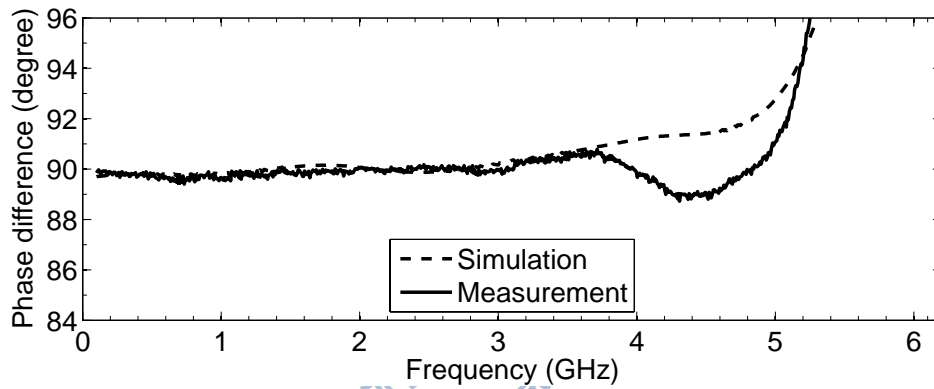


Fig. 5-35. Measured result of the five-section directional coupler.



(a)



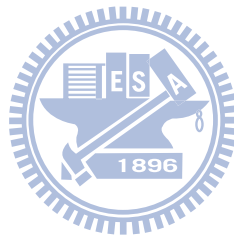
(b)

Fig. 5-36. (a) Amplitude difference between the coupled and through ports. (b) Phase difference between the coupled and through ports.

## 5.7 Summary

Two types of enhanced coupling structures have been presented to solve the coupling strength problem of the conventional parallel-coupled microstrip lines. The coupling strength can be easily varied by adjusting the size of the ground-plane aperture and the width of inserted signal strips. This allows the relaxation of fabrication tolerances since strict dimensions are avoided. The proposed structures are easily fabricated on a single-layer substrate by the conventional PCB process. A four-pole  $\lambda/4$  parallel-coupled filter and a four-pole  $\lambda/4$

hairpin filter were constructed to demonstrate their convenient applications in many resonator configurations to enhance the coupling between adjacent resonators. Furthermore, the proposed two structures have good compatibility with the conventional coupled microstrip lines. Three 3-dB directional couplers with one, three, and five coupling sections, respectively, have been designed and fabricated by combining the conventional coupled microstrip lines with the proposed two types of tight-coupling sections. As a result, the implemented 3-dB directional couplers have a simple configuration and are very attractive for broadband applications.



## ***Chapter 6 CONCLUSION AND FUTURE WORKS***

### **6.1 Conclusion**

In this dissertation, novel low-impedance microstrip lines and tightly coupled microstrip lines have been presented to improve some important features of filters and to solve the realization difficulty of single- or multi-section 3-dB directional couplers. All of the proposed structures are easily incorporated with the conventional microstrip line on a single-layer low-dielectric-constant substrate. To demonstrate the generality of the proposed structures, all the circuits were fabricated on a commonly used substrate, namely, a Rogers RO4003 substrate with a dielectric constant of 3.58 and a thickness of 0.508 or 1.524 mm, by the conventional printed circuit board (PCB) process.

In chapter 3, the signal and ground strips have been placed on the same plane to obtain the low-impedance microstrip line. This structure is particularly useful in the low-impedance section of the stepped-impedance resonator (SIR) to further decrease the impedance ratio. As a result, the designed filter has a smaller size and a higher spurious frequency compared to the conventional one. In addition, since the conventional SIR filter is very sensitive to etching tolerances, by properly choosing the number of ground strips inside the low-impedance microstrip line, two fabrication-tolerant SIR filters were successfully realized.

In chapter 4, two interdigital coupling structures have been presented to achieve strong coupling. These two structures are used in the low-impedance section of the SIR to maintain the low impedance ratio of the SIR and to obtain large coupling between adjacent SIRs. In addition, the filter fractional bandwidth is easily varied by adjusting the parameters of interdigital coupling elements. Four four-pole wideband bandpass filters (BPFs) were designed and fabricated. All the filters have the advantages of compactness, wide bandwidth, wide stopband range, and ease of fabrication.

In chapter 5, two enhanced coupling structures have been proposed to design wideband

BPFs and tightly coupled directional couplers. Since there are many physical parameters in these two structures, design flexibility can be achieved and strict dimensions are avoided for practical applications. Two four-pole wideband BPFs have been implemented to demonstrate their facility in many filter configurations. Furthermore, the conventional coupled microstrip lines and two types of proposed tight-coupling sections have good compatibility with each other. We have designed the one-, three-, and five-section 3-dB directional couplers for future broadband applications (e.g., ultra-wideband (UWB)).

Since the proposed microstrip lines have signal or ground strips on both sides of the substrate via via-holes, they require the double-sided fabrication process. Thereby, compared to the conventional microstrip line, misalignment between different layers during the fabrication process may become a critical factor in the proposed structures. As a matter of fact, misalignment in the conventional PCB process is usually very small so that it would not contribute to the severe deviation from the specified response in the proposed circuits. On the other hand, via-holes are necessary and will become a limitation for the proposed structures as the frequency of the designed circuit is high. This is because, compared to the line width and gap spacing, the via-hole has a larger minimum size and cannot be reduced according to the frequency in the conventional PCB process.

## **6.2 Future Works**

In chapters 3 and 4, a pair of transmission zeros are realized by a thin cross-coupling microstrip line on the top or bottom of the filter. The length of the microstrip line should be short enough so that its first resonant frequency would be higher than the first spurious frequency of the filter. However, if a high-dielectric-constant substrate (e.g., RT/Duroid 6010 substrate with a dielectric constant of 10.8) is used, the line will be too short to produce a pair of transmission zeros on both sides of the passband. Therefore, other filter configurations may

be adopted to introduce a cross coupling between nonadjacent resonators directly, instead of by a cross-coupling microstrip line.

In chapter 5, due to the unequal even- and odd-mode phase velocities of the proposed enhanced coupling structures, the directional coupler cannot have high directivity. Since there are many physical parameters for design flexibility in these two structures, we may adjust these physical parameters to obtain enough coupling along with the same even- and odd-mode effective dielectric constants.

The enhanced coupling structures in chapters 4 and 5 may have the potential to design a BPF that covers the UWB passband. Since the first spurious passband is a critical point in the wideband filter design, we can use the SIRs with the same fundamental resonant frequency but with different spurious resonant frequencies to further widen the upper stopband, as mentioned in [13] and [15]. Moreover, the proposed two coupling structures in chapter 5 are suitable for other microwave component design, such as rat-race couplers [64] and asymmetric directional couplers [65]. In addition to the PCB circuit, they can be applied to the monolithic microwave integrated circuit (MMIC).

## REFERENCES

- [1] S. B. Cohn, "Parallel-coupled transmission-line-resonator filters," *IRE Trans. Microw. Theory Tech.*, vol. MTT-6, no. 2, pp. 223–231, Apr. 1958.
- [2] C. Y. Chang and T. Itoh, "A modified parallel-coupled filter structure that improves the upper stopband rejection and response symmetry," *IEEE Trans. Microw. Theory Tech.*, vol. 39, no. 2, pp. 310–314, Feb. 1991.
- [3] M. Makimoto and S. Yamashita, "Compact bandpass filters using stepped impedance resonators," *Proc. IEEE*, vol. 67, no. 1, pp. 16–19, Jan. 1979.
- [4] M. Makimoto and S. Yamashita, "Bandpass filters using parallel coupled stripline stepped impedance resonators," *IEEE Trans. Microw. Theory Tech.*, vol. MTT-28, no. 12, pp. 1413–1417, Dec. 1980.
- [5] M. Sagawa, M. Makimoto, and S. Yamashita, "A design method of bandpass filters using dielectric-filled coaxial resonators," *IEEE Trans. Microw. Theory Tech.*, vol. MTT-33, no. 2, pp. 152–157, Feb. 1985.
- [6] Y. Qian, K. Yanagi, and E. Yamashita, "Characterization of a folded stepped impedance resonator for miniature microstrip bandpass filter applications," in *Proc. 25th Eur. Microw. Conf.*, Bologna, Italy, Sep. 1995, vol. 2, pp. 1209–1211.
- [7] M. Sagawa, M. Makimoto, and S. Yamashita, "Geometrical structures and fundamental characteristics of microwave stepped-impedance resonators," *IEEE Trans. Microw. Theory Tech.*, vol. 45, no. 7, pp. 1078–1085, Jul. 1997.
- [8] S. Y. Lee and C. M. Tsai, "New cross-coupled filter design using improved hairpin resonators," *IEEE Trans. Microw. Theory Tech.*, vol. 48, no. 12, pp. 2482–2490, Dec. 2000.
- [9] M. Makimoto and S. Yamashita, *Microwave Resonators and Filters for Wireless*



*Communication: Theory, Design and Application*. Berlin, Germany: Springer-Verlag, 2001.

- [10] J. T. Kuo and E. Shih, "Microstrip stepped impedance resonator bandpass filter with an extended optimal rejection bandwidth," *IEEE Trans. Microw. Theory Tech.*, vol. 51, no. 5, pp. 1554–1559, May 2003.
- [11] C. W. Tang and H. H. Liang, "Parallel-coupled stacked SIRs bandpass filters with open-loop resonators for suppression of spurious responses," *IEEE Microw. Wireless Compon. Lett.*, vol. 15, no. 11, pp. 802–804, Nov. 2005.
- [12] C. F. Chen, T. Y. Huang, and R. B. Wu, "Compact microstrip cross-coupled bandpass filters using miniaturized stepped impedance resonators," in *Proc. Asia-Pacific Microw. Conf.*, Suzhou, China, Dec. 2005, vol. 1, pp. 493–496.
- [13] C. F. Chen, T. Y. Huang, and R. B. Wu, "Design of microstrip bandpass filters with multiover spurious-mode suppression," *IEEE Trans. Microw. Theory Tech.*, vol. 53, no. 12, pp. 3788–3793, Dec. 2005.
- [14] C. F. Chen, T. Y. Huang, and R. B. Wu, "Novel compact net-type resonators and their applications to microstrip bandpass filters," *IEEE Trans. Microw. Theory Tech.*, vol. 54, no. 2, pp. 755–762, Feb. 2006.
- [15] S. C. Lin, P. H. Deng, Y. S. Lin, C. H. Wang, and C. H. Chen, "Wide-stopband microstrip bandpass filters using dissimilar quarter-wavelength stepped-impedance resonators," *IEEE Trans. Microw. Theory Tech.*, vol. 54, no. 3, pp. 1011–1018, Mar. 2006.
- [16] A. Djaiz and A. Denidni, "A new compact microstrip two-layer bandpass filter using aperture-coupled SIR-hairpin resonators with transmission zeros," *IEEE Trans. Microw. Theory Tech.*, vol. 54, no. 5, pp. 1929–1936, May 2006.
- [17] T. H. Huang, H. J. Chen, C. S. Chang, L. S. Chen, Y. H. Wang, and M. P. Houn, "A novel compact ring dual-mode filter with adjustable second-passband for dual-band applications," *IEEE Microw. Wireless Compon. Lett.*, vol. 16, no. 6, pp. 360–362, Jun.

2006.

- [18] J. Lange, "Interdigitated stripline quadrature hybrid," *IEEE Trans. Microw. Theory Tech.*, vol. MTT-17, no. 12, pp. 1150–1151, Dec. 1969.
- [19] R. Waugh and D. LaCombe, "Unfolding the Lange coupler," *IEEE Trans. Microw. Theory Tech.*, vol. MTT-20, no. 11, pp. 777–779, Nov. 1972.
- [20] D. M. Pozar, *Microwave Engineering*, 3rd ed. New York: Wiley, 2005.
- [21] Y. Konishi, I. Awai, Y. Fukuoka, and M. Nakajima, "A directional coupler of a vertically installed planar circuit structure," *IEEE Trans. Microw. Theory Tech.*, vol. 36, no. 6, pp. 1057–1063, Jun. 1988.
- [22] S. Y. Zheng, W. S. Chan, and K. F. Man, "Broadband coupler using improved vertically installed planar structure," in *Proc. 4th Eur. Conf. Antennas Propag.*, Barcelona, Spain, Apr. 2010.
- [23] T. Tanaka, K. Tsunoda, and M. Aikawa, "Slot-coupled directional couplers between double-sided substrate microstrip lines and their applications," *IEEE Trans. Microw. Theory Tech.*, vol. 36, no. 12, pp. 1752–1757, Dec. 1988.
- [24] F. Tefiku, E. Yamashita, and J. Funada, "Novel directional couplers using broadside-coupled coplanar waveguides for double-sided printed antennas," *IEEE Trans. Microw. Theory Tech.*, vol. 44, no. 2, pp. 275–282, Feb. 1996.
- [25] H. Okazaki and T. Hirota, "Multilayer MMIC broad-side coupler with a symmetric structure," *IEEE Microw. Guided Wave Lett.*, vol. 7, no. 6, pp. 145–146, Jun. 1997.
- [26] K. Sachse and A. Sawicki, "Quasi-ideal multilayer two- and three-strip directional couplers for monolithic and hybrid MIC's," *IEEE Trans. Microw. Theory Tech.*, vol. 47, no. 9, pp. 1873–1882, Sep. 1999.
- [27] A. Sawicki and K. Sachse, "Novel coupled-line conductor-backed coplanar and microstrip directional couplers for PCB and LTCC applications," *IEEE Trans. Microw. Theory Tech.*, vol. 51, no. 6, pp. 1743–1751, Jun. 2003.

- [28] G. L. Hanley, "Parallel line microstrip coupler design for tight coupling values," in *Proc. 1st Eur. Microw. Conf.*, Sep. 1969, pp. 307.
- [29] M. Nakajima and E. Yamashita, "A quasi-TEM design method for 3 dB hybrid couplers using a semi-reentrant coupling section," *IEEE Trans. Microw. Theory Tech.*, vol. 38, no. 11, pp. 1731–1733, Nov. 1990.
- [30] K. S. Chin, M. C. Ma, Y. P. Chen, and Y. C. Chiang, "Closed-form equations of conventional microstrip couplers applied to design couplers and filters constructed with floating-plate overlay," *IEEE Trans. Microw. Theory Tech.*, vol. 56, no. 5, pp. 1172–1179, May 2008.
- [31] J. C. Chiu, C. M. Lin, and Y. H. Wang, "A 3-dB quadrature coupler suitable for PCB circuit design," *IEEE Trans. Microw. Theory Tech.*, vol. 54, no. 9, pp. 3521–3525, Sep. 2006.
- [32] C. P. Chang, J. C. Chiu, H. Y. Chiu, and Y. H. Wang, "A 3-dB quadrature coupler using broadside-coupled coplanar waveguides," *IEEE Microw. Wireless Compon. Lett.*, vol. 18, no. 3, pp. 191–193, Mar. 2008.
- [33] Y. Tajima and S. Kamihashi, "Multiconductor couplers," *IEEE Trans. Microw. Theory Tech.*, vol. MTT-26, no. 10, pp. 795–801, Oct. 1978.
- [34] G. Kemp, J. Hobdell, and J. W. Biggin, "Ultra-wideband quadrature coupler," *Electron. Lett.*, vol. 19, no. 6, pp. 197–199, Mar. 1983.
- [35] J. S. Izadian, "A new 6-18 GHz, -3 dB multisection hybrid coupler using asymmetric broadside, and edge coupled lines," in *IEEE MTT-S Int. Microw. Symp. Dig.*, Jun. 1989, vol. 1, pp. 243–246.
- [36] C. Person, J. P. Coupez, S. Toutain, and M. Morvan, "Wideband 3 dB/90° coupler in multilayer thick-film technology," *Electron. Lett.*, vol. 31, no. 10, pp. 812–813, May 1995.
- [37] A. M. Abbosh and M. E. Bialkowski, "Design of compact directional couplers for UWB

- applications,” *IEEE Trans. Microw. Theory Tech.*, vol. 55, no. 2, pp. 189–194, Feb. 2007.
- [38] A. M. Abbosh and M. E. Bialkowski, “Design of ultra wideband 3DB quadrature microstrip/slot coupler,” *Microw. Opt. Technol. Lett.*, vol. 49, no. 9, pp. 2101–2103, Sep. 2007.
- [39] M. Nedil and Tayeb A. Denidni, “A new ultra wideband directional coupler based on a combination between CB-CPW and microstrip technologies,” in *IEEE MTT-S Int. Microw. Symp. Dig.*, Atlanta, GA, USA, Jun. 2008, pp. 1219–1222.
- [40] A. Moscoso-Martir, J. G. Wanguemert-Perez, I. Molina-Fernandez, and E. Marquez-Segura, “Slot-coupled multisection quadrature hybrid for UWB applications,” *IEEE Microw. Wireless Compon. Lett.*, vol. 19, no. 3, pp. 143–145, Mar. 2009.
- [41] H. C. Chen and C. Y. Chang, “Modified vertically installed planar couplers for ultrabroadband multisection quadrature hybrid,” *IEEE Microw. Wireless Compon. Lett.*, vol. 16, no. 8, pp. 446–448, Aug. 2006.
- [42] L. Zhu and K. Wu, “Multilayered coupled-microstrip lines technique with aperture compensation for innovative planar filter design,” in *Proc. Asia-Pacific Microw. Conf.*, Singapore, Nov. 1999, vol. 2, pp. 303–306.
- [43] S. Im, C. Seo, J. Kim, Y. Kim, and N. Kim, “Improvement of microstrip open loop resonator filter using aperture,” in *IEEE MTT-S Int. Microw. Symp. Dig.*, Jun. 2002, vol. 3, pp. 1801–1804.
- [44] M. D. C. Velazquez-Ahumada, J. Martel, and F. Medina, “Parallel coupled microstrip filters with ground-plane aperture for spurious band suppression and enhanced coupling,” *IEEE Trans. Microw. Theory Tech.*, vol. 52, no. 3, pp. 1082–1086, Mar. 2004.
- [45] M. K. Mandal and S. Sanyal, “Compact wideband bandpass filter,” *IEEE Microw. Wireless Compon. Lett.*, vol. 16, no. 1, pp. 46–48, Jan. 2006.
- [46] P. H. Deng, C. H. Wang, and C. H. Chen, “Novel broadside-coupled bandpass filters using both microstrip and coplanar-waveguide resonators,” *IEEE Trans. Microw. Theory*

- Tech.*, vol. 54, no. 10, pp. 3746–3750, Oct. 2006.
- [47] T. N. Kuo, S. C. Lin, C. H. Wang, and C. H. Chen, “Compact bandpass filters based on dual-plane microstrip/coplanar-waveguide structure with quarter-wavelength resonators,” *IEEE Microw. Wireless Compon. Lett.*, vol. 17, no. 3, pp. 178–180, Mar. 2007.
- [48] M. K. Mandal and S. Sanyal, “Compact wide-band bandpass filter using microstrip to slotline broadside-coupling,” *IEEE Microw. Wireless Compon. Lett.*, vol. 17, no. 9, pp. 640–642, Sep. 2007.
- [49] M. Tran and C. Nguyen, “Modified broadside-coupled microstrip lines suitable for MIC and MMIC applications and a new class of broadside-coupled band-pass filters,” *IEEE Trans. Microw. Theory Tech.*, vol. 41, no. 8, pp. 1336–1342, Aug. 1993.
- [50] J. T. Kuo and E. Shih, “Wideband bandpass filter design with three-line microstrip structures,” in *IEEE MTT-S Int. Microw. Symp. Dig.*, May 2001, vol. 3, pp. 1593–1596.
- [51] W. Menzel, L. Zhu, K. Wu, and F. Bogelsack, “On the design of novel compact broad-band planar filters,” *IEEE Trans. Microw. Theory Tech.*, vol. 51, no. 2, pp. 364–370, Feb. 2003.
- [52] Y. C. Chiou, J. T. Kuo, and E. Cheng, “Broadband quasi-Chebyshev bandpass filters with multimode stepped-impedance resonators (SIRs),” *IEEE Trans. Microw. Theory Tech.*, vol. 54, no. 8, pp. 3352–3358, Aug. 2006.
- [53] C. L. Hsu, F. C. Hsu, and J. T. Kuo, “Microstrip bandpass filters for ultra-wideband (UWB) wireless communications,” in *IEEE MTT-S Int. Microw. Symp. Dig.*, Jun. 2005, pp. 679–682.
- [54] T. N. Kuo, S. C. Lin, C. H. Wang, and C. H. Chen, “New coupling scheme for microstrip bandpass filters with quarter-wavelength resonators,” *IEEE Trans. Microw. Theory Tech.*, vol. 56, no. 12, pp. 2930–2935, Dec. 2008.
- [55] M. Dishal, “Alignment and adjustment of synchronously tuned multiple-resonant-circuit filters,” *Proc. IRE*, vol. 39, no. 11, pp. 1448–1455, Nov. 1951.

- [56] G. L. Matthaei, L. Young, and E. M. T. Jones, *Microwave Filters, Impedance-Matching Networks, and Coupling Structures*. Norwood, MA: Artech House, 1980.
- [57] J. S. Hong and M. J. Lancaster, *Microstrip Filters for RF/Microwave Applications*. New York: Wiley, 2001.
- [58] R. Mongia, I. Bahl, and P. Bhartia, *RF and Microwave Coupled-Line Circuits*. Norwood, MA: Artech House, 1999.
- [59] E. G. Cristal and L. Young, "Theory and tables of optimum symmetrical TEM-mode coupled-transmission-line directional couplers," *IEEE Trans. Microw. Theory Tech.*, vol. MTT-13, no. 5, pp. 544–558, Sep. 1965.
- [60] J. S. Wong, "Microstrip tapped-line filter design," *IEEE Trans. Microw. Theory Tech.*, vol. MTT-27, no. 1, pp. 44–50, Jan. 1979.
- [61] J. S. Hong, E. P. McErlean, and B. M. Karyamapudi, "A high-temperature superconducting filter for future mobile telecommunication systems," *IEEE Trans. Microw. Theory Tech.*, vol. 53, no. 6, pp. 1976–1981, Jun. 2005.
- [62] M. D. C. Velazquez-Ahumada, J. Martel, and F. Medina, "Parallel coupled microstrip filters with floating ground-plane conductor for spurious-band suppression," *IEEE Trans. Microw. Theory Tech.*, vol. 53, no. 5, pp. 1823–1828, May 2005.
- [63] Y. S. Lin, C. H. Wang, C. H. Wu, and C. H. Chen, "Novel compact parallel-coupled microstrip bandpass filters with lumped-element  $K$ -inverters," *IEEE Trans. Microw. Theory Tech.*, vol. 53, no. 7, pp. 2324–2328, Jul. 2005.
- [64] S. March, "A wideband stripline hybrid ring," *IEEE Trans. Microw. Theory Tech.*, vol. MTT-16, no. 6, pp. 361, Jun. 1968.
- [65] R. Levy, "Tables for asymmetric multi-element coupled-transmission-line directional couplers," *IEEE Trans. Microw. Theory Tech.*, vol. MTT-12, no. 3, pp. 275–279, May 1964.

# 簡 歷

姓 名：梁正憲

性 別：男

出生年月日：民國 71 年 11 月 5 日

出生地：台灣省屏東縣

學 歷：



高雄市立高雄高級中學 (民國 87 年 9 月~90 年 6 月)

國立交通大學電信工程學系 (民國 90 年 9 月~94 年 6 月)

國立交通大學電信工程研究所碩士班 (民國 94 年 9 月~96 年 6 月)

國立交通大學電信工程研究所博士班 (民國 96 年 9 月~)

論文題目：

具低阻抗及強耦合之改良微帶線及被動元件之應用

**Modified Microstrip Lines with Low Impedance and  
Enhanced Coupling for Applications in Passive Circuits**

## *Publication List*

### **A. Journal paper:**

- [1] **Cheng-Hsien Liang**, Chin-Hsiung Chen, and Chi-Yang Chang, “Fabrication-tolerant microstrip quarter-wave stepped-impedance resonator filter,” *IEEE Trans. Microw. Theory Tech.*, vol. 57, no. 5, pp. 1163–1172, May 2009.
- [2] **Cheng-Hsien Liang**, Wei-Shin Chang, and Chi-Yang Chang, “Enhanced coupling structures for tight couplers and wideband filters,” *IEEE Trans. Microw. Theory Tech.*, vol. 59, no. 3, pp. 574–583, Mar. 2011.
- [3] **Cheng-Hsien Liang** and Chi-Yang Chang, “Compact wideband bandpass filters using stepped-impedance resonators and interdigital coupling structures,” *IEEE Microw. Wireless Compon. Lett.*, vol. 19, no. 9, pp. 551–553, Sep. 2009.

### **B. Conference paper:**

- [1] **Cheng-Hsien Liang**, Wei-Shin Chang, and Chi-Yang Chang, “Novel low-impedance microstrip structures for miniaturized microstrip quarter-wave stepped-impedance resonator filters,” in *Proc. Asia-Pacific Microw. Conf.*, Hong Kong, China, Dec. 2008.
- [2] **Cheng-Hsien Liang** and Chi-Yang Chang, “Novel microstrip stepped-impedance resonator for compact wideband bandpass filters,” in *Proc. Asia-Pacific Microw. Conf.*, Singapore, Dec. 2009, pp. 941–944.
- [3] **Cheng-Hsien Liang**, Wei-Shin Chang, and Chi-Yang Chang, “Compact microstrip bandpass filters using miniaturized quarter-wavelength resonators,” in *Proc. Asia-Pacific Microw. Conf.*, Yokohama, Japan, Dec. 2010, pp. 263–266.
- [4] Wei-Shin Chang, **Cheng-Hsien Liang**, and Chi-Yang Chang, “Compact microstrip bandpass filters using miniaturized slow-wave quarter-wavelength resonators,” in *Proc. Asia-Pacific Microw. Conf.*, Yokohama, Japan, Dec. 2010, pp. 1958–1961.